UNIVERSITY OF KWAZULU-NATAL
SCHOOL OF GEOLOGICAL AND COMPUTER SCIENCES

TECTONIC EVOLUTION OF WESTERN CENTRAL MOÇAMBIQUE

By

Bernardo Miguel Bene

Submitted in fulfilment of the academic requirements for the degree of Doctor of Philosophy
in the School of Geological and Computer Sciences,
University of Kwazulu-Natal,
Durban

November 2004

DECLARATION

This thesis represent original work by the author and has not otherwise been submitted in any form for any degree or diploma to any tertiary institution. Where use has been made of the work of others it is duly acknowledged.

Bernardo M. Bene

November 2004

DEDICATION

Dedicated to the memory of
Miguel Bene
(1920-1989)

ABSTRACT

This thesis examines the geological history of western central Moçambique, with a particular emphasis on the enigmatic relationships between the Umkondo Group and the Frontier Formation. In the region the geological units can be broadly subdivided, from west to east, into the Archaean Basement Complex, the Umkondo Group, Gairezi Group and Proterozoic Báruè Complex. The Basement Complex represents the eastern edge of the Archaean Zimbabwe craton that, near its margin, has been reworked by Kibaran and Pan-African events. The Umkondo Group comprises mainly sedimentary rocks that are weakly metamorphosed and mildly deformed. These rocks unconformably overlie the Basement Complex and are overthrust by the Gairezi Group in the east. The Gairezi Group is a highly metamorphosed and strongly deformed sequence subdivided into the quartzite-schist Frontier Formation and the gneiss-schist Nházonia Formation. This group tectonically overlies the reworked eastern margin of the Zimbabwe craton. The Báruè Complex comprises all the geological units in the Moçambique Belt that was accreted to the Zimbabwe craton during the Kibaran event and reworked during the Pan-African event.

Geothermobaromtery and structural signatures show an increase up to granulites facies and an increase in deformation from west to east across the Zimbabwe craton to the Báruè Complex. No evidence could be found for a proposed sinistral strike-slip zone between the Zimbabwe craton and the Moçambique Belt. Structural and AMS data indicate the contact is an 8 Km wide duplex zone formed by the thrusting of the Moçambique Belt over the Zimbabwe craton.

Evidence from single zircon SHRIMP ages indicates that the Gairezi Group sediments were derived from the Zimbabwe craton and Limpopo Belt. They were deposited either between 1800 Ma and 1430 Ma or between 1430 Ma and 1300 Ma, depending on the interpretation of the age of one discordant zircon. This event is interpreted as rifting of the Zimbabwe craton and formation of a passive continental margin. Geological and geochronological evidence show that this sequence was deformed and metamorphosed, and underwent uplift and erosion before deposition of the Umkondo Group. The sediments of the Umkondo Group were deposited in braided stream and shallow marine environments in a peripheral foreland basin. Before lithification they were intruded by dolerites sills dated at 1105 ± 5 Ma. Palaeocurrent data in previous studies indicate a source region to the west and north-west. The geochemistry presented here indicates a cratonic source and a recycled orogen source while SHRIMP ages reveal that these sources were the Zimbawe craton and Limpopo Belt.

The Umkondo Group and the Ritschersflya Supergroup of western Dronning Maud Land, Antarctica, have been considered sequences that were originally deposited in the same sedimentary basin. However, geochemical evidence reveals that the Ritschersflya sediments were derived from an active arc that must have separated the two sequences. Consequently two separate basins must have formed during Kibaran times, one on the Zimbabwe craton and another on the Archaean Grunehogna Province in Antarctica. This needs to be taken into consideration in tectonic models for the Kibaran and in any reconstruction of Rodinia and Gondwana.

ACKNOWLEDGMENTS

I would like to thank World Bank, SAREC, DAAD and Eduardo Mondlane University for all financial support.

I owe special gratitude to Professor Mike K. Watkeys, for his supervision, criticism, encouragement and patience. Thank you so much. Many thanks to Dr. J. Reinhardt for his co-supervision, helpful assistance and advice.

Many thanks to the staff members in the school for their interest and encouragement and to Debbie Mackrory for logistical and administration work.

Grateful acknowledgements are made to Roy Seyambu, Pat Suthan, Mukesh Seyambu and Mark David for their technical assistance, car lifts and unforgettable Friday lunches.

Thank you to the postgraduate and undergraduate students, in special Samantha Perrit and Claire Grant for their helpful assistance, encouragement and discussion. The comments and reviews by S. Perrit are much appreciated. I am thankful to Rio Leuci and Charl Bosman for constant GIS assistance, support and motivation.

I wish to acknowledge and thank the following people:
*Dr. Richard Armstrong of the Research School of Earth Sciences of the Australian National University for his great help with U-Th-Pb SHRIMP analyses.
*Professor A. Mitchell of the Department of Geology of the University of Durban-Westville for his support with Microprobe analyses.
*Dr. Martin Klausen for his comments, ideas and helpful input.
*Frank Sokolic of the School of Life & Environmental Sciences for his great constant GIS assistance. Thank you Frank.
*Mark David Davis for his support with scanner and his comments.
*Soren Greenwood for his constant computer assistance.

Many thanks to my flatmate Gilberto Mahumane and to Jorge Sitoe for companionship, car lifts and for many constant constructive (?) interruptions and discussions making my stay in Durban very enjoyable.

Special thanks must go to Julieta Mucabele and Francisco Simango for their constant assistance and moral support to my family during my absence. Thanks, I will not forget.

I wish to thank my mother Carlota, sisters and brothers for their support during my all study period.

Finally special gratitude must go to my wife Gina and my kids Tilinha, Nandinho and Denny for their all inspiration, constant support, and tolerance through long periods of solitude and weekend social life sacrifices. I love you.

CONTENTS

CHAPTER 1

INTRODUCTION

1.1 PURPOSE AND AIMS

The study area in western central Moçambique has been the subject of only limited reconnaissance geological work with a small number of the short reports describing various aspects of the geology (Figure 1.1).

In spite of these studies, very little is known about the nature of metamorphism and deformation, the ages of these events, relationships between the crustal units and the geochemical and tectonic evolution of the area. The metamorphism of the study area is known only from petrographic data without considering in any quantitative detail the compositions of the minerals along the P-T paths.

The main aim of this thesis is to establish the tectonic development of the various lithostratigraphic units that crop out within the area under investigation, the conditions of metamorphism during structural events and the age of these events. This main objective has been achieved by:

1.The selection of critical areas for detailed study to establish the relationship between important units.

2. The mapping of those areas and collection of samples for laboratory analyses.

1.2 LOCATION AND GEOGRAPHICAL SETTING

The area under investigation is situated between the latitudes 18° 55' South and 20° 29' South and longitude 33° 30' East and by the Zimbabwe-Moçambique international border in west. It lies entirely within Manica Province along the western margin of Moçambique "mobile belt" in central Moçambique (Figure 1.1). The study area has a north-south length of approximately 170 km and an east-west width of approximately 70 km, covering an area of 12 000 km^2.

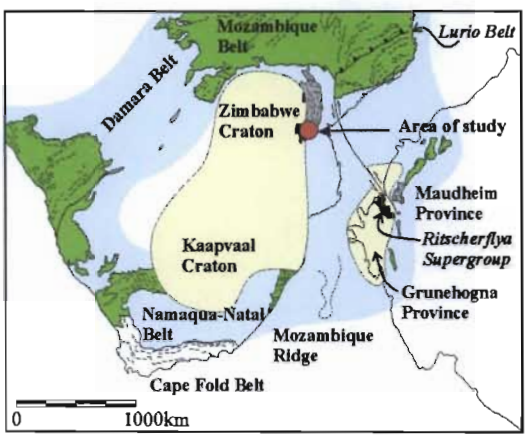

Figure1.1 Location of the study area within 'loose-fit' model for southeast Africa and western Dronning Maud Land, Antarctica, during Proterozoic time (After Perritt & Watkeys, 2003)

Gravel roads link the main towns and localities (Espunbagera-Dacata-Dombe-Sussundenga-Mavita-Rotanda), except Manica and Chimoio, which are the most important towns and are linked by railway and tarred road (Figure 1.2). The railway also links Beira (Moçambique) at the coast to Mutare (Zimbabwe).

The area is bounded by a mountainous region extending from the Chimanimani Mountains and Sitatonga Ranges, along the Zimbabwe-Moçambique international border in the south, through a series of outliers in the Sussundenga and Chicamba Real Dam area to the Bandula region in the north. These mountains are formed by deformed erosion-resistant quartzite intercalated with mica-schist reaching an

altitude of 2437 m above sea level on the *Monte Binga*. In the east the area is dominated by a plateau.

The northern part of the area is drained by the Messica and Révuè Rivers, which flow southwards through the Chicamba Real Dam. The principal drainage is by way of the Búzi River and its tributaries (Révuè, Lucite and Mussapa Rivers) in the south, flowing eastwards into the Indean Ocean.

The vegetation consists mainly of grasses and various tree species. The most widespread trees in the area is *Brachystegia* species with some patches of *Swartzia madagascarensis, Pterocarpos angolenses, Dalbergia melanoxylon* and *Khaya nyasica* (Sousa, 1951).

The climate is subtropical with dry and cold winters in the Chimanimani mountain regions and wet tropical conditions in the savannahs in the eastern part of the study area.

1.3 PREVIOUS GEOLOGICAL WORK

The Precambrian rocks within the study area in the Manica province, central Moçambique had only been investigated previously by reconnaissance geological work. The area is unpromising from an economic minerals point of view and a small number of short reports describing various aspects of the geology.

The initial work was by Andrade in 1894 who recognised the main lithological groups. Between 1911 and 1914 many geologists of the Imperial Institute of the United Kingdom reported on the general prospecting for occurrences of gold, asbestos, coal and marble. In 1923, Teale produced his report, "The geology of the Portuguese East Africa between the Zambezi and Sabi Rivers", which covered general geological aspects of the area between those two rivers. Andrade (1929) published a short report in which he discussed the Moçambican crystalline rocks and correlated them with units in Zimbabwe.

The first structural map of Moçambique, at a scale of 1:300 000, was compiled by Dias (1956) who showed the general structure of the country. Martins (1957) observed the occurrence of serpentinite and asbestos in the Mavita region. In the explanatory notes of the geological map of Moçambique (1:2 000 000), which replaced the map that was published in 1949, Freitas (1957) described the various rock formations, which were accompanied by stratigraphic tables. He showed field relationship between different formations in various parts of the territory and in some cases between these and those of neighbouring areas. All this previous geological work was patchy and conducted only at a reconnaissance level to delineate the lithological groups.

Vail (1964) was the first geologist to report in detail geological aspects of Moçambique and Zimbabwe, and publish a (1:250 000) geological map of the region between the Rotanda and Lucite River. He described three geological units: gneiss of the Moçambique Belt, quartzite and pelites of the Umkondo System and recent sedimentary cover. In 1965 he presented the main lithological formations of the eastern part of central Africa. He discussed their structural relations, geochronological aspects and correlated the geology of Moçambique to the neighbouring countries. Araújo & Gouveia (1965) worked in the Precambrian formations of the Manica province and produced a geological report. In 1966 Vail in his work, "Aspects of the stratigraphy and the structure of the Umkondo System in the Manica Belt of Southern Rhodesia and Moçambique an outline of the regional geology" provided a description of new concepts about the lithology and regional sedimentation, structure, metamorphism and he identified correlation problems.

Pinto (1969) investigated the central and western parts of the Manica and Sofala districts describing the field occurrence, petrography, geochemistry and petrogenesis of the Sofala and Manica granites. He reported the occurrence of three types of

granites: cratonic granites, granites of the Moçambique Belt (synkinematic granites) and the Serra Gorongosa granites (anorogenic granites).

Rebolo (1972) analysed the geochemistry of the Umkondo Group rocks and Umkondo dolerites of the Mavita, Gogoi and Espungabera areas.

Pinna *et al.* (1987) studied the greenstones, granitoids and metasediments of the Archaean Manica Group and Frontier Formation. The Frontier Formation was included in the Gairezi Group and the granitoids of the Madzuire and Matambo Groups were included in the Moçambique Belt.

Manuel (1992) described the geology, petrography, and geochemistry and mineral deposits of the Manica Greenstone Belt. Manhiça (1998) studied the boundary relationships between the Zimbabwe Archaean Craton and the Moçambique "mobile belt" and the geology of the latter.

From the above summary, it can be seen that the area studied in this thesis has been the subject of various geological investigations, but none of them are detailed. Very little is still known about the metamorphism during the structural events, the ages of these events and relationships between the crustal units and the geochemical and tectonic evolution.

1.4 OUTLINE OF GEOLOGY

The area under investigation is constrained between the latitudes 18° 55' South and 20° 29' South, and longitude 33° 30' East and by the Zimbabwe-Moçambique international border in west (Figure 1.2). It lies entirely within the Manica Province along the western margin of the Moçambique "mobile belt" in central Moçambique and is underlain by rocks of Precambrian age.

On the basis of the lithostratigraphic principles the Precambrian is subdidivided into the Manica Group, Gairezi Group, Umkondo Group and Báruè Complex.

1.4.1 MANICA GROUP

The Manica Group represents the eastern edge of the Archaean Zimbabwe Craton (Figure 1.3). It is subdivided into the Macequece Formation, the Vumba granite gneiss and the Messica granite gneiss.

The Macequece Formation (green and grey on Figure 1.3) is the oldest unit and occurs as very small discontinuous bodies for the most part of the study area (Figure 1.3). The main rock types are peridotite, serpentinite, amphibolite, tremolite-, actinolite- and chlorite-schists intercalated with banded magnetite quartzite and banded iron formation (Araújo *et al.*, 1973). In general, the Macequece Formation is characterized by a cleavage striking northwest-southeast, dipping steeply to either the northeast or southwest. Locally, east-west striking and steeply north dipping steeply cleavage also occurs.

The Vumba granite gneiss (light pink on Figure 1.3) intrudes the Macequece Formation. To the west it continues into Zimbabwe where it is termed the Umtali Batholith, also known as "Old Granite" (Oberholzer, 1964).

The Messica granite gneiss (dark pink on Figure 1.3) forms a narrow north-south zone (Figure 1.3).

It is distinguished by a consistently near north-south striking cleavage, dipping between 60° and 86° either to the west or east. Eastwards, the cleavage becomes close to vertical and strikes north-south.

1.4.2 GAIREZI GROUP

The Gairezi Group forms a series of outliers across the study area (Figure 1.4). It consists of the Nhazónia (brown in Figure

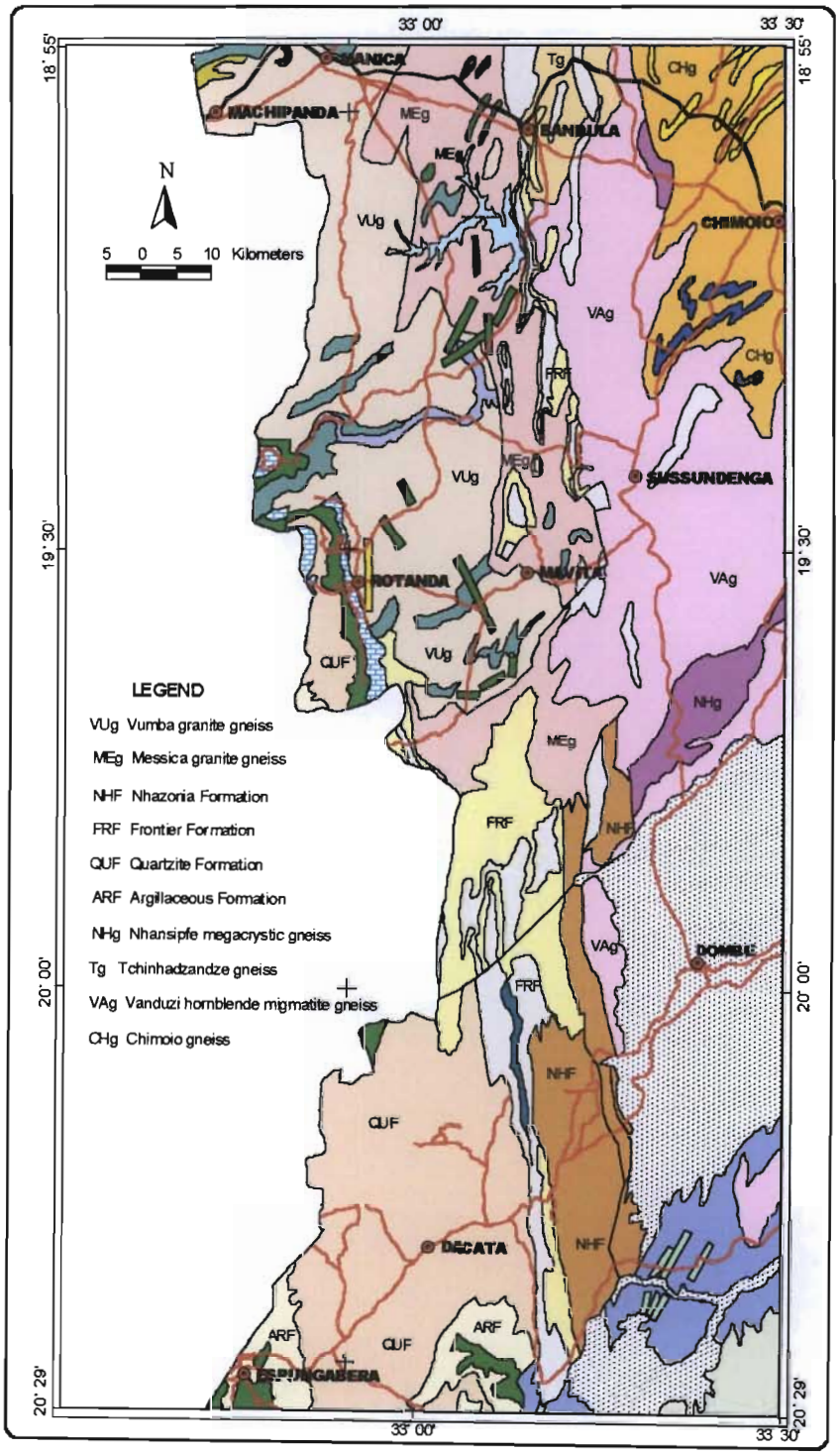

Figure 1.2 Geological map of the study area

1.4) and Frontier (yellow and light grey on Figure 1.4) Formations. According to Afonso (1978) the Nhazónia Formation underlies the Frontier Formation.

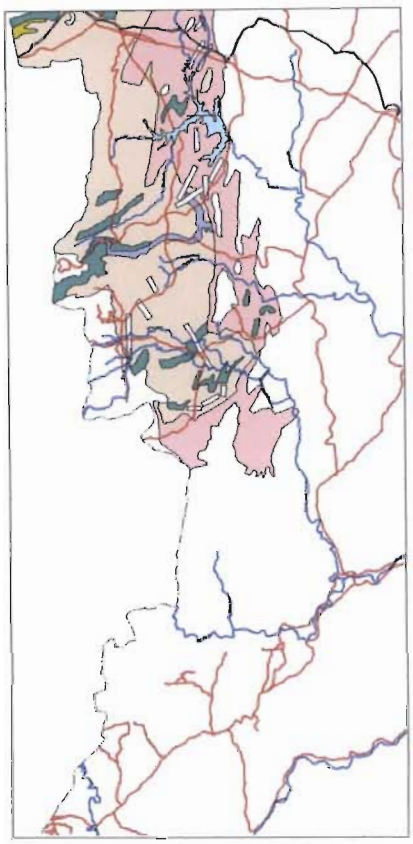

Figure 1.3 Geological map showing Manica Group. Scale 1:22500. (See Figure 1.1 for legend)

The Nhazónia Formation constitutes an association of mica-schists (feldsphathic and staurolite-garnet-mica schist) and quartzofeldspathic gneisses. The cleavage generally strikes north-south and dips very steeply to the east.

The Frontier Formation is a quartzite-schist complex (Pinna *et al.*, 1987) forming a stack of duplexes representing a large thrust zone (Watson, 1969).

The base rests unconformaby on the Manica

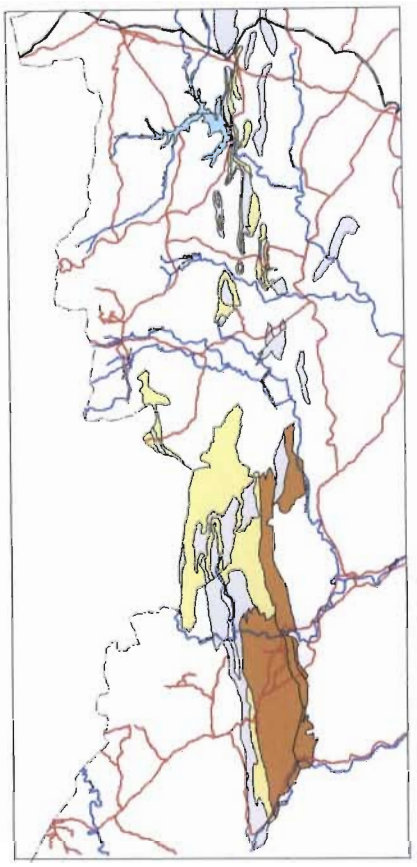

Figure 1.4 Geological map showing of Gairezi Group. Scale 1:22500. (See Figure 1.1 for legend)

Group or, is separated from it by a thrust plane (Watson, 1969). Evidence suggests that the Gairezi Group underwent folding and enough low-grade metamorphism to convert the original sand beds to quartzites before the Umkondo Group was deposited (Watson, 1969). The cleavage strikes north-south and dips steeply (~55°) to either the east or west.

1.4.3 UMKONDO GROUP

In the study area, the Umkondo Group (brown, light brown and blue on Figure 1.5) is unconformably deposited upon granitic gneisses of the Manica Group and the Gairezi Groups. In Zimbabwe it attains a maximum thickness of 3650 m in the south

(Watson, 1969) compared to 200 m further north in the Inyanga region (Stocklmayer, 1978). It comprises four formations: Calcareous Formation, Lower Argillaceous Formation, Quartzite Formation and Upper Argillaceous Formation.

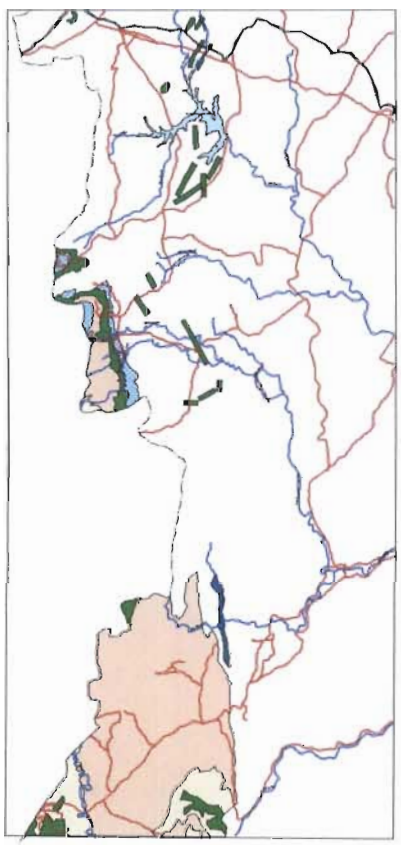

Figure 1.5 Geological map showing Umkondo Group rocks. Scale 1:22500. (See Figure 1.1 for legend).

The Umkondo Group sediments were intruded by thick dolerite sills (green on Figure 1.5) at 1100 Ma (Wingate, 2001). The total thickness of the intrusions is estimated to range from 600 m to 1200 m (Watson, 1969), whilst the individual sheets are 70-200 m thick (Swift, 1962; Watson 1969). They are metamorphosed to lowermost greenschist facies in the west and

to mid-greenschist facies in eastern Zimbabwe (Munyanywia, 1999).

1.4.4 BÁRUÈ COMPLEX

The *ca* 1100 Ma Báruè Complex forms part of the Moçambique Belt and occurs east of the Garezi Group (Figure 1.6), consisting of intensively deformed amphibolite-granulite facies gneisses.

It has a north-south striking foliation, dipping steeply (61°-87°) either to the east or west. It is composed of four units of Neoproterozoic age: Chimoio gneiss, Vanduzi hornblende migmatite gneiss, Tchinhadzandze gneiss and Nhansipfe megacrystic orthogneiss (Manhiça *et al.*, 2001).

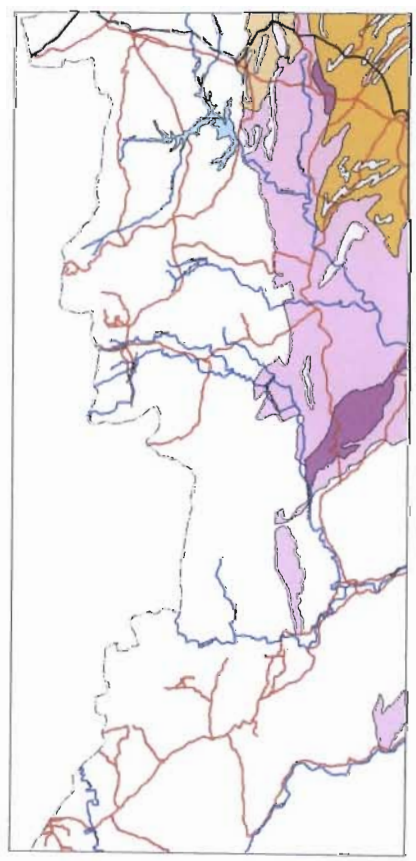

Figure 1.6 Geological map showing Báruè Complex. Scale 1:22500. (See Figure 1.1 for legend).

The Chimoio gneiss (ochre on Figure 1.6) varies between granodioritic and tonalitic orthogneisses with migmatitic melting and xenolithic enclaves rich in mafic minerals (biotite and hornblende). The Vanduzi hornblende migmatite gneiss (pink on Figure 1.6) is a heterogenous migmatitic supracrustal sequence, which contains layered, dominantly felsic rocks with subordinate mafic rocks and semipelitic gneiss. Its age is uncertain.

The Tchinhadzandze gneiss (light ochre on Figure 1.6) is composed of feldspar, quartz, biotite and hornblende. The youngest lithology of the Báruè Complex is the Nhansipfe megacrystic orthogneiss (purple on Figure 1.6) characterized by very coarse-grained feldspar augen.

CHAPTER 2

FIELD RELATIONSHIPS AND PETROGRAPHY

2.1 STRATIGRAPHIC NOMENCLATURE

The Precambrian stratigraphic nomenclature in central Moçambique was problematic for years. The earliest division was proposed by Andrade (1894) followed by Taele & Wilson (1915) and later by Andrade (1929). Freitas (1957) came with following division: *Moçambiquian System, Umkondo System and Basement Complex.* Local geologists, on stratigraphic basis, contested the creation of the *Moçambiquian System,* though the term has been used by several authors in neighbouring countries (Araújo and Gouveia, 1965).

Gouveia (1965) proposed the following stratigraphic nomenclature: *Báruè Complex, Umkondo Group*, and *Basement Complex*. Oberholzer & Afonso (1977) established new sub-divisions as follow: *Tectonic Province of Medium Zambeze, Umkondo System* and *Rhodesian Craton.* They subdivided the *Rhodesian Archaean Craton* in to the *Manica System* and the *Granite-Gneiss Complex.*

Pinna *et al.* (1987) proposed a new stratigraphic nomenclature, which is in use presently: *Báruè Complex, Umkondo Group, Gairezi Group* and *Basement Complex*.

There has been great controversy regarding the stratigraphic nomenclature of the Mesoproterozoic metasediments in Moçambique as well as in Zimbabwe. Brackenbury (1906) first introduced the term of *Umkondo Formation* during the geological work around the Umkondo Mine in Zimbabwe. Similar rocks in Moçambique were called the *Spungabera Series* by Teale & Wilson (1915) and Teale (1924), who were the first to describe these sediments (Vail, 1966).

Mennell (1920) demonstrated that the Umkondo rocks in the Sabi Valley, the Melsetter-Chipinga area and the Spungabera plateau were all related and called them the *Sabi System*, a name that has fallen into disuse. Because of their greater degrees of deformation and metamorphism he separated the rocks forming the Chimanimani Mountains from his *Sabi System* and named them the *Frontier System* (Watson, 1969). Similar rocks in Moçambique were referred as the *Chimanimani Series* by Andrade (1894), a term that has never been widely used.

Johnson (1963) recognized the Frontier sequence, the Gairezi sequence, the Melsetter sequence, and the Inyanga sequence and tentatively proposed the name *Manica Series*. It has been decided, after discussions among Directors of the geological Surveys of Southern Rhodesia and Moçambique, to call all these rocks the *Umkondo System* (Vail, 1966).

In Cashel, Melsetter and Chipinga areas, Watson (1969) subdivided the *Umkondo System,* largely on lithostratigraphic grounds, into the following series in descending age order: eastern succession *Frontier Series*, made up of strongly deformed quartzite and chlorite schist and western succession *Calcareous, Lower Argillaceous, Quartzite, and Upper Argillaceous Series* made up of less deformed and slightly metamorphosed.

Stocklmayer (1978) divided the *Umkondo Group* in Nyanga area into the *Inyanga Facies*, which is characterized by flat-lying sediments relatively less deformed and slightly metamorphosed in the west and the *Gairezi Facies* intensively deformed and relatively highly metamorphosed in the east. The name *Umkondo System* was subsequently changed to *Umkondo Group* to comply with recommended Precambrian lithostratigraphic terminology (Stocklmayer,

1981). On the basis of broad lithologic similarities, and similar metamorphic and structural setting supracrustals in Nyanga and Chimanimani, Stocklmayer (1981) subsequently subdivided the *Umkondo Group* into the *Zimbabwe Facies* representing less deformed and slightly metamorphosed metasediments to the west and *Moçambique Facies* representing intensively deformed and highly metamorphosed metasediments to the east (Munyanyiwa, 1997).

The stratigraphic terms used in this these were adopted from the system of nomenclature used by Geological Survey of Moçambique proposed by Pinna *et al.* (1987), Manuel (1992) and Manhiça (1998) with some modifications (Table 2.1).

TABLE 2.1

STRATIGRAPHIC TERMINOLOGY USED IN THIS THESIS

AGE	ERA	TECTONIC BLOCK	GEOLOGICAL FORMATION	LITHOLOGICAL UNIT	ROCK TYPE
PRECAMBRIAN	NEOPROTEROZOIC	MOÇAMBIQUE BELT BARUE COMPLEX		NHANSIPFE MEGACRYSTIC GNEISS	GNEISS
			MATAMBO GROUP	TCHINHADZANDZE GNEISS	GNEISS
				VANDUZI HORNBLENDE MIGMATITE GNEISS	GNEISS
			MADZ-UIRE GROUP	CHIMOIO GNEISS	GNEISS
	MESOPROTEROZOIC			UMKONDO DOLERITES	DOLERITE
		"UNDEFORMED" ROCKS	UMKONDO GROUP (autochthon)	UPPER ARGILLACEOUS FORMATION	SHALE, PHYLLITE, SILTSTONE
				QUARTZITE FORMATION	ORTHOQUARTZITE, SHALE, SILTSONE, SANDSTONE
				LOWER ARGILLACEOUS FORMATION	SHALE, SILTSTONE
				CALCAREOUS FORMATION	SILICEOUS, CALC-HORNEFLS
		"DEFORMED" ROCKS	GAIREZI GROUP (allochthon)	FRONTIER FORMATION	QUARTZITE, MICA-SCHIST
				NHAZONIA FORMATION	QUARTZOFELDSPATHIC SCHIST, QUARTZOFELDSPATHIC GNEISS, STAUROLITE-GARNET-SCHIST
	ARCHAEAN	BASEMENT COMPLEX	MANICA GROUP	MESSICA GRANITE GNEISS	GRANITE GNEISS
				VUMBA GRANITE GNEISS	GRANITE GNEISS
				MACEQUECE FORMATION	SERPENTINITE, PERIDOTITE, TREMOLITE-,ACTINOLITE-, CHLORITE –SCHIST, BANDED IRONSTONE, BANDED MAGNETITE QUARTZITE

3.2 INTRODUCTION

The area under investigation lies entirely within the Manica province along the western margin of the Moçambique "mobile belt" in western central Moçambique.

It is difficult to establish lithostratigraphic sequences and the contact of the different units because of the poor exposures and access difficulty due not only to the terrain but also the landmines especially within the Umkondo Group. Therefore outcrop studies are restricted to river and to road-cuts. The best exposures were studied in detail.

2.2.1 BASEMENT COMPLEX

2.2.1.1 INTRODUCTION

The Basement Complex is represented by the Manica Group that consists of Macequece Formation and of a variety of granitic rocks of Archaean age along the eastern edge of Zimbabwe Craton (Oberholzer, 1964). The intrusive granitic rocks were deformed and metamorphosed, resulting in Vumba granite gneiss and Messica granite gneiss showing a wide variation in intensity of fabrics.

2.2.1.2 MACEQUECE FORMATION

2.2.1.2.i FIELD DATA

The Macequece Formation is the oldest unit and occurs as very small discontinuous bodies only in the northeast, south, and southwest of at Mavita region (Araújo *et al.*, 1973) within Vumba granite gneiss and Tsetsera-Himalaya Farm.

The main mafic and ultramafic rock types occurring in the Macequece Formation are amphibolite, chlorite-schist and serpentinite intercalated by banded iron formation and banded magnetite quartzite. Araújo *et al.* (1973) observed occurrence also of peridotite and tremolite-actinolite-schist within the study area. All of these rocks are cut by quartz and pegmatite veins of different thicknesses and directions.

No evidence could be found for pillow structures in the field. The massive greenstone, which is serpentinite in hand specimen is dark green to greenish in colour, fine-grained, hard, with conchoidal fracture, and a well-jointed rock without any schistosity. Northeast of the Mavita village asbestos were observed related to actinolite and serpentinite of antigorite type (Araújo *et al.*, 1973). Where the massive greenstone has been sheared it has become a finely laminated chlorite-schist:

greenstone → greenschist → chlorite schist

The chlorite-schist is not hard rock, but fine to medium-grained, green in colour, with a strong cleavage, microfolded and characterized by common occurrence of garnet porphyroblasts of pyrope-almandine series with grain-size ranging between 2 mm and 20 mm.

The most common type of ferruginous rock is the banded iron formation, but in some places banded magnetite quartzite crops out. They form the tops of the highest hills, because of their hardness although they sometimes occur on low ground within the granitic rocks (Figure 2.1). In hand specimens they are approximately similar. They are heavy, fine to medium-grained, hard, grey to dark grey in colour and they are characterized by banded alternation between quartzite-rich band and magnetite-rich band.

The amphibolite is a medium to coarse massive rock, heavy, black to black green in colour. It is mainly composed of amphibole and plagioclase.

2.2.1.2.ii PETROGRAPHY

The *chlorite-schist* in thin section is composed of quartz, garnet porphyroblasts, iron oxide and parallel green flakes of chlorite.

The quartz grains (up to 30% by volume) are commonly elongate and occur throughout the rock. The quartz grains vary in size up to 1 mm long and contain faint inclusion trails. The garnet grains vary in size from 2 mm to 20 mm and they occur as porphyroblasts with quartz inclusions (Figure 2.2). They are commonly euhedral to subhedral. The iron oxide (up to 5% by volume) is euhedral to subhedral, and is probably magnetite, which occurs throughout the rock. The magnetite grain size ranges between 0.25 mm and 0.5 mm.

A penetrative schistosity is caused by the alignment of the chlorite and the elongation of quartz. The curvature of S_i (internal schistosity) is probably caused by relative rotation between the garnet porphyroblast and the matrix foliation (Figure 2.2).

The *banded iron formation* in thin section is mainly consisted of quartz, grunerite, euhedral to enhedral iron oxide probably magnetite, Ca-amphibole, epidote and hematite.

The quartz (~65% by volume) is the main constituent of the rock. The quartz grain boundary is picked out by yellow iron oxide probably limonite. The magnetite (up to 26% by volume), and change of grain size of quartz grains are parallel to the Ca-amphibole (up to 6% by volume) alignment, which defined the cleavage in the rock.

The mineral composition alteration consists of finely alternating bands of quartz and iron-rich layers that occurs in millimetre scale.

Within the iron-mica domains, there is a predominance of muscovite grains ~0.5 mm in length, elongate anhedral quartz grains up to 1 mm long in size and subhedral to euhedral magnetite grains range between 0.25 mm and 0.5 mm in diameter, showing interlocking relations. Within quartz the domains, quartz grains up to 1 mm predominate with granoblastic polygonal texture. The quartz-rich bands are generally more dominant than the iron-rich bands.

The *banded magnetite quartzite* in thin section, is mainly composed of quartz grains, white mica (probably muscovite) and euhedral to enhedral iron oxide suggesting magnetite. It shows a foliation due to grain size, and mineral composition alteration. It differs from the banded iron formation but magnetite content is low (up to 16% by volume) and consequently the content of quartz is high (up to 75% by volume).

The *amphibolite* in thin section consists of hornblende needles that are generally preferentially orientated, pleochroic from green to yellow-brown green in the very fine to fine-grained amphibolite. The actinolite-tremolite association occurs in the coarse-grained amphibolite, and granular feldspar, occurring together with low percentage of chlorite, quartz, epidote/clinozoisite series and opaque minerals. Epidote/clinozoisite series are common accessory minerals. The occurrence of opaque minerals is appreciable in the very fine to fine-grained amphibolite. Biotite is quite rare.

The hornblende (up to 90% by volume) is subhedral and acicular aggregates show preferential orientation with accentuated cleavage. The very fine to fine-grained amphibolite is characterized by high occurrence of epidote/clinozoisite series (up to 5% by volume). It exhibits seriate, sometimes random texture, and parallel growth showing interlocking relations.

The actinolite-tremolite (up to 90% by volume) in coarse-grained amphibolite is elongate fibrous prismatic crystals can be up to 5 mm long but lacking preferred orientation of the crystals and showing their interlocking relations. The actinolite usually shows normal twinning especially in elongated crystals. In the coarse-grained amphibolite the occurrence of epidote/clinozoisite series is rare.

The feldspar (5% by volume) is plagioclase but it is difficult to identify the composition. The plagioclase contains microlite inclusions with subsidiary quartz showing

Figure 2.1 An outcrop of banded iron formation (BIF) striking north-south and steeply dipping to the east around Mavita area (E 033° 05' 51.9"; S 19° 30' 36.6"). Scale bar = 50 m. View looking north.

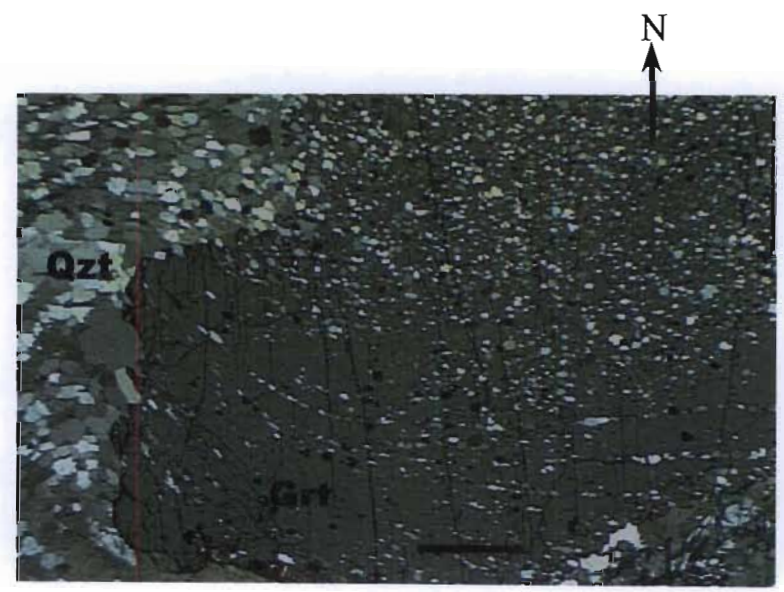

Figure 2.2 Photomicrograph of the chlorite-schist at Mavita region (E 033° 05' 51.9"; S 19° 30' 36.6") showing how quartz elongate crystals are incorporated into the garnet prophyroblast. Scale bar = 1000μm.

undulose extinction. The epidote/clinozoisite series form the medium-grained aggregates, which are pale brownish in colour. It is present as inclusions in actinolite as well as in the matrix. Small grains of opaque minerals probably magnetite, with euhedral to subhedral form, occur throughout the rock. The chlorite occurs probably as an alteration product of amphibole and epidote/clinozoisite series occurs as an alteration product of plagioclase (Deer 1992).

The granoblastic matrix of the rock is largely of fine-grained quartz, and epidote/clinozoisite series.

The *serpentinite* in thin section consists of almost completely of colourless serpentine-group minerals in the very fine to fine-grained serpentinite. In the metamorphosed serpentinite the actinolite-tremolite are replaced partially by serpentine.

2.2.1.2.iii DISCUSSION

The Macequece Formation occurs as remains of the eastern extension of the Mutare greenstone belt of Zimbabwe Archaean craton, which was subsequently deformed and metamorphosed and was intruded by granitic rocks of different Archaean ages. The volcanic rocks were metamorphosed, being subjected to different temperatures and pressures in the various parts of the greenstone belt (Phaup, 1964). As a result the greenstones now differ considerably in appearance and mineral composition.

Ages of greenstone, granites and gneiss within the Zimbabwe craton range from 3500 Ma to 2600 Ma (Blenkinsop *et al.*, 1997). Manuel (1992) established the age of the Mutare-Manica greenstone belt and the Vumba granite gneiss ranging between 3400 Ma and 2600 Ma (Rb/Sr, whole-rock). Petrographically and geochronological the Macequece Formation is well correlated to the Upper Bulawayan Supergroup forming the Zimbabwe Archaean Craton giving SHRIMP ages between 2700 Ma and 2600 Ma (Jelsma *et al.*, 1996) and Rb-Sr whole-rock isochron ages from 2720 ± 140 Ma to 2530 ± 28 Ma (Hawkesworth *et al.*, 1975).

2.2.1.3 VUMBA GRANITE GNEISS

2.2.1.3.i FIELD DATA

The Vumba granite gneiss extends from the south of Rotanda village to Manica town. The Archaean granitoids in Manica have been collectively, but informally, termed the Vumba granite after the Vumba Mountain (Manhiça, 1998). It intrudes the Macequece Formation and is unconformably overlain by quartzite-schist complex of the Frontier Formation and the Umkondo Group. To the west it continues into Zimbabwe where it is termed Umtali Batholith, also known as "Old Granite" (Oberholzer, 1964).

The granite gneiss is meso- to leucocratic depending on the presence of biotite and hornblende, medium to coarse grained, with granular texture but sometimes appears with strong cleavage. It is composed of quartz, feldspar, biotite and others ferromagnesian minerals. Near the Macequece Formation, the granitoid becomes more fine-grained and darker in colour due to the presence of biotite.

Near Rotanda village the granitic rock becomes coarser-grained and more granodioritic. Quartz-pegmatite and mafic veins of different sizes up to 100 cm striking approximately north-south cut the granitic rocks. It seems that they are related with brecciation of the granitoid. The mafic dykes vary from gabbros to dolerites and are characterized by plagioclase, clinopyroxene and black short prismatic to acicular amphibole grains.

Inequigranular megacrystic granitic rocks occur in the Chicamba area. They are characterised by feldspar porphyroclasts and granoblastic textures.

Further south the granitoid locally becomes

highly foliated, with intensive cleavage dipping southwest and mica flakes show remarkable parallelism with quartz bands and some strained quartz porphyroblasts.

2.2.1.3.ii PETROGRAPHY

In thin section the *Vumba granite gneiss* consists of feldspar, quartz, hornblende, epidote/clinozoisite series, chlorite, sphene and mica (Table 2.2, Appendix 2). It shows consertal intergrowth texture, and patches of plagioclase intergrown with vermicular quartz forming myrmekitic texture. The matrix is built up by quartz, microcline, plagioclase and biotite.

Feldspar is mainly plagioclase with some microcline and microperthite, suggesting that these rocks are granodioritic to tonalitic in composition. Manhiça *et al.*, (2001) suggest that the Vumba granite gneiss is typical of the tonalite-trondjhemite component of most Archaean granite-greenstone terrains.

According to the Michel-Lévy Method the plagioclase of the composition An_{12-21} (oligoclase) vary in percentage place to place (from 31% up to 68% by volume) as does the grain size between 1 mm and 5 mm. It occurs as equant to inequigranular granoblastic grains, showing subhedral to anhedral form. The oligoclase has a speckled appearance in its cores because of high sericitisation

Quartz varies from 28% to 58% by volume, showing anhedral form, with grain size ranging between 1 mm and 4 mm. It occurs as an essential mineral as well as secondary mineral. The microcline is a more common alkali-feldspar, showing tartan twining with a large percentage variation (1-45% by volume) characterized by anhedral form and different grains size from 0.5 mm up to 6.5 mm.

Epidote, rutile, chlorite, sericite, biotite, muscovite, and opaque minerals occur as minor accessory minerals. The biotite appears as interstitial flakes, pleochroic from dark green to brown or pale brown and readily alters to chlorite through chloritization. The rutile occurs as needle intergrowths within chloritized biotite grains. The sericite is an alteration product of plagioclase, and sericitization can result in indistinct plagioclase grain boundaries.

The matrix of the rock is made up of quartz, biotite, and muscovite, which have undergone metamorphic recrystallisation. The cleavage, where it appears, is defined by the alignment of quartz. There is also much fine-grained, interstitial quartz-feldspathic material, some of it in fine, myrmekitic intergrowths.

The feldspar has almost lost its igneous texture and the quartz shows the dynamic recrystallization with irregular grain boundary formed in response to grain growth.

2.2.1.3.iii DISCUSSION

The Vumba granite gneiss represents the continuation of Umtali batholith and intruded the Mutare-Manica greenstone belt. It gave an Rb-Sr, whole rock age between 3385 ± 255 Ma north and 2527 ± 632 Ma south of the greenstone terrain (Manuel, 1992), which represents the study area.

The Vumba granite gneiss is equivalent to the Sesombi granite in Zimbabwe dated at 2700-2600 Ma (Hawkesworth *et al.*, 1975; Blenkinsop *et al.*, 1997).

According to the petrographic characteristic, the granitic rocks suggest that they are granodioritic to tonalitic in composition. The upper Bulawayan is intruded by the Sesombi suite of granitoid of tonalitic-granodioritic in composition giving ages of about 2700 Ma with low initial ratios (Blenkinsop *et al.*, 1997) and 2602 ± 50 Ma (Hawkesworth *et al.*, 1975). The Vumba granite gneiss of tonalitic-trondjhemitic composition observed by

Manhiça *et al.* (2001) is associated to the "Old Granite" exposed north of the Mutare-Manica greenstone belt. Two $^{40}Ar/^{39}Ar$ ages on biotite samples from near Manica have yield ages of ~1084 Ma and ~1067 Ma (Manhiça *et al.*, 2001) showing thermal Kibaran event.

2.2.1.4. MESSICA GRANITE GNEISS

2.2.1.4.i FIELD DATA

The Messica granite gneiss within the study area forms a narrow zone from north of Binga Mountain to Bandula region through Chicamba Real Dam. It is bounded by Vumba granite gneiss in the west and by quartzite-schist complex of Frontier Formation in the east. No contact between Vumba granite gneiss and Messica granite gneiss was observed in the field.

Generally it is weathered in outcrop showing strong planar cleavage. It is leucocratic in colour, fine to coarse grained, and granoblastic to granolepidoblastic in texture where the phyllosilicates minerals are characterized by preferential orientation and feldspar porphyroclasts up to 6 mm in grain size. The granite gneiss becomes coarser in grain size and because of biotite it becomes darker in colour.

The Messica granite gneiss is intruded by amphibolitized mafic dykes and felsic dykes, striking north-south (Figure 2.3). In some places the pegmatite and quartz veins are boudinaged and folded. The mafic dykes vary from gabbros to dolerites and are characterized by plagioclase, clinopyroxene and black short prismatic to acicular amphibole grains.

3.2.1.4.ii PETROGRAPHY

The *Messica granite gneiss* in thin section is inequigranular as it ranges from fine to very coarse. It is composed of feldspar, quartz, mica, chlorite, apatite, sphene, and epidote (Table 2.3, Appendix 2). The percentage of biotite is considerably increased, as compared to the Vumba granite gneiss, defining a planar fabric. The Messica granite gneiss is leucocratic granite characterized by biotite and subordinate muscovite and locally, garnet (Manhiça *et al.*, 2001).

The most common feldspar is plagioclase, microcline but some places appear perthite and microperthite. The feldspar appears with inclusions of quartz, biotite, muscovite and sericite.

The plagioclase according to the Michel-Lévy Method is oligoclase (An_{10-13}). In some places microcline predominates. The sericitization of oligoclase grains (27%-62% by volume) generally is rare and they are characterized by inclusions of microlites and quartz, inequigranular, subhedral to anhedral form, showing intergrowth texture. The oligoclase grains range between 1.5 mm and 5 mm in diameter. The oligoclase is sometimes zoned. The presence of the myrmekitic and micrographic textures are common.

Rutile occurs as needle intergrowths within some chloritized biotite grains. Apatite occurs as hexagonal euhedral crystals.

Quartz grains (up to 43% by volume) are inequigranular, interlobate, subhedral to anhedral form, monocrystalline showing polygonal texture, polycrystalline with irregular grain boundaries formed probably in response to grain boundary recrystallisation. Normally elongate quartz grains are developed parallel to phyllosilicates minerals, which show a preferential orientation east-west. The quartz is picked up by thin red rim of iron oxide probable hematite. Accessory minerals are, biotite, sphene, epidote, muscovite, and magnetite. The muscovite is very uncommon and the plagioclase is commonly sericitised.

The continuous foliation is defined by subparallelism of biotite flakes.

In relation to the Vumba granite gneiss, in the Messica granite gneiss the grain-size of the main constituents increases, occurrence of feldspar decreases, biotite becomes more abundant, giving the rocks gneissic texture.

2.2.1.4.iii DISCUSSION

The Messica granite gneiss by its petrological, and geochronological characteristics is correlated to the Chilimanzi granite suite and is interpreted as the last major granitic event of the Zimbabwe Archaean Craton (Blenkinsop *et al.* 1997).

The occurrence of greenstone xenoliths within Messica granite gneiss is rare and it gives Rb-Sr ages between 2618 ± 472 Ma (Manuel, 1992) and 2578 ± 468 Ma (Manhiça *et al.*, 2001). The Chilimanzi suite granites, Zimbabwe and Masvingo batholiths provided Rb-Sr whole-rock ages of 2566 ± 56 Ma, 2618 ± 29 Ma and 2610 ± 39 Ma respectively and Hickman (1975), provided an average age of 2595 ± 25 Ma (Goodwin, 1981). Jelsma *et al.* (1996) who have yield a conventional TIMS U/Pb zircon age of 2601 ± 14 Ma observed that these post-tectonic Chilimanzi suite granites were generated through remobilisation of older granitoids.

2.2.2 GAIREZI GROUP

2.2.2.1 INTRODUCTION

The Gairezi Group consists of metasediments. It extends from Sitatonga Ranges and Chimanimani Mountains in the south, through a series of outliers in the Chicamba Dam area to the Bandula region and is bounded by Messica granite gneiss in the west and the Báruè Complex in the east.

Due the deformation complications it is difficult to determine the stratigraphic sequence. The Gairezi Group reaches its maximum thickness of 2040 m south of the Mussapa Gap in the Chimanimani Mountains (Stocklmayer, 1978).

The primary structures in the Gairezi Group have been obliterated by metamorphism and deformation, which took place during the Moçambique Belt events. The nature of the contact between the Basement Complex and the Gairezi Group is difficult to establish, because of poor exposure even along the rivers and road-cuts.

Because of numerous thrust, imbricate stacks and duplexes indicating westward movement during the Moçambique belt deformation (Tennant, 1995), the Gairezi Group has been referred to as an allochthonous sequence juxtaposed against the Umkondo Group (Allsopp *et al.*, 1989). It has been related in Zimbabwe to the Moçambique and the Gairezi Facies (Stocklmayer, 1978) and Frontier Series (Watson, 1969) of the Umkondo the Group.

The Gairezi Group comprises two formations: the Nhazónia Formation and Frontier Formation. Unfortunately the contact between them could not established.

2.2.2.2 NHAZÓNIA FORMATION

2.2.2.2.i FIELD DATA

The Nhazónia Formation bounded by the Frontier Formation in the east and by the Báruè Complex and the overlying Quaternary Formation in the west. It constitutes an association of quartzofeldspathic mica-schists, quartzofeldspathic gneiss, and staurolite-garnet-schist. The quartzofeldspathic mica-schist exhibits granolepidoblastic texture but the rocks in this formation are characterized by mylonitic and micromylonitic textures (Afonso, 1978). The cleavage in general strikes north-south as do the pegmatite and quartz veins. The Nhazónia Formation has been considered to form the basement rocks of the Frontier quartzites (Afonso, 1978).

2.2.2.2.ii PETROGRAPHY

The *quartzofeldspathic mica-schist* is characterised by a continuous foliation (schistosity) mainly defined by subparallel biotite and muscovite (Figure 2.4).

In thin section it is predominantly composed of quartz (~ 70% by volume) muscovite (up to 20% by volume) feldspar (up to 4% by volume) and scarce, tourmaline, apatite, garnet and chlorite. The common feldspar is plagioclase with inclusions of sericite. It was difficult to identify the plagioclase composition through Michel-Lévy Method because of sericitization.

The *quartzofeldspathic gneiss* in thin section is essentially composed of quartz, biotite, garnet, epidote, opaque minerals, muscovite, and plagioclase. It is characterised by continuous foliation (schistosity) essentially defined by subparallel biotite and muscovite. The texture is in generally granolepidoblastic. Under the microscope it shows signs of recrystallization and dynamic metamorphism.

The quartz crystals up to 2 mm long are characterised by irregular shape, undulose extinction and subgrains. The irregular shape of quartz might be the result of secondary grain growth and subgrains are probably due to late deformation after grain growth (Passchier & Trouw, 1996).

The *staurolite-garnet-mica schist* in thin section is composed of quartz, biotite, scarce muscovite, garnet, staurolite, chlorite and opaque minerals. The garnet occurs as porphyroblasts with iron oxide and quartz inclusions, showing that they are rotated. The quartz crystals are incorporated into the growing crystal as slightly elongated inclusions.

3.2.2.2.iii DISCUSSION

The number of observations on these rocks is very limited due to poor outcrops and inaccessible, which makes field descriptions very difficult. Not possible to confirm or contradict that the Nhazónia Formation is older than the Frontier Formation.

2.2.2.3 FRONTIER FORMATION

2.2.2.3.i FIELD DATA

The Frontier Formation is also known as quartzite-schist complex (Pinna *et al.*, 1987) and contains a stack of duplexes and represents a large thrust zone (Watson, 1969) that separates the Báruè Complex in the east from the Basement Complex in the west. Basically it consists of white crystalline sugary quartzite and intercalated mica-schist, which can be traced northwards from Chimanimani Mountains and Sitatonga Ranges in the south, through a series of outliers in the Bandula region in the north throughout the Mavita region.

In the Chimanimani area the quartzite is white, sacaroide type and milk in hand specimen, whereas in the Chicamba Real Dam the rock is grey in the hand specimen. Further south, the quartzites are sacaroide type, leucocratic in colour, fine to coarse in grain-size, and predominantly lepidoblastic. The quartzite is well foliated, the foliation dipping east, while the bedding dips westwards. Quartzites around the Mussapa Gap reach their maximum thickness of 304 m (Vail, 1966). In the Sitatonga Range the quartzite is sacaroide, white, and crystalline intercalated with narrow beds of mica-schists at times highly weathered, with foliation steeply dipping to the east. The contact between the quartzite and shales of the Umkondo Group is not clearly exposed, but Vail (1966) observed that there is a sharp change from garnet-bearing metapelites in the ranges to gently dipping chloritic schists in the west.

In the Bandula region the quartzites are typically white, sugary rocks with subordinate metapelitic schists and forms north-south oriented synformal outliers (Manhiça *et al.*, 2001), in which

Figure 2.3 Messica granite gneiss in the Bandula area (E 033° 09' 53.4"; S 19° 02' 04.1") showing amphibolite dyke, which strikes north-south. View looking north.

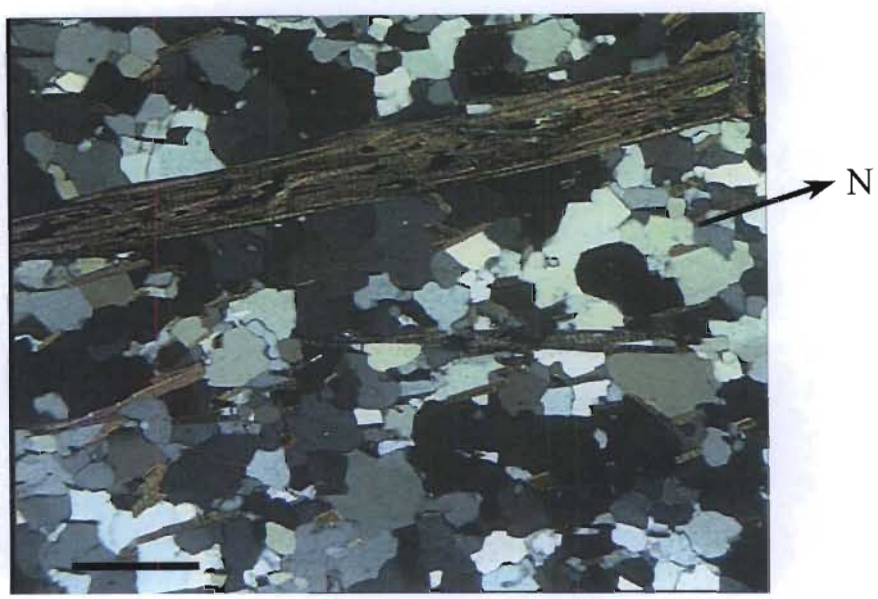

Figure 2.4 Photomicrograph of quartzofeldspathic mica-schist of Nhazónia Formation in the Sitatonga region (E 033° 11' 08.4"; S 20° 15' 08.6") showing continuous foliation defined by subparallel mica. Scale bar = 500μm.

sedimentary features are obliterated by recrystallisation of the cleavage planes (Vail, 1966). The very thick quartzite development of the southern region is absent in the north where mica-schists predominate. The quartzites rest unconformably on the granitic gneiss floor or are separated from it by a thrust plane (Watson, 1969).

2.2.2.3.ii PETROGRAPHY

The samples were collected in Sitatonga Range, Chimanimani Mountains and Chicamba Real Dam regions.

Micaceous quartzites in the Sitatonga range are composed of quartz (up to 98% by volume) and muscovite (up to 2% by volume), chlorite and tourmaline. They are characterised by a continuous foliation (schistosity) mainly defined by subparallel muscovite, subhedral grains, a complete gradation of fine to coarse grained, with irregular grain boundary geometry (interlobate) as a result of secondary grain growth (Figure 2.5). Because of the late deformation, after grain growth, the quartz grains display undulose extinction. The rock is characterized by polygonal grain boundary geometry, equigranular and granoblastic texture. The polygonal fabric of quartz grains formed by static recrystallization, which is supported by the presence of crystals with straight or smooth curved grain boundaries, which lack undulose extinction (Passchier & Trouw, 1996).

The *staurolite-chlorite-garnet-schist* in thin section is mainly composed of quartz (up to 80% by volume), scarce biotite, sericite (up to15% by volume), staurolite, chlorite (up to 3% by volume), garnet, probably almandine, tourmaline and opaque minerals.

The chlorite grains vary between 1 mm to 4 mm in length and it is greenish in colour, tabular habit with quartz and opaque minerals inclusions. The chlorite occurs as post-tectonic porphyroblasts, because it does not show any strain effects and characterised by random distribution (Figure 2.6).

The *garnet mica-schist* in thin section is composed of quartz, biotite, muscovite and garnet prophyroblast. The elongate quartz crystals are parallel to the mica giving the rock a penetrative schistosity.

In the Chimanimani area, the rocks in thin section are largely composed of almost pure quartz grains (~ 98% by volume) and muscovite (~ 2% by volume) as accessory mineral. The quartz is characterized by straight grain boundaries, anhedral form and interlobate texture. They have bimodal grain size distribution where the aggregates of small grains of approximately uniform size between large grains showing undulose extinction. The uniform size of new grains resulted from deformation and dynamic recrystallization at a specific differential stress (Passchier & Trouw, 1996).

Interbedded with the quartzites of the Chimanimani region are a number of metapelite bands, which are composed of sericite, chlorite as the main minerals, with quartz, magnetite occasional tourmaline, and rare detrital zircon as accessories (Vail, 1966).

In the Chicamba Real Dam, thin sections reveal coarse-grained quartz (up to 90% by volume) with some microlites, muscovite (up to 10% by volume) and a small amount of opaque minerals. The quartz grains range between 2 mm and 3 mm and muscovite between 1 mm and 2 mm in size. They consist of inequigranular, interlobate texture, and anhedral form. The quartz grains vary in size from place to place, becoming coarser (up to 5 mm) where the quartzite is composed of ~100% quartz, characterised by granoblastic texture. The schistosity where it appears is mainly defined by subparallelism between muscovite grains and some quartz elongate grains and strained grains characterised by preferential orientation east-west.

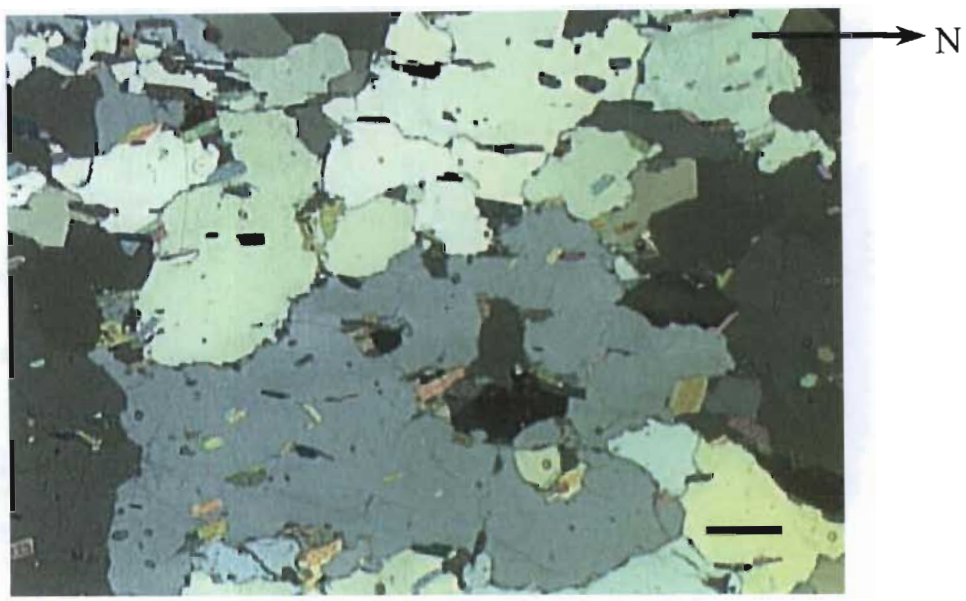

Figure 2.5 Photomicrograph of micaceous quartzites at Sitatonga Range area (E 033° 09' 51.2"; S 20° 14' 27.3") showing continuous foliation, which is defined by subparallel micas and subhedral quartz grains. Scale bar = 250 μm.

Figure 2.6 Photomicrograph of staurolite-chlorite-garnet-schist of quartzite-schist complex of Frontier Formation at Sitatonga region (E 033° 09' 51.2"; S 20° 14' 27.3") showing post-tectonic chlorite porphyroblast with quartz inclusions. Scale bar = 250 μm.

In the Bandula region the metapelites are coarse-grained, schistose and contain quartz, biotite, muscovite, sillimanite and garnet. Quartz forms granoblastic lenses separated by mica (biotite and muscovite), garnet and sillimanite, defining a strong planar fabric (Manhiça *et al.*, 2001).

2.2.2.3.iii DISCUSSION

Watson (1969) suggests that the Gairezi Group underwent folding and enough low-grade metamorphism to convert the original sand beds to quartzites before the Calcareous and Lower Argillaceous Formation were deposited. Prior to the deposition of the sedimentary rocks underwent prolonged erosion which reduced their surface to a pleneplain.

The quartzites are typical of a turbulent, high-energy environment, and the mica-schists reflect calmer, deeper water and a migrating shoreline (Watson, 1969). As consequence after deposition of the coarse sediment in a high-density turbidity current, any continuing flow may rework the sediment surface or deposit finer-grained sediments, in relatively short periods of time above the coarse bed.

The K-Ar age of 465 ± 20 Ma in muscovite of Chicamba quartzite obtained by Vail (1965) is interpreted as cooling age associated with final episode of the Pan-African event.

2.2.3 UMKONDO GROUP

2.2.3.1 INTRODUCTION

The stratigraphic nomenclature adopted within the Umkondo Group is that of the Zimbabwean Geological Survey following the proposal by Watson (1969), but the word Series is replaced by Formation. This is because the Umkondo Group is better studied in Zimbabwe. In the study area, the Umkondo Group extends from the south of Espungabera village area to the Lucite River in the north. It is bounded by the Gairezi Group in the east and extends westwards into Zimbabwe.

The age of the Umkondo Group has been a subject of several publications. The similarity of palaeomagnetic poles and isotopic ages from a large number of igneous units across much of southern Africa suggests that the Umkondo dolerites were intruded during a craton-wide event at ~1100 Ma (Jones and McElhinny, 1966; Allsopp *et al.*, 1989; Hargraves *et al.* 1994; Hanson *et al.*, 1998; Munyanyiwa, 1999). The best estimate age of crystallisation of the sill based on data for baddeleyite and the four most concordant zircons (1099 ± 9 Ma) yields a mean of 1105 ± 5 Ma (Wingate, 2001).

The Umkondo Group was slightly metamorphosed and deformed during the Moçambique Belt events (Watson, 1969). It has been referred to as an autochthonous sequence (Stocklmayer, 1978; Allsopp *et al.*, 1989), and it has been subdivided in Zimbabwe into the Zimbabwe and Inyanga facies of the Umkondo Group (Stocklmayer, 1978 & 1981).

Due to the discontinuous outcrops, poor exposure and disturbance of the stratigraphic sequence by Umkondo dolerite sills and dykes it is not possible to construct accurate stratigraphic sequence. In Zimbabwe it attains a maximum thickness exceeding 3650 m in the south (Watson, 1969) compared with 200 m at Inyanga region (Stocklmayer, 1978). It was deposited in shallow-marine to fluvial environments (Button, 1977). The sedimentation was into a basin, shallow in the west and deepening eastwards (Stocklmayer, 1978).

The Umkondo Group comprises four formations: Calcareous Formation, Lower Argillaceous Formation, Quartzite Formation, and Upper Argillaceous Formation.

2.2.3.2 CALCAREOUS FORMATION

2.2.3.2.i FIELD DATA

The Calcareous Formation and the Lower Argillaceous Formation were not observed within the study area due to their sporadic occurrence and access difficulty.

The Calcareous Formation is the lowest unit of the Umkondo Group within the study area and occurs only along the west of Rotanda village and in the Tsetsera-Himalaya Farm where it has been thermally metamorphosed to siliceous and calc-hornefls by large intrusive sheets of Umkondo dolerite (Pinna *et al.*, 1987). The Formation lies with a distinct unconformity on the granitic floor and it is mainly composed almost entirely of fine-banded, almost cryptocrystalline, grey, cherty calc-hornfels with a conchoidal fracture (Watson, 1969).

The basal Calcareous Formation unconformably overlies the quartzites of Frontier Formation (Araújo *et al.*, 1973). It is characterised by sporadic appearance and may thin reaching up to 245 m thick in Melsetter-Chipinga region, thinning to nothing eastwards (Watson, 1969) and up to 20 m in the Inyanga area (Stocklmayer, 1975). The lower 60 m of the Calcareous Formation in the Chipinga region, comprises a basal conglomerate and arenite.

2.2.3.2.ii PETROGRAPHY

The *calc-silicate* in thin section is predominantly composed of fine-grained groundmass of small percentage of quartz ± carbonate, plagioclase, microcline, albite, diopside, zoisite, tremolite-actinolite, muscovite, sphene and iron oxide (Pinna *et al.*, 1987).

The *calc-hornfels* has a fine-grained groundmass of zoisite with subsidiary quartz and chlorite, possibly after tremolite (Watson, 1969).

2.2.3.2.iii DISCUSSION

The lower 60 m of the Calcareous Formation in the Chipinga region, comprises a basal conglomerate and arenite, representing reworked detritus, overlain by dolomites and red siltstone of tidal-flat-lacustrine origin, whilst the upper 30 m is composed of calcareous hornfels overlain by limestone and a calc-silicate layer has formed during the shallow marine shelf, within the photic zone (Button, 1977). The Calcareous Formation reflects a low energy, still water and possibly lagoonal environment where the colloidal precipitation of calcium, silica and iron play a major part (Watson, 1969). The fine-grained sediments of the Clacareous Formation, a thin but extremely persistent horizon, were deposited on a flat peneplained surface in a restricted lagoonal environment (Stocklmayer, 1978).

2.2.3.3 LOWER ARGILLACEOUS FORMATION

2.2.3.3.i FIELD DATA

The Lower Argillaceous Formation crops out in the west of the Sitatonga range and in the Tsetsera-Himalaya Farm (Pinna *et al.*, 1987) and overlies conformably the Calcareous Formation in the Melsetter-Chipinga area (Watson, 1969) as well as in the Inyanga region (Stocklmayer, 1978).

The Lower Argillaceous Formation basically comprises shale and siltstone intercalated with narrow bands of schist quartzite and schist (Pinna *et al.*, 1987), whereas in the Melsetter-Chipinga area it comprises shale, siltstone, and phyllitic zones, especially those at the base of the Lower Argillaceous Formation contiguous with the Frontier Formation (Watson, 1969). It has an average thickness of 235 m in the Chipinga area (Button, 1977).

2.2.3.3.ii PETROGRAPHY

The *phyllite* consists of fine-grained groundmass of oriented quartz, sericite, and a little chlorite and wisps of iron-ore dust (Watson, 1969).

The *siltstone* consists of quartz, biotite, microcline, plagioclase and iron-ore (Pinna *et al.*, 1987).

2.2.3.3.iii DISCUSSION

The lagoon, with its minor algae colonies persisted throughout the deposition of the muddy Lower Argillaceous Formation (Stocklmayer, 1978), while Button (1977) suggested that the bulk of the Lower Argillaceous Formation was deposited on a shallow-marine shelf, probably below wave base, but within the photic zone.

The phyllitic zones occur at the base of Lower Argillaceous Formation are interpreted as being contiguous with Frontier Formation by Watson (1969). The development of phyllite only close the Frontier quartzite might relate to the slight increases in metamorphic grade eastwards within the study area.

2.2.3.4 QUARTZITE FORMATION

2.2.3.4.i FIELD DATA

The Quartzite Formation overlies the Lower Argillaceous Formation conformably (Watson, 1969). It is essentially composed of orthoquartzite and sandstone with shale and silty bands, which dominate the Umkondo Group within the study area. The unit reaches the maximum thickness in the Chipinga area of approximately 700-800 m from geological cross-sections (Watson, 1969; Button, 1977) and 75 m in the Inyanga region (Stocklmayer, 1978).

In hand specimen the orthoquartzite is medium to coarse-grained, green to dark green, usually hard and it breaks with conchoidal fracture and shows cross bedding. The sandstone in hand specimen is fine to coarse-grained, dark grey to grey-greenish and green to dark green, usually very hard and it breaks with a conchoidal fracture. On weathered surfaces the sandstone is brown. Sandstone beds are separated by greenish shale layer less then 10 cm thick. The shale in hand specimen is greenish, very fine to fine-grained rock characterised by lamination, defined by alteration of composition and colour usually up to 6 mm thick.

The Quartzite Formation tends to be very deeply weathered and as consequence of this it does not crop out continuously in the area under investigation. It has been slightly folded with fold axis plunging gently northerly and bedding striking north-south (Figure 2.7).

2.2.3.4.ii PETROGRAPHY

The *orthoquartzite* in thin section is mainly composed of quartz and scarce plagioclase feldspar. The quartz (up to 98% by volume) is well sorted but not well rounded, with few clay minerals. Due to the intense sericitization it is difficult to determine the composition of plagioclase (trace up to 1% by volume) through petrographic methods.

Accessory minerals include chlorite (up to 2% by volume), epidote (up to 2% by volume), biotite (< 1% by volume), zircon (<1% by volume), zoisite (<1% by volume) and opaque minerals, which occur throughout the rock.

The *sandstone* in thin section has quartz (up to 46% by volume) that is poorly sorted, not well rounded, monocrystalline rarely polycrystalline grain, angular form. A characteristic is the high percentage of fine-grained phyllosilicate matrix that consists of chlorite, biotite, sericite and silt-sized grains of quartz.

According to the percentage of quartz, feldspar, and rock fragments in the QFR triangle (Folk *et al.*, 1970), the rocks of the Quartzite Formation plot in quartzarenite

and lithicarenite fields as shown in the Figure 2.8 and Table 2.4 (Appendix 2).

The *siltstone* in thin section is composed of very fine-grained minerals, but occasionally angular quartz grains, actinolite and biotite are embebbed in a very fine-grained matrix consisting of sericite, biotite and pale green chlorite. The biotite shows one cleavage direction and is altered. The actinolite shows one cleavage direction and very altered, and both show interlocking relations. The chlorite occurs as an alteration product of actinolte.

2.2.3.4.iii DISCUSSION

The Quartzite Formation marks the onset of a braided deltaic system prograding into the lagoonal basin in which the Lower Argillaceous Formation was deposited (Button, 1977). It bears witness to a somewhat higher energy environment, reflecting a period of deltaic deposition, with transportation being mainly from the southwest (Button, 1977).

The lack of lithological variation observed within the Quartzite Formation, is interpreted as probably responsible for the relative paucity of Umkondo dolerites sills, which are preferentially emplaced along contacts of contrasting rock types.

The formation displays a transitional upward-coarsening relationship with the underlying Lower Argillaceous Formation and Button (1977) interpreted as a fan delta complex in which a braided alluvial plain prograded directly onto the shallow marine shelf where longshore reworking underlain immature arenite.

The formation is characterized by little occurrence of siltstone and shale. This feature was interpreted as typical braided stream depositional environment by Boothroyd and Ashley (1975).

The sandstone, representing the lower part is characterised by sediment transport vectors to the east and northeast. This is is interpreted as the palaeoslope, which controlled the orientation of braided streams on the fan-delta. The upper part shows northerly and northwesterly palaeocurrent patterns.The reworked fan-delta sediments are thought to represent "contour-currents" on the submerged marine shelf (Button, 1977).

2.2.3.5 UPPER ARGILLACEOUS FORMATION

2.2.3.5.i FIELD DATA

In Inyanga the Upper Argillaceous Formation is composed of a variety of fine-grained shales and argillites that are capped by grey feldspathic sandstones (Stocklmayer, 1978). In Chipinga, Melsetter areas the Upper Argillaceous Argillaceous Formation are mainly composed of phyllite, slates and cleaved mudstone, which weather to creamy pink or lilac. Interbedded with them are siltstone and fine to medium-grained, massive, feldspathic sandstone (Watson, 1969). Therefore the Upper Argillaceous Formation of the study area can be related to those occurring in Zimbabwe.

The Upper Argillaceous Formation is the highest horizon in the Umkondo Group and conformably overlies the Quartzite Formation (Watson, 1969). The Argillaceous Formation crops out northeast of Espungabera village and around Rotanda region. In the Chipinga area in Zimbabwe, it is about 570 m thick (Button, 1977) and characterised by marked change in rock colours.

The formation is composed of a great variety of fine-grained sedimentary rocks, mainly shale, siltstone, and slate. The siltstones are intercalated by fine to medium grained and massive sandstones, which are intruded by Umkondo dolerites. In the Mussapa area on the Moçambique border north of Melsetter, the Upper Argillaceous Formation is a thick pile of foliated and

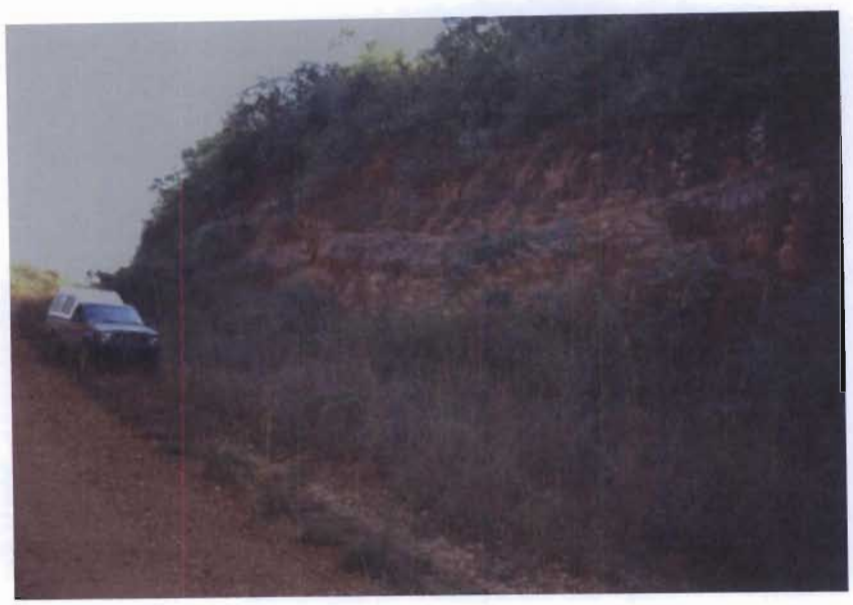

Figure 2.7 Typical Umkondo Group sandstone roadside exposure in the Espungabera region (E 033° 02' 08.9"; S 20° 17' 37.8"). It is slightly folded with limbs gently dipping to the north-northwest and south-southeast. View looking northwest.

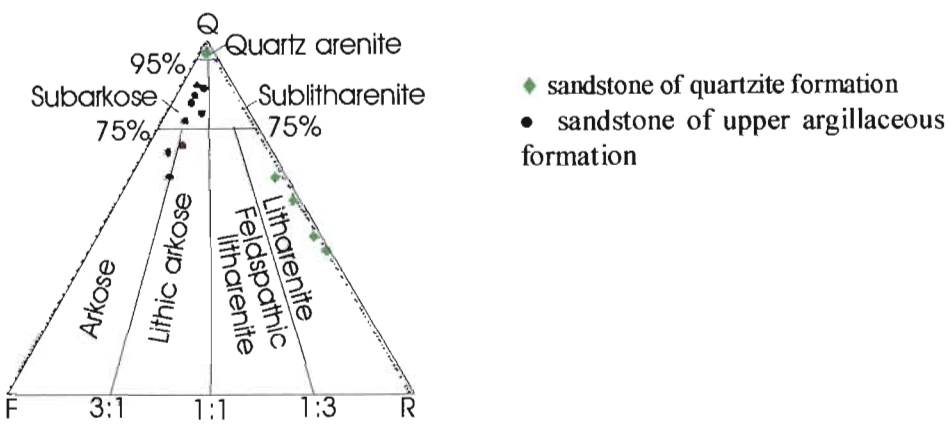

Figure 2.8 Ternary diagram (Folk *et al.*, 1970) showing Umkondo Group sandstone of Quartzite Formation plotting in quartzarenite and lithicarenite fields. Q = monocrystalline and polycrystalline quartz (excluding chert), F = monocrystalline feldspar, R = rock fragments (igneous, metamorphic, and sedimentary including chert).

folded phyllites with fold axis trends to the north-northeast, and siltstone with some sandstones and quartzites (Watson, 1969).

The siltstone in hand sample is red to purple, brown, green, depending on presence of different iron oxide minerals in the rocks with very fine to fine-grained, micaceous and slightly laminated.

The phyllite is fine-grained, brown and greenish in hand specimen. The cleavage and the banding are well developed in brown slate, in which the banding is defined by changes in mineralogical composition and in grain size.

In the field the sandstone is usually red, brown, yellow, and rarely white, which result typically from presence of ferric oxide cement (hematite), goethite (hydroxide), limonite and colourless rocks, such as quartz-cemented quartz sandstone. The different intensities of red colouration can been seen, reflecting the fact that most hematite forms after a sediment is deposited. The sandstone in hand specimen is multi coloured, hard, characterised by conchoidal fracture, that becomes soft and unconsolidated when it is weathered.

2.2.3.5.ii PETROGRAPHY

The *siltstone* in thin section consists of quartz, white mica, iron oxide, clay minerals and chlorite embebbed in the very fine-grained matrix. The small-scale structures, the laminae are defined either by changes in grain size (laminated siltstones) and quartz grains increasing with decreasing amounts clay minerals. The platy minerals in the rock are parallel to the orientation of mica. The fine-grained quartz and mica occur as matrix of siltstone. The quartz grains are picked out by thin red-brown rim of iron oxide most likely hematite.

The *phyllite* in thin section comprises quartz, feldspar, and white mica probably muscovite, biotite flakes, iron oxide, chlorite and clay minerals. More common feldspars are orthoclase and plagioclase.

The *sandstone* in thin section consists of quartz, feldspar, mica, chlorite, rock fragments, and opaque minerals. The quartz grains (up to 73% by volume) are made up of monocrystalline and polycrystalline crystals, showing undulose extinction as the result of plastic deformation. The quartz overgrowths and the detrital cores of each grain show uniform colours interference, it is obvious that the overgrowth grew in optical continuity with the grains on which they nucleated where overgrowths are well developed (Figure 2.9). A thin red-brown rim of iron oxide probably hematite picks out the quartz grain boundaries, which give the rocks a red-brown colour. The contact between the quartz grains is irregular (concavo-convex) and wavy, but a few show straight contacts, in which the hematite is absent. The quartz grains are characterised by dust trails vary in size from 0,25 mm to 1 mm are moderately to well sorted, angular to subangular and not well rounded with inequigranular to granular form of crystal aggregates.

The feldspar consists of orthoclase (up to 4% by volume), plagioclase (up to 2% by volume), microperthite (trace), perthite (trace). Some feldspar show microperthite characterised by spindle shaped, exolution lamellae of sodic and potassic felsdpar. Orthoclase grains up to 1 mm in size are moderate to well sorted subangular to angular and not well rounded. Because of alteration the orthoclase is cloudy in appearance. It is highly fractured and sericitised with microlitic inclusions.

Accessory minerals include muscovite (< 1% by volume), chlorite (<1% by volume), iron oxide (<1% by volume), in which the chlorite and mica are present as alteration products. Zircon grains ±0.1 mm occurs as a detrital mineral. The matrix is made up by, muscovite rock fragments and fine-grained quartz.

According to QFR triangle of Folk *et al.* (1970) the sandstone consists between

subarkose to arkose (Table 2.4, Appendix 2), because of the percentage of quartz grains vary in abundance from 62% to 88%, feldspar grains range between 7% and 28% and rock fragments grains vary from 4% to 10% (Figure 2.10). The sandstones vary between mature to immature according with mineralogical and textural characteristics.

2.2.3.5.iii DISCUSSION

The palaeocurrent analysis shows that the mean sediment transport of Argillaceous Formation was usually easterly and northeasterly (Button, 1977).

The siltstone and shale association is thought to represent material deposited in the flood basin during when the meandering rivers overtopped their natural levees. The siltstone-sandstone association is typical of levee deposits and is the result of overtopping of the natural levee, deposition of thin sandy layers, followed by silty material during the falling stages of the flood The sandstone probably represents crevasse-splay deposits, formed by breaching of the natural levee during flood stages, and tapping of bed-load material into the flood-basin Button (1977).

2.2.4 UMKONDO DOLERITES

2.2.4.1 INTRODUCTION

According to the palaeomagnetic studies of McElhinny and Opdyke (1964) two distinct group of dolerites exist in eastern Zimbabwe: the Mashonaland dolerites restricted to the Archaean Basement Complex and the Umkondo dolerites that intruded into the Mesoproterozoic metasediments and adjacent basement granitoids. In this thesis all the dolerites belong to the latter group.

2.2.4.2 FIELD DATA

Thick sheets of dolerite have extensively intruded all the sedimentary rocks of the Gairezi and Umkondo Groups with sills being more common than dykes. But the Umkondo dolerites are less widespread in the Gairezi Group and according to the Watson (1969) they are intensively tectonised and structurally conformable bodies within the Frontier quartzites. The dolerites preferentially intrude near the base of the Umkondo sedimentary pile (Calcareous Formation), decreasing in the Lower Argillaceous and virtually Quartzites Formations and almost absent in the Upper Argillaceous Formation.

The total thickness of intrusions is estimated to range from 600 m to 1200 m (Watson, 1969), whilst the individual sheets have been estimated to be 70-200 m thick (Swift, 1962; Watson, 1969).

In the field locally they show evidence of intrusion before lithification of the host sedimentary rocks. Near the contact with the dolerite sills, the sedimentary rocks have been thermally metamorphosed to hornfels (Munyanyiwa, 1999). The Umkondo dolerite sills differ from the basalt lavas, which crop out within the study area by their baked contacts, by grain size, by absence of amygdales and by weathering to rounded boulders set in a red soil.

The Umkondo dolerite is usually dark grey to greenish-grey and massive in hand specimen. It is a medium to coarse-grained rock that has well developed ophitic to hypidiomorphic granular and not uncommon porphyritic texture. The dolerite that intruded the Upper Argillaceous Formation in the Espungabera area, south of the study area is a medium to coarse-grained rock, with well-developed sub-ophilitic to ophilitic texture.

They are metamorphosed to lowermost greenschist facies in the west and to mid-greenschist facies in the east of Zimbabwe (Munyanywia, 1999).

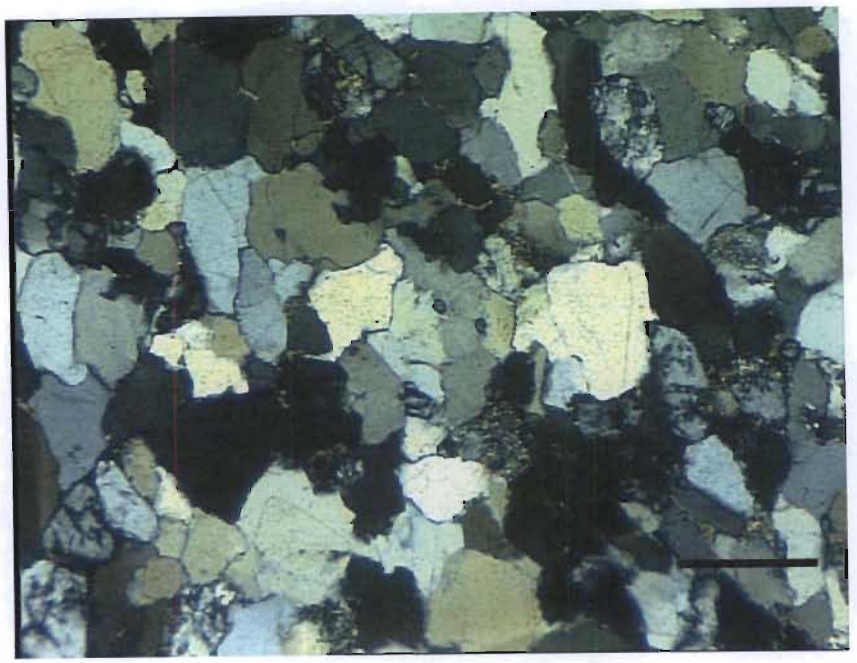

Figure 2.9 Photomicrograph of sandstone of Upper Argillaceous Formation at Espungabera area (E 033° 02' 08.9"; S 20° 17' 37.8") shows quartz overgrowth and irregular contact between quartz grains. Scale bar = 500 μm.

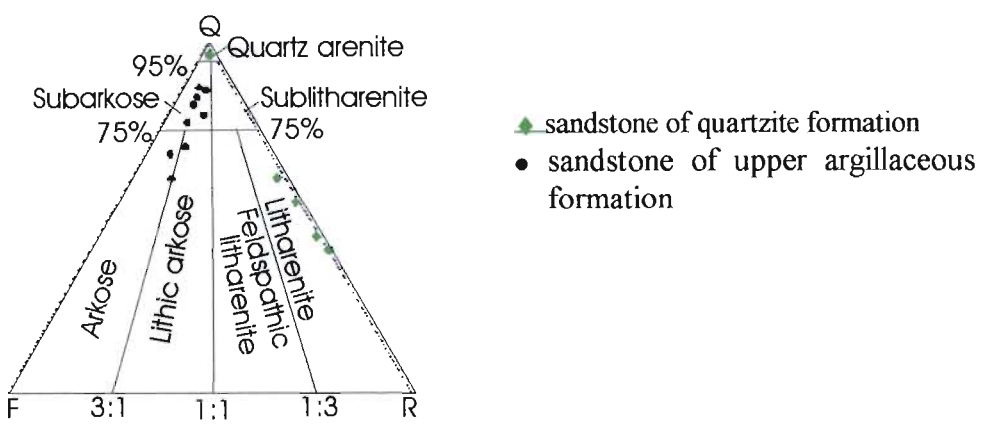

Figure 2.10 Ternary diagram (Folk *et al.*, 1970) showing Umkondo Group sandstone of Upper Argillaceous Formation plotting in arkose and subarkose fields. Q = monocrystalline and polycrystalline quartz (excluding chert), F = monocrystalline feldspar, R = rock fragments (igneous, metamorphic, and sedimentary including

2.2.4.3 PETROGRAPHY

The *Umkondo dolerite* in thin section essentially consists of pyroxene, feldspar, amphibole and olivine, and accessory opaque minerals, mica and epidote. The pyroxene is anhedral, which has been replaced by amphibole probably actinolite. The composition of plagioclase is very difficult to determine. It is elongate-prismatic, subhedral to anhedral in form. The opaque minerals are characterised by subhedral to euhedral form probably magnetite develops throughout the rock. The biotite occurs as an alteration product of amphibole, while the alteration product of pyroxene is chlorite. The sericite occurs as an alteration product of plagioclase as well as matrix together with fine-grained plagioclase and quartz. The subsidiary quartz shows undulose extinction.

The phenocrysts of pyroxene occur sometimes as skeletal type, which is embedded in intergranular textural elongate crystals of plagioclase-rich matrix. The plagioclase is characterised by elongate and skeletal shape and some show discontinuously zoning.

2.2.4.4 DISCUSSION

Based on similarity of palaeomagnetic poles and geochronological data from several southern Africa igneous units, including the Umkondo dolerites and the basalt lavas, Jones and McElhinny (1966); Allsopp *et al.* (1989); Hargraves *et al.* (1994); Hanson *et al.* (1998); Munyanyiwa (1999) concluded that the Umkondo igneous suite is part of the activity that was widespread throughout southern Africa, and of significant duration, around the time of intrusion of the Umkondo dolerites at 1100 Ma. The Umkondo dolerites ages have also been reset as they yielded an K-Ar whole-rock ages between 430 Ma and 760 Ma reported by Stocklmayer (1978). This shows that they or some of them had been affected by Pan-African orogenic event.

2.2.5 BÁRUÈ COMPLEX

2.2.5.1 INTRODUCTION

The Báruè Complex forms part of the Moçambique Belt. It extends from the Lucite River in the south and is bounded by the Gairezi Group and by the Messica granite gneiss in the west, and by the Nhazónia Formation in the south. The area consists of intensively deformed granite gneiss reaching granulite facies.

The transition between Archaean rocks in the west and Mesoproterozoic Báruè Complex is often difficult to recognise in the field because as observed Pinna *et al.* (1987) both granitoids are affected by metamorphism and deformation, which took place between Mesoproterozoic and Neoproterozoic period.

The stratigraphic terminology used here is adopted from the system nomenclature proposed by Manhiça (1998).

The Vanduzi hornblende migmatite gneiss is the predominant lithology of the Báruè Complex. It is characterised by strong foliation and lineation. The gneiss consist of quartz and pegmatite veins, and a large mafic enclave boudinaged. In general the rocks have a porphyroblastic texture.

The Chimoio, Vanduzi and Tchinhadzandze gneisses are characterized by intense north-trending fold axis with syn-tectonic metamorphism of amphibolite facies, accompanied by migmatization. In the field are recognised two phases of migmatisation: older stromatic migmatising phase resulted in leucosome development parallel to the gneiss layering striking northeast-southwest which is apparently cut by younger secondary leucosome development defines lenticular patches, which have a consistent north-south orientation (Manhiça *et al.*, 2001).

2.2.5.5 CHIMOIO GNEISS

2.2.5.5.i FIELD DATA

The Chimoio gneiss crops out between Nhansipfe megacrystic gneiss in the west and eastern limit of the study area.

The unit in composition varies between granodioritic to tonalitic orthogneisses with migmatitic melting and xenolithic enclaves rich in mafic minerals (biotite and hornblende).

In the field the granitic gneiss consists of feldspar and quartz representing felsic minerals intercalated by mafic minerals, hornblende and biotite. Strong planar fabric striking northwest-southeast dipping to the northeast characterizes the Chimoio gneiss. The granitic rocks are intruded by pegmatite veins up to 60 cm wide and by undeformed fine to medium-grained granite parallel to the foliation, which strikes north-south.

The amphibolite and intercalated gneissic and migmatitic bands are intensely deformed resulting in various types of folds and boundins in the leucosome (Manhiça, 1998).

2.2.5.5.ii PETROGRAPHY

The *Chimoio gneiss* in thin section consists essentially of quartz and plagioclase, with some hornblende and biotite as mafic minerals. The plagioclase is calcic oligoclase (An_{23-24}) in composition. The biotite, epidote, garnet and opaque minerals are accessory minerals. Manhiça *et al.* (2001) observed that the zircon is short prismatic generally enclosed by feldspar and hornblende and apatite occurs as fine hexagonal grains generally included in feldspar, hornblende and quartz.

Quartz occurs as anhedral grains, showing partial recrystallization and undulatory extinction. Aligned biotite generally associated with hornblende gives the rocks a strong schistosity. The dominant texture is granitic inequigranular medium to coarse-grained and patches of plagioclase intergrown with vermicular quartz provide myrmekitic texture throughout the rocks. Some hornblende grains contain inclusions of quartz and opaque minerals.

The gneiss by its mineral assemblages is tonalitic with mafic enclaves that do not show a high degree of deformation.

2.2.5.4 VANDUZI HORNBLENDE MIGMATITE GNEISS

2.2.5.4.i FIELD DATA

The Vanduzi hornblende migmatite gneiss is bounded by the Frontier Formation and Messica granite gneiss in the west and in the east by the Nhansipfe gneiss.

The lithology is heterogenous migmatitic supracrustal sequence, which contains layered, dominantly felsic, rocks with subordinate mafic rocks and semipelitic gneiss (Manhiça *et al.*, 2001). It has been intruded by fine to medium grained granite.

Near the Vanduzi river, Manhiça (1998) observed two partial melt layers. The older one was folded and parallel to layering in palaeosome and the younger was oriented north-south and cross-cut both the planar fabric (foliation) in the palaeosome and the earlier migmatitic layer.

2.2.5.4.ii PETROGRAPHY

The *Vanduzi hornblende migmatite gneiss* in thin section is coarse-grained, granular textured and composed of feldspar, hornblende, quartz, biotite, that make up the bulk of the rock. Chlorite, epidote, sericite and opaque minerals occur as accessory minerals.

Two assemblages are recognized in the samples, namely (1) plagioclase, biotite, hornblende, K-feldspar and quartz and (2)) plagioclase, biotite, garnet, K-feldspar and quartz.

The common feldspars (~ 68% by volume) are microcline as K-feldspar and plagioclase with microlite inclusions. Occasionally the plagioclase shows discontinuous zoning and myrmekitic texture is present throughout the rock. The grain size varies between 1,5 mm and 4 mm. The hornblende (~ 15% by volume) is green and varies in grain size between 2 mm and 3 mm. The hornblende occurs with inclusions of quartz, biotite and opaque minerals. The biotite is randomly oriented and occurs together with hornblende, where it occurs. Chlorite occurs as an alteration product of mafic minerals such as hornblende and biotite, while the alteration of plagioclase and hornblende has given rise to sericite and a secondary biotite respectively in the rock.

The Vanduzi hornblende migmatite gneiss is characterised by inequigranular texture.

The *mafic enclave* comprises garnet, hornblende, plagioclase and clinopyroxene assemblage. The biotite, quartz, epidote, and iron oxide, occur as accessory minerals.

The *granite*, which has intruded Vanduzi hornblende migmatite gneiss is composed of feldspar (plagioclase and microcline), monocrystalline quartz, and as accessory minerals pyroxene sphene, biotite, and magnetite.

2.2.5.3 TCHINHADZANDZE GNEISS

2.2.5.3.i FIELD DATA

The Tchinhadzandze gneiss is bounded by the Gairezi Group in the west and by the Vanduzi hornblende migmatite gneiss.

In the field the Tchinhadzandze gneiss is composed by feldspar, quartz, biotite and hornblende and is characterised by strong foliation, striking almost north-south (170°) dipping 38° to the east. The shear zones with azimuth northwest-southeast (330°) show sinistral sense of movement.

The unit is cut by quartz-feldspar and pegmatitic veins, which are oriented northeast-southwest and north-south.

2.2.5.3.ii PETROGRAPHY

The *Tchinhadzandze gneiss* in thin section is composed of feldspar, quartz, hornblende and biotite. The common feldspars (~68% by volume) are microcline with microlite inclusions and plagioclase being predominant. The plagioclase is oligoclase (An_{16-22}) in composition. The microcline and plagioclase occur as anhedral grains, which sizes vary between 1.5 mm and 4 mm. The feldspar presents inclusions of sphene, quartz and biotite and is characterized by incipient sericitization as well as myrmekitic texture. Epidote, sericite, chlorite, sphene and opaque minerals occur as accessory minerals.

Quartz is anhedral (up to 23% by volume) with inclusions of microcline, oligoclase and biotite. The undulatory extinction and quartz grains of different sizes suggest deformation.

The hornblende and biotite have the same modal percentage in the rock and both show preferred orientation defining the planar fabric in the rock. The hornblende contains inclusions of feldspar and quartz. Chlorite occurs as an alteration product of mafic minerals most likely hornblende and biotite, while the alteration of plagioclase and hornblende has given rise to sericite and epidote in the rock.

2.2.5.2 NHANSIPFE MEGACRYSTIC ORTHOGNEISS

2.2.5.2.i FIELD DATA

The Nhansipfe megacrystic orthogneiss is bounded by Vanduzi migmatite gneiss in the west and by Chimoio gneiss in the east.

The rock is characterised by granular texture with very coarse-grained feldspar (>25 mm), which form porphyroclastic

augen. It has been intruded by mafic dykes striking northeast-southwest, with relict granulite facies assemblages (Manhiça *et al.*, 2001). In some places the rocks contain undeformed aplite intrusions, which represent post-tectonic igneous emplacement. Kinematic indicators in the form of porphyroclastic feldspar are locally developed showing both dextral and sinistral sense of movement. The biotite defines two generations of planar fabric in the rocks, the older one folded striking northeast-southwest (S_1) and younger unfolded striking approximately north-south (S_2) with a near vertical dip.

2.2.5.2.ii PETROGRAPHY

The *Nhansipfe megacrystic orthogneiss* in thin section is composed of alkali and plagioclase feldspar, quartz, biotite, and hornblende as shown in the Table 2.5 (Appendix 2). The accessory minerals consist of scarce chlorite, sphene, and magnetite.

Biotite and hornblende show preferred orientation and are deformed and oriented along foliation planes. Hornblende is anhedral with quartz, chlorite and opaque mineral inclusions.

The common feldspar is plagioclase (up to 45% by volume) and microcline (up to 33% by volume), which grain size occasionally reaches 6 mm. The plagioclase is characterised by inclusions of quartz and biotite. The plagioclase is oligoclase to calcic oligoclase (An_{20-25}) in composition. Locally the plagioclase and quartz grains are characterized by granoblastic texture showing boundaries with interfacial angles of about 120°.

Quartz (up to 15% by volume) presents undulatory extinction, with grains showing different sizes, probably related to the partial recrystallization. The biotite exhibit preferred orientation along planes of foliation associated with hornblende.

2.2.5.6 DISCUSSION

The $^{207}Pb/^{206}Pb$ SHRIMP age of the Chimoio gneiss and the Nhansipfe megacrystic orthogneiss is 1108 ± 12 Ma and 1112 ± 18 Ma with biotite has yielded a cooling $^{40}Ar/^{39}Ar$ age of ~550 Ma 460 Ma respectively (Manhiça *et al.*, 2001). From description and map Chimoio gneiss seems to be older than Nhansipfe gneiss. This observation is supported by geochemistry analysis, where the Chimoio gneiss plots in volcanic arc and syn-collisional fields and Nhansipfe gneiss plots in within plate field.

The $^{207}Pb/^{206}Pb$ ages show that these rocks were emplaced during Moçambique Belt orogeny, but they were deformed and metamorphosed, reaching granulite facies during Pan-African event confirming Kröner's *et al.*, (1997) observations and interpretations.

The age of the Tchinhadzandze gneiss and Vanduzi hornblende migmatite gneiss is uncertain.

Within the Chimoio, Vanduzi and Tchindzandze gneisses are developed two phases of migmatisation: older stromatic migmatising phase resulted in leucosome development parallel to the gneiss layering striking northeast-southwest is apparently cut by younger secondary leucosome development defines lenticular patches, which have a consistent north-south orientation. In the field, it is not clear if the two phases are developed during one migmatisation event or represent time gap between them.

The occurrence of migmatisation on these granitic gneisses might indicate that the Vanduzi hornblende migmatite gneiss to be at least as old as the Chimoio gneiss and the Nhansipfe megacrystic orthogneiss (Manhiça *et al.*, 2001).

The presence of mafic enclaves in theses granitic gneisses suggests quenched blobs of hot mafic magma emplaced into a partial molten tonalite host (Reid & Barton 1983).

CHAPTER 3

GEOCHEMISTRY

3.1 INTRODUCTION

The only previous geochemistry investigation was been done by Manhiça (1998) north of the study area along Manica-Chimoio road. Therefore very little is still known about regional geochemical characteristics of the units in the study area.

The purpose of this chapter is to present new geochemical data for different units and in the light of these data to:

- classify different rock types, which occur within the study area.
- discuss the geochemical relations between different units, compare and correlate to similar units in the region, especially in Zimbabwe.
- Establish protolith of different units
- establish tectonic setting

3.2 BASEMENT COMPLEX

3.2.1 MACEQUECE FORMATION

3.2.1.1 INTRODUCTION

Four amphibolites, three serpentinites and one chlorite schist were analysed from this formation. Representative XRF analyses of major and trace elements of these are given in Table 3.1 and in Table 3.2 are shown the correlation matrix of chemical elements (Appendix 3). Tests have been made for mobility of elements in case metamorphic events have disturbed the whole-rock chemical system, which can lead to misleading tectonic reconstruction, major and trace element chemistry.

3.2.1.2 MAJOR ELEMENT GEOCHEMISTRY

Bivariate Harker variation diagrams of major oxide elements versus SiO_2 (Figure 3.1) show in generally that the mafic rocks (amphibolites) are characterised by decrease in major elements with an increase in SiO_2 content. However the ultramafic rocks (serpentinites and chlorite schist) are characterised by slightly increases in Al_2O_3, Fe_2O_3, TiO_2 and P_2O_5 contents and slightly decreases in MgO content with an increase in SiO_2 content.

Commonly, the serpentinites show lower total alkalis and CaO content together with chlorite schist, lower Al_2O_3 content and higher MgO content than amphibolites. The chlorite schist exhibits highest percentage of Fe_2O_3.

Although the total alkalis are likely to be mobilized during alteration and metamorphism of volcanic rocks (Rollinson, 1993), the total alkalis versus silica (TAS) discrimination diagram (MacDonald and Katsura, 1964) the mafic and ultramafic rocks show subalkaline affinity and they plot within the basalt field (Figure 3.2).

Volcanic rocks of the sub-alkaline series can be subdivided on the basis of their concentrations of K_2O and SiO_2 (Peccerillo & Taylor, 1976). As shown in the Table 3.1 (Appendix 3) the greenstones contain a low K_2O (0-0.27 wt%) contents that characteristic of tholeiitic basalts (Figure 3.3).

On Al_2O_3-(Fe_2O_3+TiO_2)-MgO ternary discrimination diagram as showing in Figure 3.4 (Jensen, 1976) amphibolites and chlorite-schist all plot entirely on the high iron tholeiite basalt field (HFTB) and serpentinites plot within peridotitic (PK)

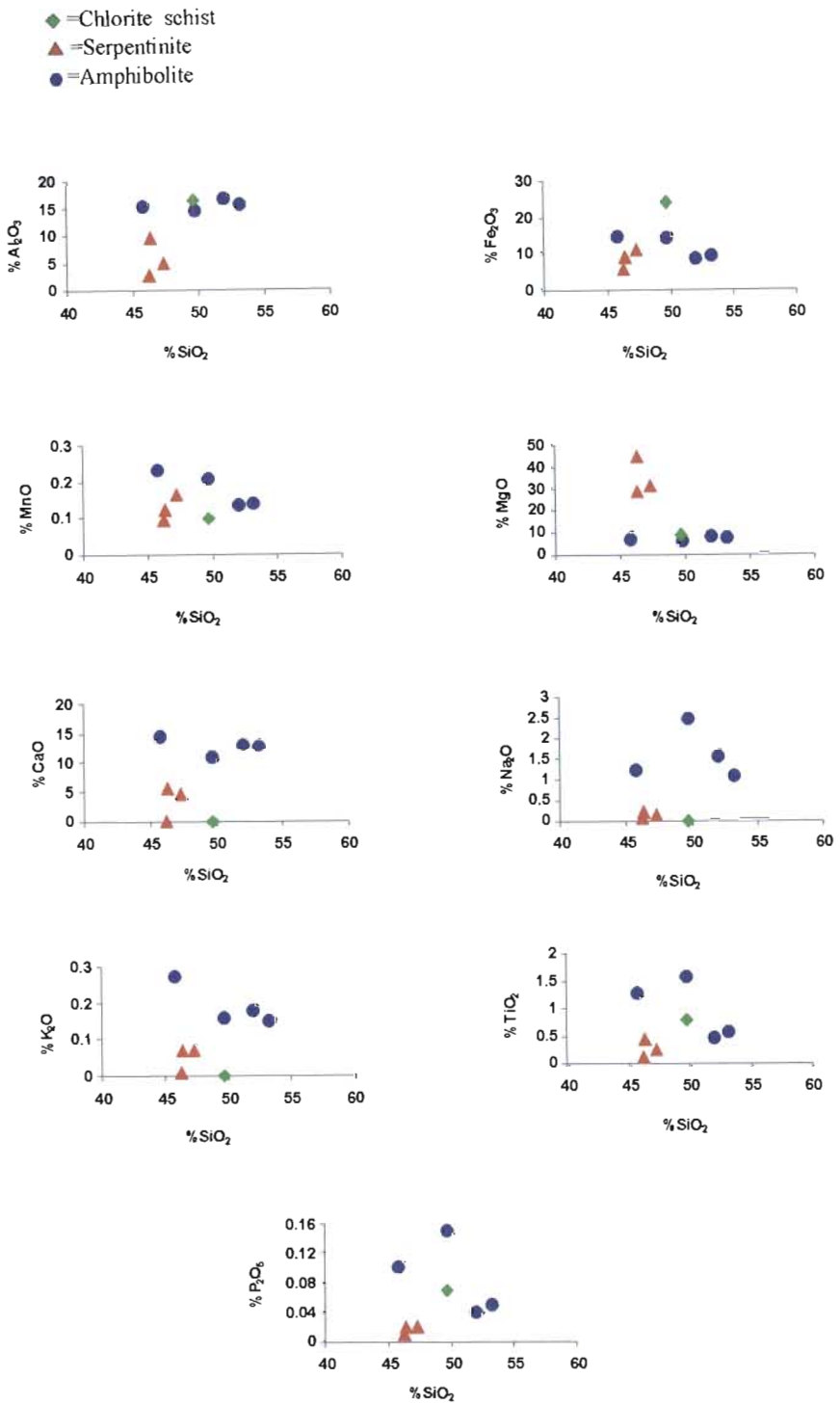

Figure 3.1 Harker variation diagrams of major oxide elements versus SiO_2 for greenstone.

- =Chlorite Schist
- =Amphibolite
- =Serpentinite

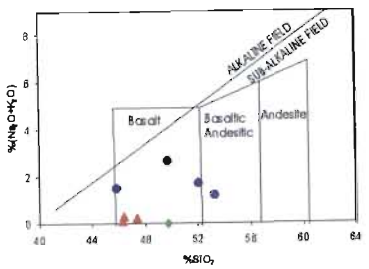

Figure 3.2 The total alkalis versus silica (TAS) diagram showing the subalkaline affinity of the basic and ultrabasic rocks. The straight line subdivides the alkaline and subalkaline rocks (MacDonald and Katsura, 1964).

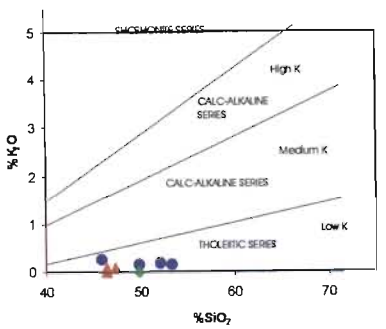

Figure 3.3 The subdivision of subalkalic rocks using the K_2O versus silica diagram. From Rollinson, 1993.

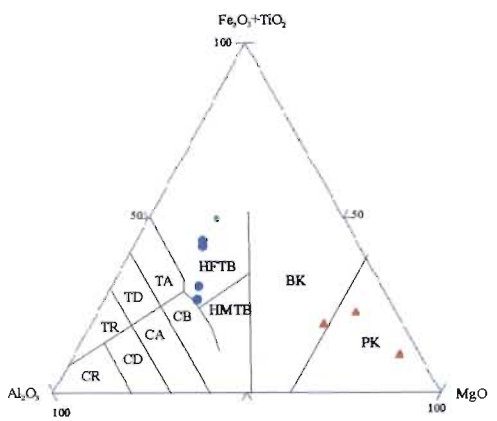

Figure 3.4 The discrimination diagram for high iron tholeiites basalt (HFTB), high magnesium tholeiites basalt (HMTB), basalt komatiites (BK), peridotitic komatiites (PK), tholeiitic rhyolites (TR), tholeiitic dacites (TD), tholeiitic andesites (TA), calc-alkaline rhyolites (CR), calc-alkaline dacites (CD), calc - alkaline andesites (CA) and calc-alkaline basalts (CB) fields (After Jensen & Pyke, 1982).

and basaltic komatiite fields confirming their high MgO contents.

3.2.1.3 TRACE ELEMENT GEOCHEMISTRY

The serpentinites and chlorite schist rocks have higher Co, Ni and Cr contents, but lower Sr, Rb, Ba, Y, Nb and Zr contents than in amphibolites (Table 3.1) (Appendix 3).

A good tectonic discrimination diagram must be constructed with elements, which are insensitive to secondary processes (Rollinson, 1993). As these elements (P, Ti, Al, Zr, Y and Nb) are generally considered "immobile" during alteration processes, it should be possible to distinguish the magma type of ancient basic volcanic (Floyd & Winchester, 1975). Therefore these elements can be used with altered and metamorphosed rocks up to medium metamorphic grades (mid–amphibolite facies) for characterisation of magma types and tectonic environment discrimination.

To test the relative immobility of those elements pairs of them were plotted as shown in Figure 3.5. Plots of Ti against Y, Zr and P show linear arrays from the origin (Figure 3.5 A, D, and K) and poor trends with Nb (Figure 3.5 G), while against Al only serpentinites show a good positive correlation (Figure 3.5 B). The immobility of P is shown in Figure 3.5 K, L, M and N when it plots against Ti, Nb, Y and Zr respectively. Al is clearly a mobile element for amphibolites, whilst the serpentinites show linear positive trends (Figure 3.5 B, C and F). The plots in the Figure 3.5 E, I and J confirm the immobility of Y and Zr. Nb was slightly mobilised since it shows a slight scatter when plotted against other elements (Figure 3.5 G, H, I, J and L).

There seems no reason to suspect mobility of P, Ti, Zr, Y in rocks subjected to amphibolite facies metamorphism.

Using discrimination diagrams based upon Zr/Y-Zr variations (Pearce and Norry, 1979) the mafic and ultramafic rocks plot in MORB and volcanic-arc basalt fields (Figure 3.6 I) and in the oceanic arc field (Figures 3.6 II). The chlorite schist and some serpentinites do not plot within the discrimination diagram because they have low Zr/Y proportions.

The TiO_2-Zr/(P_2O_5*10 000) and P_2O_5-Zr discrimination diagrams (Floyd & Winchester, 1975) plot unequivocally on the fields of tholeiitic basalt as showing in the Figures 3.7 and 3.8 respectively. The Zr/P_2O_5 ratio of mafic and ultramafic volcanic rocks remains constant, showing predominantly vertical trend (Figure 3.7), whilst in the Figure 3.8 the greenstones show a low P_2O_5 (0.02- 0.15wt%) contents characteristic of tholeiitic basalts and low Zr ppm less than 100 ppm. The discrimination diagrams gave an excellent separation.

The Nb/Y versus Zr/(P_2O_5*10 000) discrimination diagram (Floyd & Winchester, 1975) produces a high-quality discrimination between alkali and tholeiittic basalts (Figure 3.9) although no meaningful tectonic separation is possible due to the substantial chemical overlap of oceanic and continental environments. The ternary TiO_2- KO_2- P_2O_5 discrimination diagram of Pearce *et al.* (1975) plots in the field of oceanic tholeiitic basalts.

3.2.1.4 DISCUSSION

In Zimbabwe the equivalent greenstones in the Odzi belt contain pillows suggesting a volcanic origin (Phaup, 1964). The consistently low K_2O, Rb, and Sr contents of greenstone within the study area may represent Archaean oceanic tholeiites.

These rocks with low SiO_2 and Al_2O_3 and high MgO contents among major elements combined with high Co, Ni and Cr contents

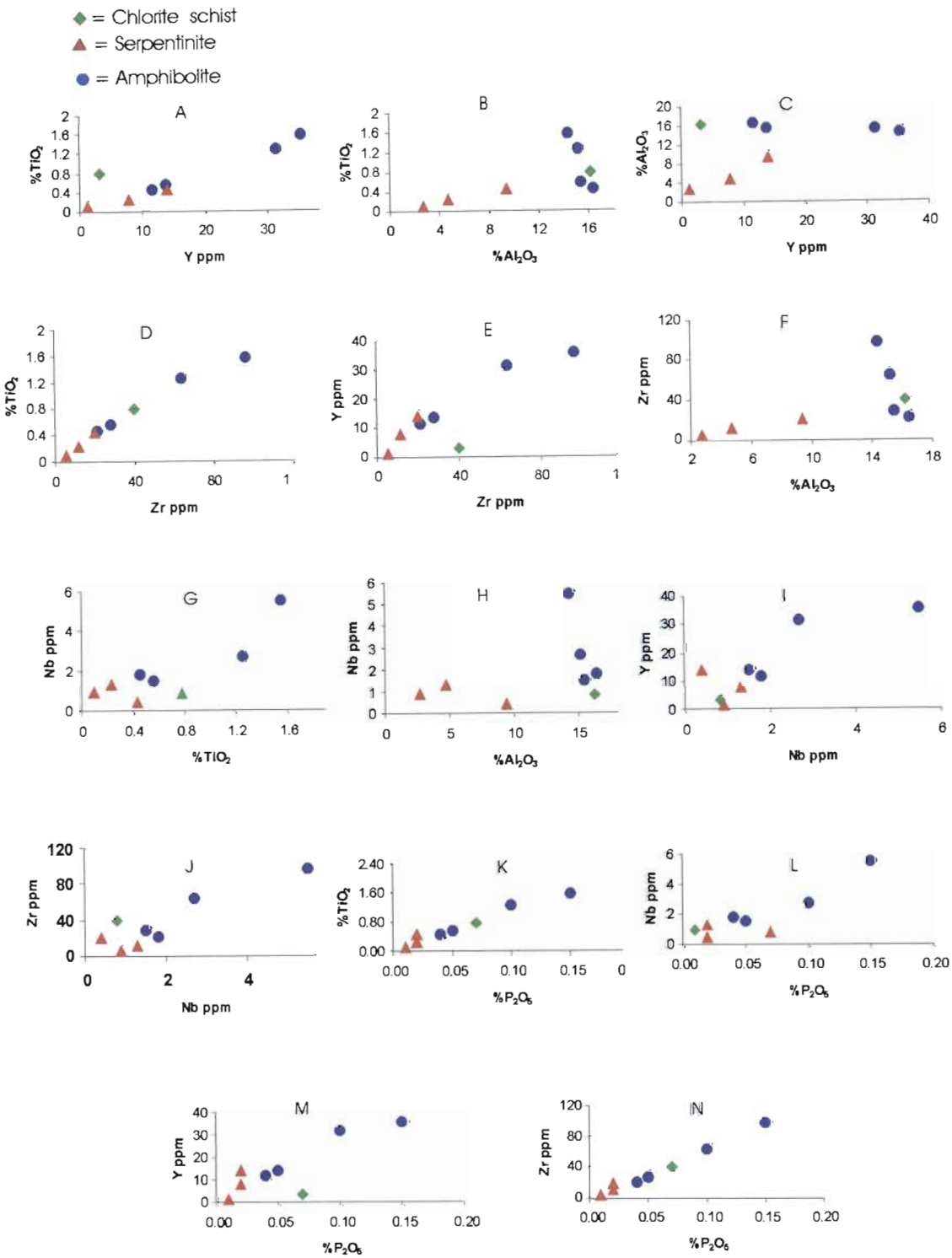

Figure 3.5 Bivariate diagrams showing relative mobility and immobility of different elements for greenstones.

◆ = Chlorite schist
● = Amphibolite
▲ = Serpentinite

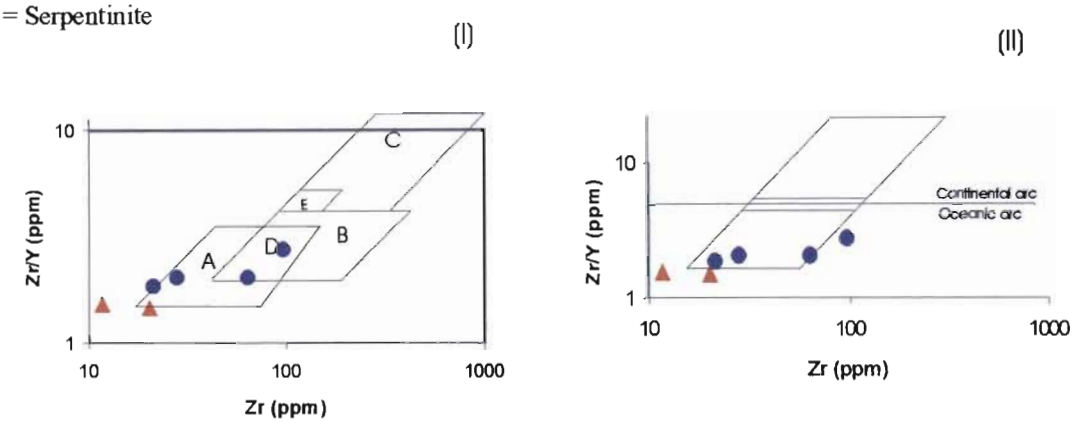

Figure 3.6 Discrimination diagram for basalt based upon Zr/Y-Zr variations; both diagrams have a logarithmic scale. (I) The fields are (A), volcanic-arc basalts;(B), MORB; (C), within-plate basalts; (D), MORB and volcanic-arc basalts; (E), MORB and within-plate basalts (after Pearce & Norry, 1979). (II) Fields of continental and oceanic-arc basalts separated on the basis of a Zr/Y value of 3. From Rollinson, 1993.

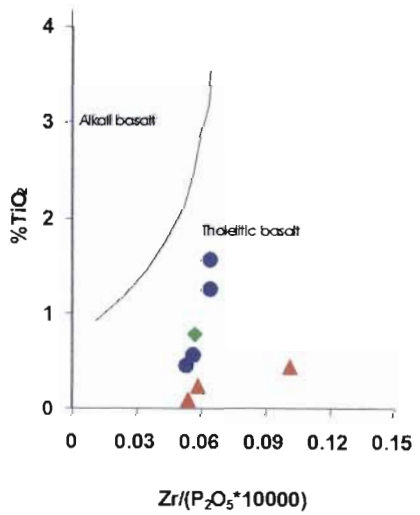

Figure 3.7 The TiO_2-Zr / (P_2O_5*10 000) discrimination diagram showing the tholeiitic character of greenstone (Winchester & Floyd, 1976).

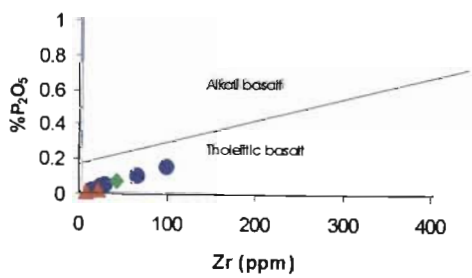

Figure 3.8 The P_2O_5-Zr (ppm) discrimination diagram showing the tholeiitic character of greenstone (Winchester & Floyd, 1976).

▲ = Serpentinite

◆ = Chlorite schist

● = Amphibolite

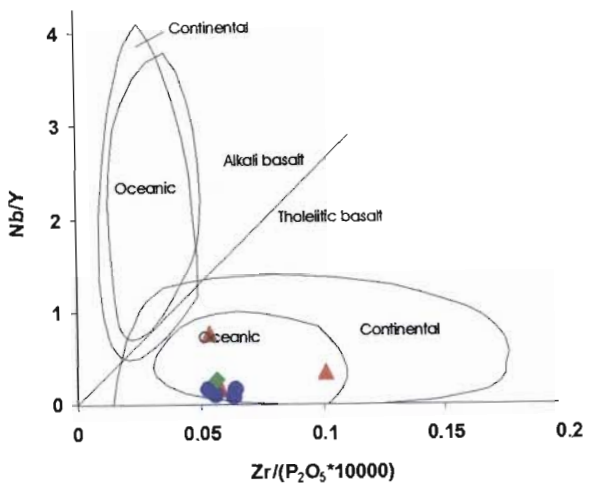

Figure 3.9 Nb/Y-Zr/(P_2O_5*10 000) discrimination diagram showing the oeanic tholeiitic affinity of serpentinite, amphibolite and chlorite schist. From Rollinson, 1993.

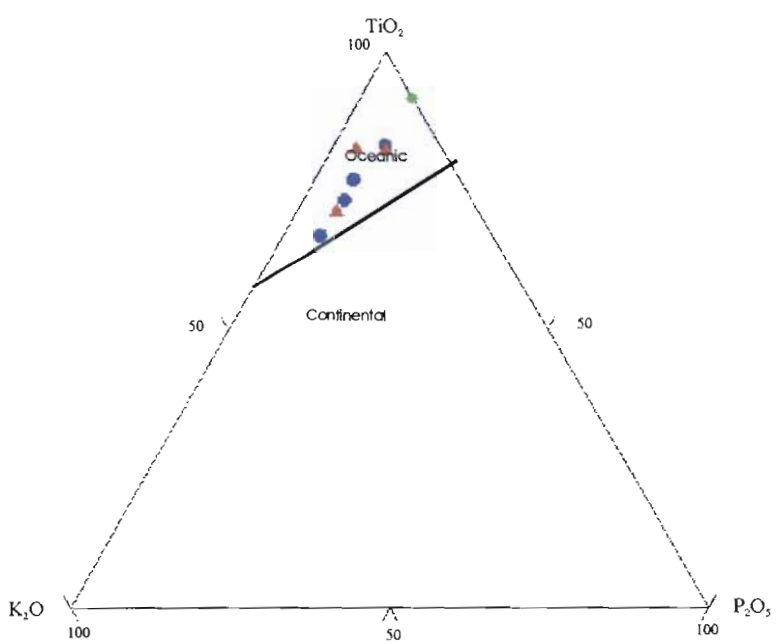

Figure 3.10 The TiO_2-K_2O-P_2O_5 discrimination diagram (Pearce *et al.*, 1975) showing the oceanic affinity of serpentinite, amphibolite and chlorite schist.

and low Li, Sr, Rb, Ba, Y, Nb and Zr contents among trace elements reflect their mafic and ultramafic character. The high Fe_2O_3 content of chlorite schist most likely is the reason for occurrence of garnet (almandine).

Based on the Al_2O_3-(Fe_2O_3+TiO_2)-MgO ternary discrimination diagram (Jensen, 1976) the amphibolite and chlorite schist can be classified as high-Fe tholeiite basalt and komatiite suite range from MgO-rich komatiite basalt to peridotitic komatiite.

3.2.2 VUMBA GRANITE GNEISS AND MESSICA GRANITE GNEISS

3.2.2.1 INTRODUCTION

Representative analyses of major and trace elements, CIPW norm calculation, and correlation matrix of chemical elements for Vumba granite gneiss are given in the Tables 3.3, 3.4 and 3.5 and for Messica granite gneiss in the Tables 3.6, 3.7 and 3.8 respectively (Appendix 3).

To classify and determine the origin of these rocks geochemistry analyses were used, which were combined with tectonic lithofacies analyses based on field observation, major element chemistry and petrography.

Only XRF trace elements (Nb and Y), which are likely to be the most effective elements were considered for tectonic discrimination of granitic rocks.

3.2.2.2 MAJOR ELEMENT GEOCHEMISTRY

Bivariate Harker variation diagrams of major oxide elements versus SiO_2 content show a general decreases in major oxide elements with an increase in SiO_2 content (Figure 3.11). The Vumba granite gneiss shows two groups. The group I is characterized by SiO_2 < 72%, CaO, Fe_2O_3 and MgO-rich, whilst the Group II characterized by SiO_2 > 72%, CaO, Fe_2O_3 and MgO contents lower than group I.

The Messica granite gneiss is likely correlated with group II of Vumba granite gneiss content. Statistically the Harker plots somewhat show two distinct segments of Vumba granite gneiss, which one is correlated very well with Messica granite gneiss representing the second segment as shown in the Figure 3.11.

Some variation diagrams (Figure 3.11) show inflections in apparent liquid line of descent, suggesting crystal-liquid fractionation processes during magmatic evolution.

The Messica granite gneiss has higher K_2O contents of 1.5-7.5wt% compared to values of 3.5-4 wt% in the Vumba granite gneiss (Manhiça, 1998).

These rocks are relatively poor in ferromagnesian elements (Fe_2O_3 + MgO + TiO_2) varying between 1.86-3.78 for Vumba and 1.5-2.4 for Messica granitoid and rich in Al_2O_3, which varies between 13.56 and 16.52 for Vumba and 11.91 and 14.74 for Messica granitic rocks. The Na_2O content is higher relatively to K_2O and CaO (Table 3.3 and 3.6).

In the ternary quartz-alkali-feldspar-plagioclase (QAP) diagram (Streckeisen, 1976) the Vumba granite gneiss plots in the tonalite, granodiorite, and monzogranite fields, whereas the Messica granite gneiss falls within the tonalite, and monzogranite fields (Figure 3.12, a). This trend is consistent with the modal classification proposed by Stildolph & Stocklmayer, (1976) for granitic rocks of Zimbabwe (Figure 3.12, b) although the Streckeisen's system depends on the light-coloured constituents being calculated to the sum of 100 (i.e. Q+A+P) whereas the Stildolph & Stocklmayer classification depends on the quartz content against the feldspar ratio, expressed as potash feldspar × 100/total

feldspar. No geochemical data are available from Zimbabwe Craton (Chilimanzi Batholith) for geochemical correlation.

This trend is supported by normative An-Ab-Or ternary diagram (Barker, 1979) whereas the Vumba granitoids plot in the tonalite, granite, granodiorite and trondhjemite fields and Messica granitic rocks fall within the granite and trondhjemite fields (Figure 3.12, c). It is clear from Figure 3.12, (b) that the Na_2O contents in these rocks are relatively higher than CaO and K_2O contents.

In the AFM diagram (Irvine & Baragar, 1971) both granitic gneisses plot near pole A in the calc-alkaline field (Figure 3.13, a) showing a high total alkali ($K_2O + Na_2O$) calc-alkaline trend of these rocks as shown in the above ternary QAP diagram. This characteristic trend of granitic rocks is supported by bivariate alkalis ($Na_2O + K_2O$) versus silica (SiO_2) diagram (Irvine & Baragar, 1971), suggesting the sub alkaline affinity (Figure 3.13, b) and by high proportion of Al_2O_3 (~14%).

The probably mixed origin of these granitoid rocks is shown in Figures 3.14 (a) and (b) where most of them fall within the peraluminous field and some of them within the metaluminous field showing their aluminium saturation ratios.

3.2.2.3 TRACE ELEMENT GEOCHEMISTRY

The two groups of Vumba granite gneiss defined on major elements are not clear with trace elements, except on plots Al_2O_3 versus Y, Nb and TiO_2 (Figure 3.16).

According to the trace elements (Table 3.3 and 3.6) the Rb, Zr, Nb and Y contents in the Vumba granite gneiss are slightly higher than in the Messica granite gneiss.

The relative immobility of Nb and Y trace elements makes them useful for characterizing the tectonic environment in which these granitoids were formed (Clarke, 1992). To test the relative immobility of Al, Ti, Y, Zr, and Nb, plotted pairs of these elements are shown in Figure 3.16. Only plots of Zr against Ti, Y and Al show somewhat linear and approximately parallel arrays from origin (Figure 3.16 D, E and F), suggesting relative immobility of Zr.

Using the Nb versus Y discrimination diagram (Pearce *et al.*, 1984) the granitoid rocks fall within both "volcanic arc granite"(VAG) and "syn-collision granite"(syn-COLG) in Figure 3.15.

3.2.2.4 DISCUSSION

The Vumba granite gneiss within study area, petrochemical is classified as tonalite-trondhjemite-granodiorite. This classification is distinctive of Archaean granitic rocks whatever their age and geographical origin, often abbreviated to TTG (Jahn *et al.*, 1981 and Martin *et al.*, 1983).

The Messica granite gneisses are classified as tonalite-trondhjemite suggesting more leucocratic than Vumba granitoid. This is supported by petrography and field observations, whereas the hornblende and biotite occur as ferromagnesian elements in the Vumba granite gneiss whilst in the Messica granite gneiss only the biotite is present as mafic component.

According to the chemical classifications (major and trace elements), Vumba and Messica granite gneisses are calc-alkalic granites originated at the crust-mantle interface (Clarke, 1992). On basis of the aluminium saturation ratio both granitic gneisses vary from peraluminous to metaluminous in composition.

Both granitic rocks are characterised by very low normative corundum, which with exception reached 1.00 and the aluminium

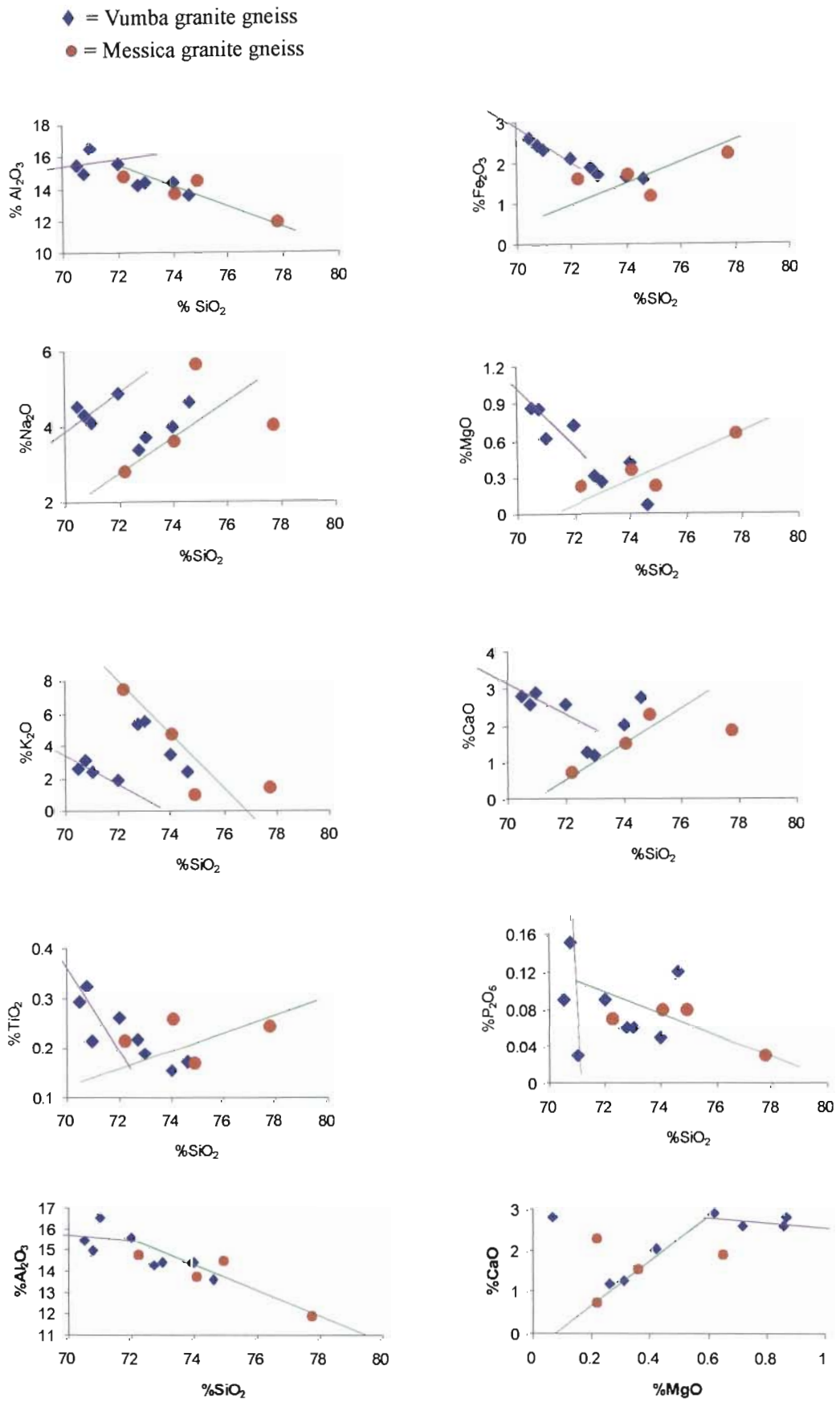

Figure 3.11 Harker variation diagrams of major oxide elements versus SiO_2 and MgO versus CaO in the granitic rocks compositions.

◆ = Vumba granite gneiss

● = Messica granite gneiss

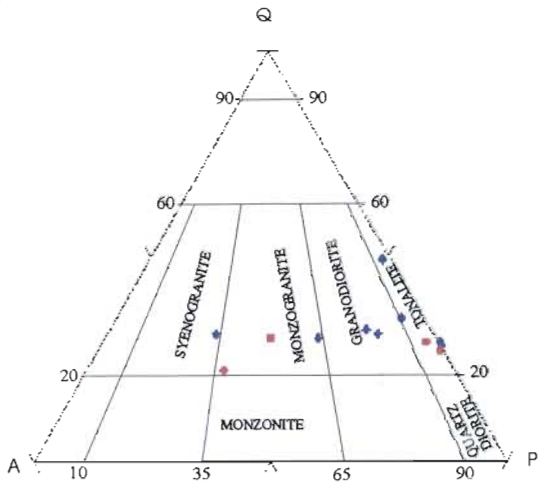

Figure 3.12 (a) Quartz-alkali-feldspar-plagioclase (QAP) diagram (Streckeisen, 1976) showing modal composition of Vumba granite gneiss and Messica granite gneiss.

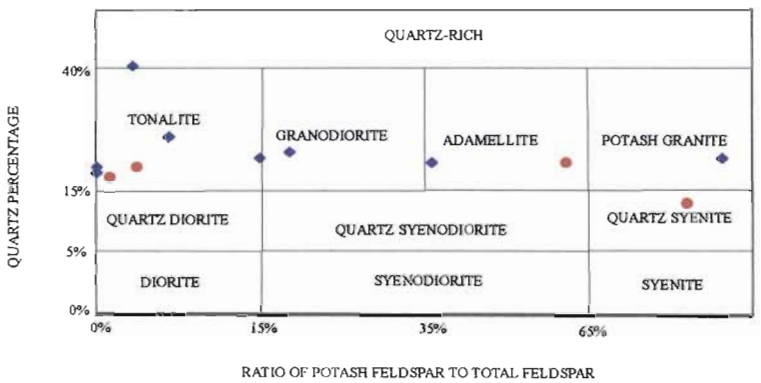

Figure 3.12 (b) Proposed modal classification of granitic rocks of Zimbabwe (Stildolph & Stocklmayer, 1976)

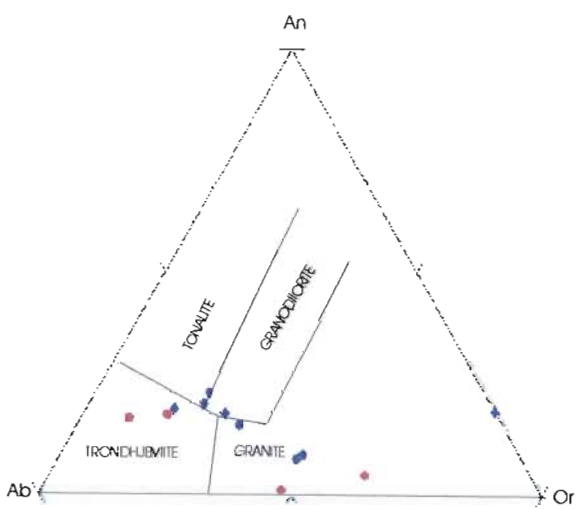

Figure 3.12 (c) Ternary normative Ab-An-Or diagram (Barker, 1979) showing different fields of granitic rocks.

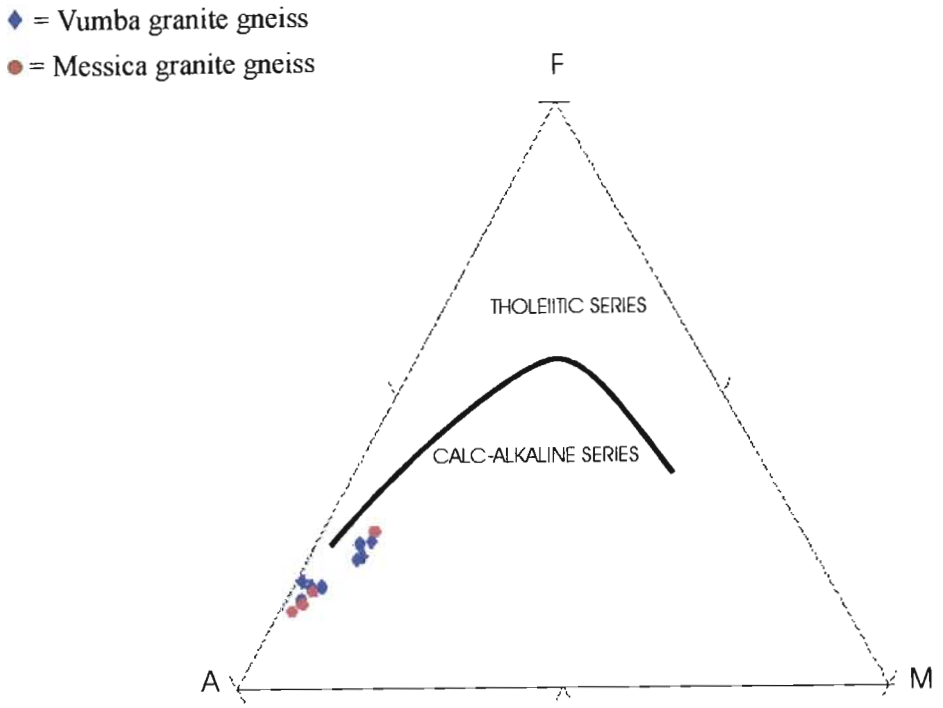

Figure 3.13 (a) Ternary AFM diagram (Irvine and Baragar, 1971), showing a calc-alkaline trend of granitoid rocks.

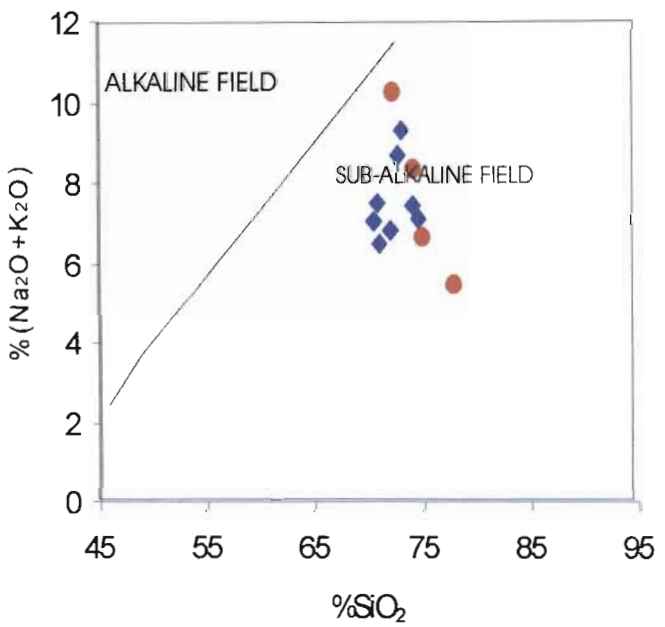

Figure 3.13 (b) Bivariate ($Na_2O + K_2O$) versus SiO_2 (TAS) diagram (Irvine &Baragar, 1971), showing subalkaline affinity

◆ = Vumba granite gneiss

● = Messica granite gneiss

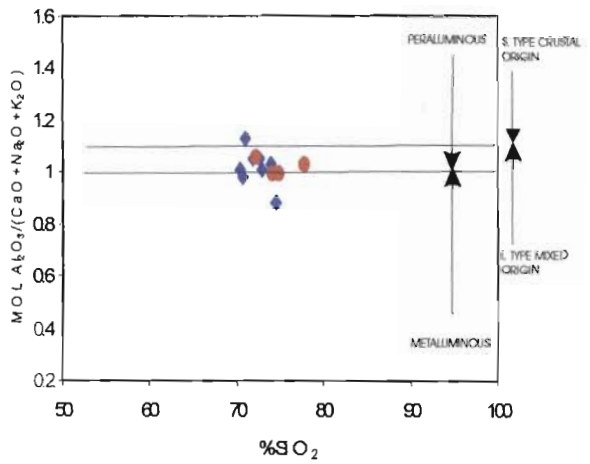

Figure 3.14 (a) Binary SiO_2 versus $Al_2O_3/[CaO+Na_2O+K_2O]$ (molar) diagram (Clarke, 1992).

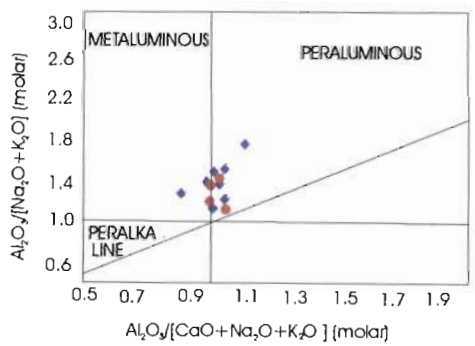

Figure 3.14 (b)) Binary $Al_2O_3/[CaO+Na_2O+K_2O]$ (molar) versus $Al_2O_3/(Na_2O+K_2O]$ (molar) diagram (Clarke 1992)

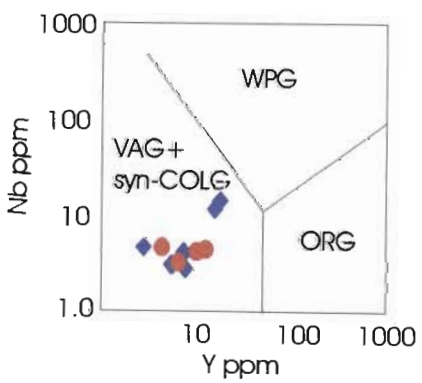

Figure 3.15 Nb versus Y discrimination diagram (Pearce *et al* , 1984) for syn -collision (Syn-COLG), volcanic arc granites (VAG), within plate granites (WPG) and oceanic ridge granites (ORG)

◆ = Vumba granite gneiss
● = Messica granite gneiss

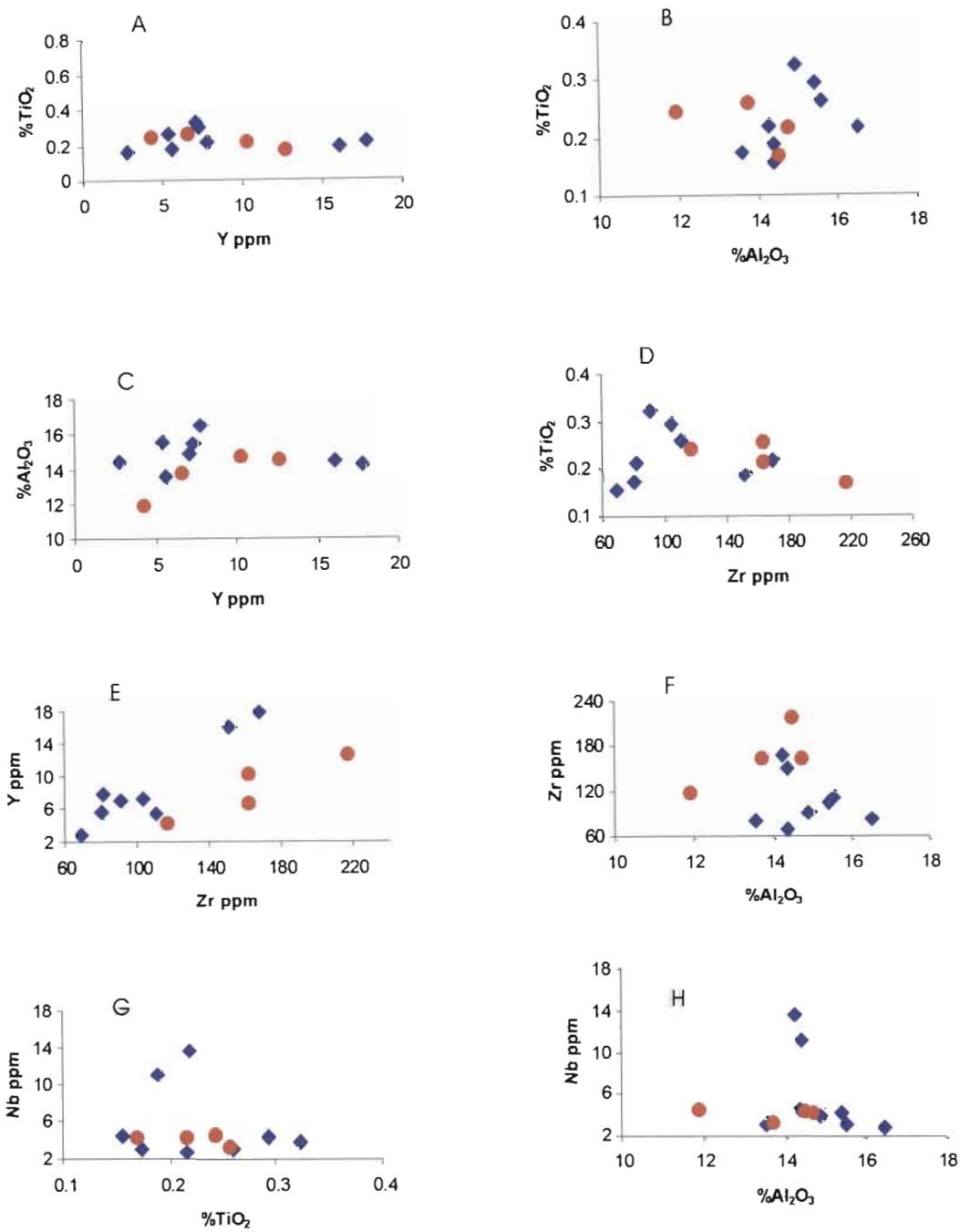

Figure 3.16 Bivariate diagrams showing relative mobility and immobility of different elements.

saturation ratio [Al_2O_3 /(NaO_2 + K_2O + CaO)] up to 1.1 suggesting derivation by anatexis of igneous rather than sedimentary parents (Chappell & White, 1974).

The positive correlation of Rb-Zr (Table 3.5 and 3.8) may indicate that the fractionation of zircon did not play a significant role during the differentiation process (Dupuy *et al.*, 1982).

The possible existence of two distinct segments in Figure 3.11 might reveal a complex mechanism related with fractional crystallization (Martin, 1987). More obviously the Group II Vumba and Messica granite gneisses (green lines) are the result of fractional crystallization of Archaean tonalite-trondhjemite-granodiorite series (Group I of Vumba granite gneiss – purple lines).

3.2.3 UMKONDO GROUP

3.2.3.1 INTRODUCTION

The chemical composition and petrographical characteristics were evaluated in order to established provenance and tectonic setting of Proterozoic Umkondo Group sediments.

Representative XRF analyses of major and trace elements of Umkondo Group sandstone and mudstone are given in the Tables 3.9 and 3.10 respectively (Appendix 3). In the Tables 3.11 and 3.12 (Appendix 3) are shown the correlation matrix of chemical elements for the Umkondo Group sandstone and mudstone samples respectively.

3.2.3.2 MAJOR ELEMENT GEOCHEMISTRY

XRF analyses of Umkondo Group mudstones in general are rich in Al_2O_3, Fe_2O_3, K_2O, and TiO_2 contents, but relatively poor in CaO and NaO_2 compared to the sandstones. The sandstones in generally are poor in major oxide elements, except for Quartzite Formation sandstone, which are very rich in CaO and Na_2O as shown in Figure 3.17 and Table 3.9 (Appendix 3). Bivariate Harker variation diagrams of major oxide elements versus SiO_2 show in general a linear negative correlation (Figure 3.17). The SiO_2 contents increase with increasing of grain-size, reflecting decreasing proportions of matrix-sized detritus as has well shown by negative linear trends for Al_2O_3, Fe_2O_3, K_2O, MgO and TiO_2. This corresponds to the mineralogical maturity of the rocks as suggested by the petrography observations.

The chemical composition is affected by the grain size of the samples analysed and so the results of any geochemical discrimination will also be influenced (Roser and Korsch, 1986). Using petrological data for ternary QFR diagram (Folk *et al.*, 1970), the majority of Argillaceous Formation sandstone plots in subarkose field and few fall between arkose and lithic arkose fields, whereas the Quartzite Formation sandstone plots in litharenite field and few in quartz arenite field (Figure 3.18 a). This geochemical classification is supported by the log (SiO_2/Al_2O_3)/log (Fe_2O_3/K_2O) diagram (Herron, 1988) as shown in the Figure 3.18 (b).

The higher Fe_2O_3/K_2O ratios of Quartzite Formation sandstone are most likely related to the enrichment of chlorite, epidote and biotite. The mudstone plots on the shale field showing higher Fe_2O_3/K_2O and lower SiO_2/Al_2O_3 ratios in relation to the sandstone.

The geochemical and petrographic classifications are supported by ternary Fe_2O_3 (tot) + MgO - Na_2O - K_2O diagram (Blatt *et al.*, 1980), in which the Quartzite Formation sandstone plots on the lithic sandstone field, showing high percentage of Fe_2O_3 (tot) + MgO, and K_2O in relation to the sandstone of Argillaceous Formation,

which plots on the arkose field (Figure 3.18 c).

The SiO_2/Al_2O_3 ratio is an indicator of sedimentary maturation (Rollinson, 1993). The ratio increases during weathering, transport and recycling, due to increase in modal framework quartz at the expense of less resistant components such as feldspar, and lithic fragments. Another useful index of chemical maturity according to the Rollinson (1993) is the alkali content ($Na_2O + K_2O$), also a measure of the feldspar content. SiO_2/Al_2O_3 ratios more than 5 in sedimentary rocks provide evidence of sedimentary maturation (Roser *et al.*, 1996). The mudstone shows consistent SiO_2/Al_2O_3 ratio values between 2 to 4, which indicate its immaturity. But the SiO_2/Al_2O_3 ratios values increase within Quartzite Formation sandstone up to 8, reaching values around 34 for Argillaceous Formation sandstone. The sedimentary sorting of Umkondo Group is consistent with petrography observations.

Using the tectonic discrimination K_2O/Na_2O ratio versus SiO_2 content diagram (Roser & Korsch, 1986), the samples plot entirely within the passive continental margin (PM) field (Figure 3.19 a). This trend is confirmed by tectonic discrimination SiO_2/Al_2O_3 ratio versus K_2O/Na_2O ratio diagram (Roser & Korsch, 1986), although the majority of Argillaceous Formation sandstones does not fall in the diagram area, because of high SiO_2/Al_2O_3 ratio values as shown in Figure 3.19 (b). The mudstone shows low SiO_2/Al_2O_3 ratios. As shown in the Table 3.13 (Appendix 3) the geochemical characteristics of Umkondo Group sandstone are correlated to the Passive Continental Tectonic Margin Setting of Bhatia (1983).

Using the ternary Q_mFL_t (Dickinson & Suczek, 1979) and QFL tectonic provenance diagrams, Quartzite Formation sandstones plot on recycled orogen and few on craton interior fields, whilst the Argillaceous Formation sandstones fall within the craton interior and few within the transitional continental and recycled orogen fields (Figure 3.20 a and b).

The good index for the influence of weathering on sediment compositions is the Chemical Index of Alteration (CIA) according to the Nesbit & Young (1982). The CIA values for Quartzite Formation sandstone are around 49 and for mudstone they vary from 71 to 75. The CIA ratios are notable higher in the Argillaceous Formation sandstone, with values ranging from 69 to 89, showing much closer to the CIA ratios typical of muscovite and illite (Figure 3.21 a, b). These values suggest that the Umkondo Group mudstone is slightly weathered, the Quartzite Formation sandstone is relatively unweathered, and Argillaceous Formation sandstone is weathered (Taylor & McLennan, 1985). The above values are indicative of greater weathering, either of the original source terrane, or during transport before deposition (Roser *et al.*, 1996)

3.2.3.3 TRACE ELEMENT GEOCHEMISTRY AND REE

Although the chemical composition of shales may be used to constrain source area composition, some factors contribute to the distribution of elements in shale (Wronkiewicz & Condie, 1987):

1) Grain-size. The hydraulic sorting of grains during weathering, erosion and deposition, which separates them by size and density, might control the chemical composition of shale.

2) Absorption of ions by clays and other finer grained material. The absorption of ions can occur during weathering, erosion and/or during the early stages of diagenesis.

3) Mobilization of elements during diagenesis and metamorphism.

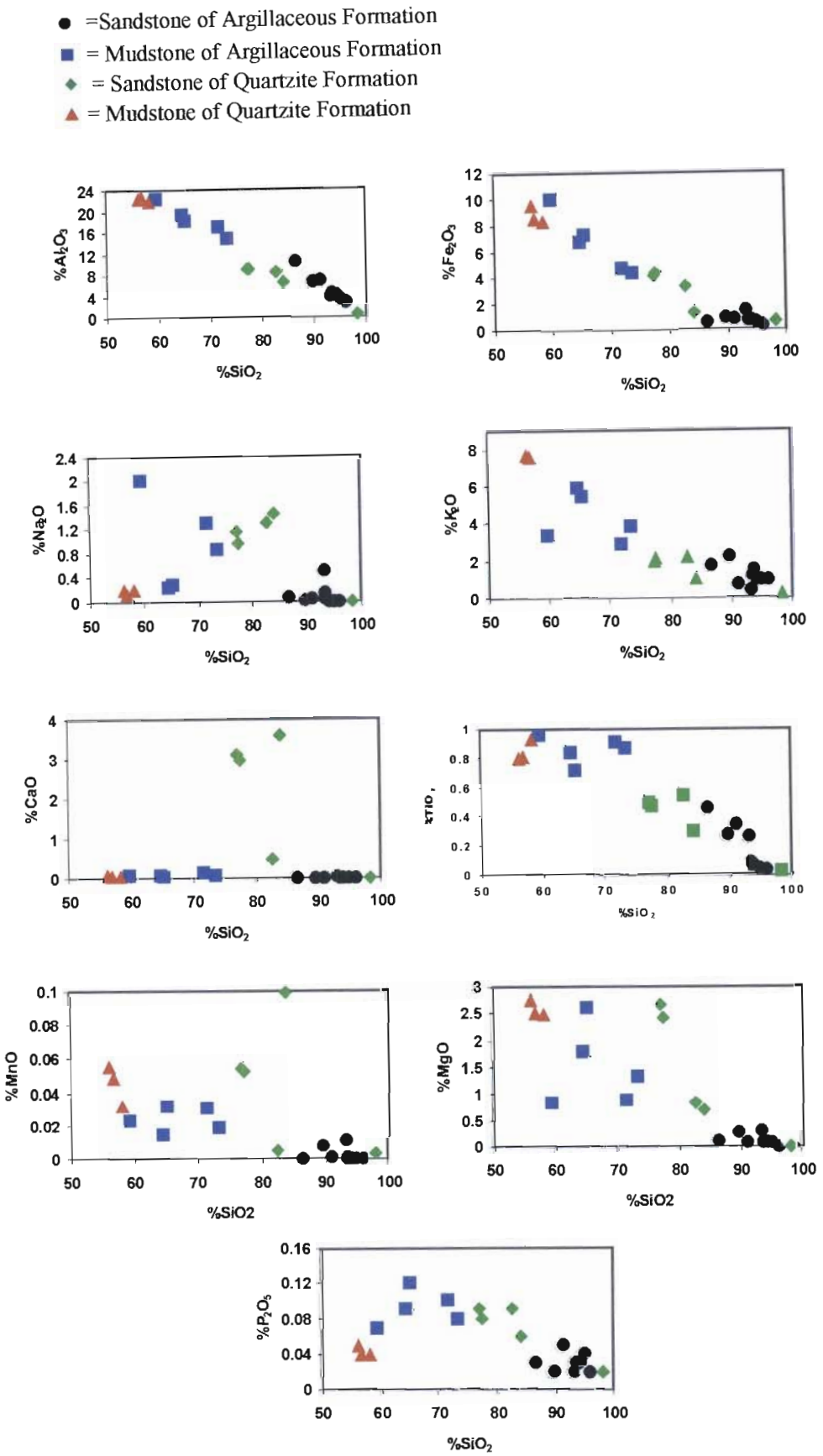

Figure 3.17 Harker variation diagrams of major oxide elements versus SiO_2 for sandstone and mudstone for Umkondo Group.

● = Sandstone of Argillaceous Formation
■ = Mudstone of Argillaceous Formation
◆ = Sandstone of Quartzite Formation
▲ = Mudstone of Quartzite Formation

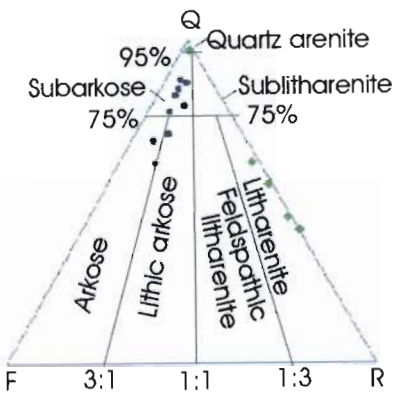

Figure 3.18 (a) Ternary QFR diagram (Folk *el al.*, 1970) showing different fields of sandstone. Q=monocrystalline and polycrystalline quartz (excluding chert), F=mono-crystalline feldspar, R=rock fragments (igneous, metamorphic and sedimentary including chert).

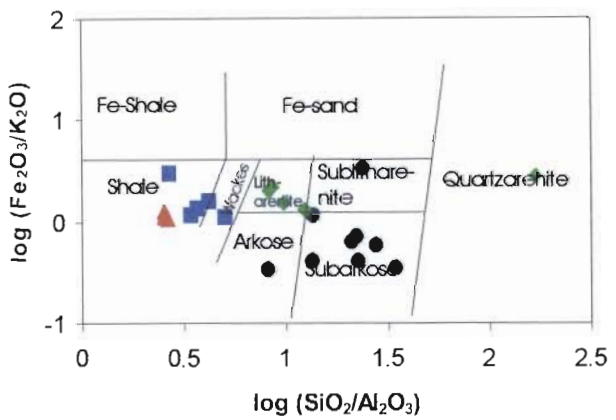

Figure 3.18 (b) The classification of terrigenous sandstone and shale using log (Fe_2O_3/K_2O) versus log (SiO_2/Al_2O_3) (after Herron, 1988)

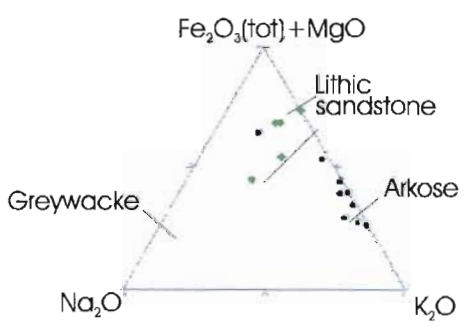

Figure 3.18 (c) Ternary Na_2O - K_2O - (Fe_2O_3 + MgO) diagram(Blatt *et al.*, 1980) distinguishing sandstone types.

● = Sandstone of Argillaceous Formation
■ = Mudstone of Argillaceous Formation
◆ = Sandstone of Quartzite Formation
▲ = Mudstone of Quartzite Formation

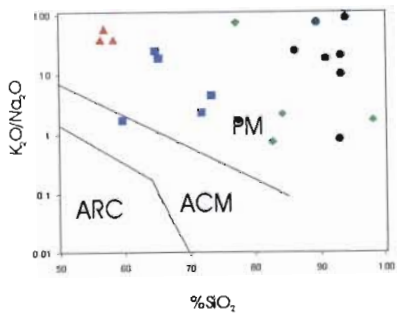

Figure 3.19 (a) Tectonic discrimination K_2O/Na_2O versus SiO_2 diagram showing passive continental margin plot (Roser & Korsch, 1986). PM = Passive Margin, ACM = Active Continental Margin and ARC = Island-Arc.

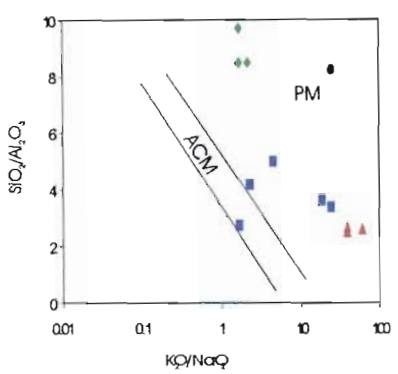

Figure 3.19 (b) Tectonic discrimination K_2O/Na_2O versus SiO_2/Al_2O_3 diagram showing continental margin plot (Roser & Korsch, 1986). PM = Passive Margin, ACM = Active Continental Margin.

4) Degree of chemical weathering of the source rock, which is dependent on climate and rates of tectonic uplift.

5) Bulk composition of the source terrane.

6) Tectonic setting and its influence on composition of the source terrane.

In order to decrease the effect of secondary processes, it is essential to rely on elements that are the least mobile under the expected range of geological condition. In this respect, the REE, Th and Sc are the best candidates for provenance studies (Taylor & McLennan, 1985).

To minimize the grain size effect it is recommended to compare sediments of approximately the same grain size and sedimentary environment (Wronkiewicz & Condie, 1987).

Pelites were chosen to determine the provenance of metasediments, because according to Cullers *et al.* (1987) the REE pattern is most faithfully represented in the clay-bearing rocks. These rocks are characterised by low post-depositional permeability and homogenous grain distributions. The diagenesis and low-grade metamorphism do not significantly affect the REE composition of mudstone since REE are generally least susceptible to remobilisation (Wronkiewicz & Condie, 1987).

Quartzites are less representative of source rock composition due to their low trace contents, pre-lithified permeability, hydraulic segregation of sand-sized particles during transport (Wronkiewicz & Condie, 1987).

To test the immobility of Al, Ti, Nb, Y, and Zr pairs of these elements were plotted as shown in Figure 3.22. Plots of Y against TiO_2 and Al_2O_3 show linear and parallel arrays from the origin (Figure 3.22 A and C). In Figure 3.22 (G and H) the Nb against TiO_2 and Al_2O_3 diagrams produce linear and parallel arrays extending through the origin as well as in the plot of Al_2O_3 versus TiO_2 (Figure 3.22 B). But plots of Zr against TiO_2, Al_2O_3, and Y (Figure 3.22 D, F, and E) do not show linear and parallel arrays from the origin. Therefore the behaviour of pairs of elements suggests that Al, Ti, Y, and Nb were immobile during sedimentary processes, while the Zr was mobile. The mobility of Zr most likely shows different provenance source of these sediments.

Th/Sc and Ce/Sc ratios increase with sedimentary maturation and/or with the supply of evolved (acidic) detritus, whereas V/La ratio decreases (Roser *et al.*, 1996). The Th/Sc and Ce/Sc ratios of Quartzite Formation sandstone shows consistent values 0.6 to 2.2 and 3.7 to 8.6 respectively, whilst in the Upper Argillaceous Formation sandstone they range between 0.7 to 0.9 and 4.9 to 11.0 respectively. V/La ratios decrease from the values 0.7 – 2.9 for Quartzite Formation sandstone to 1.3 – 1.5 for Upper Argillaceous Formation sandstone.

The rare earth elements (REE) are the most useful of all trace elements. They are regarded as relatively immobile during low grade metamorphism, weathering and hydrothermal alteration (Rollinson, 1993), therefore they reflect the chemistry of their source.

Within the study area the mudstone has much higher total REE concentration than the sandstone. Light REE ranges from 20 to 312 × chondrite and heavy REE from 9 to 32 × chondrite. The chondrite normalized REE pattern (Figure 3.23) shows that the Umkondo Group mudstone is characterised by small to moderate negative Eu anomalies (Eu/Eu* = 0.6-0.7) and by better developed negative Ce anomaly and LREE enrichment with high $(La/Yb)_N$ varying between 7.0 and 18.9. This suggests that they were derived from an evolved felsic crustal source, which is supported by low percentage of Co, Cr, and Ni elements as shown in the Table 3.14 (Appendix 3). HREE are flat and relatively depleted,

● = Sandstone of Argillaceous Formation

◆ = Sandstone of Quartzite Formation

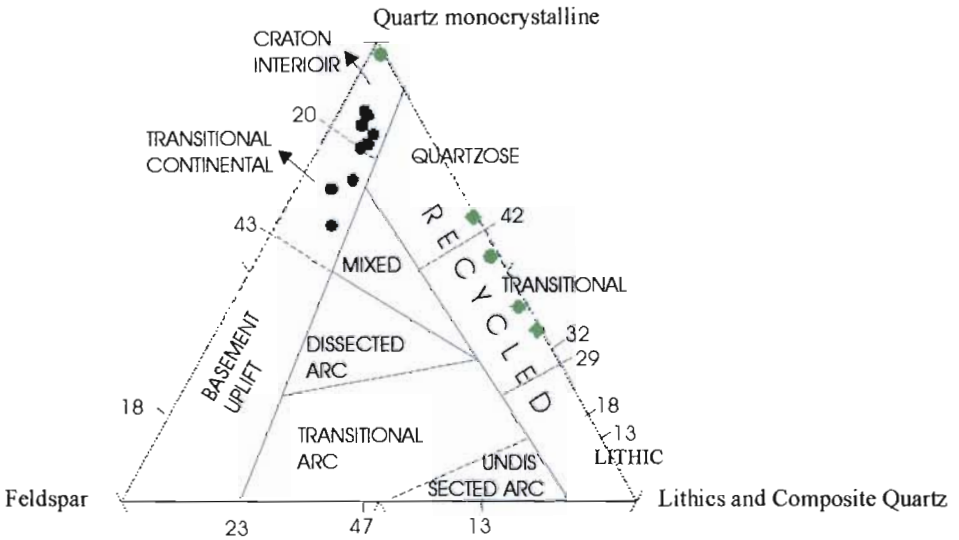

Figure 3.20 (a) Ternary QmFLt (Dickinson & Suczek, 1979) diagram plot of sandstone of Argillaceous and Quartzite Formations showing different types of provenance.

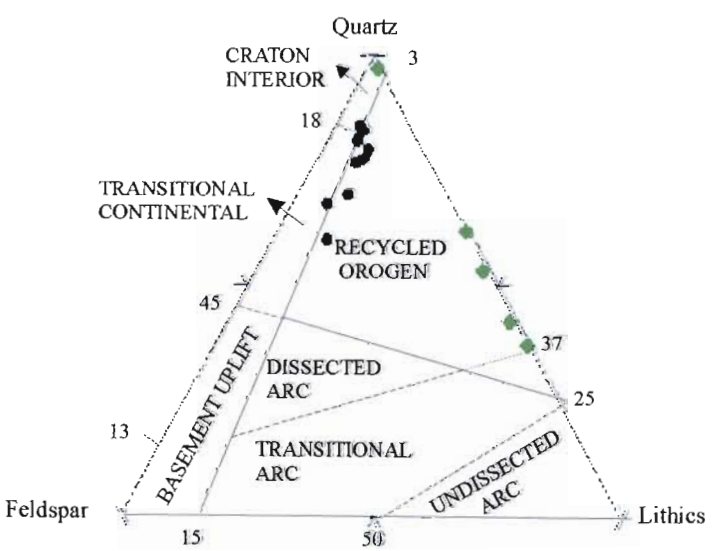

Figure 3.20 (b) Ternary QFL (Dickinson & Suczek, 1979) diagram showing Argillaceous and Quartzite sandstones plot on recycled orogen field.

● = Sandstone of Argillaceous Formation
■ = Mudstone of Argillaceous Formation
◆ = Sandstone of Quartzite Formation
▲ = Mudstone of Quartzite Formation

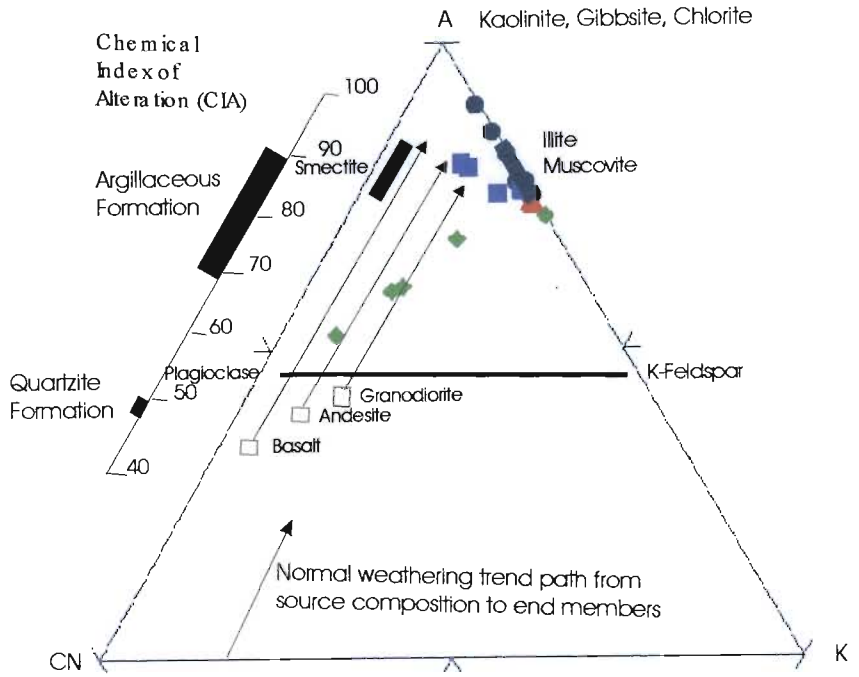

Figure 3.21 (a) Ternary plot of A-CN-K where , in mole fraction, $A=Al_2O_3$, C=CaO (silicate fraction only), $N=Na_2O$ and $K=K_2O$ (after Nesbitt & Young, 1984, 1989)

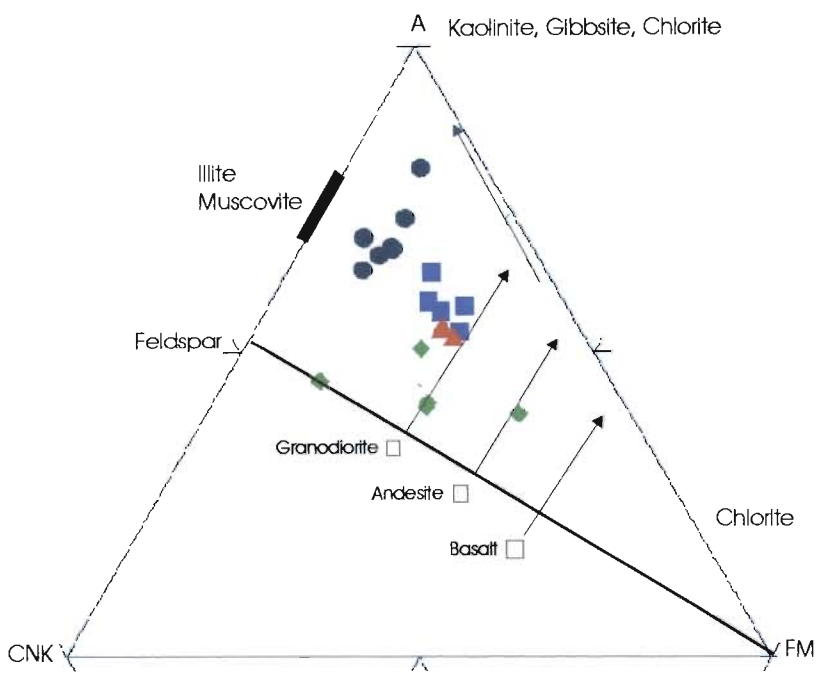

Figure 3.21 (b) Ternary plot of A-CNK-FM where, in mole fraction, $A=Al_2O_3$, C=CaO (silicate fraction only), $N=Na_2O$, $K=K_2O$, F=total Fe as FeO, and M=MgO (after Nesbitt & Young, 1984, 1989)

● = Sandstone of Argillaceous Formation
■ = Mudstone of Argillaceous Formation
◆ = Sandstone of Quartzite Formation
▲ = Mudstone of Quartzite Formation

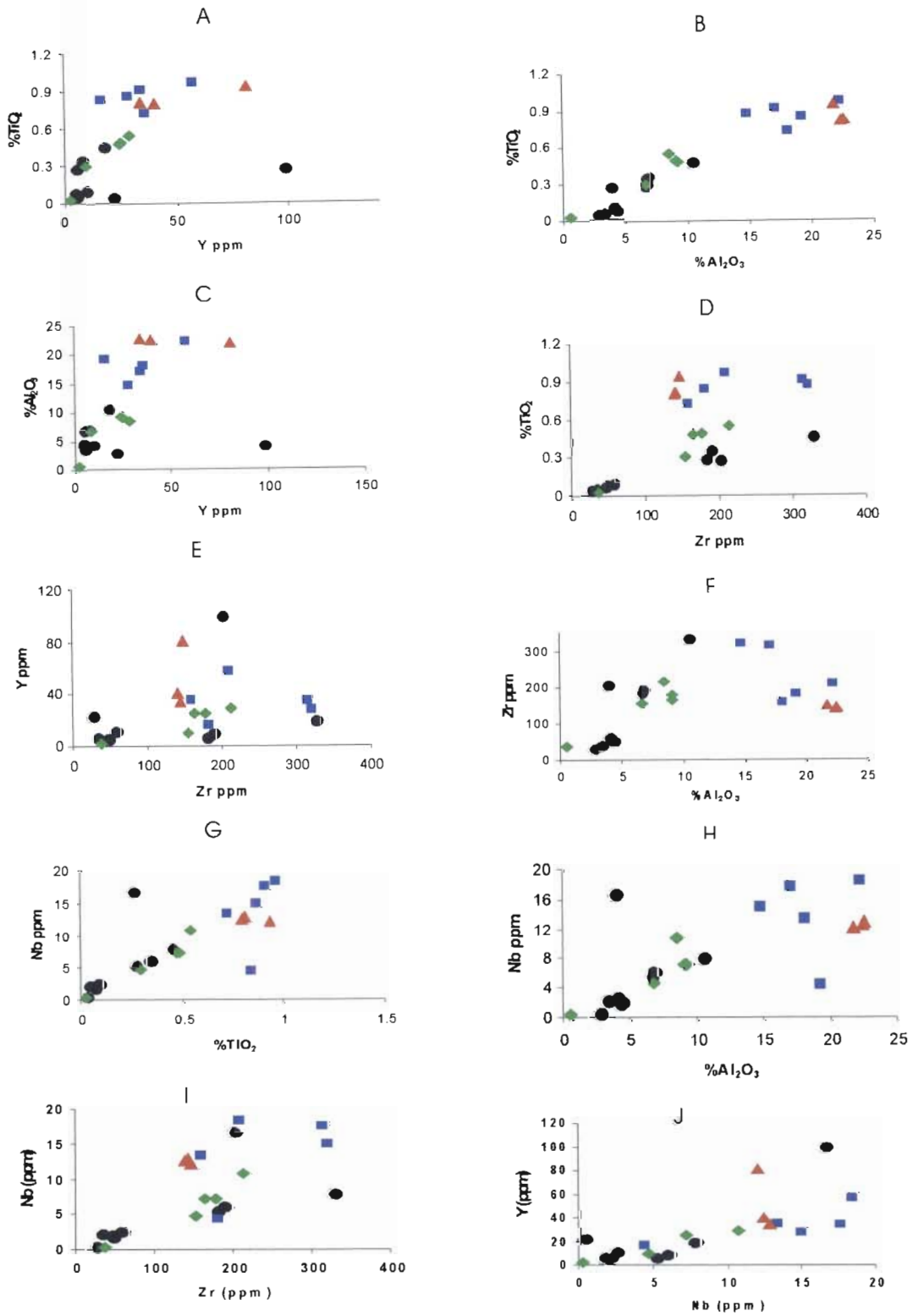

Figure 3.22 Bivariate diagrams showing relative mobility and immobility of different elements.

suggesting a little fractionation with $(Gd/Yb)_N$ average around 1.65 (Table 3.14)

On ternary diagram for La-Th-Sc (Figure 3.24) the pelites plot along the mixing line dominated by granitic rock (TT) with less contribution of mafic-ultramafic rocks (AMV).

The element ratios such as La/Th, La/Sc, and Th/Sc can minimize the effect of mineral fractionation (Taylor & Maclennan, 1985). The mudstones of Umkondo Group have lower Th/Sc ratio (0.42) as well as La/Sc (1.49) and high ratio La/Th (3.58) as shown in Table 3.15. These are similar to the Archaean shales, suggesting a certain percentage of mafic-ultramafic components in the metasediments from a partially melted Archaean source (Taylor & McLennan, 1985).

The Ni/Co, Cr/V and V/Ni ratios of the Umkondo shales are comparable to the average given for late Archaean shales, reflecting a certain contribution of mafic-ultramafic rocks (Taylor & McLennan, 1985). The relative contribution of granitic and ultramafic sources is reflected in the distribution of Zr and Cr in the shale (Wronkiewicz & Condie, 1987). The very low Cr/Zr ratio (0.9-1.3) in the Umkondo Group mudstone indicates the relative importance of granitic component to ultramafic component.

4.2.3.5 DISCUSSION

The Mesoproterozoic sediments of Umkondo Group are characterised by high K_2O/Na_2O and SiO_2/Al_2O_3 ratios and high CIA, reflecting a dominance of granitoid source and relatively high weathering respectively (McLennan *et al.*, 1993). The Th/Sc, Ce/Sc ratios and bivariate Harker variation diagrams of major oxide elements versus SiO_2 are suggestive that they are characterised by relatively immaturity to mature sediments. The Umkondo Group sediments are remarkably more mature than those of the Ritscherflya Supergroup (Perritt, 2001).

Furthermore the sandstones are generally enriched in SiO_2 and depleted in Na_2O, CaO and TiO_2. They have low Fe_2O_3+MgO ratio and high K_2O/Na_2O, SiO_2/Al_2O_3 and $Al_2O_3/(CaO+Na_2O)$ ratios (Table 3.13) and on A-CN-K discrimination diagram (Nesbit & Young, 1984, 1989) they plot on the Al_2O_3-K_2O join (Figure 3.21 a). These features indicate their relatively high-recycled nature with the enrichment of quartz and depletion of chemical unstable grains e.g. feldspar and matured nature, suggesting passive margin type tectonic setting (Bhatia, 1983; Cox *et al.*, 1998). The chemical features are consistent with petrographic observations, where the quartz overgrowths and quartz-rich nature of sands also suggest a cratonic and/or recycled orogen provenance signature of these sandstones (McLennan *et al.*, 1993). The Ritscherflya Supergroup sediments indicate a predominance of continental island arc and active continental margin tectonic signatures, although passive margin settings are also observed (Perritt, 2001).

The Upper Argillaceous Formation sediments are characterised by quartz-rich, feldspar-poor and relatively weathered, they were probably derived from continental blocks (Schwab, 1986). The Umkondo Group mudstones are characterised by high abundance of incompatible trace elements, such as LREE and Th, high concentration of trace elements (Nb, Y, and Zr) and by high ratios of $(La/Y)_N$, Ce/Sc, Th/Sc, La/Sc and Tc/Co. The low concentration of ferromagnesian elements Cr (188 ppm) and Ni (65 ppm) show that the importance of felsic source relative to mafic-ultramafic source (Taylor & McLennan, 1985).

The Umkondo Group mudstone is well correlated to the Vumba granite gneiss of Archaean Zimbabwe Craton as reported in the Figure 3.25.

In conclusion the Umkondo Group sediments were most likely derived from a

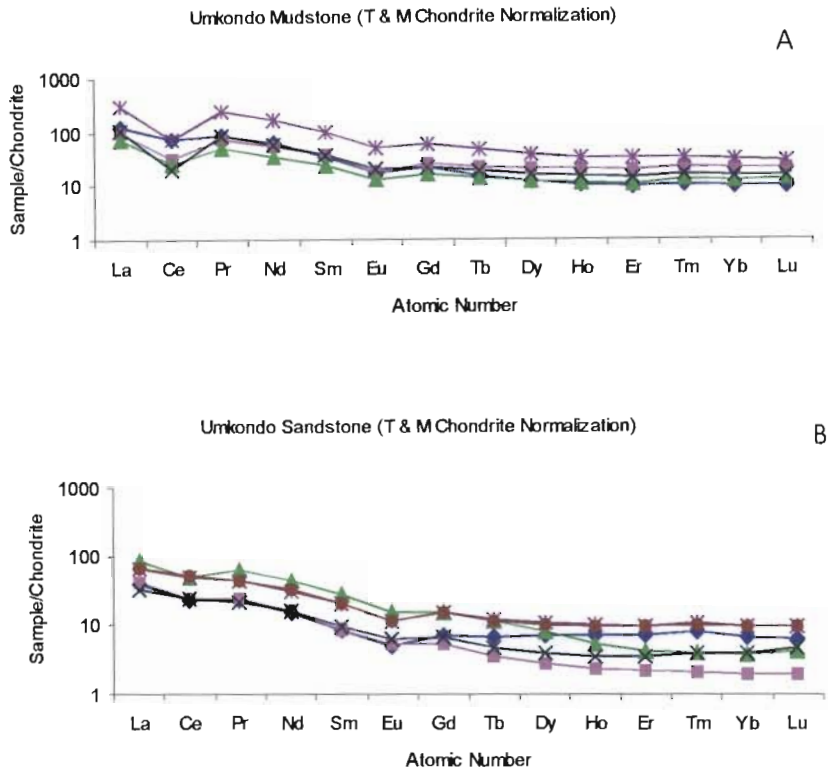

Figure 3.23 Chondrite-normalized rare earth element plots for Umkondo Group Mudstones of Quartzite and Argillaceous Formations (A) and Umkondo Group Sandstone of Quartzite and Argillaceous Formations (B).

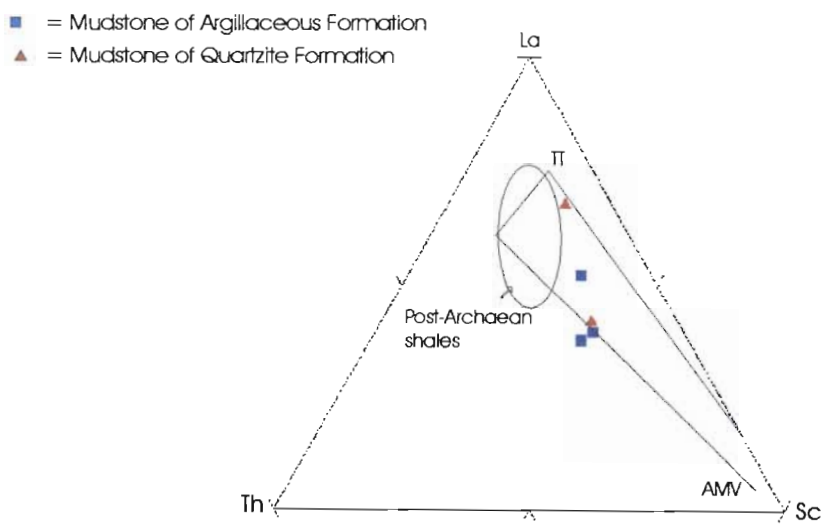

Figure 3.24 Ternary diagram for La-Th-Sc data for Umkondo Group mudstone. TT is average felsic igneous rocks and AMV is Archaean Mafic Volcanics (Taylor and McLennan, 1985).

Table 3.15 Ratio of REE in Archaean, Post-Archaean shales (Taylor & Mclennan, 1985) and Umkondo Group mudstone.

Ratio	Archaean		Post-Archaean	Umkondo Mudstone
La/Th	3.5 ± 0.3		2.8±0.2	3.58
Th/Sc	0.43 ± 0.07		1.0 ± 0.1	0.42
La/Sc	1.3 ± 0.2		2.7 ± 0.3	1.49
Cr/V	Early	Late	0.9 ± 0.1	1.23
	5.3 ± 1.0	1.5 ± 0.3		
Ni/Co	11.6 ± 1.6	3.0 ± 0.7	2.6 ± 0.2	3.21
V/Ni	051 ± 0.28	1.7 ± 0.7	2.1 ± 0.2	2.34

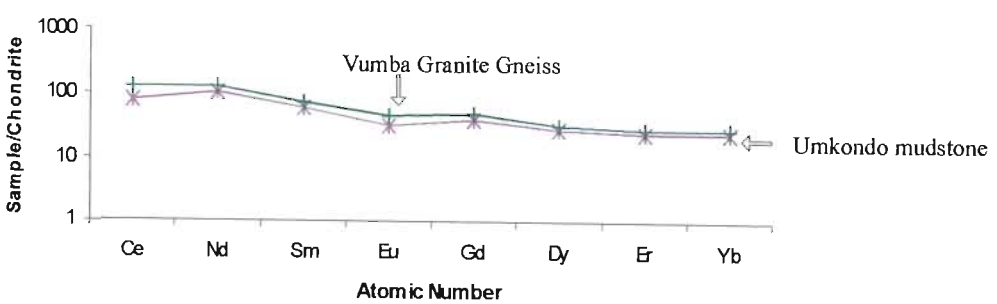

Figure 3.25 Chondrite-normalized rare earth element plots for Vumba Granite Gneiss (Manhica, 1998), for Umkondo Group mudstone.

source rich in tonalitic-trondjemitic-granodiorite (TTG) composition with less mafic-ultramafic composition. A Greenstone belt may serve as the mafic and ultramafic sources for these sediments, as well as from reworked metasediments.

Button (1977) reports palaeocurrent directions towards the east, northeast and north. The nearby Archaean continental nucleus preserves similar chemical features as the Umkondo Group metasediments. Therefore the Umkondo Group sediments originated from Limpopo Belt, southern margin of Zimbabwe Craton.

3.2.4 BÁRUÈ COMPLEX

3.2.4.1 INTRODUCTION

Báruè Complex is poorly exposed within the study area. As the name implies, it consists of a wide variety of lithologies with complex relationships. A comprehensive geochemical study is beyond the scope of this study. The Chimoio, Tchinhadzandze and Nhansipfe gneisses were previously studied by Manhiça (1998). Samples of the main granitic units were analysed for comparison with previous work and the Vumba granite gneiss and Messica granite gneiss. Of these four belong to the Nhansipfe megacrystic gneiss (NMG), one to the Tchinhadzandze gneisses (TG) and one to the Chimoio gneiss (CG).

Representative analyses of major and trace elements, CIPW norm calculation, and correlation matrix of chemical elements for

gneisses are given in the Tables 3.16, 3.17, and 3.18 respectively (Appendix 3).

Only the trace elements (Nb and Y), which are likely to be the most effective elements. were considered for tectonic discrimination of granitic rocks.

3.2.4.2 MAJOR ELEMENT GEOCHEMISTRY

The NMG, TG and CG in Bivariate Harker variation diagrams of major oxide elements versus SiO_2 show a general decrease in major oxide elements with an increase in SiO_2 content, only the content of K_2O is positively correlated with SiO_2 content (Figure 3.26).

In general these rocks are characterised by relatively high ferromagnesian elements (Fe_2O_3 + MgO + TiO_2) compared to the Vumba and Messica granite gneiss varying between 3.54 and 13.96 and rich in Al_2O_3 (13.56-17.97). The total alkali (Na_2O + K_2O) contents are > 6.30 wt%, showing considerable amount of alkali feldspar as shown in Table 3.16. Furthermore the $Al_2O_3/(CaO + Na_2O + K_2O)$ values (molar) are less than 1, showing their metaluminous characteristics.

Using the ternary quartz-alkali-feldspar-plagioclase (QAP) diagram (Streckeisen 1976) the NMG plot in the granite (Manhiça, 1998), quartz monzonite and granodiorite fields (Figure 3.27 a). This is supported by normative An-Ab-Or ternary diagram (Barker, 1979) plotting in the granodiorite and quartz monzonite fields (Figure 3.27 b). In the QAP diagram the CG plots in the quartz monzodiorite (Manhiça, 1998) and quartz monzonite fields, while in the An-Ab-Or they plot on granodiorite field (Manhiça, 1998) and quartz monzonite. The TG plots in the granodiorite and in between granite and granodiorite fields boundary (Manhiça, 1998) on both ternary diagrams.

In the AFM diagram (Irvine & Baragar, 1971) NMG plots almost on the boundary between calc-alkaline and tholeiitic fields showing iron enrichment, confirming Manhiça's (1998) observations and interpretations. In general these rocks show a lower total alkali than Vumba and Messica granite gneiss (Figure 3.28 a).

In the bivariate alkalis (Na_2O + K_2O) versus

silica (SiO_2) diagram (Irvine & Baragar, 1971), these rocks show the sub-alkaline affinity, except for CG (Figure 3.28 b).

In Figure 3.29 (a) and (b) all gneisses plot generally in the metaluminous field showing a probably mixed (crustal and mantle) origin of the magma, although some (NMG) plot just on the boundary between metaluminous and peraluminous fields supporting (Manhiça, 1998) observations and interpretations.

3.2.4.3 TRACE ELEMENT GEOCHEMISTRY

To test the immobility of Al, Ti, Nb, Y and Zr pairs of these elements were plotted as shown in Figure 3.30. Plots of Y against TiO_2 and Zr (Figure 3.30 A and E), TiO_2 versus Zr and Nb (Figure 3.30 B, D, and G) and Zr versus Nb (Figure 3.30 H) show linear arrays from origin, suggesting that TiO_2, Y, Zr and Nb were immobile during alteration processes, while the Al_2O_3 was mobile. The relative immobility of Nb and Y trace elements makes them useful for characterizing the tectonic environment in which these gneisses were formed (Clarke, 1992).

Using the Nb versus Y discrimination diagrams (Pearce *et al.*, 1984) the NMG fall in both "volcanic arc granite"(VAG) and "within plate granites (WPG) fields. The CG and TG plot on the VAG + syn-COLG (syn-collision) field as shown in Figure 3.31.

The NMG is characterised by high content of HFS elements (Nb, Y, Zr and Ce), low content of total Al_2O_3, MgO, Na_2O, and CaO, high content of K_2O and low Na_2O/K_2O ratio. On Zr + Nb + Ce + Y (ppm) versus FeO*/MgO and (Na_2O + K_2O)/CaO diagram (Whalen *et al.*, 1987) these samples plot in the A-type granitoid field exhibiting evidence of slight fractionation, although occasional samples plot in the unfractionated M-, I- and S-type granites field (Figure 3.32).

Whereas the CG and TG show low HFS element content (Nb, Y, Zr and Ce), and relatively high content of Al_2O_3, MgO, Na_2O, CaO and Sr, low content of K_2O and high Na_2O/K_2O ratio. On Zr + Nb + Ce + Y (ppm) versus FeO*/MgO and (Na_2O + K_2O)/CaO diagram (Whalen *et al.*, 1987) these rocks plot in the unfractionated M-, I- and S-type granites field. Occasional samples plot in the A-type granite field (Figure 3.32).

4.2.4.4 DISCUSSION

The NMG are classified as granodiorite, which are "within plate A-type granites". The NMG probably represents a late stage of emplacement of Kibaran orogen. Eby (1990) observed that the A-type granites occur in within plates or in plate tectonic subduction-related orogeny. This feature is supported by AFM diagram (Figure 4.29 a) where the NMG plot on extensional tectonic suite field, although few of them plot on the boundary between extensional and compressional tectonic suite fields of Petro *et al.* (1979).

The CG and TG are "I-type"granodiorites of a "syn-collision setting. They are related to the crust-forming event of continental collision environment, originated at the crust-mantle interface and involving crust and mantle derived components of metaluminous and slightly peraluminous in composition.

◆ = Tchinhadzandze gneiss
■ = Chimoio gneiss
● = Nhansipfe gneiss
◆ = Tchinhadzandze gneiss (Manhica, 1998)
■ = Chimoio gneiss (Manhica, 1998)
● = Nhansipfe gneiss (Manhica, 1998)
◇ = Vumba granite gneiss
○ = Messica granite gneiss

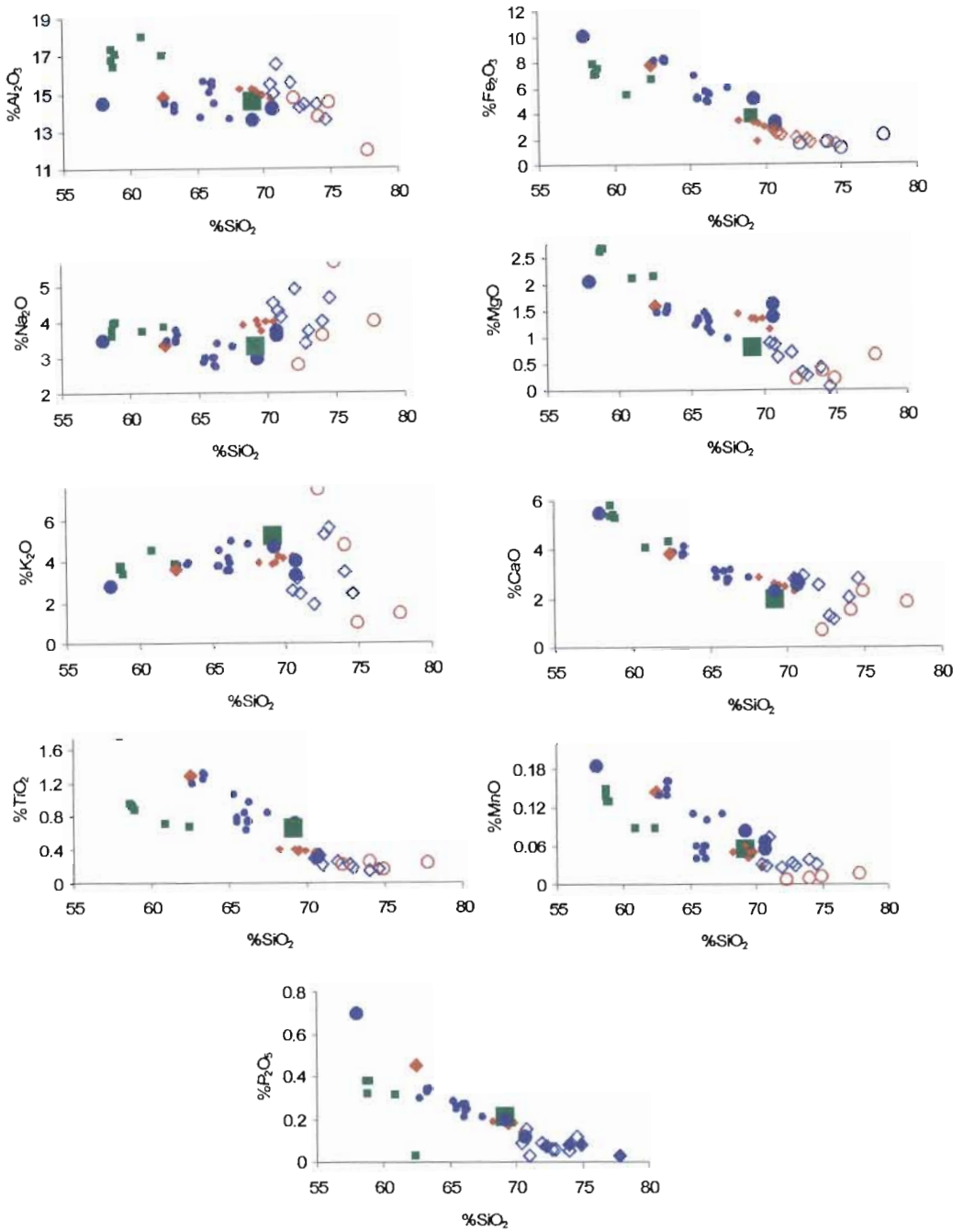

Figure 3.26 Harker variation diagrams of major oxide elements versus SiO_2 in the gneissic rocks.

◆ = Tchinhadzandze gneiss
■ = Chimoio gneiss
● = Nhansipfe gneiss
◆ = Tchinhadzandze gneiss (Manhica, 1998)
■ = Chimoio gneiss (Manhica, 1998)
● = Nhansipfe gneiss (Manhica, 1998)
◊ = Vumba granite gneiss
O = Messica granite gneiss

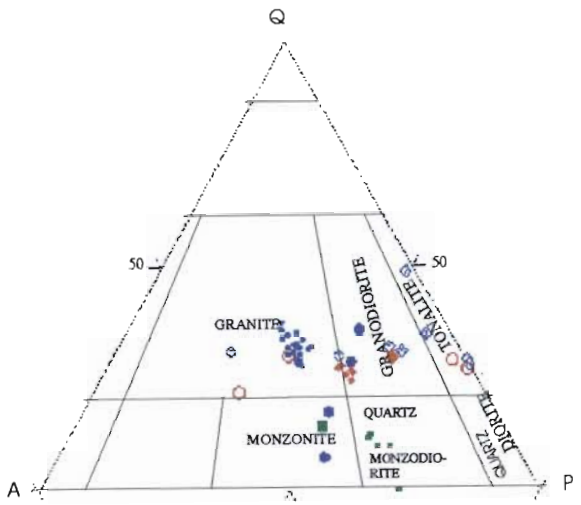

Figure 3.27 (a) Quartz-alkali-feldspar-plagioclase (QAP) diagram (Streckeisen, 1976), showing modal composition of gneiss.

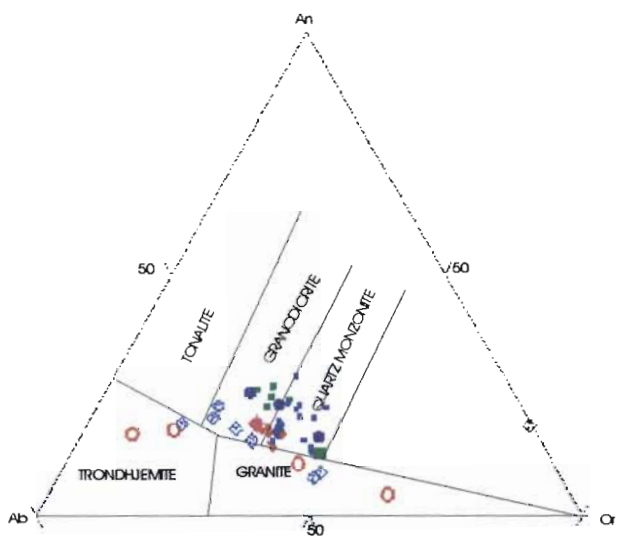

Figure 3.27 (b) Ternary normative Ab-An-Or diagram (Barker, 1979), showing different fields of gneiss.

◆ = Tchinhadzandze gneiss
■ = Chimoio gneiss
● = Nhansipfe gneiss
◆ = Tchinhadzandze gneiss (Manhica, 1998)
■ = Chimoio gneiss (Manhica, 1998)
● = Nhansipfe gneiss (Manhica, 1998)
◇ = Vumba granite gneiss
○ = Messica granite gneiss

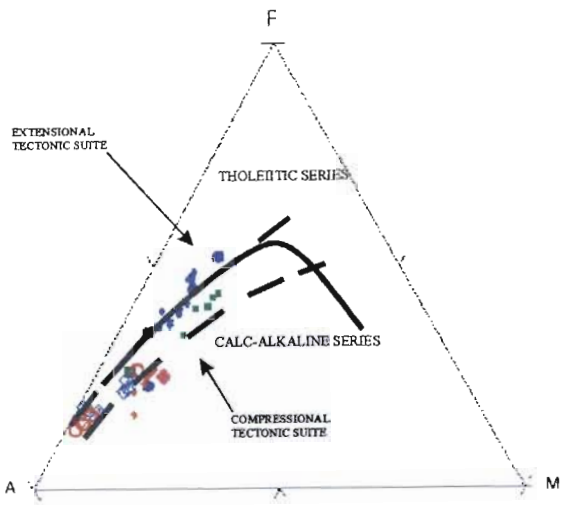

Figure 3.28 (a) Ternary AFM diagram (Irvine & Baragar, 1971), showing a calc-alkaline trend of gneiss. Extensional and compressional plutonic suite fields are from Petro *et al.*, (1979).

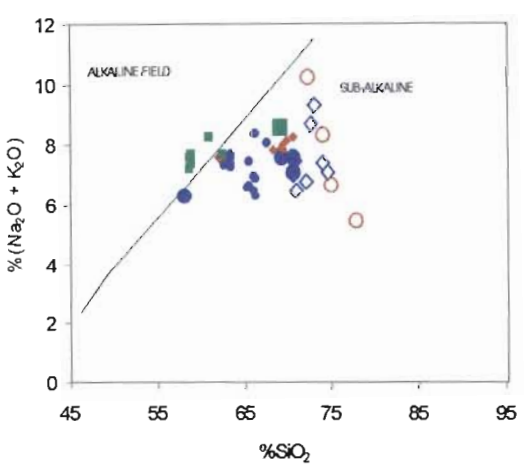

Figure 3.28 (b) Bivariate ($Na_2O + K_2O$) verus SiO_2 (TAS) diagram (Irvine & Baragar, 1971), showing subalkaline affinity.

◆ = Tchinhadzandze gneiss
■ = Chimoio gneiss
● = Nhansipfe gneiss
◆ = Tchinhadzandze gneiss (Manhica, 1998)
■ = Chimoio gneiss (Manhica, 1998)
● = Nhansipfe gneiss (Manhica, 1998)
◇ = Vumba granite gneiss
O = Messica granite gneiss

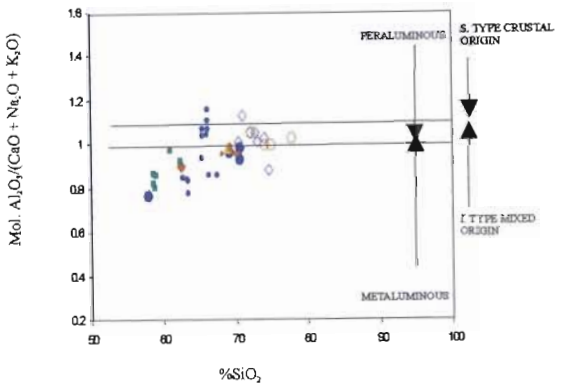

Figure 3.29 (a) Binary SiO_2 versus $Al_2O_3/[CaO+Na_2O+K_2O]$ (molar) diagram (Clarke, 1992).

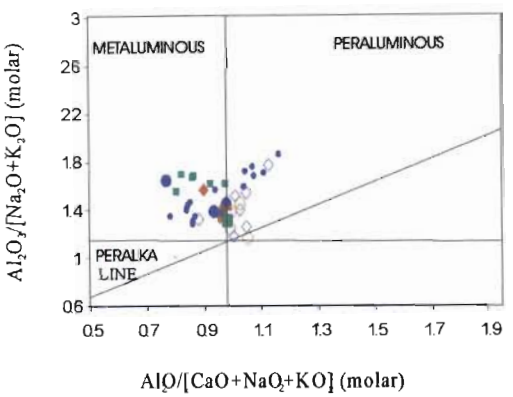

Figure 3.29 (b) Binary $Al_2O_3/[CaO+Na_2O+K_2O]$ (molar) versus $Al_2O_3/(Na_2O+K_2O]$ (molar) diagram (Clarke, 1992).

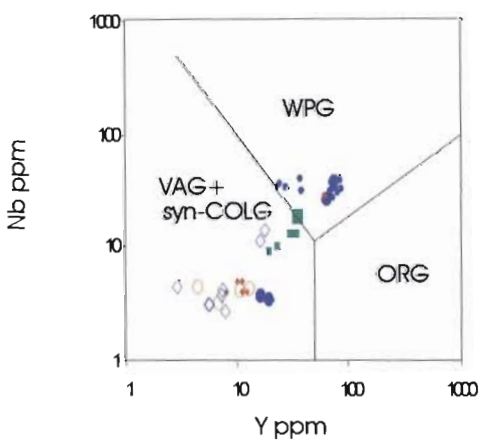

Figure 3.31 Nb versus Y discrimination diagram (Pearce *et al.*, 1984) for syn -collision (syn-COLG), volcanic arc granites (VAG), within plate granites (WPG) and ocean ridge granites (ORG).

◆ = Tchinhadzandze gneiss
■ = Chimoio gneiss
● = Nhansipfe gneiss
◆ = Tchinhadzandze gneiss (Manhica, 1998)
■ = Chimoio gneiss (Manhica, 1998)
● = Nhansipfe gneiss (Manhica, 1998)
◇ = Vumba granite gneiss
○ = Messica granite gneiss

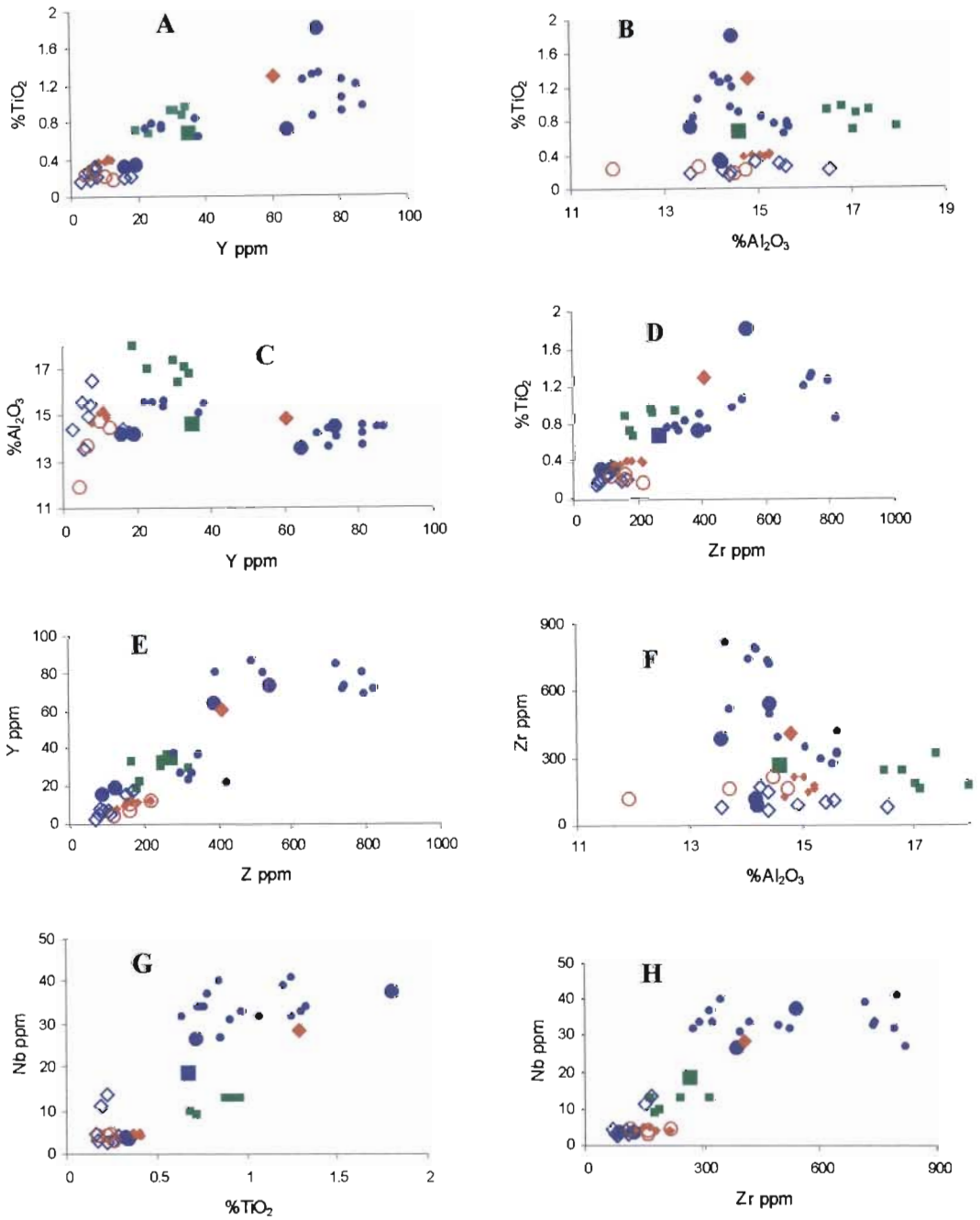

Figure 3.30 Bivariate diagrams showing relative immobility of different elements for gneisses.

◆ = Tchinhadzandze gneiss
■ = Chimoio gneiss
● = Nhansipfe gneiss
◆ = Tchinhadzandze gneiss (Manhica, 1998)
■ = Chimoio gneiss (Manhica, 1998)
● = Nhansipfe gneiss (Manhica, 1998)
◇ = Vumba granite gneiss
○ = Messica granite gneiss

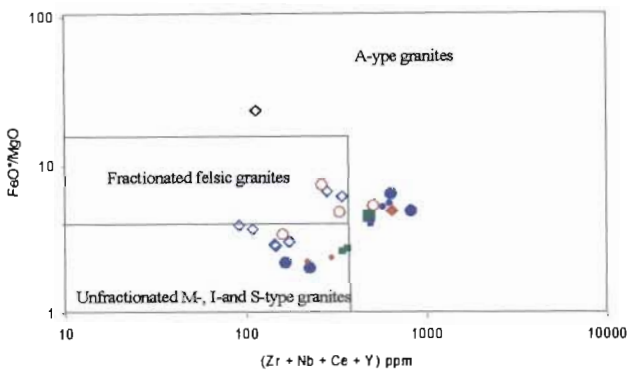

Figure 3.32 (a) Zr + Nb + Ce + Y (ppm) versus FeO*/MgO discriminant diagram for A-type granitoid and for fractionated felsic granites and unfractionated M-, I- and S-type granites (OGT) (Whalen *et al.*, 1987).

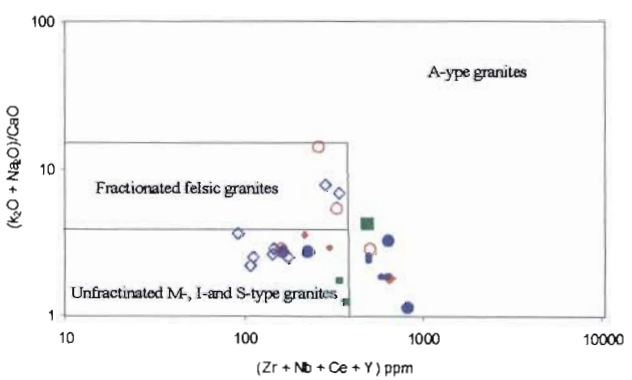

Figure 3.32 (b) Zr + Nb + Ce + Y (ppm) versus $(K_2O + Na_2O)/CaO$ discriminant diagram for A-type granitoid and for fractionated felsic granites and unfractionated M-, I- and S-type granites (OGT) (Whalen *et al.*, 1987).

CHAPTER 4

STRUCTURAL GEOLOGY

4.1 INTRODUCTION

The analysis of structural geology attempts to work out the complex history of deformation of the area under investigation. The aims of this chapter are to determine the geometry and orientation of the major structures, and structural history from a study of the types and relationships of major and minor structures of the study area. For this purpose structural data that were collected included dip and strike of bedding, layering, fracture and cleavage planes, plunge and plunge direction of fold axes, lineations, and slickenlines. Oriented cores from 30 stations were drilled for anisotropy of magnetic susceptibility (AMS).

The Calcareous Formation and Lower Argillaceous Formation of the Umkondo Group and Nhazónia Formation of the Gairezi Group are very poorly exposured within the area under investigation, therefore the structural analysis of the first two formations is not considered. Additionally, the structural analysis of the Nhazónia Formation is given only slight consideration due to restricted outcrop.

In the southeast of the area, the limit with Báruè Complex polyphase deformation has been recognized. Recognition of the polyphase deformation is based on the recognition of interference patterns caused by an early set of folds refolded by a later set, and the study of the stereographic projections of the structural data.

On the basis of variations in structural style, the area has been subdivided into five structural domains (A to E) as shown in Figure 4.1. Domain A consists of the eastern edge of the Zimbabwe craton and domain B is mainly underlain by the Umkondo Group. Domain C contains the Zimbabwe craton and Gairezi Group, rocks clearly affected by deformation related to Moçambique Belt. Domain D contains the Umkondo and Gairezi Groups that have also been affected by Moçambique Belt deformation while Domain E is entirely underlain by the Moçambique Belt.

4.2 TERMINOLOGY

The term foliation is used here as a general term to describe planar element that occurs penetratively in a body of rock. It may refer to thin rhythmic bedding in a sedimentary rock, to compositional layering in igneous rocks or to cleavage, schistosity, or other planar structures in metamorphic rocks (Passchier & Trouw, 1996). It is designated by S_0 for bedding and original layering/banding, S for secondary foliation. The magnetic foliation (K_3) is direction perpendicular to the magnetic lineation (Borradaile, 1988).

The term fracture is employed here, as a field term to describe all breaks in a rock mass where cohesion was lost. It covers faults, where the two sides are displaced relative to each other, and joints, where the two sides show no differential displacement (Ramsay & Huber, 1987).

Lineation (L) refers to any linear feature that occurs penetratively in a body of rock. It includes intersection lineation, crenulation lineation, stretching lineation, mineral lineation defined by the preferred mineral orientation, and fold axis (F) (Passchier & Trouw, 1996). Magnetic lineation is direction of strongest magnetization (K_1) (Borradaile, 1988).

Deformation phase is used to describe a period of deformation during which a group of structures has formed, separated from other structures by overprinting criteria.

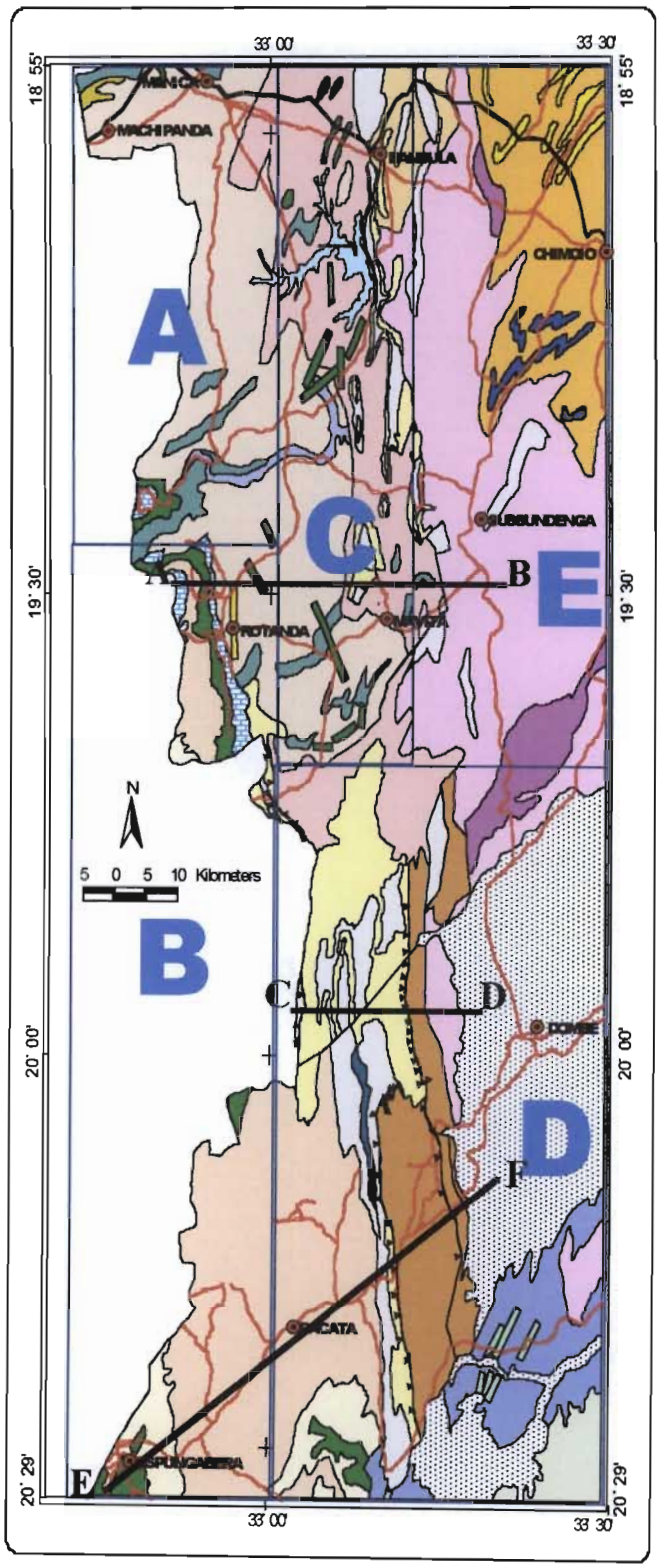

Figure 4.1 Geological map of the study area showing the general overview of different Domains of western central Moçambique and cross sections.

Successive deformation phases may merge into each other or may be separated by time intervals with little or no deformation, during which metamorphic conditions and the stress field may have changed (Passchier & Trouw, 1996).

Kibaran orogenic event is used to describe a deformational phase varying between *circa* 1100 and 850 Ma (Pinna *et al.*, 1993). In the literature this is sometimes also termed Grenvillian. Pan-African orogen is used as a general term describing a series of deformational events that took place between *circa* 800 and 550 Ma (Shackleton, 1986; Pinna *et al.*, 1993; Stern, 1994). The term Moçambique "mobile belt" is used to characterize polycyclic structural terrains extending along eastern margin of the area under investigation, which is a product of Mesoproterozoic (Kibaran times) to Neoproterozoic (Pan-African times) activity (Kennedy, 1964).

Previous geological work as well as field and laboratory evidence suggests that the structural history of this study area can be divided into four distinct tectonic events. Deformation phases are represented by D_1, D_2, D_3, D_4 and D_5:

D_1 - Archaean tectonic events related to the formation and deformation of the Basement Complex consisting of the Mutare-Manica greenstone belt of the Zimbabwe Archaean Craton and the respective cratonic granite gneisses.

D_2- Pre-Kibaran orogenic events that affected the Basement Complex and Gairezi Group sedimentary rocks. This event was most likely responsible for the deformation of Gairezi metasediments prior the deposition of the Umkondo Group.

D_3- Kibaran tectono-metamorphic event, related to the formation of the Báruè Complex and deformation of pre-existing rocks.

D_4- Pan-African tectono-metamorphic event, which has affected and deformed all pre-existing formations, but with greater intensity in those that crop out in the eastern part of the study area.

D_5- Fracturing related to deposition of Karoo Supergroup and Gondwana break-up (including reactivation of older trends).

4.3 DOMAIN A

Domain A lies in the northwest of the study area (Figure 4.1) and represents the eastern edge of the Zimbabwe Craton. The Vumba granite gneiss and the Macequece Formation underlie Domain A, which is bounded by the Messica granite gneiss in the east and by the Zimbabwe-Moçambique border in the west. The structural analysis of the Macequece Formation is only given minor consideration in this work. This is because this formation is characterized by poor exposures and crops out only as very limited discontinuous bodies, representing remnants of the Mutare-Manica greenstone belt of the Zimbabwe Archaean Craton. The structural features and geological structures summary of the domain are presented in Figure 4.2 and in Table 4.1 respectively.

4.3.1 DUCTILE DEFORMATION

In general, the domain is characterized by northwest-southeast striking cleavage (S/D_3), dipping steeply (up to 65°) to the either northeast or southwest. Locally, east-west striking cleavage (S/D_1) appears to dip steeply (65°) to the north (Figure 4.3). Manhiça *et al.* (2001) recognized a similar structural pattern westwards of the Vumba granite gneiss and the Mutare-Manica greenstone belt, which are characterized by east-west to slightly east-northeast/west-southwest striking cleavage (S/D_1 or S/D_2), dipping either north or south (Figure 4.3).

The cleavage strike changes from east-west and east-northeast/west-southwest in the Mutare-Manica greenstone belt to

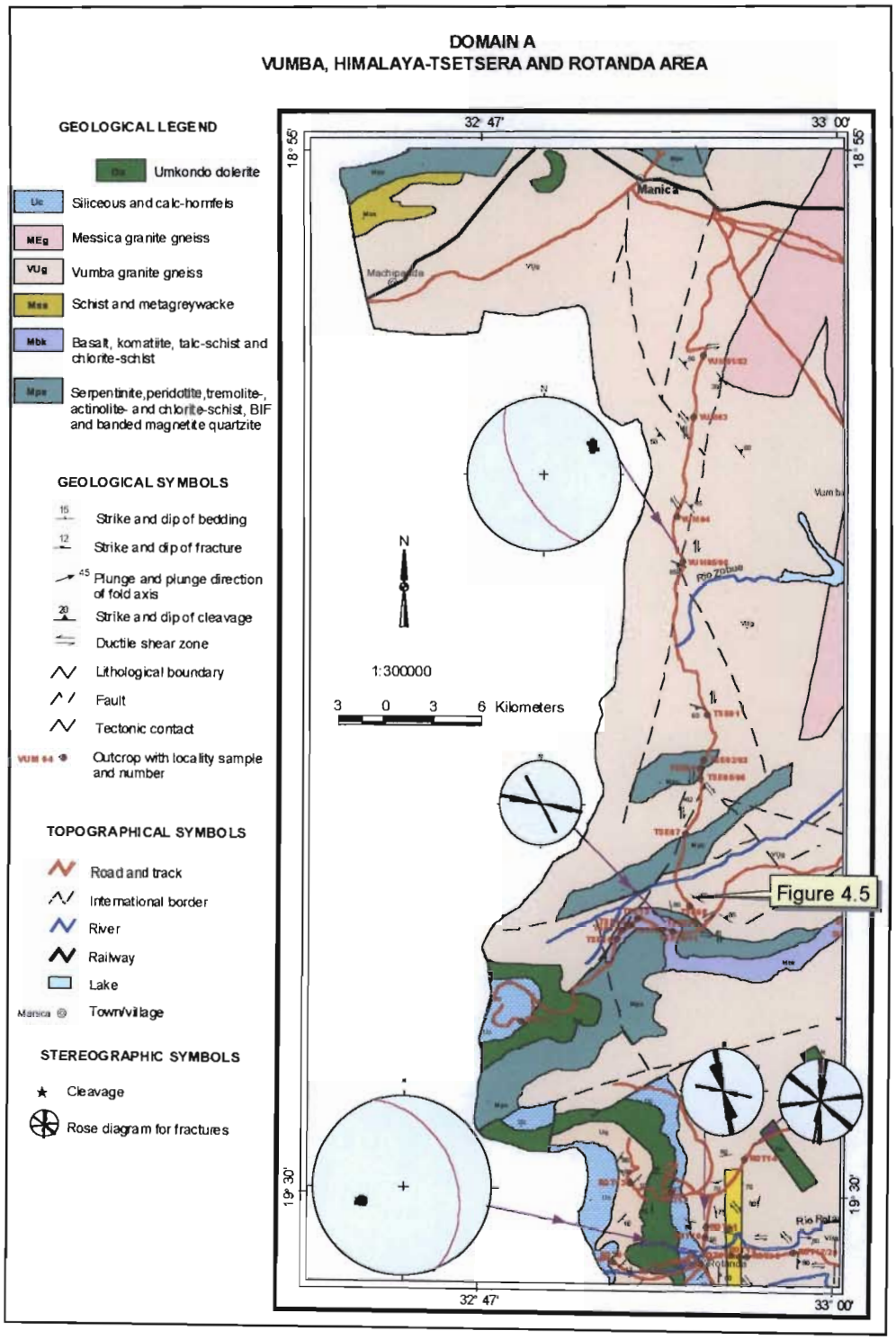

Figure 4.2 Domain A showing different stations, stereographic projections representing poles to cleavage (S/D_3), and rose diagrams indicating dominant fractures orientation.

Table 4-1 Summary of the geological structures in Domain A

Deformation phase	Cleavage	Fracture	Shear zones	Mineral lineation	Fold axis
D_1	S/D_1 : E-W S/D_1 : ENE-WSW (?)				E
D_2	S/D_2 : ENE-WSW (?)				
D_3	S/D_3 : NW-SE	WNW-ESE ENE-WSW	NW-SE (dextral) E-W (sinistral) N-S (dextral)	ESE	NW
D_4	S/D_4 : NNW-SSE	NW-SE	WNW-ESE (dextral)		
D_5		N-S			

northwest-southeast eastwards. This suggests that there is change in the compressive stress regime from north-south in the Archaean event (D_1) to northeast-southwest (D_3) in the Kibaran event.

Eastwards, the Vumba granite gneiss becomes highly foliated with intensive cleavage dipping southwest and micas with flakes exhibiting a remarkable parallelism with quartz bands and some strained quartz porphyroblasts. The orientation of this cleavage suggests that it is Kibaran (S/D_3) in age.

Manhiça *et al.* (2001) observed that in the western area of this domain, the mineral lineations have a constant trend characterized by plunge of 60° towards 108° (L/D_3) and the fold axes plunge 30° towards east (F/D_1) while in the eastern the fold axes plunge to northwest (F/D_3) as shown on Figure 4.4.

Southwards, from Rotanda to Mavita the cleavage (S/D_4) strikes north-northwest/ south-southeast, dipping 75° to the east-northeast. East-west trending sinistral strike-slip shear zones and northwest-southeast trending dextral strike-slip shear zones occur in this area (Figure 4.4).

4.3.2 BRITTLE DEFORMATION

The Vumba granite gneiss is intensely fractured, with the fractures dipping steeply (77°-85°) to the north-northeast and northeast, striking dominantly west-northwest/east-southeast and northwest-southeast respectively. The distribution of quartz and pegmatite veins in the domain is controlled by the fractures, which also dip steeply and exhibit similar strike orientations.

North-south trending dextral strike-slip brittle shear zones have been identified throughout the Domain (Figure 4.5). Southwards, near the Zóbue River close to Zimbabwe-Moçambique border, northwest and west-northwest trending dextral strike-slip shear zones occur.

Southwards, from Rotanda to Mavita the strike of the fractures in the Vumba granite gneiss vary between north-south and east-northeast/west-southwest. These fractures control the distribution of the majority of the quartz and pegmatite veins in the region.

4.3.4 DISCUSSION

The east plunging folds axis and east trending cleavage, are considered to be related to Archaean tectonic event (D_1). The east-northeast trending most likely produced by either late D_1 or early D_2.

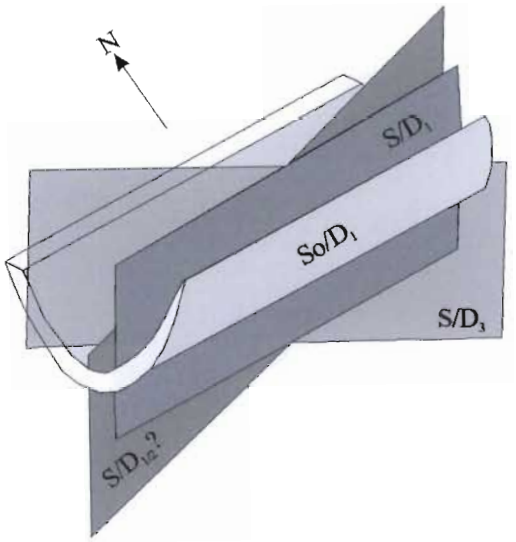

Figure 4.3 Sketch of fabrics in Macequece Formation and Vumba granite gneiss.

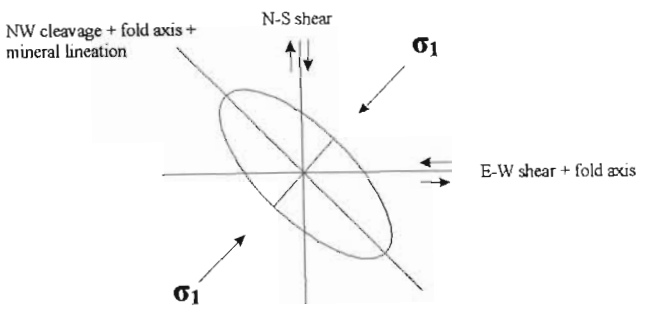

Figure 4.4 Sketch of strain ellipse within Domain A, showing cleavage, shear zone, fold axis and mineral lineation.

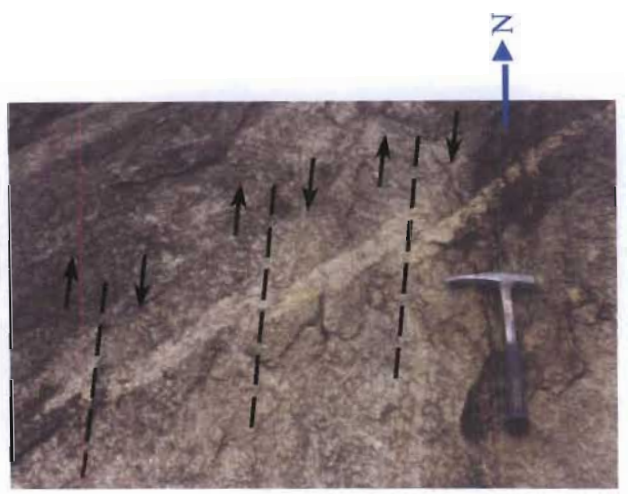

Figure 4.5 Plan view of North-south trending dextral strike-slip shear zones in the Vumba granite gneiss at south of Bonde River. (See Figure 4.2 for locality).

The eastern and southern parts of the regions are characterized by northwest trending cleavage, northwest plunging fold axis, fractures striking northwest, west-northwest and east-northeast and by north-south (dextral), east-west (sinistral) and northwest-southeast (dextral) shear zones. These structural patterns are interpreted as being related to the Kibaran deformation because similar structural patterns directions were observed in Inyanga (Stocklmayer 1978) and in Inyanga North-Malaka (Stocklmayer, 1980), which were related to the pre-Umkondo basement deformation. Thus a northwest trending Kibaran front can probably be traced from the Vumba granite gneiss near Manica town to the Inyanga North-Malaka area.

The north-south trending fractures may be associated with younger events related to Gondwana break-up. Such fractures affect the Karoo Supergroup rocks west of the Umkondo Group in south-east Zimbabwe (Swift *et al.*, 1953 and Swift, 1962)

4.4 DOMAIN B

Domain B lies in the southwest part of the study area (Figure 4.1) in the Espungabera and Rotanda regions. It is predominantly underlain by Upper Argillaceous and Quartzite Formations of the Umkondo Group. The dominant rocks types are essentially orthoquartzite or quartzarenite and argillaceous rocks. The structural features and geological structures of this domain are presented in Figure 4.6 and in Table 4.2 respectively.

4.4.1 PRIMARY STRUCTURE: S_0

The dominant lamination is characterized by either change or variations in grain-size and change in composition. The variation in composition and thickness of layering (lamination) in the rock suggests bedding.

In the western part of the Espungabera region the bedding strikes west-northwest and east-northeast and is shallowly dipping 8°-14° towards south-southwest and south-southeast respectively. However, the strong preferred orientation of phyllosillicate minerals parallel to bedding suggests that there is also cleavage present. In other words, cleavage (S/D_3) is parallel to bedding (S_0/D_3) in the west (Figure 4.7).

In the eastern part of Espungabera region, bedding is shallowly dipping (11°-13°) towards to the southeast and southwest, striking northeast-southwest and northwest-southeast respectively. The cleavage is better developed than in the west and is moderately dipping between 20° and 55° northeast. Northwards, in the Rotanda region, the Quartzite Formation is characterized by bedding dipping gently (~15°) to the southeast and southwest, striking northeast-southwest and northwest-southeast respectively as shown in Figure 4.6/9.

4.4.2 DUCTILE DEFORMATION

Folding is evident in the form of a sub-horizontal to gently plunging synclines with fold axes (F/D_4) plunging between 02° and 12° to the south-southeast and south-southwest. This is the same as those in the Chipinga-Mount Selinda area in Zimbabwe (Watson, 1969), which lies west of Espungabera village. There the folds in the Upper Argillaceous Series (Formation) are also very gentle, often broad, and of low amplitude. The fold axes trend south-southeast.

4.4.3 BRITTLE DEFORMATION

In the Espungabera area, the rocks are intensely and extensively fractured with the planes characteristically steeply dipping to vertical (70°-90°) forming three systematic

DOMAIN B
ESPUNGABERA AND ROTANDA AREA

GEOLOGICAL LEGEND

- Du — Umkondo dolerite
- Uua — Shale, phyllite and siltstone with sandstone bands
- Uq — Quartzarenite intercalated with shale bands
- Uc — Siliceous and calc-hornefls

GEOLOGICAL SYMBOLS

- 20 — Plunge and plunge direction of lineation
- 25 — Strike and dip of fracture
- 30 — Plunge and plunge direction of fold axis
- 14 — Strike and dip of bedding
- 50 — Strike and dip of cleavage
- Ductile shear zone
- VAN 15 — Outcrop with locality sample and number
- Lithological boundary
- Fault

TOPOGRAPHICAL SYMBOLS

- River
- Road track
- International border
- Rotanda — Town/village
- Macuiana — Mountain name

STEREOGRAPHIC SYMBOLS

- Bedding
- Fold axis
- Cleavage
- Rose diagram for fractures
- Plot for conjugate fractures

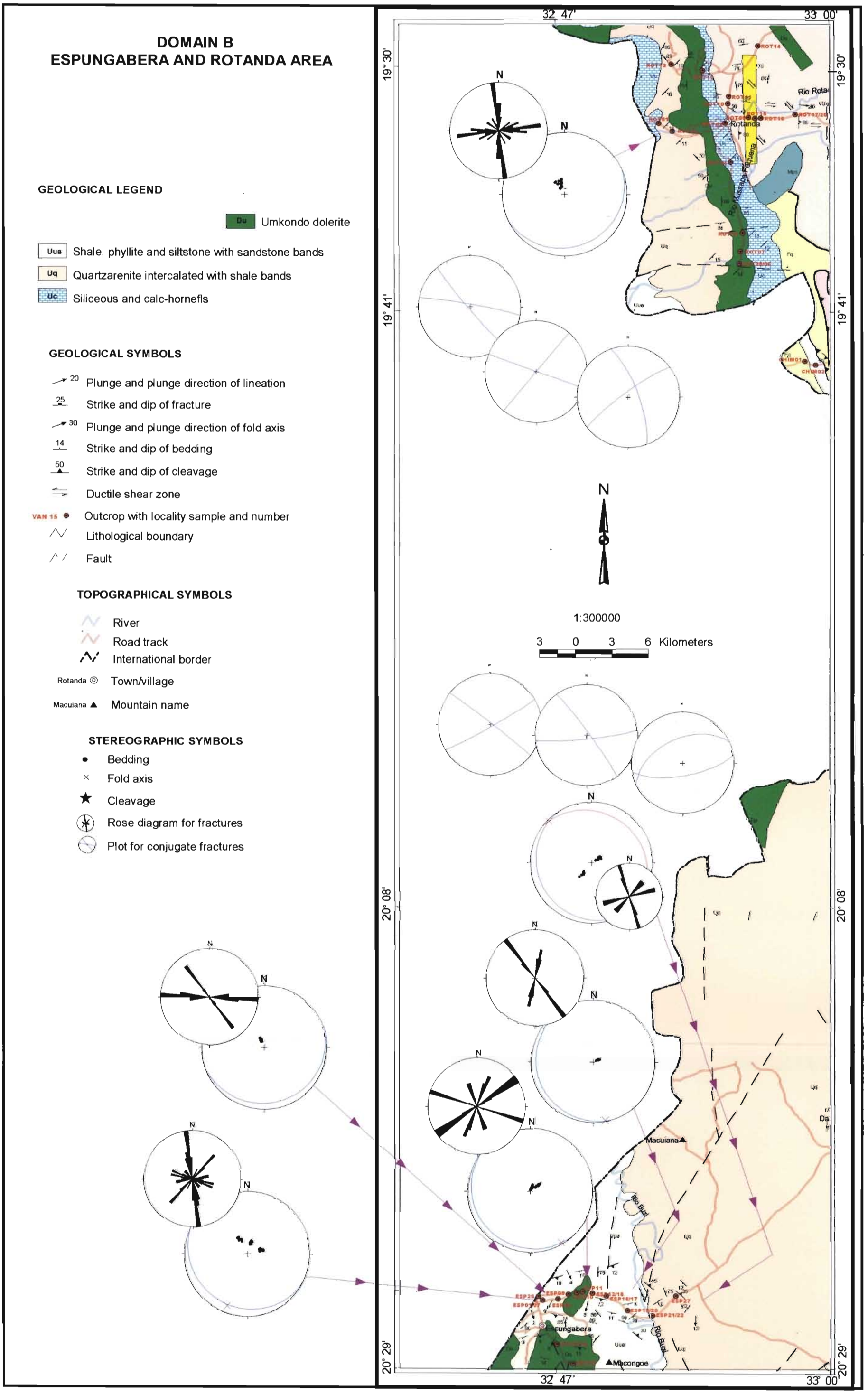

Figure 4.6 Structures features of the Umkondo Group meatsediments around Espungabera and Rotanda regions.

Table 4.2 Summary of the geological structures in Domain B

Deformation phase	Bedding	Cleavage	Fold axis	Fracture	Fault
D_1					
D_2					
D_3	WNW-ESE ENE-WSW	S/D_3 : WNW-ESE S/D_3 : ENE-WSW NW-SE			
D_4	NE-SW NW-SE	S/D_4 : NE-SW	SSE SSW	WNW-ESE NE-SW	NW-SE
D_5				ENE-WSW NNW-SSE N-S	ENE-WSW E-W

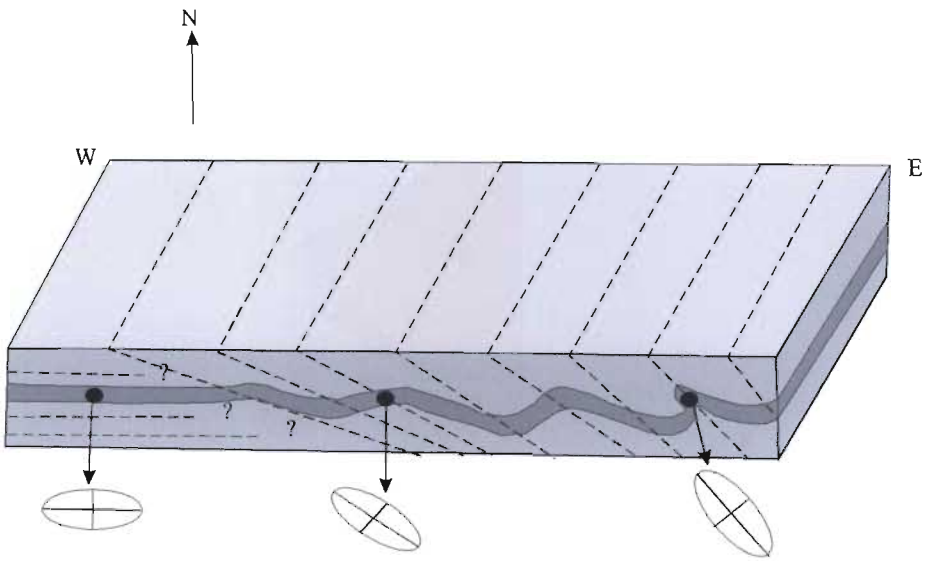

Figure 4.7 Sketch of bedding, cleavage and axial planar cleavage of Espungabera and Rotanda regions.

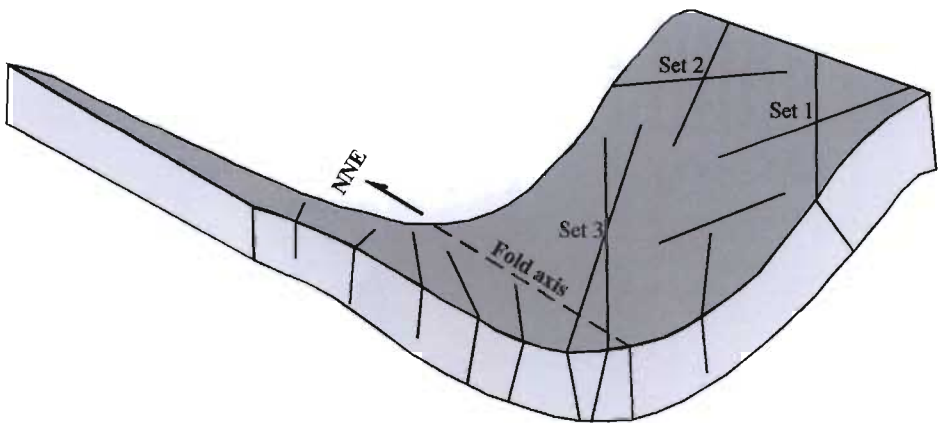

Figure 4.8 Sketch of the primary fracture orientations recorded from an east limb of syncline in the Espungabera area, showing three dominant sets of conjugate fractures.

preferred orientations. The predominant fracture set trends between north-northwest, north and northeast. The two less dominant fractures strike east-northeast and west-northwest.

The spatial relationships of the fractures are prominent and usually make V and X-shaped patterns. The fracture surfaces range from tens of centimetres to a few metres. The field relationships of some suggest that they are conjugate sets of joints enclosing dihedral angles of less than 45°. Faults are consistently parallel to the fractures. As in the Chipinga region of Zimbabwe, these faults mostly likely represent reactivated fractures during Karoo times and Gondwana break up.

Northwards, in the Rotanda region, in general, the field and spatial relationships of fractures are same as in the Espungabera area. They are predominantly striking north-northwest and east-northeast with steep and near vertical dips between 70° and 88°.

The stress ellipsoid orientation was established using conjugate fractures (Table 4.3). Three dominant pairs of conjugate fractures were identified (Figure 4.6/4.8). The first set is steeply dipping (88°NE and 86°SE), striking 308° and 060° respectively with the angle between maximum compressive stress and fracture approximately 34°. The second pair is steeply dipping (84°S and 86°NE) striking 084° and 324° with the angle between maximum compressive stress and fracture around 24°. The third set is moderately to steeply dipping (70°S and 50°NW) and striking 080° and 246° respectively with the angle between maximum compressive stress and fracture around 32°.

Analysis of these conjugate pairs suggests that the first and second sets are related to strike-slip faulting (Table 4.3). The third set appears to be associated with normal faulting.

In the Chipinga region of Zimbabwe, the rocks have been broken into slices and blocks by normal steeply dipping to vertical faults with east-northeast and north-northwest strikes (Watson, 1969). The downthrown side is usually to the south for east-northeast. The east-northeast trending faults (Umvumvumvu and Tanganda-Lusitu faults) form the largest and most important group. The Tanganda-Lucite fault continues in Moçambique along the Lucite River and is connected to a normal fault, which strikes northeast-southwest through Chimanimani Mountain. The Umvumvumvu fault continues in Moçambique through the Rotanda area.

Table 4.3 Orientation of principal stress axes from conjugate fractures sets in Domain B.

Set	σ1	σ2	σ3	Fault
1	07°→274°	82°→100°	02°→004°	Strike-slip
2	12°→301°	76°→112°	02°→029°	Strike-slip
3	74°→078°	10°→255°	09°→163°	Normal

4.4.4 DISCUSSION

In the western region of Espungabera, the cleavage being parallel to the bedding could be a consequence of diagenetic compaction of sediments with little or no deformation. Alternatively the region represents the footwall of a thrust system and the cleavage is the result loading by the hangingwall thrust sheets.

The latter explanation is preferred because, eastwards and northwards around Rotanda area, the cleavage becomes oblique to the folded bedding (Fig. 4.7). The cleavage here is clearly due to the Pan-African compressive tectonic regime that is associated to the thrusting event and also caused the gently plunging folds in the Chipinga-Mount Selinda area in Zimbabwe (Watson, 1969). Joint sets 1 and 2, which have a strike-slip appearance (Table 4.3), developed during this deformation. The acute angle between the fractures was

bisected by the maximum compressive stress during the Pan-African shortening (D_4). The variation in this direction between the two sets is due to a change in the maximum compressional stress across the area, which is also reflected in the variation of the fold axes.

Joint set 3, which is related to normal faulting (Table 4.3), is in the same direction as faults found further west in the basement of the Zimbabwe craton and Limpopo Belt. These faults represent reactivation of older structures during faulting of the Karoo Supergroup and during Gondwana break-up (Watkeys, 2002). Such evidence of reactivation makes it difficult to interpret of the structural history of the area. What is clear, however, is that the area was affected by "slightly" multi-deformation phases, reflecting changes in compressive stress orientation.

4.5 DOMAIN C

Domain C lies east of Domain A and northern parts of Domain B. It comprises the Messica granite gneiss of the Archaean Zimbabwe Craton and the quartzite-schist complex of the Frontier Formation, both of which are clearly deformed in post-Archaean events. The structural data and geological structures of the domain are presented in Figure 4.10 and in Table 4.4.

4.5.1 DUCTILE DEFORMATION

This domain is distinguished by consistently near north-south striking cleavage (S/D_4) dipping between 60° and 86° either to the west or east and by westwards thrusting as shown in Figure 4.11. Eastwards, the cleavage becomes close to vertical and strikes north-south. This is similar to the structural pattern previously recognized by Manhiça (1998) in the Messica area.

In the central part of the domain, from the outcrop pattern it was possible to identify fold closures related to the change in vergence across major fold surfaces. The most pervasive minor structure is the folding of the initial axial planar cleavage, producing a second axial planar cleavage. Both the first and second fold axes (F_1/D_4 and F_2/D_4) plunge sub-horizontally to the north (Figure 4.12).

The differential movement direction, a_2, of the second phase lies at a high angle to the first fold axial planes and the b_2 direction lies very close to the first fold hinge line F_1. This results in both the first and second deformation phases fold axial direction tending to be sub-parallel. The fold interference pattern is therefore classified as a Type 3 superimposed interference pattern (Ramsay, 1962).

The first generation of folding (F_1/D_4), produced folds with sub-horizontal fold axes plunging 10° to north, as measured from fold closures in the field. The second generation (F_2/D_4) produced folds with upright inclined (82°), east dipping, axial planar cleavage (S/D_4) striking north-south and fold axes plunging gently (28°) to the north. The mineral lineation (L/D_4) plunges around 02° to the north. The cleavage of early folds plots along a great circle that contains the poles to layering.

4.5.2 BRITTLE DEFORMATION

The domain contains small-scale north-south trending sinistral strike-slip shear zones. In the south, close to the Frontier Formation, northeast-southwest trending dextral strike-slip shear zones were observed (Figure 4.13).

The rocks are commonly intensively fractured and the fractures are filled by quartz and pegmatite. Around the Chicamba Dam area, fractures in the quartzite are common and strike moderately

DOMAIN C
CHICAMBA REAL DAM AREA

GEOLOGICAL LEGEND

- NHg — Nhansipfe megacrystic gneiss
- TCg — Tchinhadzandze gneiss
- VAg — Vanduzi hornblende migmatite gneiss
- Du — Umkondo dolerite
- Fg — Micaceous and white quartzite
- Fs — Staurolite-garnet-chlorite schist and garnet-schist
- MEg — Messica granite gneiss
- VUg — Vumba granite gneiss
- Uua — Shale, phyllite and siltstone with sandstone bands
- Uq — Quartzarenite intercalated with shale bands
- Uc — Siliceous and calc-hornefls
- Mbk — Basalt, komatiite, talc-schist and chlorite-schist
- Mps — Serpentinite, peridotite, tremolite-, actinolite- and chlorite-schist, BIF and banded magnetite quartzite

GEOLOGICAL SYMBOLS

- 12 — Plunge and plunge direction of minor fold axis
- 20 — Plunge and plunge direction of lineation
- 25 — Strike and dip of fracture
- 30 — Plunge and plunge direction of fold axis
- 14 — Strike and dip of layering
- 50 — Strike and dip of cleavage
- Ductile shear zone
- CHI 01 — Outcrop with locality sample and number
- Lithological boundary
- Fault
- Thrust
- Tectonic contact

TOPOGRAPHICAL SYMBOLS

- River
- Road and track
- Railway
- Mavita — Town/village
- Nhaungoe — Mountain name
- Lake

STEREOGRAPHIC SYMBOLS

- Layering
- Cleavage
- Fold axis
- Mineral lineation
- Fault plane

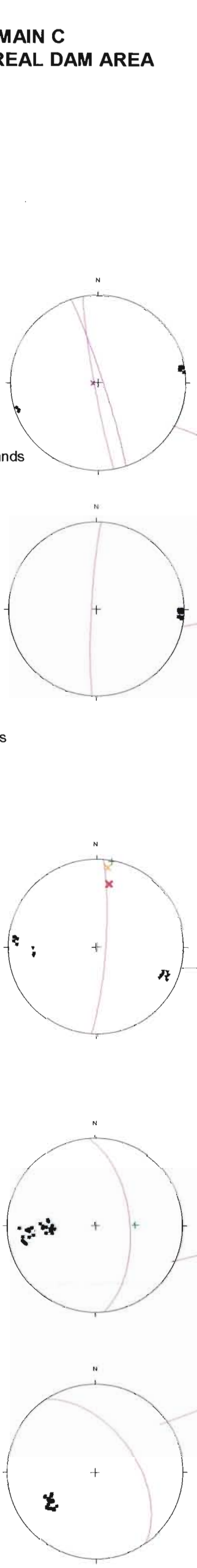

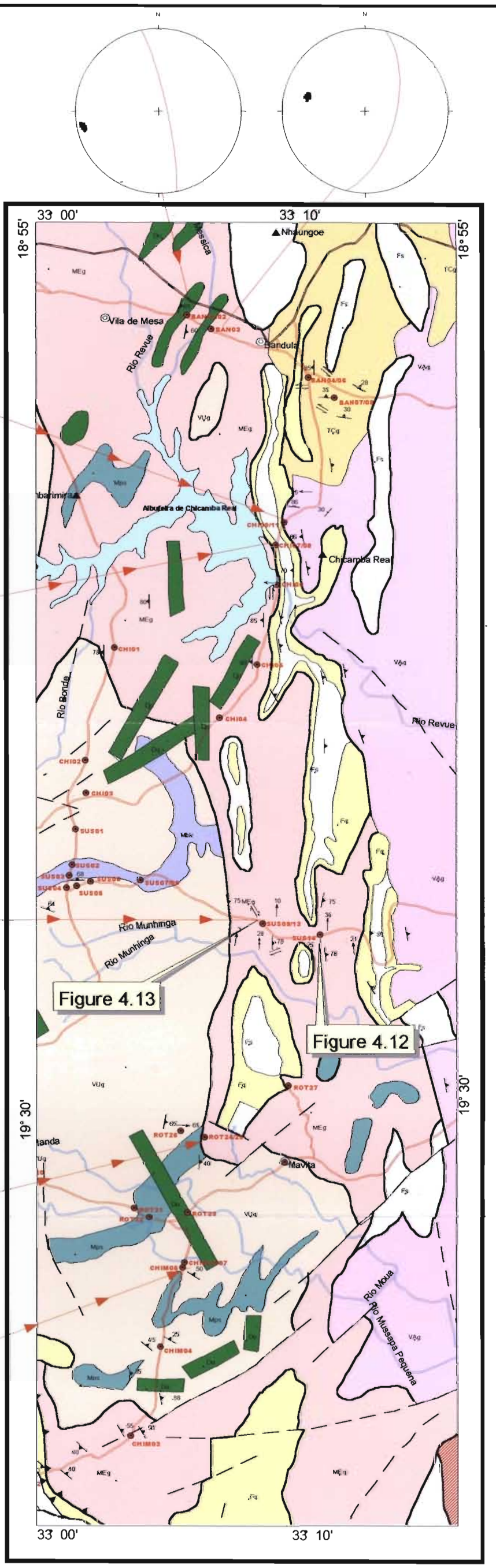

1:300000

3 0 3 6 Kilometers

Figure 4.10 Domain C showing different structural data of the Vumba granite gneiss and Frontier Formation.

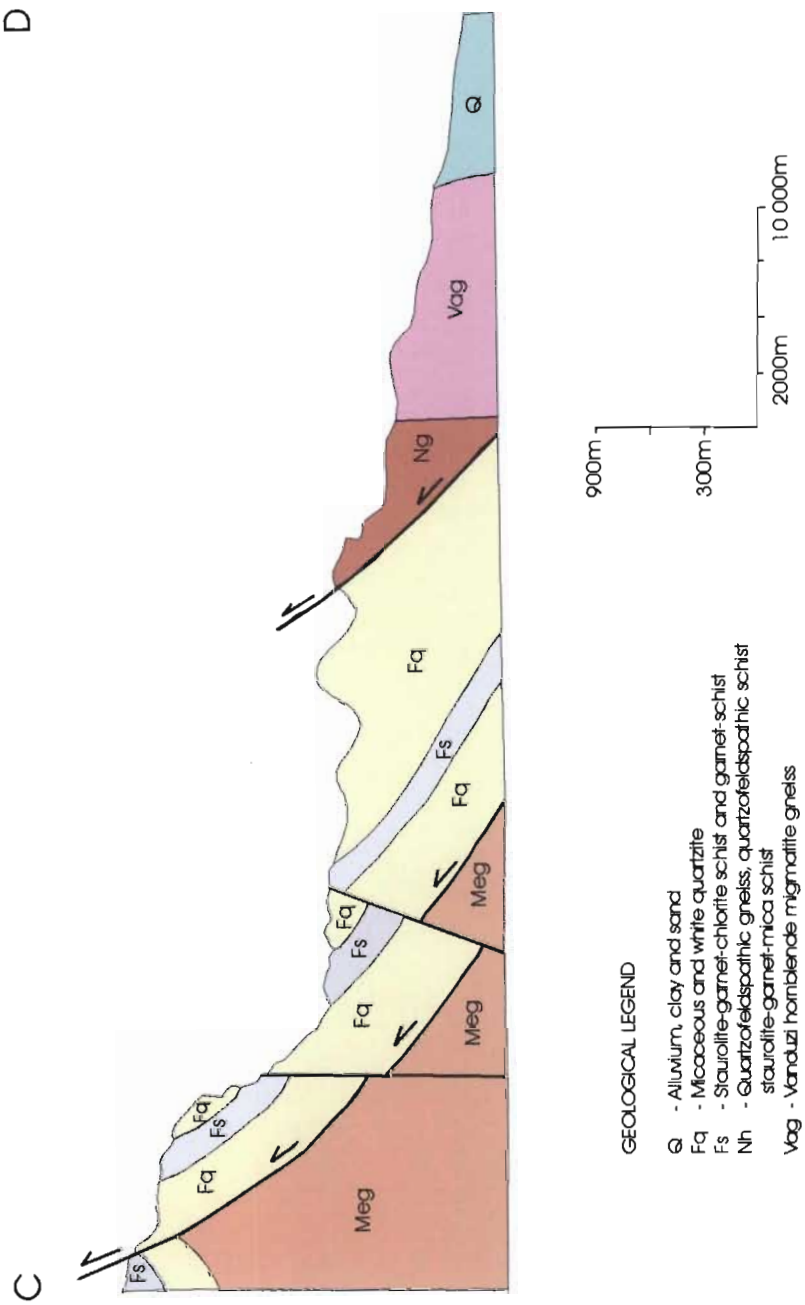

Figure 4.11 Cross-section between Chimanimani Mountain and Mussapa Pequena River showing westwards thrusting.

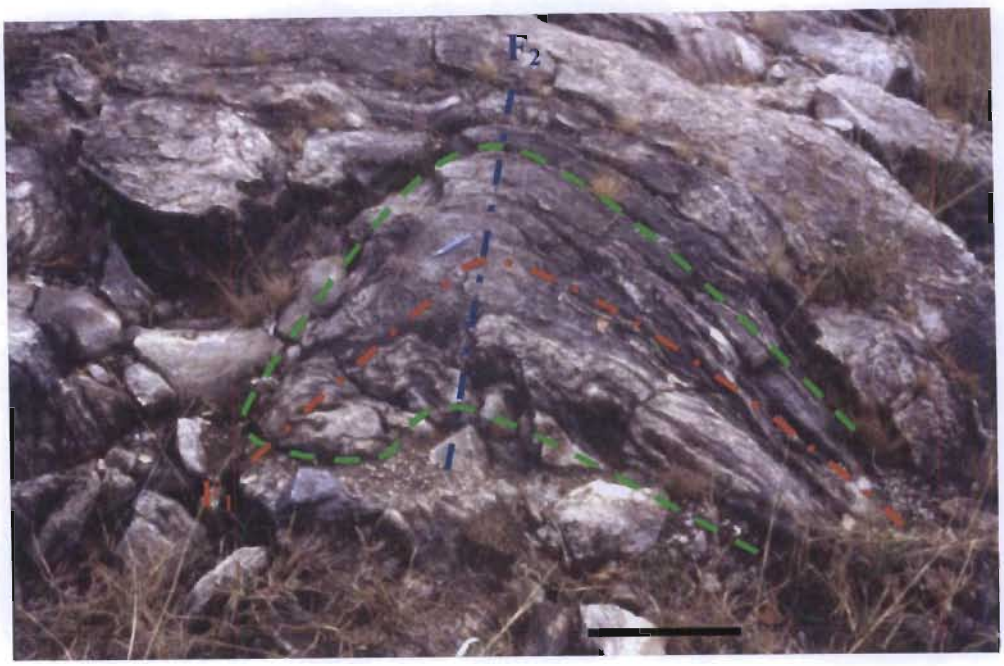

Figure 4.12 Section view of Type 3 superimposed fold (Ramsay 1962) within the Messica granite gneiss terrane around Munhinga River region. Scale bar = 50 cm. (See Figure 4.10 for locality). View looking NW.

Figure 4.13 Plan view of (A) northeast-southwest dextral strike-slip shear zone. (B) northeast-southwest dextral strike-slip shear zone where the displacement has been indicated by a δ-type porphyroblast of K-feldspar (See Figure 4.10 for locality).

Table 4.4 Summary of the geological structures in Domain C

Deformation phase	Cleavage	Planar cleavage	Fracture	Fault	Shear zones	Fold axis	Mineral lineations
D_1							
D_2							
D_3			NE-SW				
D_4	S/D_4 : N-S	N-S NE-SW	NW-SE		NE-SW (dextral) N-S (sinistral)	N	N
D_5			N-S	N-S			

northeast-southwest, northwest-southeast and north-south. These fractures are filled by pegmatite and quartz.

Faults striking north-south and dipping steeply (~80°) to the east contain slickenlines on the fault plane steeply plunging (78°) to the north-northeast (078°). The maximum compressive stress is approximately vertical (σ_1 = 75°/268°), the intermediate compressive stress is horizontal (σ_2 = 00°/000°) and the minimum compressive stress is almost horizontal (σ_3 = 13°/085°). These faults are, therefore, sub-vertical normal faults with slight oblique movement.

4.5.3 DISCUSSION

To the west of Domain C, the dominant structures in Domain A suggest that the planar fabrics and folds in the Vumba granite gneiss and the Mutare-Manica greenstone belt predated the emplacement of the Messica granite gneiss. In Domain C, these features are overprinted by D_4 deformation which is associated with the Pan-African tectono-metamorphic event.

East-west compression during the Pan-African event was responsible for westwards thrusting of the Gairezi Group over the Umkondo Group (Figure 4.11) as well as the first and second generation folding and mineral lineation of D_4 (Figure 4.14). As the fold axes and mineral lineation are approximately parallel each other, it suggests that they are related to the same compressional event. Both bedding and initial axial planar cleavage most likely buckled synchronously during a single progressive deformation phase as a result of a smooth and systematic change in stress and incremental strain during Pan-African deformation (Ramsay and Huber, 1987).

This Pan-African event may also have been responsible for the northeast trending dextral and north-south trending sinistral strike-slip shear zones (Table 4.4; Figure 4.15). These may be a conjugate pair of ductile shears from a slight clockwise rotation of the maximum compressional direction from north-south to north-west/southeast. The north trending fault and fractures, which are the youngest features, probably represent reactivation of older structures during the Gondwana break-up event.

4.6 DOMAIN D

Domain D is located in the southeast of the study area (Figure 4.1) around Sitatonga and is bounded to the west by Domain B and to the east by the eastern boundary of the study area. It is underlain mainly by the Quartzite Formation, Umkondo Group and by the Frontier and Nhazónia Formations of the Gairezi Group. Because of the poor nature of the exposures of Nhazónia Formation, its structural analysis

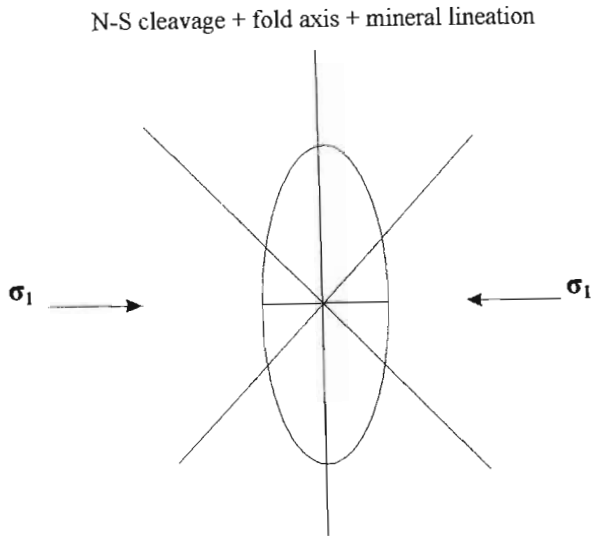

Figure 4.14 Sketch of strain ellipse showing north trending cleavage and north plunging fold axis and mineral lineation.

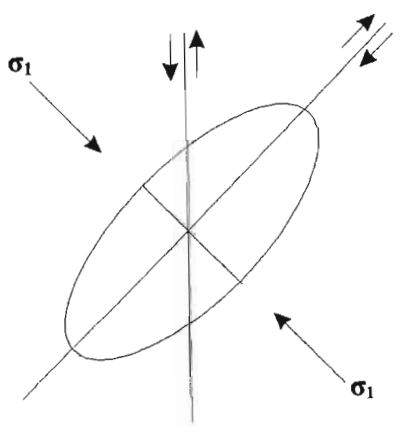

Figure 4.15 Sketch of strain ellipse showing northeast trending dextral and north-south trending strike slip shear zones.

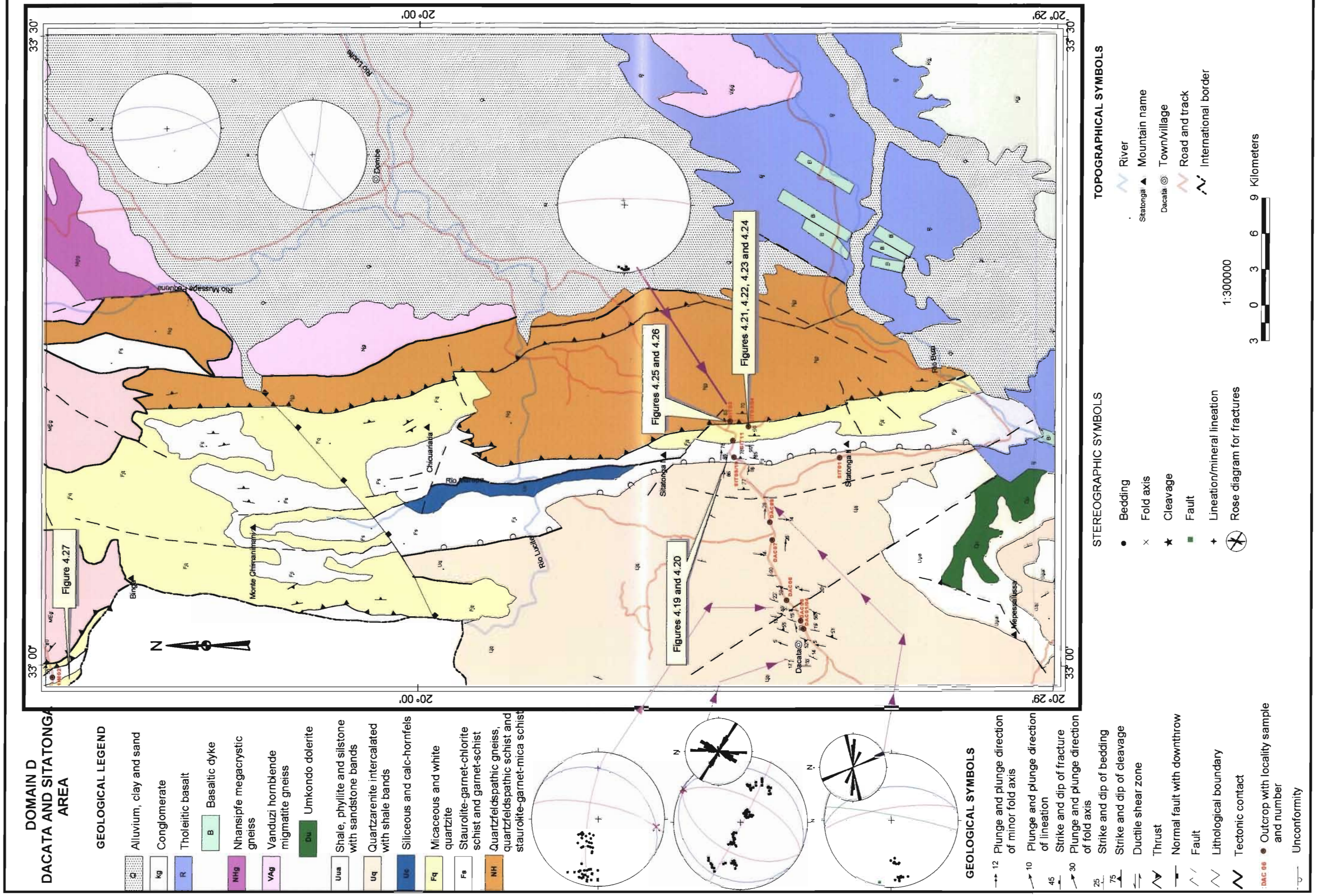

Figure 4.16 Domain D showing localities sampled, structural data and stereographic projections.

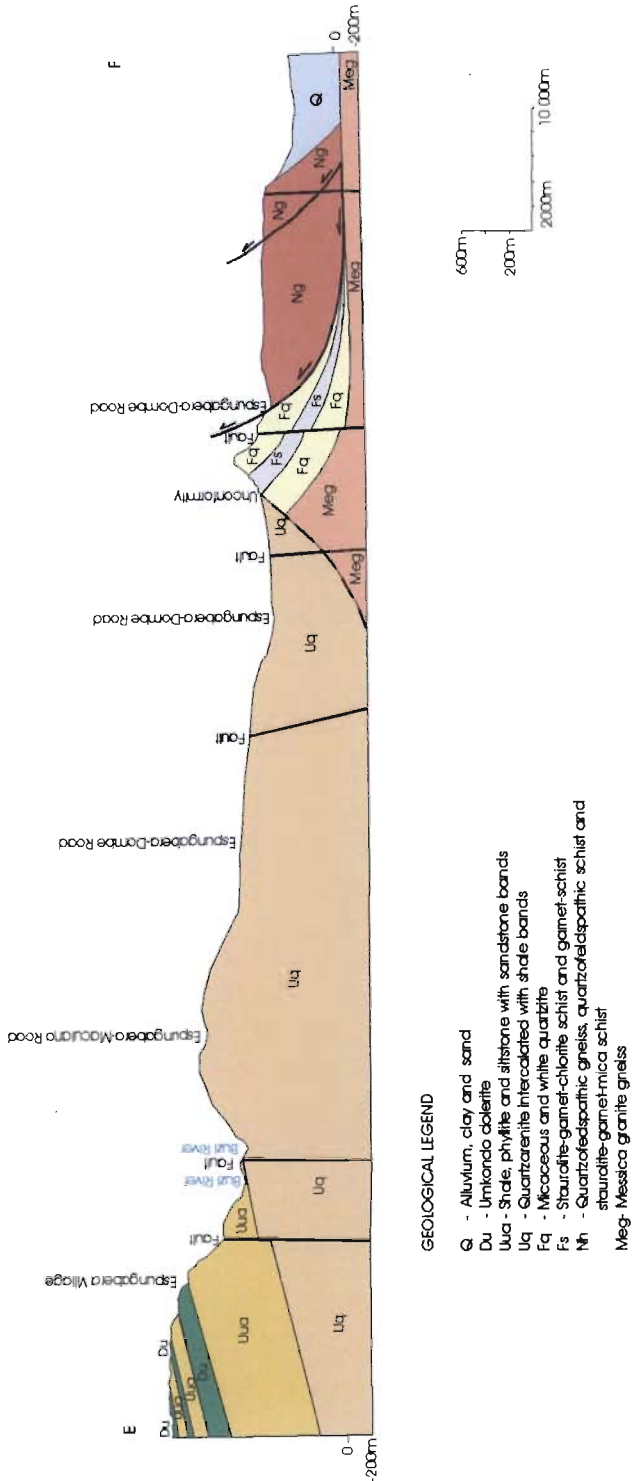

Figure 4.17 Cross-section between Espungabera Village and Sitatonga Range showing the relationship between Umkondo Group (Uua, Uq) bedding and Gairezi Group (Fq, Fs) (See Figure 4.1 for locality).

forms only a minor aspect in this work. The structural data and geological structures of the domain are presented in Figure 4.16 and in Table 4.5.

4.6.1 PRIMARY STRUCTURE: S_o

The bedding in the Umkondo Group is characterized by gentle to moderate dips from Dacata village to Sitatonga Range (Figure 4.16/18), with the average dip increasing from 14° to 51° respectively. The bedding (So/D_4), as well as the cleavage (S/D_4), changes strike from north-northeast/south-southwest around the Dacata area to north-south at Sitatonga Range approximately (Figure 4.16/18).

The Frontier Formation is characterized by a general absence of both bedding and sedimentary structures, although some vague (false?) bedding may be present. The cleavage dips steeply (~77°) to the east in the quartzites and there is a lack of fold-closures.

4.6.2 DUCTILE DEFORMATION

The Quartzite Formation beds around the Dacata region are slightly folded with limbs striking north-northeast/south-southwest and gently dipping (14°-22°) to the west-northwest and east-southeast. The cleavage dips more steeply than the bedding with an average dip of between 51° and 85° either to the east or west, increasing to the northeast (Figure 4.18). The fold axis (F/D_4) is sub-horizontal, plunging up to 05° to the north-northeast and is parallel to the intersection lineation, suggesting that the folds and cleavage developed during the same deformation phase (D_4) as shown in the Figure 4.18. The axial planar cleavage is perpendicular to the bedding and probably formed in response to total strain and developed perpendicular to the direction of maximum total shortening (Dieterich, 1969).

In the Sitatonga Range the quartz-mica schist of the Umkondo Group is characterized by asymmetrical folding with a long limb dipping gently to the east-southeast and a steeply inclined and overturned shorter, western limb (Figure 4.19). Overturning of the western limb may be the result of simple shear. The axial planar cleavage (S/D_4) strikes nearly north-south and dips approximately 70° to the east, while the fold axes (F/D_4) plunge gently (14°) to the south. The stretching mineral lineation(L/D_4), plunging 26° to east, is at right angles to the southerly plunging fold axis, suggesting possible westwards directed thrusting (Figure 4.17). The quartz veins in the fold limbs are parallel to the cleavage.

Due to the absence of road access and land mine clearance, the Chimanimani Mountains could not be mapped. Nevertheless, it is possible to understand the geology of this area from previous work. Vail (1966) observed very strong cleavage in quartzites striking north-south and dipping 50°-70° eastwards, while in the metapelites, two cleavages are recognisable with the one sub-parallel to the bedding being folded.

The mica-schist within the Frontier Formation intercalated with quartzite is strongly foliated and exhibits well-developed garnet and feldspar porphyroblasts. In thin section, the garnet porphyroblasts of pyrope-almadine composition most likely reflect post-tectonic growth, as indicated by a lack of deflection of external schistosity (S_e) and a lack of strain shadows (Figure 4.20). This is considered to indicate that the garnet crystals grew after the development of the cleavage (Passchier & Trouw, 1996).

The quartz grains are elongate, equigranular, with straight grain boundary and are intercalated by subparallel mica (sericite and muscovite), defining the schistosity (continuous mineral foliation) as shown in Figure 4.21. The shape of quartz grains is a consequence of

Table 4.5 Summary of the geological structures in Domain D.

Deformation phase	Bedding	Cleavage	Planar cleavage	Shear zone	Fracture	Fault	Fold axis
D_1							
D_2							
D_3				N-S (dextral)	NE-SW		
D_4	NNE-SSW N-S	S/D_4:NNE-SSW S/D_4: NE-SW S/D_4: N-S	N-S	N-S (sinistral)	ENE-WSW WNW-ESE NW-SE E-W	ENE-WSW	NNE N
D_5					NNE-SSW NNW-SSW N-S	N-S	

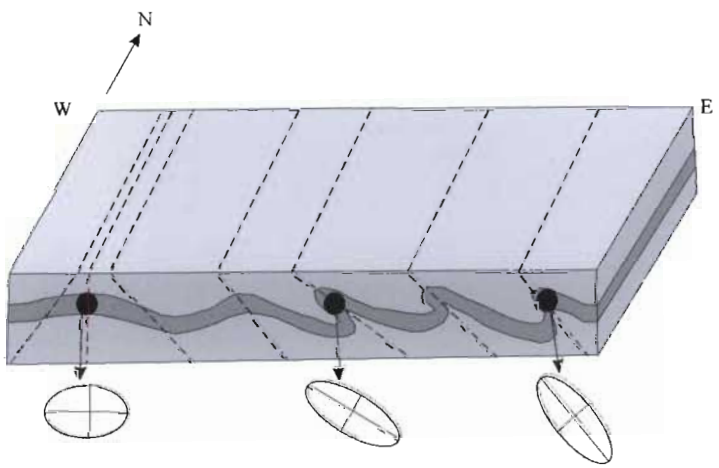

Figure 4.18 Sketch of relationships between bedding, cleavage and axial planar cleavage in the Umkondo Group in the Dacata area (W) and the Frontier Formation in the Sitatonga Range (E).

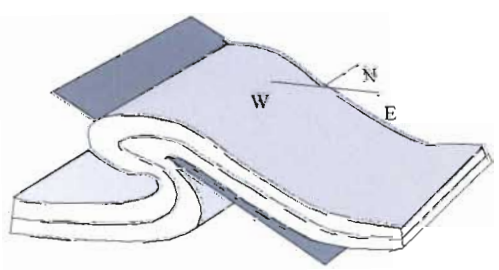

Figure 4.19 Sketch of asymmetrical folding showing the north-south striking axial planar cleavage within the quartz-mica schist in the Sitatonga Range.

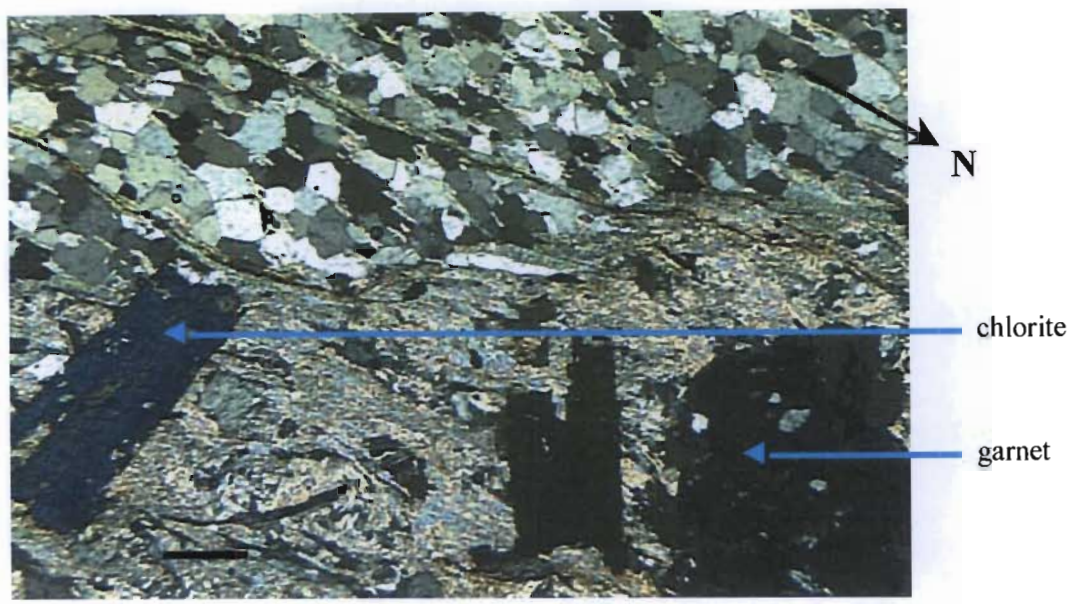

Figure 4.20 Photomicrograph of the Frontier Formation garnet-chlorite schist showing the relationship between garnet and chlorite porphyroblasts and cleavage. Scale bar = 250μm. (See Figure 4.16 for locality).

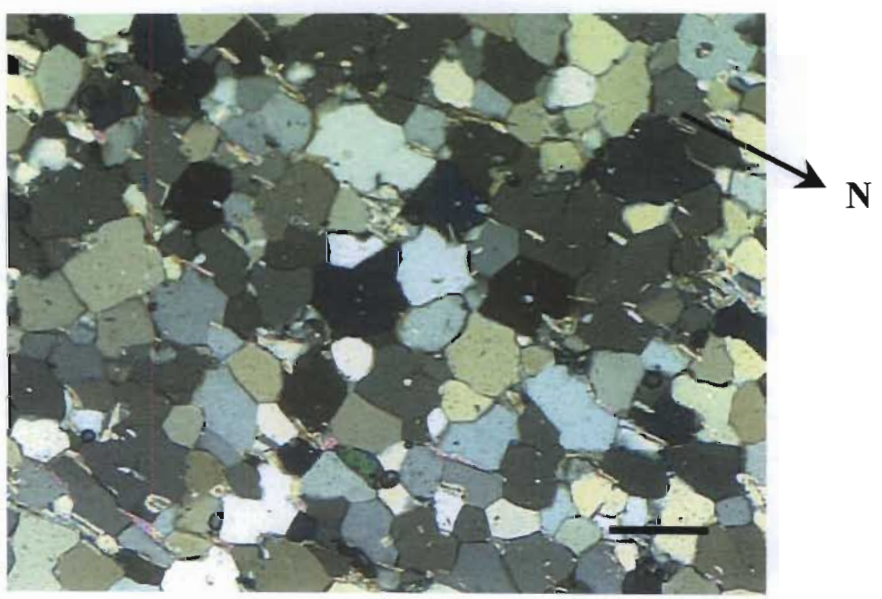

Figure 4.21 Photomicrograph of the Frontier Formation quartzite showing the continuous mineral foliation, essentially defined by parallel micas within elongate quartz crystals. Scale bar = 250μm. (See Figure 4.16 for locality).

secondary grain growth during deformation.

The cleavage in the Frontier Formation quartz mica-schist shows a sigmoidal shape (Figure 4.22). Rather than being the result of later shearing, the shape is more probably due to the refraction of the axial planar cleavage through an incompetent unit on the limb of fold (Figure 4.23).

The quartzofeldspathic gneiss and feldspathic-mica schist of the Nházonia Formation, which lies on the eastern side of the Frontier Formation, are characterized by a continuous mineral foliation. This is defined by parallel and subparallel micas and by irregularly shaped of quartz crystals (Figure 4.24). This cleavage (S/D_4) dips up to 83° to the east or to west, striking north-south. Near vertical mineral lineations (L/D_4) plunge 85° to the east.

The Nházonia Formation staurolite-garnet-mica schist has snowball garnet porphyroblasts with quartz inclusions that indicate rotations of up to 90° with a clockwise sense of movement (Figure 4.25). The structure was presumably generated during a single deformation phase and might be related to differential movement on the limb of a fold undergoing shearing due a flexural deformation mechanism (Figure 4.26). The quartz crystals were incorporated into the growing crystals as slightly elongate inclusions. The curvature of internal schistosity (S_i) is caused by relative rotation between the garnet porphyroblasts and the matrix foliation (S_e). The rotational porphyroblast was produced by recrystallization of the schistosity into a new orientation during the later stages of its growth (Passchier & Trouw, 1996).

4.6.3 BRITTLE DEFORMATION

The Quartzite Formation at Dacata region is intensively fractured. The fractures, as well as the quartz veins, are characterized by moderate to steep dips usually between 40° and 90°, and form two distinct sets. The first and more widespread fracture set is characterized by north-northeast (012°) and south-southeast (168°) strikes and dips east-southeast (60°) and west-southwest (82°) respectively. The second fracture set strikes east-southeast (100°) and northeast-southwest (055°) dipping near vertical to the south-southwest (85°) and northwest (84°) respectively. Analysis of the stress ellipsoids causing these fractures indicate that the first set is related to normal faulting and the second set to strike-slip faulting (Table 4.6).

East-northeast trending fractures have developed in brittle quartzites. In places faulting occur along these fractures such as the Skeleton Gap Fault in the north and Lucite Fault in south, which is a continuation of the Zunguni and Tanganda-Lucite faults respectively in Zimbabwe.

Table 4.6 Orientation of principal stress axes from conjugate fracture sets in Domain D.

Sets	σ1	σ2	σ3	Fault
1	78→072	03→188	10→280	Normal
2	13→080	75→251	00→352	Strike-slip

4.6.4 DISCUSSION

Whereas in Domain C, the increasing effects of the Pan-African events were observed in the Archaean basement, in Domain D, the effects are seen in the Proterozoic Umkondo Group overlying that basement. The intensity of deformation in the latter domain clearly increases from west to east (Figure 4.18). The onset of asymmetrical folding coincides with the Frontier Formation which, further east, forms a duplex zone over which units have been thrust towards the west Figure 4.17). When considering the cross-sections of Domain C (Figure 4.9) and Domain D

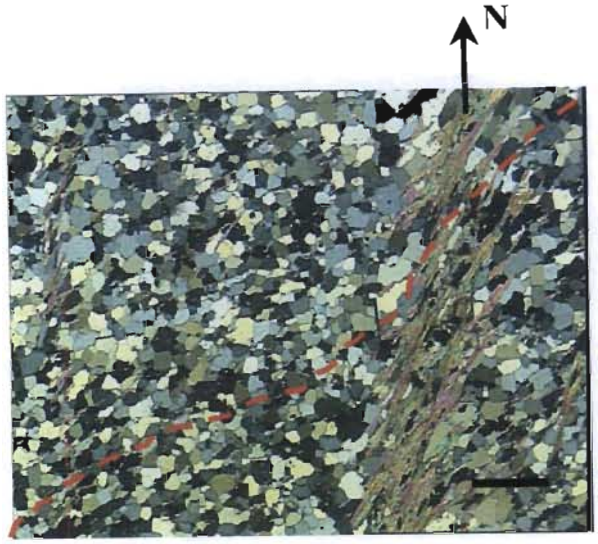

Figure 4.22 Photomicrograph of the Frontier Formation mica-schist around Sitatonga area showing refraction of axial planar cleavage through incompetent unit. Scale bar = 250μm. (See Figure 4.16 for locality).

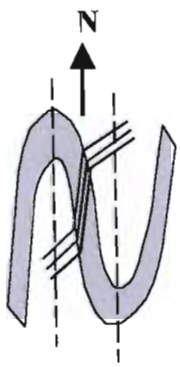

Figure 4.23 Sketch explaining the sigmoidal cleavage in Figure 4.22 as being due to refraction of axial planar cleavage between an incompetent unit (shaded) and a competent unit on the west limb of a northerly plunging synform or east limb of a northerly plunging antiform.

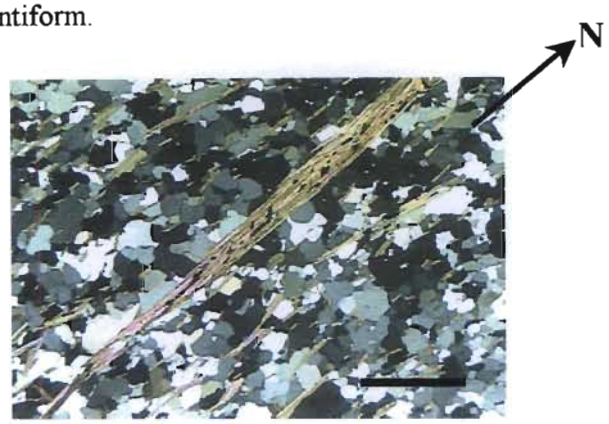

Figure 4.24 Photomicrograph of the Nhazónia Formation quartzofeldspathic-mica schist showing continuous mineral foliation defined mainly by subparallel micas and irregularly shaped quartz crystals at Sitatonga region. Scale bar = 250μm. (See Figure 4.16 for locality).

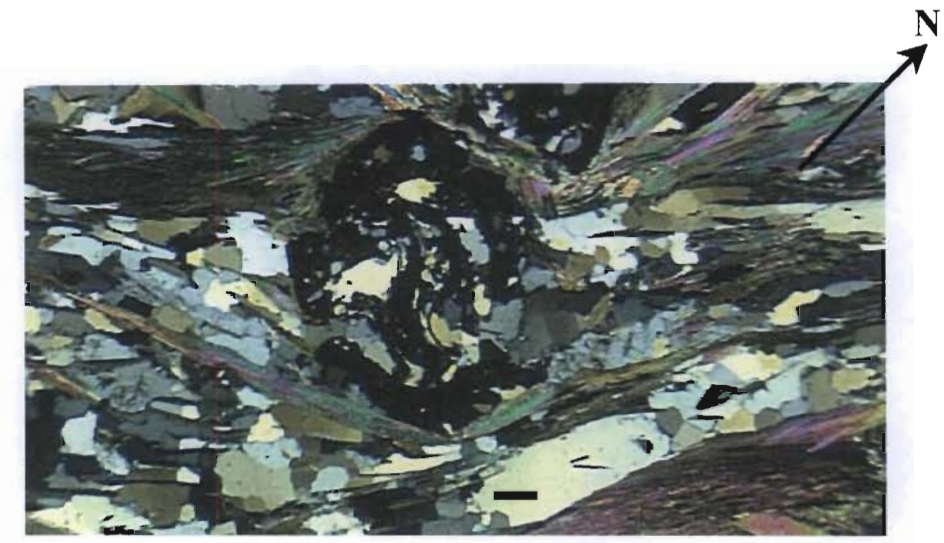

Figure 4.25 Photomicrograph of the straurolite-garnet-mica schist of Nhazónia Formation showing the relationship between garnet porphyroblast with inclusions and cleavage in around Sitatonga region. Scale bar = 250μm. (See Figure 4.16 for locality)

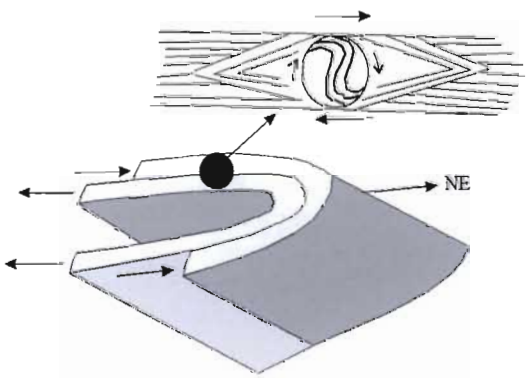

Figure 4.26 Sketch explaining the garnet rotation on left limb of antiform in Figure 4.25.

Figure 4.27 Strong cleavage within Chimanimani quartzites striking north-south and steeply dipping to the east. Scale bar = 5 m (See Figure 4.16 for locality). View looking south

(Figures 4.11 and 4.17), it is appears that this thrusting is thin-skinned and only affects the Proterozoic cover. The Nházonia Formation, which lies to the east and structurally above this duplex zone, exhibits a higher grade of metamorphism and more ductile deformation than the Frontier Formation. Considering the structural position of the Nházonia Formation, it seems that this metamorphism and deformation probably predates the Pan-African thrusting event.

As regards the brittle features, the second conjugate fracture set with a strike-slip nature (Table 4.6) are probably of the same D_4 origin as the fracture sets with similar orientations in Domain B (Table 4.3). There is an apparent progressive clockwise rotation of the maximum compressional stress from fracture set 2 in Table 4.6, to fracture set 1 in Table 4.3 and then fracture set 2 in Table 4.3. This may relate to a change in regional stress either in space or time (possibly both) but more data are required to confirm such an interpretation.

The approximately north-south trending conjugate fractures with a normal fault system origin are lacking in Domain B but are present in Domain C. It would seem that they tend to occur along the duplex zone, which is, essentially, the contact zone between the Zimbabwe craton and the Moçambique Belt. Consequently they could represent an early Palaeozoic extensional event due to gravitational collapse following on from the Pan-African thrusting. However, from regional considerations, it is apparent that such faults affect the Phanerozoic Karoo Supergroup so it appears more likely that they are related to Gondwana break-up. During this D_5 event, the contact zones between different crustal terranes were reactivated during extension.

The different orientations of the fractures suggest the presence of more than one deformation phase throughout the domain D. Joint set 1, which is related to normal faulting (Table 4.6) and north trending fractures probably represent reactivation of older structures during Gondwana break-up event.

5.7 DOMAIN E

Domain E forms the northeast part of the study area (Figure 4.1). It is underlain by the Báruè. Complex of the Moçambique Belt and comprises high grade metamorphic rocks that have undergone multiple deformations (Manhiça, 1998). The complexity of this 3132 km^2 domain is such that it requires a far more detailed investigation than was possible during this study. The prominent structural features and geological structures of the domain are presented in Figure 4.28 and in Table 4.7.

4.7.1 DUCTILE DEFORMATION

The most remarkable feature of the domain is the north-south striking foliation (S/D_4), dipping steeply (61°-87°) either to the east or west, although northeast-southwest striking cleavage, steeply dipping (80°-87°) to the southeast was observed in a few places. The mineral lineations (L/D_4) plunge sub-horizontally to gently between north and north-northeast, while the fold axes (F/D_4) of folded quartz and pegmatite veins plunge almost parallel to the lineation, 30° to the north.

In the Vanduzi migmatite gneiss, the north-south S/D_4 fabric is predated by the primary compositional layering. Manhiça (1998) reports the presence of an east-west planar fabric in this unit parallel to this layering that dips moderately north and south. In the north of this domain, the Vanduzi gneiss is characterized by two anatectic vein events. Manhiça *et al.* (2001) concluded that the northeast-southwest veins predate the north-south veins that are almost parallel to the S/D_4 cleavage. The older veins are folded together with the gneiss, and the fold

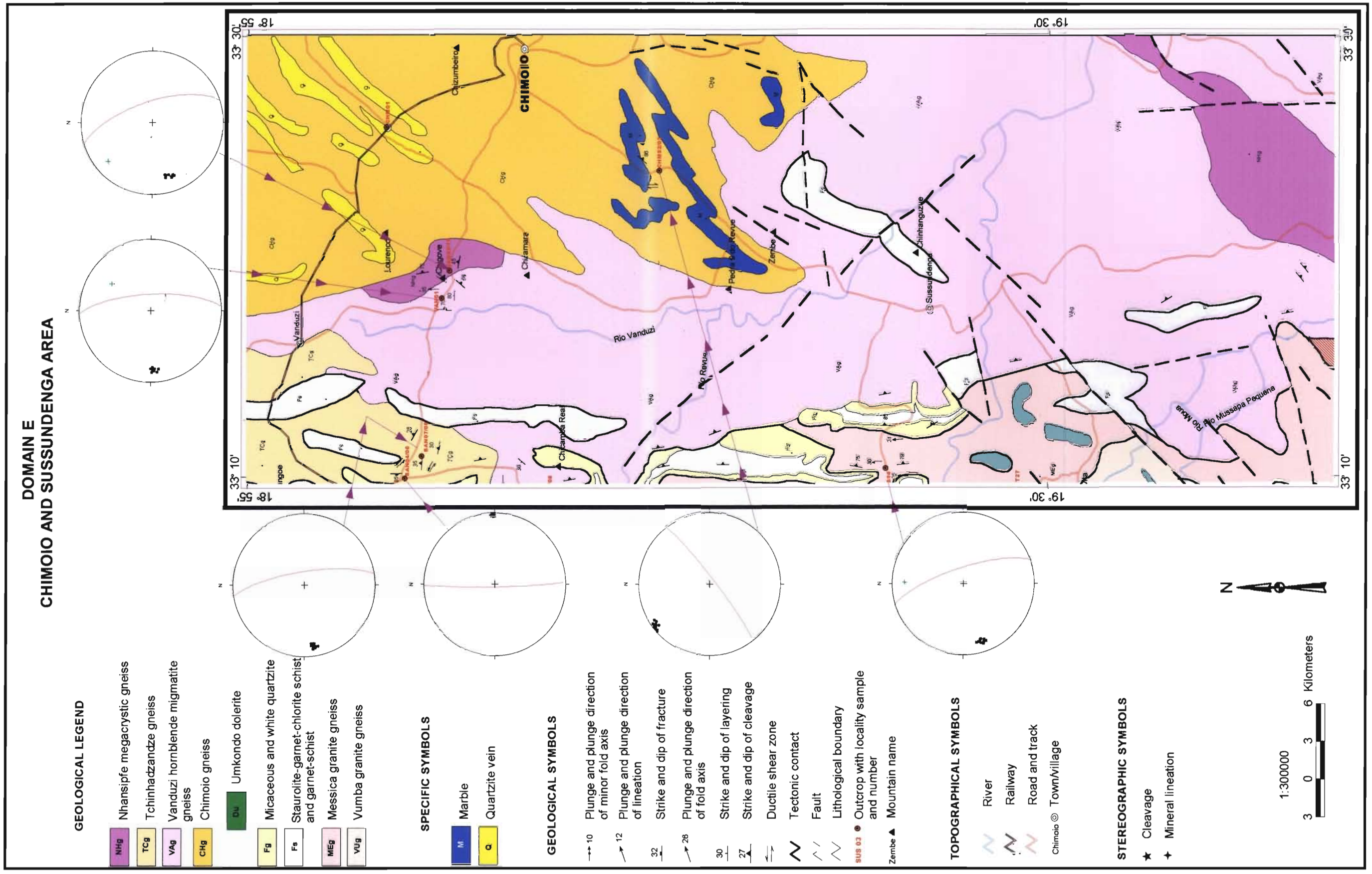

Figure 4.28 Domain E showing localities sampled and stereographic projections of cleavage.

axes plunge 35° to the north-northeast and north. In some places antiformal structures were observed in the gneiss in which the leucocratic pegmatite vein was folded within the enclosing gneiss. The rocks were intruded by leucocratic granite dykes and contain mafic enclaves that are boudinaged.

This domain contains north and north-northeast trending sinistral strike-slip shear zones. Locally north-northwest trending sinistral strike- slip shear zones and north-northeast trending occur.

4.7.2 BRITTLE DEFORMATION

The rocks are intensively fractured by near vertical, northwest-southeast, northeast-southwest, and north-south joints. These are normally filled by pegmatite and quartz, veins.

4.7.3 DISCUSSION

The oldest structure recognised in the Báruè Complex is the compositional layering and the fabric parallel to that layering. The origin of this fabric was not discussed by Manhiça (1998) nor by Manhiça *et al.* (2001), but it implies an early north-south compressional event. In light of the Kibaran dates obtained from the units in this domain (Manhiça *et al.*, 2001), this may be related to events of that age.

The layering and this fabric then underwent northwest-southeast compression to form the folds with axes and cleavage trending north-east during D_4. The outcrop pattern of the marbles to the southwest of Chimoio is largely due to this event, as is the pattern of quartzites to the north of Chimoio, although not so obviously (see (Figure 4.28 and the Geological Map of Western Central Moçambique at back of thesis). The age of this folding is unknown; it could be due to Kibaran or Pan-African events.

Regionally the north-east trending axial planes rotate anticlockwise in the western parts of this domain, to become subparallel to the north-south S/D_4 cleavage. This relationship implies that either the S/D_4 cleavage was formed in a younger and separate event than the northeast trending folding (i.e. Kibaran folding overprinted by a Pan-African deformation) or that there is a rotation of the strain ellipsoid in a single progressive event.

Manhiça *et al.* (2001) interpret the contact between the Zimbabwe craton and the Moçambique Belt as being a sinistral strike-slip zone. This interpretation is in agreement with the sense of movement of the small-scale north-south trending shears observed in this study. It also explains the anticlockwise rotation of the northeast fold axes in Domain D and the outcrop pattern of the Macequece Formation in the Manica greenstone belt at the eastern edge of the Zimbabwe craton.

However, during this study no evidence was found of kinematic indicators nor s:c fabrics supporting the presence of such a wide ductile shear zone. Evidence of simple shear is confined to small-scale ductile shears. It is logical that formation of the north-south orientated S/D_4 cleavage took place during Pan-African east-west compression. Simple shear associated with this event seems to have been related to overthrusting and the development of a duplex zone between the craton and the mobile belt, rather than to major strike-slip movement between these two crustal provinces. Rotation of the northeast trending fold axes may, therefore, be the result of a contact strain effect during east-west Pan-African compression. The small-scale ductile shears may be a response to this rather than being indicative of a major regional strike-slip system.

As with the other domains, the brittle north-south striking fractures probably represent reactivation of older structures during Gondwana break-up event.

Table 4.7 Summary of the geological structures in Domain E

Deformation phase	Cleavage	Fracture	Shear zone	Fold axis	Mineral lineation
D_1					
D_2					
D_3					
D_4	S/D_4 : NE-SW S/D_4 : N-S	NW-SE NE-SW	NNE-SSW (sinistral) NNW-SSE (sinistral) N-S (sinistral)	NNE N	NNE
D_5		N-S			

4.8 ANISOTROPY OF MAGNETIC SUSCEPTIBILITY (AMS)

4.8.1 INTRODUCTION

Manhiça *et al.* (2001) proposed that the contact between the Zimbabwe craton and the Moçambique Belt is a strike-slip zone. As explained above, the field evidence in the study area does not seem to support such a conclusion. However when anisotropies are weak, planar and linear fabrics are difficult to determine directly in the field, especially the linear fabrics, (Bouchez & Gleizes 1995). Consequently, a preliminary AMS study was undertaken across the eastern margin of the Zimbabwe craton to characterise and quantify the change in strain where the craton is reworked by deformation associated with the Moçambique Belt. Three east-west traverses were selected and oriented cores collected from 30 stations that sampled the Vumba and Messica granite gneisses (Figure 4.29 and Appendix 1). The results are presented in Tables 4.1 and 4.2 (Appendix 4).

Magnetic susceptibility (K) reflects the magnetization (M) acquired when a rock is subjected to an inducing magnetic field (H) where K=M/H. (Borradaile 1988). This is carried by magnetic minerals, which include Fe-oxides, such as magnetite, Fe-sulphides and Fe-bearing silicates such as biotite, hornblende and chlorite.

There are two main types of magnetic susceptibility in rocks: paramagnetic and ferromagnetic. In a paramagnetic rock, the magnetic susceptibility is weak and reflects the petrographic fabrics of the Fe-bearing silicate minerals (Gleizes *et al.*, 2001). In a ferromagnetic rock, the magnetic susceptibility is high due to the susceptibility of magnetite being two orders of magnitude higher for the same amount of Fe in paramagnetic minerals

Magnetic susceptibility may be approximated to a second rank tensor. This may be represented geometrically by an ellipsoid with principal axes $K_1 \geq K_2 \geq K_3$ while the bulk susceptibility $K = (K_1 + K_2 + K_3)/3$. The orientation of the ellipsoid can be represented on a stereographic projection while the shape can be plotted on a Flinn diagram (P_{Flinn}) or by using the T parameter (Jelinek, 1981) (Appendix 1). The K_1 axis represents the susceptibility lineation while the susceptibility foliation is the plane containing K_1 and K_2.

As the anisotropy of magnetic susceptibility is carried by biotite and sometimes by hornblende, the plane normal to the short axis K_3 of the magnetic anisotropy ellipsoid or magnetic foliation, is parallel to the mineral foliation defined by the average planar disposition of the biotite flakes and hornblende when it occurs. The long axes K_1 of the magnetic anisotropy ellipsoid is parallel to the lineation defined by the zonal axis of orientation of the biotite crystals and mean alignment of the hornblende (Bouchez & Gleizes 1995).

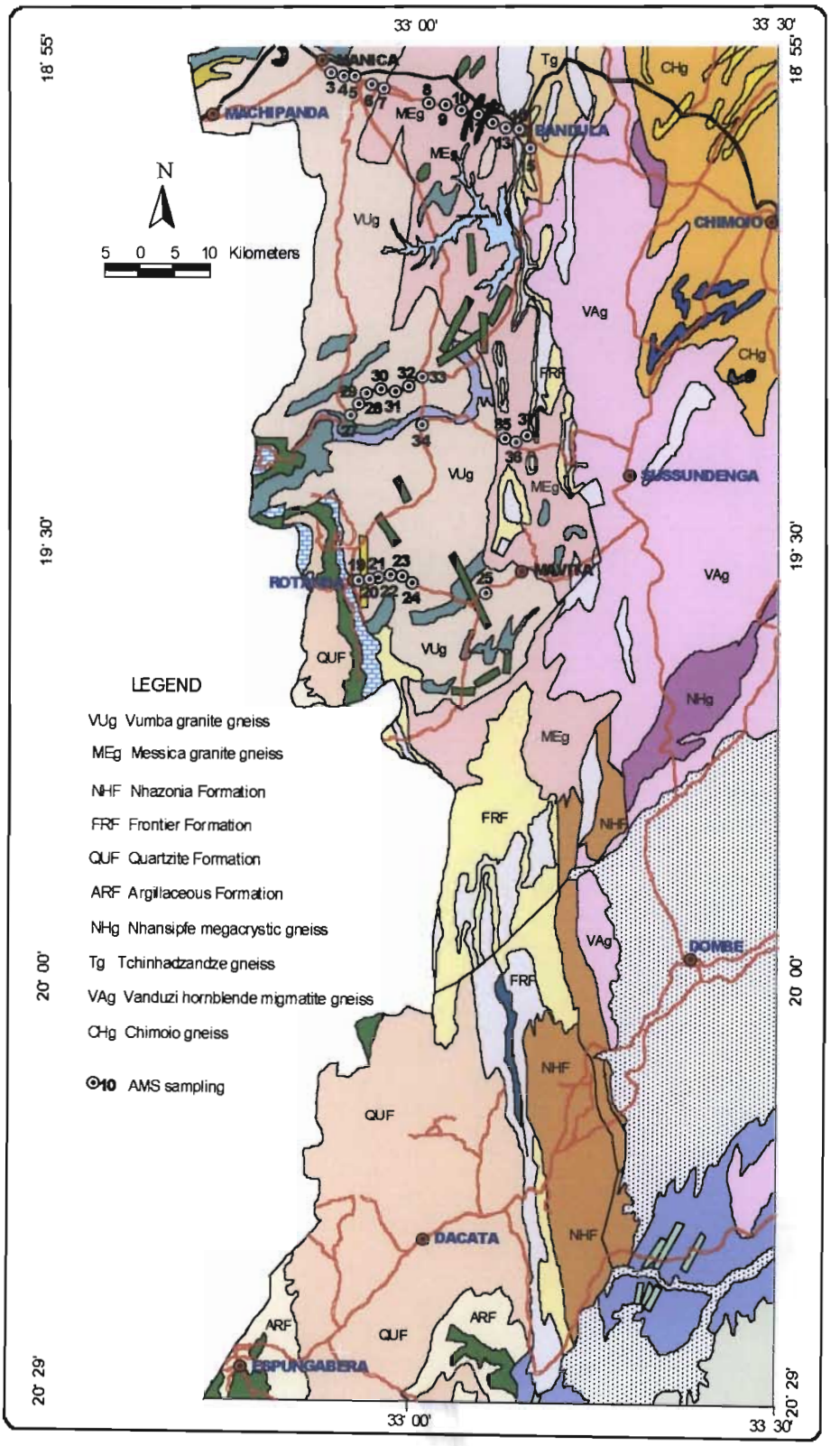

Figure 4.29 Geological map of the study area showing AMS sample sites.

4.8.2 AMS CHARACTERISTICS

4.8.2.1 NORTHERN TRAVERSE

In the Vumba granite gneiss magnetite grains are rare but where present are elongate, with their long axes parallel to hornblende and biotite. Overall the rock is paramagnetic, because magnetic anisotropy values in general lower than 500 μSI (Rochette 1987; Jover *et al.*1989; Bouchez *et al.*, 1990) and the susceptibility is weakly positive. The gneiss (samples BM003-006, Figure 4.30A) has a well-defined magnetic lineation plunging to the northeast (Figure 4.31) and a weak planar magnetic fabric that is steeply dipping and striking northwest-southeast (Figure 4.32).

The magnetic anisotropy (P) ranges from 1.6 to 24.7%, (Table 4.1, Appendix 4). The shape of the anisotropy ellipsoid is prolate according to the P_{Flinn} classification as the values are greater than 1 (Figure 4.30B). By T parameter of Jelinek it is cigar-shaped, as it has negative values (Table 4.1, Appendix 4).

The Messica granite gneiss underlies the eastern part of this traverse. Taking into account the structures and the AMS results, it can be divided in: western and eastern portions.

The petrography and AMS characteristics of the western Messica granite gneiss are almost identical to the Vumba granite gneiss (samples BM0007-009, Figure 4.30A). The magnetic anisotropy varies between 0.7 and 26% (Table 4.1, Appendix 4). The magnetic foliations trend north-northeast and dip almost vertical (Figure 4.32). The magnetic lineation plunges vertically to the north-northwest (Figure 4.31).

The Messica granite gneiss in the eastern portion (samples BM010-013, Figure 4.30A) contains notably more magnetite than in the western portion. These are often more or less elongate and parallel to the paramagnetic mineral biotite. The gneiss is ferromagnetic with a total anisotopy higher than 500 μSI (Rochette 1987: Jover *et al.*, 1989: Bouchez *et al.*, 1990). It is characterized by a strong positive susceptibility with good planar magnetic fabric striking north-south (Figure 4.32) and a poor linear magnetic fabric plunging plunges moderately to either to north or to south (Figure 4.31).

The magnetic anisotropy is high and varies between 9.8 and 25.2%. The shape of the anisotropy ellipsoid is essentially oblate according to the P_{Flinn} classification as the values are less than (Figure 4.30B) which agrees with the disk-shape according to the T parameter of Jelinek (1981 (Table 4.1, Appendix 4).

This granite gneiss was deformed in the solid-state, therefore the magnetic fabric is the sum of the magmatic fabric and of an intense solid-state fabric. The magnetic foliations reflect the cleavage defined by the biotite and, therefore, the foliation measured in the field (Table 4.1, Appendix 4).

4.8.2.2 CENTRAL TRAVERSE

The Vumba granite gneiss of central traverse (samples BM027-034, Figure 4.33A) has the same petrographical and AMS characteristics as those of northern traverse. The magnetic anisotropy is more variable than along the northern traverse (between 2.1 and 47.6%) (Table 4.1, Appendix 4). The plunge of the magnetic lineation is steep and follows the contact of the greenstone belt (Figure 4.31).

In the eastern portion, the Messica granite gneiss (samples BM035-037, Figure 4.33A) has a high anisotropy (8.7-32.8%). The magnetic foliation consistently strikes north-south while the magnetic lineation plunges steeply to the north (Figures 4.31 and 4.32).

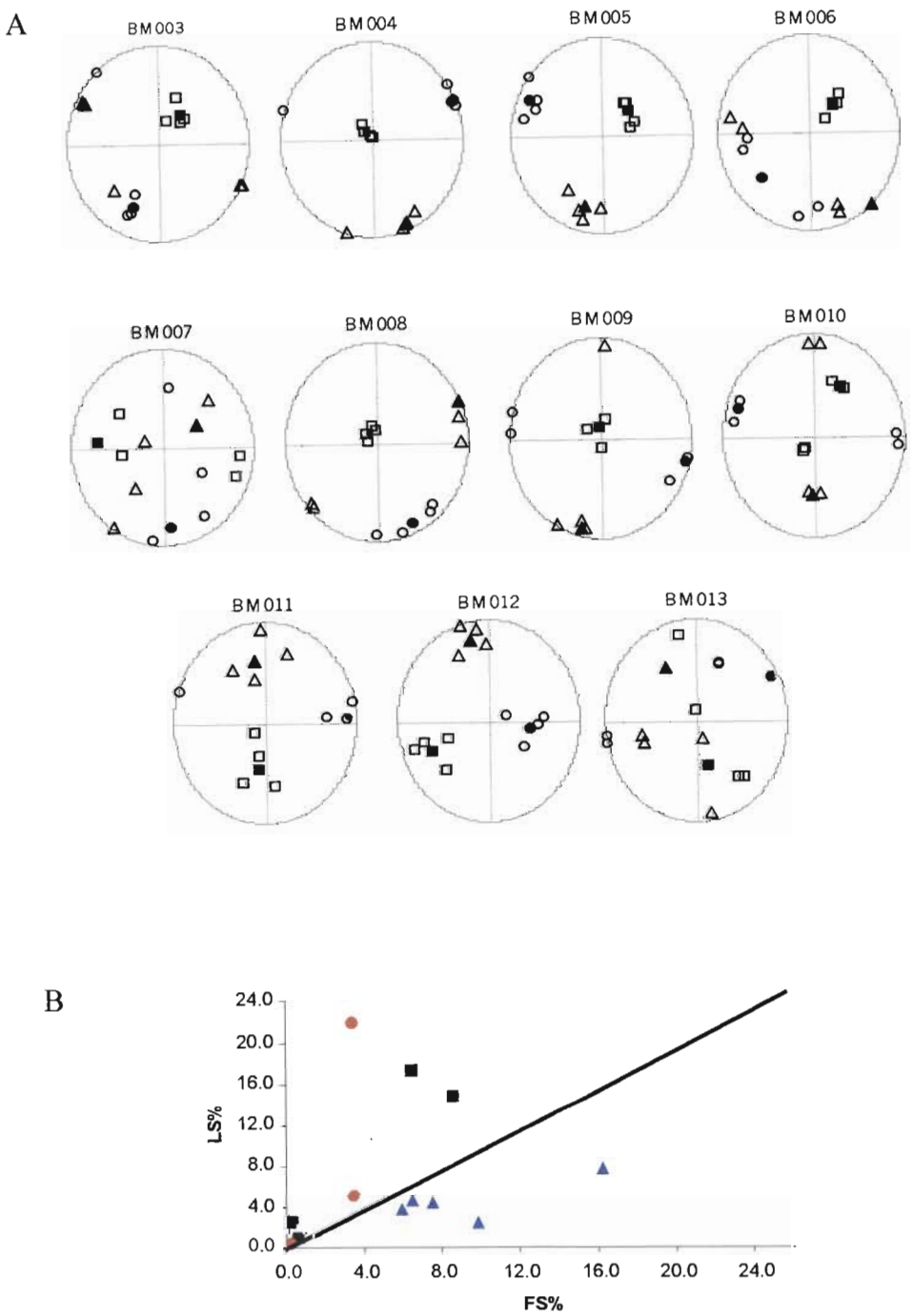

Figure 4.30 A) Stereographic diagrams (lower hemisphere) of magnetic ellipsoid axes of northern traverse. BM003-006 = Vumba granite gneiss, BM007-009 = western Messica granite, BM010-013 = eastern Mesica granite gneiss. □ = K_1, Δ = K_2, ○ = K_3

B) The Flinn graph showing the shape of strain ellipsoid of Vumba granite gneiss. ■ =Vumba granite gneiss, ● = western Messica granite gneiss, ▲ = eastern Messica granite gneiss.

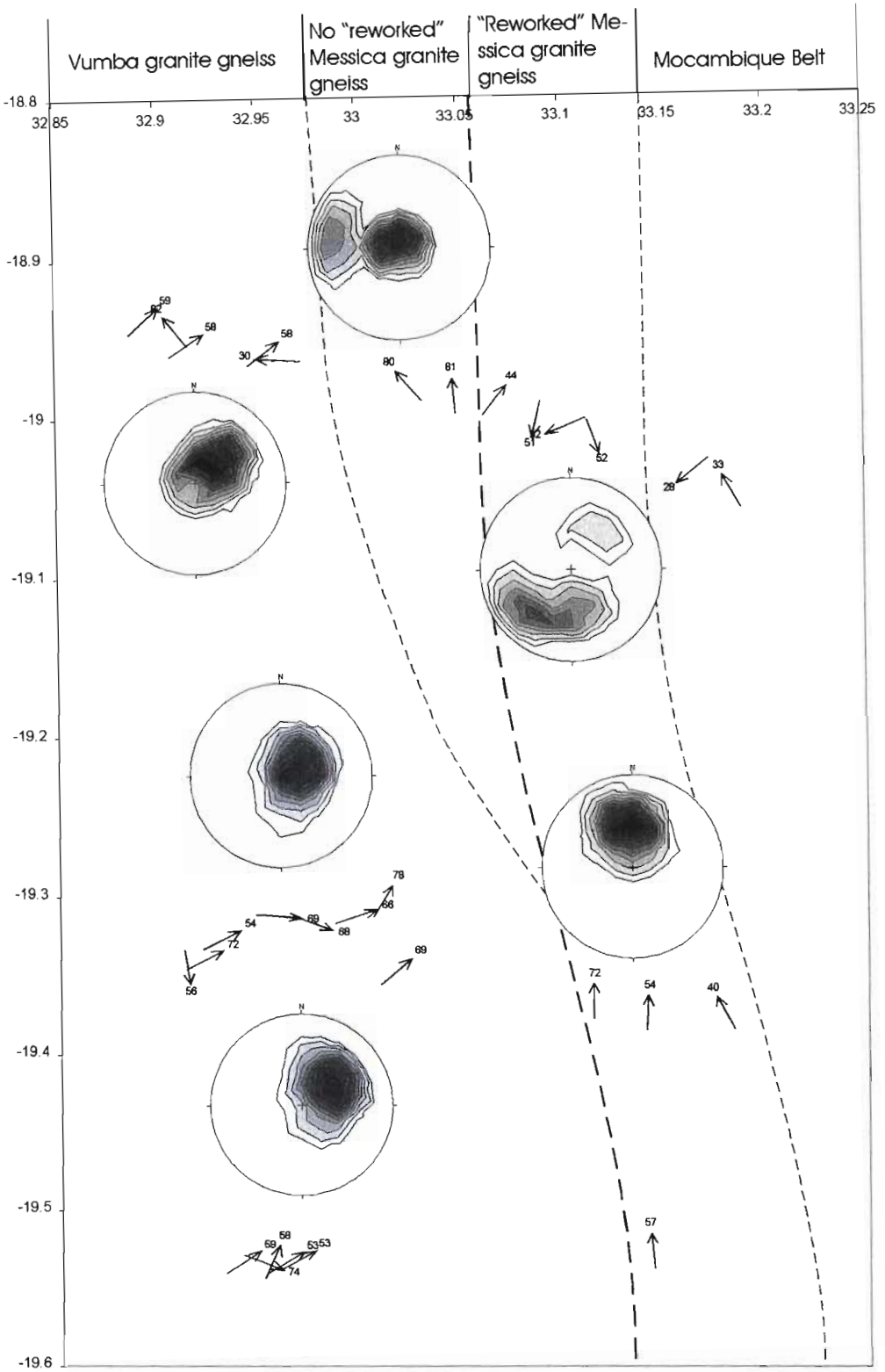

Figure 4.31. Plan of the traverses with K_1 axes of Vumba and Messica granite gneisses contoured with respective stereographic diagrams (lower hemisphere).

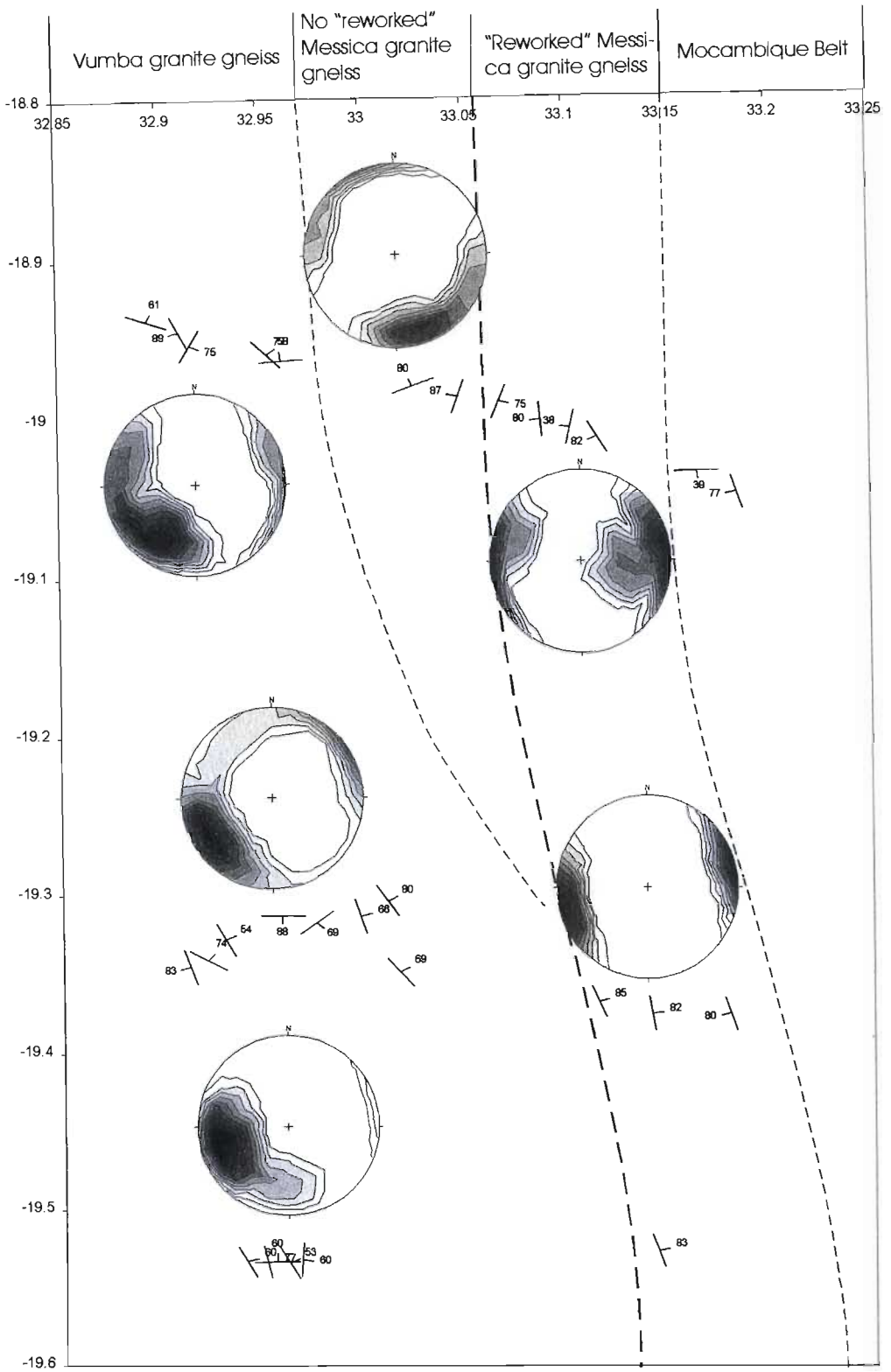

Figure 4.32. Plan of the traverses with K_3 axes of Vumba and Messica granite gneisses contoured with respective stereographic diagrams (lower hemisphere).

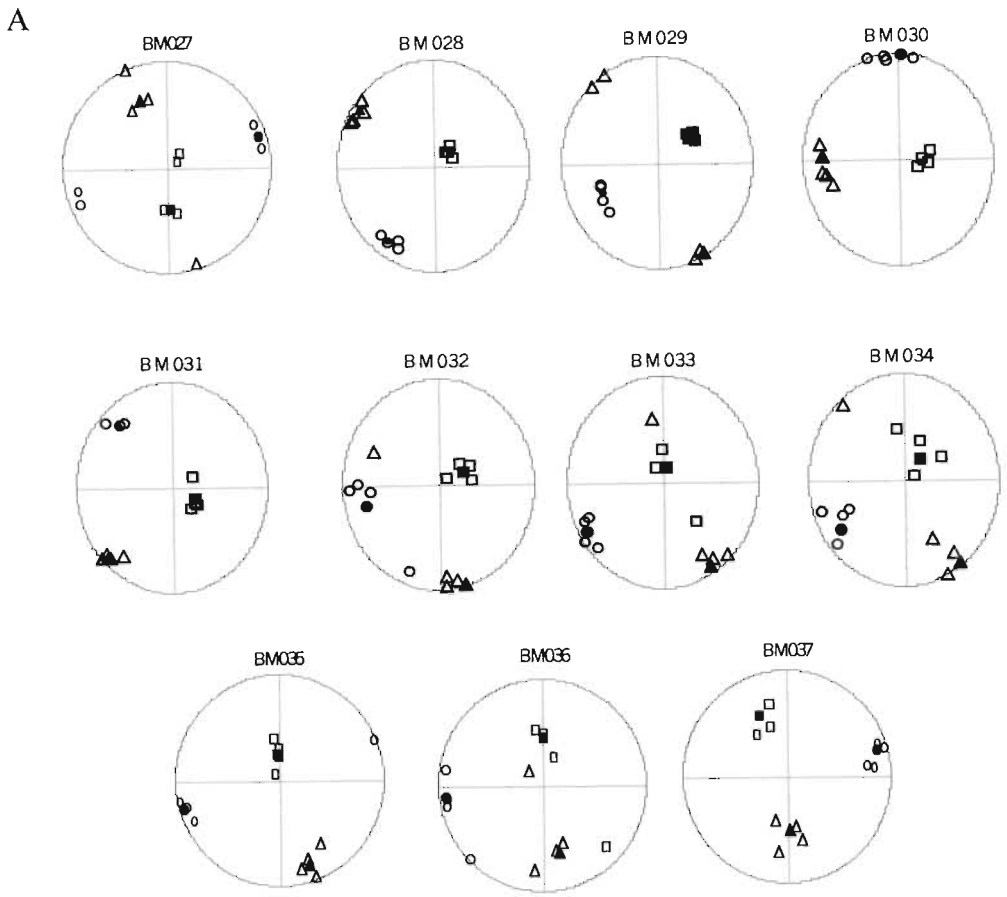

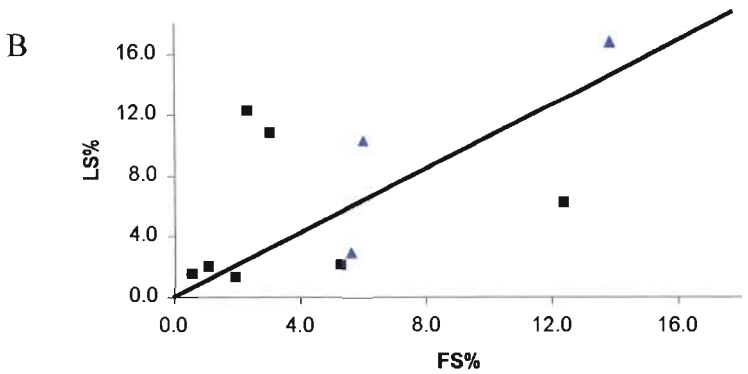

Figure 4.33 A) Stereographic diagrams (lower hemisphere) of magnetic ellipsoid axes of central traverse. BM027-034 = Vumba granite gneiss, BM035-037 = eastern Mesica granite gneiss. □ = K_1, Δ = K_2, ○ = K_3
B) The Flinn graph showing the shape of strain ellipsoid of Vumba granite gneiss. ■ =Vumba granite gneiss, ▲ = Messica granite gneiss.

4.8.2.3 SOUTHERN TRAVERSE

The Vumba granite gneiss of southern traverse (samples BM020-024, Figure 4.34A) has the same petrographical and AMS characteristics as those of northern and central traverses. However the magnetic anisotropy is relatively low, varying between 3.0 and 4.7% (Table 4.1, Appendix 4). The magnetic lineation generally plunges moderately steeply northeast while the weak planar fabric strikes northwest dipping steeply northeast (Figures 4.31 and 4.32). The single Messica granite gneiss sample along this traverse (sample BM025, Figure 4.34A) has a strong steeply dipping, north-south striking planar fabric and a lineation plunging moderately towards the north.

4.8.3 DISCUSSION

Manhiça *et al.* (2001) proposed sinistral strike-slip movement between the Zimbabwe craton and the Moçambique Belt. The sole evidence cited in support of this is the change in strike of the planar fabrics in the Mutare-Manica greenstone belt from an east-west to a more east-northeast orientation on approaching the Moçambique Belt. The AMS results of this study indicate that the planar fabric in the Vumba granite gneiss and Messica granite gneiss west of the reworked zone, also seem to rotate in a similar fashion from a southwest to an east-northeast orientation. However, other structural work in this study indicates that the main deformation in the zone of reworking was overthrusting to the west. Consequently these two tectonic possibilities need to be compared.

Assuming that the granite gneisses along the eastern edge of Zimbabwe craton were isotropic prior to being affected by the Pan-African events, the expected AMS pattern resulting from a strike-slip event can be compared with that expected for a thrusting event. In the case of sinistral strike-slip movement, K_1 would be expected to have a horizontal plunge towards the northeast-southwest, while the planar fabric would strike between northeast-southwest and north with a vertical dip (Figure 4.35A). In the case of the east-to-west thrusting, K_1 would be expected plunge moderately to shallowly towards the east, while the planar fabric would strike north-south, dipping to the east (Figure 4.35B). It is quite apparent that the results of the AMS study do not fit either model.

Both models, however assume that the granites were isotropic prior to the Pan-African events, and this is clearly not the case. The Vumba granite gneiss at the western end of the traverses lies beyond the zone of obvious Pan-African reworking and is not isotropic as it contains a strong linear fabric as does the Messica granite gneiss.

These pre-Pan-African AMS fabrics require some consideration. Low magnetic anisotropy and steep magnetic lineations in granitic rocks tend to typical of magmatic fabrics (Bouchez & Gleizes 1995). Therefore the fabric in the Vumba granite gneiss and the Messica granite gneiss, where it has not been reworked, may be interpreted as being magmatic in origin. If this is the case the occasionally high anisotropy in the Vumba granite gneiss may relate to the local solid state deformation. The difference in orientation of this possible magmatic fabric between the Vumba granite gneiss and the adjacent Messica gneiss may reflect different times and direction of intrusion.

This interpretation is at a variance with the observations during field work and in thin-section where the fabric appeared to be of tectonic origin. It is interpreted as developing in the solid state as the S/D_3 planar fabric rather than being an Archaean magmatic fabric. Taken overall, it appears that the magnetic fabric has resulted from deformation of a paramagnetic granite in the solid state with the higher anisotropy rocks reflecting higher strains.

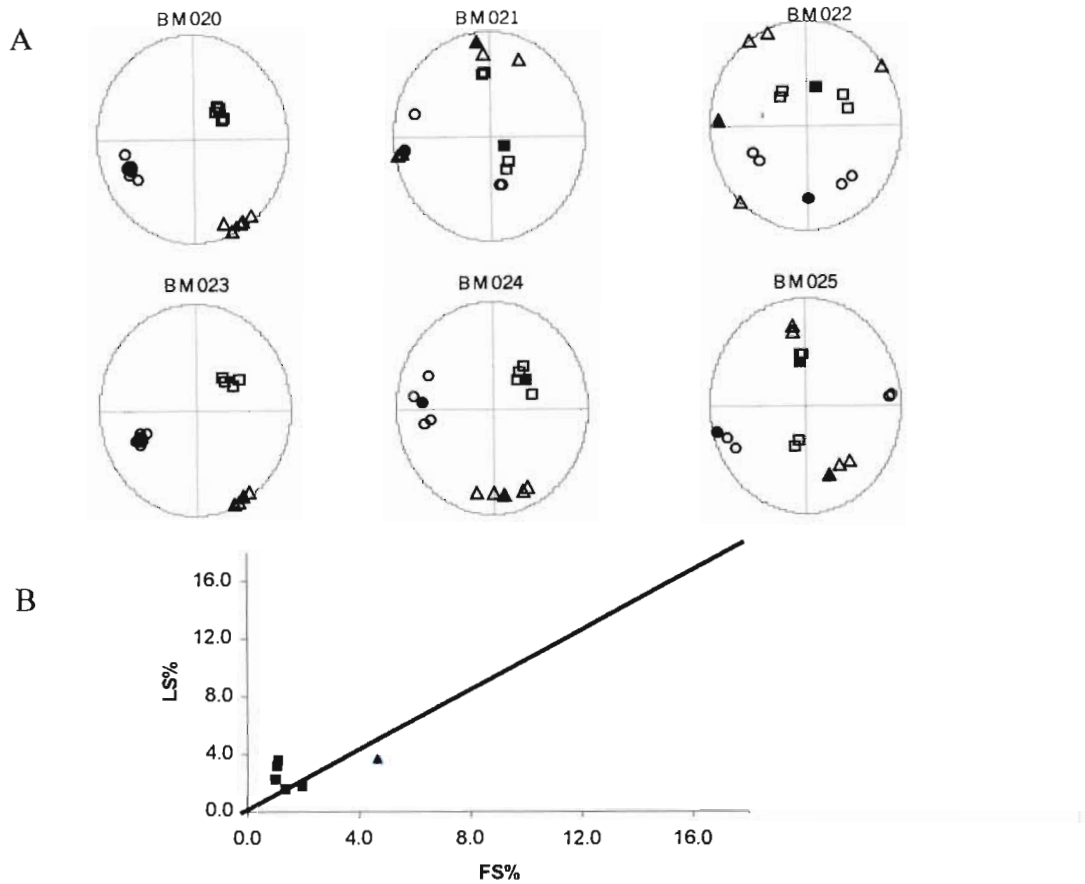

Figure 4.34 A) Stereographic diagrams (lower hemisphere) of magnetic ellipsoid axes of southern traverse. BM020-024 = Vumba granite gneiss, BM025 = eastern Mesica granite gneiss. □ = K_1, Δ = K_2, ○ = K_3
B) The Flinn graph showing the shape of strain ellipsoid of Vumba granite gneiss. ■ =Vumba granite gneiss, ▲ = Messica granite gneiss.

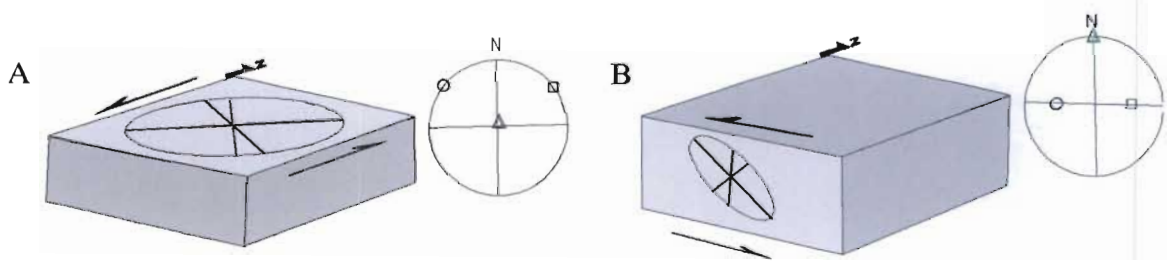

Figure 4.35 Sketch showing sinistral strike-slip model (A) and thrusting model (B) with respective stereographical diagrams (lower hemisphere). □ = K_1, Δ = K_2, ○ = K_3

In contrast to the above paramagnetic rocks, the reworked Messica granite gneiss contains high anisotropies indicating that the magnetic fabric was clearly acquired during solid-state deformation. The shape of AMS ellipsoid is oblate in all but two cases, so that the dominant fabric is planar due to shape of the biotite, which is parallel to the rare magnetite grains that are sometimes elongated (Olivier & Archanjo 1994). This strong north-south striking planar magnetic foliation is result of Pan-African deformation and relates to S/D_4 observed in the field.

One possibility that has to be considered is that the moderately plunging lineations of the ferromagnetic Messica granite gneiss are due to the steeply plunging lineations of the paramagnetic Messica granite gneiss rotating towards the horizontal in the proposed sinistral strike-slip regime. There are two arguments against this.

Firstly it is clear that the magnetic characteristics of the Messica granite gneiss changed when it was reworked. The "ferromagnetic" ellipsoid reflects a new fabric rather than the "paramagnetic" fabric being orientated into a new orientation. Consequently the "ferromagnetic" ellipsoid is due dominantly to Pan-African event rather than rotation of the older paramagnetic fabric.

Secondly the orientation of the contact between the Zimbabwe craton and the Moçambique Belt is north-south. The lineation in the reworked zone of southern and central traverses plunges moderately towards the north while the planar fabric strikes north-northwest. This geometry cannot be produced by sinistral strike-slip movement, but oblique dextral movement is a possibility.

Interpretation of the AMS data, however, cannot be considered in isolation. If major strike-slip movement had taken place in the reworked zone, the strain would have been dominantly due to simple shear. Given that the proposed strike-slip zone separates two major crustal provinces and that it contains a strong penetrative planar fabric, there should be numerous kinematic indicators showing the sense of movement but this is not the case as was stated by Manhiça *et al* (2001).

If the thrusting scenario is considered, the AMS data do not correspond to the situation shown in Figure 4.35. However, this situation represents the flat portion of a thrust system. If the ramp is considered (Figure 4.36), the K_1 axis would be subvertical, while K_2 and K_3 axes would be near horizontal. This geometry closely represents the results obtained in the reworked zone. The orientation of the K_1 lineation and weak planar fabric indicates that compression was more from the east-northeast rather than east-west. This implies that the deformation involved transpression and some component of dextral movement.

Without more detailed strain and AMS analysis it is not possible to be categorical about the exact nature of the deformation in the reworked zone. It is clear, however, that the deformation is not due to sinistral strike-slip movement. Consequently the evidence presented regarding the rotation of fabrics in the greenstone belt and granite gneisses may simply be a fortuitous situation. Elsewhere on the Zimbabwe craton, greenstone belts and their surrounding granitic rocks show such curvature, which is due to folding in the Archaean rather than Pan-African reworking.

In the study area itself, the AMS fabrics of the central traverse follow the margins of a small greenstone belt. This belt continues right to the zone of reworking without displaying any signs of being rotated or offset by strike-slip movement. The Mutare- Mutare-Manica belt is probably a similar situation. The curvature present at the eastern end of the belt is part of the Archaean deformation. In light of the structural work and the AMS results, the zone of Pan-African reworking is interpreted as involving east-west to east-

northeast transpression, which formed the strong planar fabric in the Messica granite gneisses and the development of duplexes in the Gairezi Group. During this deformation, the strain ellipsoids in the Messica granite gneiss were dominantly oblate with the weak lineation showing variable plunge through the area, possibly indicative of non-cylindrical folding. The two prolate ellipsoids come from the only sites where the Messica granite gneiss was flanked to the north and south by the Gairezi Group. Here it is possible that local variations in strain resulted in prolate strain.

4.8.4 CONCLUSIONS

In the study area, the western domains (A and B) represent regions of Archaean granite-greenstone basement overlain by the Proterozoic Umkondo Group. Deformation in the Umkondo Group is confined to brittle events whereas the Archaean rocks exhibit ductile and brittle deformation. The Vumba and western Messica granite gneisses in these domains have a paramagnetic characteristic with a well developed magnetic lineation but a weak planar fabric.

In the eastern domains, Domain C is characterised by a north to north-northwest striking subvertical planar fabric and a ferromagnetic signature to the eastern Messica granite gneiss. Taking in account structural features and AMS results, the eastern Messica granite gneiss can be considered being reworked during the Pan-African deformation by east-west to east-north-east compression. This event involved an element of transpression and may have included some slight dextral movement. There no evidence of a sinistral strike-slip zone between the Zimbabwe craton and the Moçambique Belt as proposed by Manhiça *et al.* (2001).

In Domain D the Gairezi Group stratigraphically underlies the Umkondo Group. In this domain, the Pan-African compression resulted in thin-skinned tectonics as the Gairezi Group was thrust westwards over the Umkondo Group. The Umkondo Group may be, itself, a large-scale nappe structure as it might be underlain by a thrust surface (Munyanyiwa, 1997) (Figure 4.37).

The eastern parts of Domains C and D consist of duplexes containing the Gairezi Group and the eastern Messica granite gneiss, over which the high grade Proterozoic Moçambique Belt (Domain E) was thrust westwards (Figure 4.37). During this Pan-African lower crustal rocks were transported to upper crustal levels. This thick-skinned event appears to have been the driving mechanism for all the other Pan-African deformation further west.

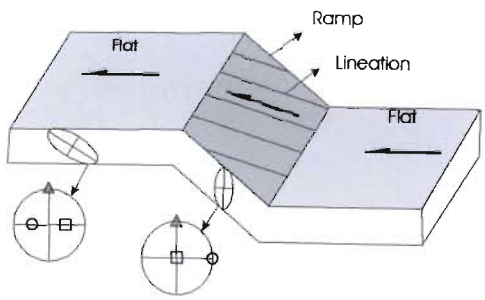

Figure 4.36 Sketch of the thrusting scenario showing the flat and ramp portions with respective stereographical diagrams (lower hemisphere). □ = K_1, Δ = K_2, ○ = K_3.

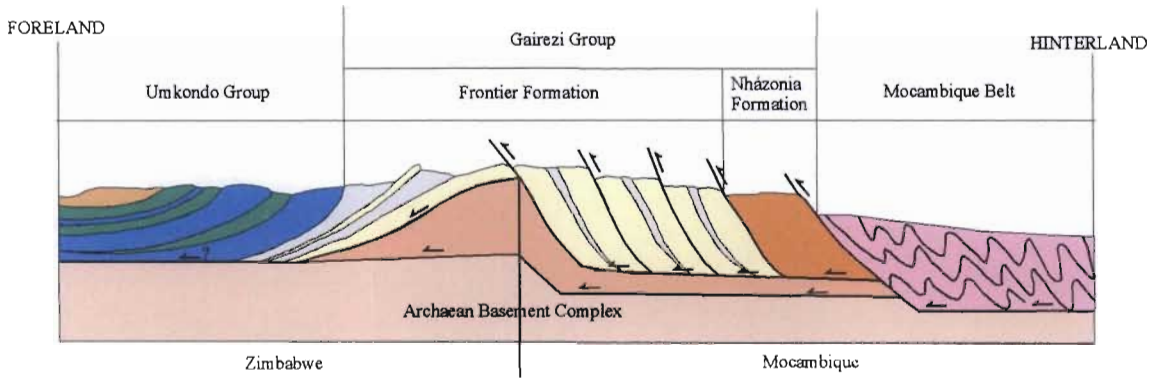

Figure 4.37 Schematic west-east cross-section between Umkondo Group and Moçambique Belt. Zimbabwe side from Watson (1969).

CHAPTER 5

METAMORPHISM

5.1 INTRODUCTION

Metamorphism in the study area is determined from petrographic data based on the presence or absence of specific mineral phases without considering in any quantitative detail the compositions of the minerals along P-T paths. Therefore the regional metamorphism studies are based on metamorphic mineral assemblages expected along typical P-T conditions.

The only previous geothermobarometry studies of the northern part of the study area have been done by Manhiça (1998). From this study was concluded that an eastward increase in the metamorphic grade has affected the Basement Complex in the northern part of the study area, as well as the younger sedimentary cover in the southern part. This is reflected by eastward change from the granite-greenstone terranes of the Zimbabwe Archaean Craton to the gneisses of the Báruè Complex of the Moçambique Belt and by the change from the psammites intercalated with shales of the Umkondo Group to the quartzite-schist complex and gneisses and schists of the Gairezi Group.

The aim of this chapter is to supplement previous work and to constrain the metamorphic history of the study area using petrographic, geothermometric and geobarometric data. For this purpose thin sections were first examined to determine critical metamorphic mineral assemblages for geothermobarometry. Geothermometry and geobarometry are the calculation of metamorphic temperatures and pressures of equilibration using the temperature and pressure dependence of the equilibrium constant as the basic yardstick (Spear, 1980).

Granite gneisses generally are devoid of suitable mineral assemblages. Therefore mafic enclaves were used. Umkondo and Gairezi quartzites do not contain suitable mineral assemblages. The pelites are less common and poorly exposed.

5.2 MINERAL CHEMISTRY

The relevant electron probe data are given in Appendix 5, in Tables: 5.1-5.7 (amphibole), 5.8-5.14 (plagioclase), 5.16-5.18 (garnet), 5.19-5.21 (biotite) and 5.24 (staurolite).

Plagioclase composition in the metabasites within the Vumba granite gneiss ranges from andesine to calcic andesine (An_{42-50}), in the Messica granite gneiss from andesine to labradorite (An_{40-67}).

Further eastwards, the plagioclase within the metabasites enclaves in the Tchinhadzandze gneiss is andesine (An_{41-42}) in composition, while those in the metabasites enclaves in the Nhansipfe megacrystic gneiss are oligoclase to calcic oligoclase (An_{22-28}). In the more felsic part of the study area, plagioclases of the gneisses are oligoclase (An_{16-22}) in composition within the Tchinhadzandze area and within Nhansipfe and Chimoio regions are oligoclase to calcic oligoclase (An_{20-25}) and (An_{23-24}) respectively.

Amphiboles in the metabasites and gneisses are characterised by $Na^{A} > 0.02$ atoms per formula unit (pfu), $Al^{VI} < 1.8$ pfu, Si in the range 6.0-7.7 pfu and $X_{an} < 0.90$. Amphiboles have $(Ca+Na) \geq 1.34$, $Na < 0.67$ and $Ca > 1.43$ indicating that the amphiboles are calcic (Leake, 1978).

The garnets of the metapelites show chemical zonation with Fe and Mg contents increasing and Mn and Ca contents

decreasing towards the rims (Figure 5.2). The garnets in the metapelites essentially consist of almandine (X_{Alm} = 0.683-0.747), while garnets from the mafic enclaves and the hornblende gneiss of the Nhansipfe megacrystic gneiss the garnets are dominated by both almandine and grossular (X_{Alm} = 0.657-0.663; X_{Gro} = 0.147-0.143) and (X_{Alm} = 0.639-0.619; X_{Gro} = 0.179-0.201) respectively.

An X_{Mg} varying between 0.530 and 0.528 generally characterizes the biotite in the metapelites and Ti contents close to zero (0.016-0.007) pfu. Within the mafic enclaves X_{Mg} of biotite varies from 0.411 to 0.412 and between 0.273 and 0.276 in the hornblende gneiss and Ti contents vary between 0.037 pfu and 0.041 pfu and from 0.045 pfu to 0.041 pfu respectively.

5.3 GEOTHERMOMETRY

Three geothermometers are used to determine the peak temperatures during metamorphism in the study area:

1) amphibole - plagioclase
2) garnet - biotite
3) garnet – amphibole

5.3.1 Amphibole – plagioclase

The amphibole-plagioclase geothermometer was applied to the hornblende-bearing metabasites (Figure 5.1):

- Vumba granite gneiss (TSE 12)
- Messica granite gneiss (BAN 03)
- Nhansipfe megacrystic gneiss (VAN 07)

and gneisses (Figure 5.1):

- Tchinhadzandze gneiss (BAN 08)
- Nhansipfe megacrystic gneiss (VAN 08, VAN 10)
- Chimoio gneiss (CHM 02).

This geothermometer has been calibrated by Spear (1981), Plyusnina (1982), Blundy & Holland (1990) and Holland & Blundy (1994). For the present study Holland & Blundy (1994) was used. As the amphiboles are classified as calcic according to the nomenclature proposed by Leake (1978) and they are in apparent textural equilibrium with plagioclase, they are suitable for the Holland & Blundy (1994) calibration. The thermometer takes into account non-ideal mixing in both amphibole and plagioclase according to the following end-members reaction (Holland & Blundy, 1994):

edenite + 4 quartz = tremolite + albite

with estimated uncertainties of around ± 35-40°C for rocks equilibrated at temperatures in the range 400-900°C.

The calculated temperature values show no great variations between core average and rim average, as shown in Table 5.15.

The west of the study area, in the Basement Complex, the amphibole-plagioclase thermometer calibration provides temperature values ranging from 619°C (core) to 627°C (rim) in the Vumba granite gneiss and within the Messica granite gneiss the temperature values vary between 664°C (core) and 662°C (rim).

Eastwards, within the Báruè Complex and around the Bandula region, the calculated temperatures vary between 681°C (core) and 671°C (rim) for sample BAN 08.

The Nhansipfe megacrystic gneiss that crops out around the Chigove mountain region yields temperatures ranging from 729°C (core) to 712°C (rim). Sample VAN 08, of the same area, gives temperature values between 729°C (core) and 741°C (rim). Sample VAN 10 yields the lowest

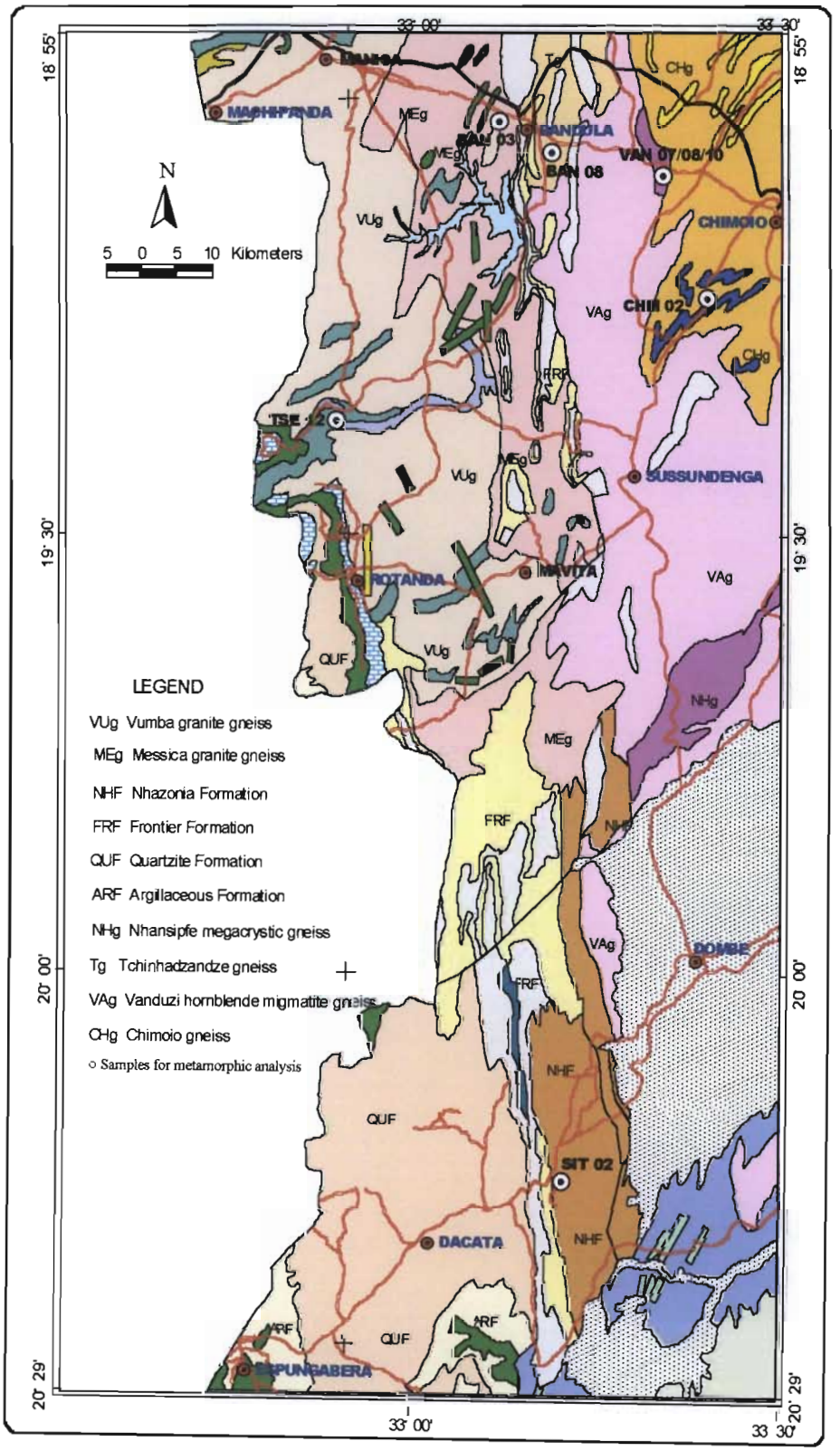

Figure 5.1 Geological map of western central Moçambique showing samples used for the metamorphic analysis.

Table 5.15 Calculated metamorphic temperatures using amphibole-plagioclase Holland & Blundy (1994) geothermometer calibration.

	K_D		X_{Ab}		X_{An}		Y_{ab}		T°C	
Sample	core	rim	core	rim	core	rim	core	rim	core	rim
TSE 12	0.198	0.198	0.523	0.526	0.471	0.470	-0.274	-0.301	**619**	**627**
BAN 03	0.331	0.260	0.478	0.421	0.520	0.578	0.270	1.030	**664**	**662**
VAN 07	0.036	0.041	0.737	0.723	0.242	0.259	0	0	**729**	**712**
BAN 08	0.060	0.070	0.786	0.779	0.203	0.213	0	0	**681**	**671**
VAN 08	0.036	0.033	0.739	0.742	0.245	0.243	0	0	**729**	**741**
VAN 10	0.054	0.044	0.773	0.764	0.213	0.223	0	0	**681**	**700**
CHM 02	0.016	0.015	0.755	0.753	0.233	0.236	0	0	**895**	**905**

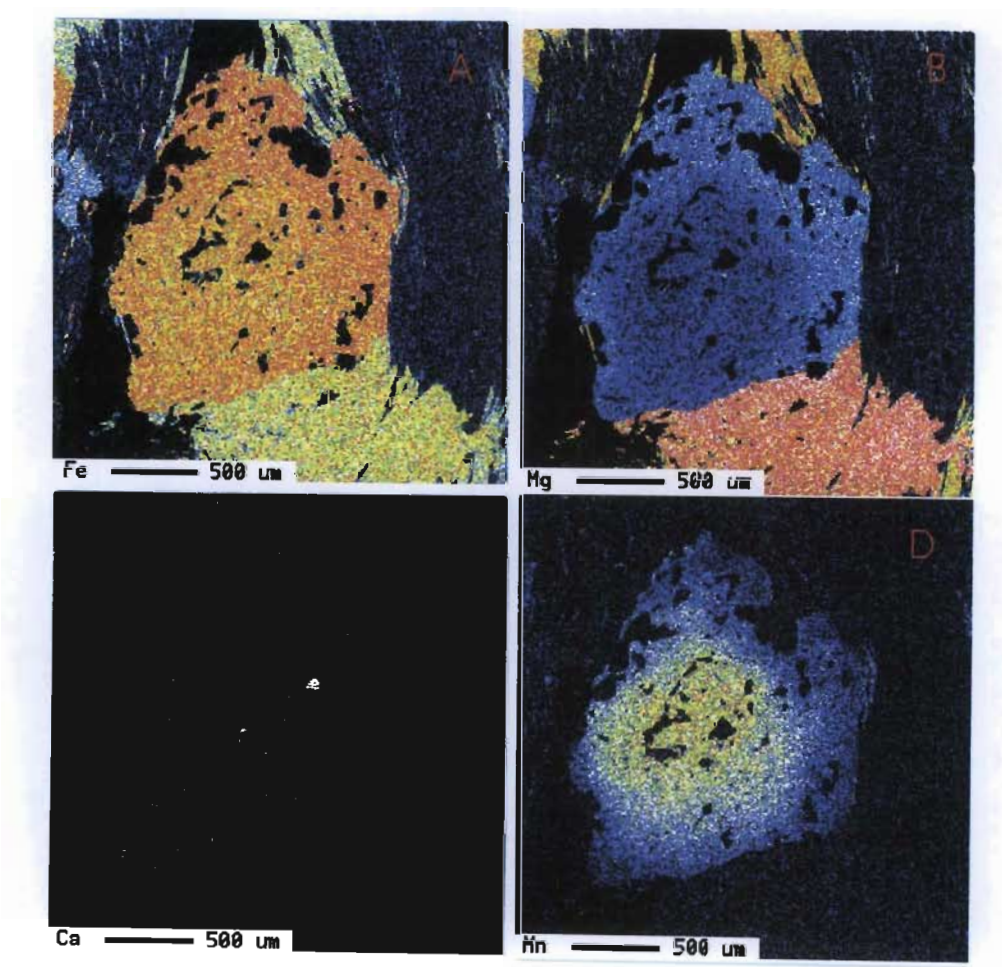

Figure 5.2 The garnet porphyroblast of staurolite-garnet-mica schist of the metapelites shows chemical zoning increasing from core to rim for Fe (A) and Mg (B) and decreases for Ca (C) and Mn (D).

temperature values of between 681°C (core) and 700°C (rim).

Near the eastern limit of the study area, estimated average temperatures for the Chimoio gneiss are higher, between 895°C (core) and 905°C (rim) as shown in Table 5.15.

5.3.2 Garnet-biotite

The garnet-biotite thermometer was applied to the staurolite-garnet-mica schist (SIT 02) of the Nhazónia Formation and to the mafic enclaves (VAN 07) and the hornblende gneiss (VAN 10) of the Nhansipfe megacrystic gneiss of the Báruè Complex (Table 5.22).

Many calibrations of the garnet-biotite geothermometer have been proposed, and in this study the following were used: Ferry & Spear (1978), Indares & Martignole (1985), Hoinkes (1986) and Dasgupta *et al* (1991) calibrations. All selected calibrations assume no pressure effect on Fe-Mg fractionation between garnet and biotite according to the continuous exchange reaction:

Fe^{2+}-garnet+Mg-biotite=Mg-garnet+Fe^{2+}-biotite

To avoid complications with Fe^{3+} in biotite as well as retrograde rim compositions only matrix biotite and garnet cores were considered in order to obtain the best estimate of prograde metamorphic temperatures (Chipera & Perkins, 1988).

The metapelites of the Nhazónia Formation (SIT 02) provide a wide range of temperatures using different geothermometer calibrations. The Ferry & Spear (1978) geothermometer calibration yields the lowest temperatures (430°C) whilst those of Hoinkes (1986) are highest (805°C). The Indares & Martignole (1985) and Dasgupta *et al.* (1991) geothermometer calibrations provide temperature values of 500°C and 535°C respectively (Table 5.22).

Only the Indares & Martignole (1985) and the Dasgupta *et al.* (1991) geothermometer calibrations yield realistic values for metapelites of amphibolite facies. These results are well constrained with metamorphic mineral assemblages (quartz + biotite + garnet + staurolite + plagioclase + chlorite) obtained by petrographic studies as shown in the Figure 5.3. Furthermore, these values are well constrained by similar pelitic metamorphic mineral assemblages in the Chimanimani mountain in Zimbabwe, indicating amphibolite metamorphic conditions of ~570°C and 5.7 kbar (Munyanyiwa, 1997).

On the other hand, Winkler (1979) demonstrated experimentally that in the metapelites of amphibolite facies staurolite appears at approximately 575°C and 8 kbar.

The Ferry & Spear (1978) geothermometer calibration for sample VAN 10 yields the lowest temperatures (620°C) and the results of Hoinkes (1986) geothermometer calibration are highest (890°C). The Indares & Martignole (1985) and the Dasgupta *et al.* (1991) thermometer calibrations indicate estimated temperature values of 756°C and 686°C respectively.

The temperature values of 686-756°C seem more reasonable and are well constrained with the amphibole-plagioclase Holland & Blundy (1994) geothermometer calibration, which gives temperature of between 681°C and 700°C for the same rock type (Table 5.15).

The low temperatures for sample VAN 10 obtained according to the Ferry & Spear (1978) thermometer calibration are most likely related to the non-ideal mixing of Fe and Mg in garnet and biotite solid solutions. The empirical overcorrection of Ca-effect in the garnet as well as ignoring the non-ideal mixing of Fe and Mg in biotite is probably responsible for the high values obtained by Hoinkes (1986).

Although this study only uses matrix biotites and garnet cores, the sample

Table 5.22 Calculated metamorphic temperatures using garnet-biotite geothermometer calibrations of Ferry & Spear (1978), Indares & Martignole (1985), Hoinkes (1986) and Dasgupta *et al.* (1991).

Samples	K_D	Grt_{XMg}	Bi_{XMg}	Grt_{XFe}	Bi_{XFe}	T°C FS	T°C IM	T°C H	T°C D *et al.*
	core	core	core	core	core	core	core	core	core
SIT 02	0.106	0.082	0.442	0.683	0.391	**430**	**500**	**805**	**535**
VAN 07	0.311	0.143	0.360	0.657	0.515	**830**	**900**	**850**	**860**
VAN 10	0.195	0.047	0.236	0.639	0.631	**620**	**756**	**890**	**686**

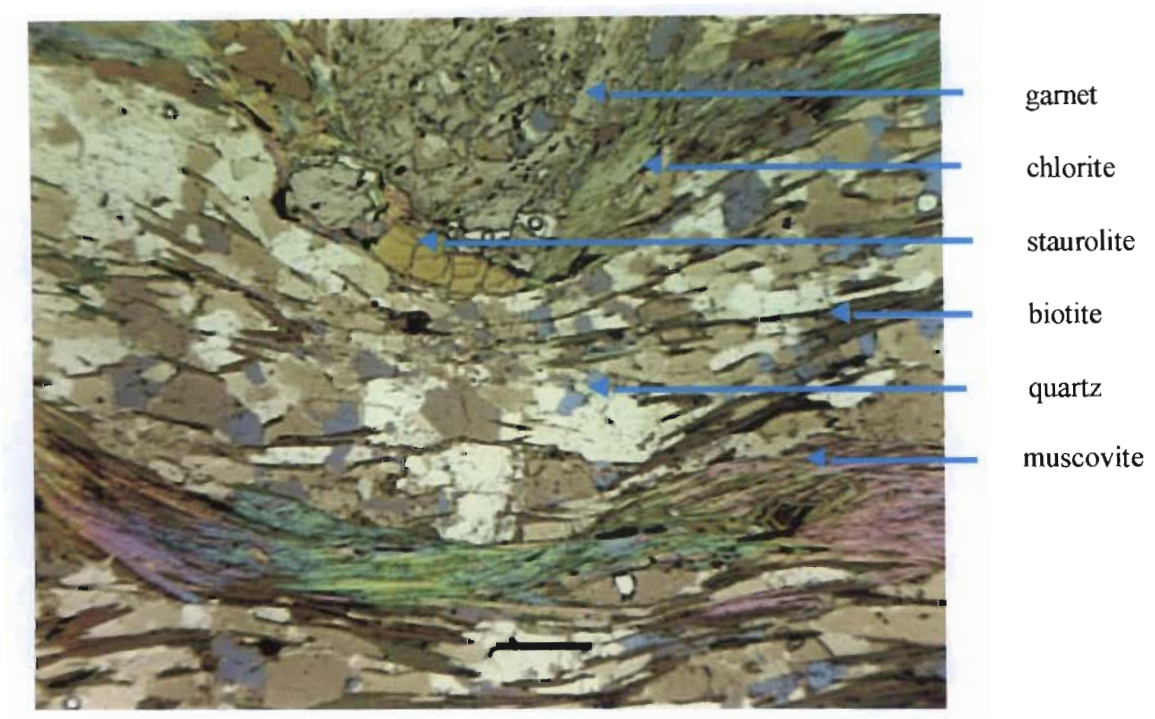

Figure 5.3 Characteristic metamorphic mineral assemblages of staurolite-garnet-mica schist of the Nhazónia Formation. Scale bar = 500 μm.(See Figure 5.1 for locality).

VAN07 still gives unrealistically high temperature values (830-900°C) for metamorphic mineral assemblages of amphibolite facies, even for the two preferred methods.

The relatively high estimated temperatures provide by all geothermometer calibrations for mafic enclaves are possibly due to the chosen matrix biotites being in contact with a ferromagnesian phase. Alternatively the mafic enclaves are may be dyke remnants, which were molten and exposed to high temperatures during metamorphism of Moçambique Belt.

5.3.3 Garnet-amphibole

The garnet-hornblende geothermometer calibration is based on Fe^{2+}-Mg exchange between garnet and amphibole, using the following continuous reaction (Graham & Powell, 1984):

Fe^{2+} - amphibole + Mg - garnet = Mg - amphibole + Fe^{2+} - garnet

The garnet-amphibole geothermometer was only applied to the VAN 07 and VAN 10 samples of the Nhansipfe megacrystic gneiss of the Báruè Complex (Table 5.23).

The lack of reactions rims between garnet and amphibole suggests that they are in petrographical and textural equilibrium (Figure 5.4).

The garnet is Mn-poor ($X_{Mn,grt} < 0.1$), with only a few samples being slightly higher than 0.1. The amphiboles with (Ca+Na) $\geq$ 1.34, Na < 0.67 and Ca > 1.43 are calcic according to the nomenclature of Leake (1978). These parameters satisfy the conditions required for using the garnet-amphibole geothermometer calibration.

In this study, all Fe_{Total} is present as Fe^{2+} in calculating Fe/Mg of the amphiboles, as it was demonstrated that the Fe^{3+}/Fe^{2+} ratio is invariable and significantly lower in those hornblendes coexist with garnet (Graham & Powell, 1984).

The Graham & Powell (1984) geothermometer calibration yields higher temperatures varying from 667°C (core) to 654°C (rim) for sample VAN 07 and lower temperatures for the VAN 10 sample from 592°C (core) to 582°C (rim) shown in Table 5.23

The lower values for sample VAN 10 are in all probability related to the relatively low X_{Mg} (0.047-0.041) as well as the Mg/(Mg+Fe) ratio, which varies between 0.068 and 0.062, and which is associated with the comparatively high X_{Mn} (0.135-0.139) in garnet.

The average temperature of ~677°C (core) given by the mafic enclave sample VAN 07 from the Nhansipfe megacrystic gneiss is consistent with petrographic data for metamorphic mineral assemblages (quartz + K-feldspar + plagioclase + biotite + garnet + hornblende) of the amphibolite facies. It also is constrained by the temperatures obtained from the amphibole-plagioclase geothermometer calibrations of Holland & Blundy (1994).

5.4 GEOBAROMETRY

Two geobarometer calibrations are used to determine the prevailing pressure conditions during metamorphism:

1) staurolite-garnet
2) garnet-hornblende-plagioclase-quartz.

5.4.1 Staurolite-garnet

The staurolite-garnet geobarometer calibration is based on equilibria between staurolite and garnet as the following reactions (Perchuk, 1991):

Table 5.23 Estimated temperature values using garnet-amphibole Graham & Powell (1984) geothermometer calibration for mafic enclave and hornblende gneiss of Nhansipfe megacrystic gneiss.

Sample	K_D		$X_{Ca,grt}$		$X_{Fe,grt}$		$X_{Fe,hb}$		$X_{Mg,grt}$		$X_{Mg,hb}$		T°C	
	core	rim	core	rim	core	rim	core	rim	core	rim	core	rim	core	rim
VAN 07	3.04	3.27	0.15	0.14	0.66	0.66	0.60	0.60	0.14	0.14	0.40	0.40	**677**	**654**
VAN 10	4.87	5.55	0.17	0.20	0.64	0.62	0.74	0.73	0.05	0.04	0.26	0.27	**592**	**582**

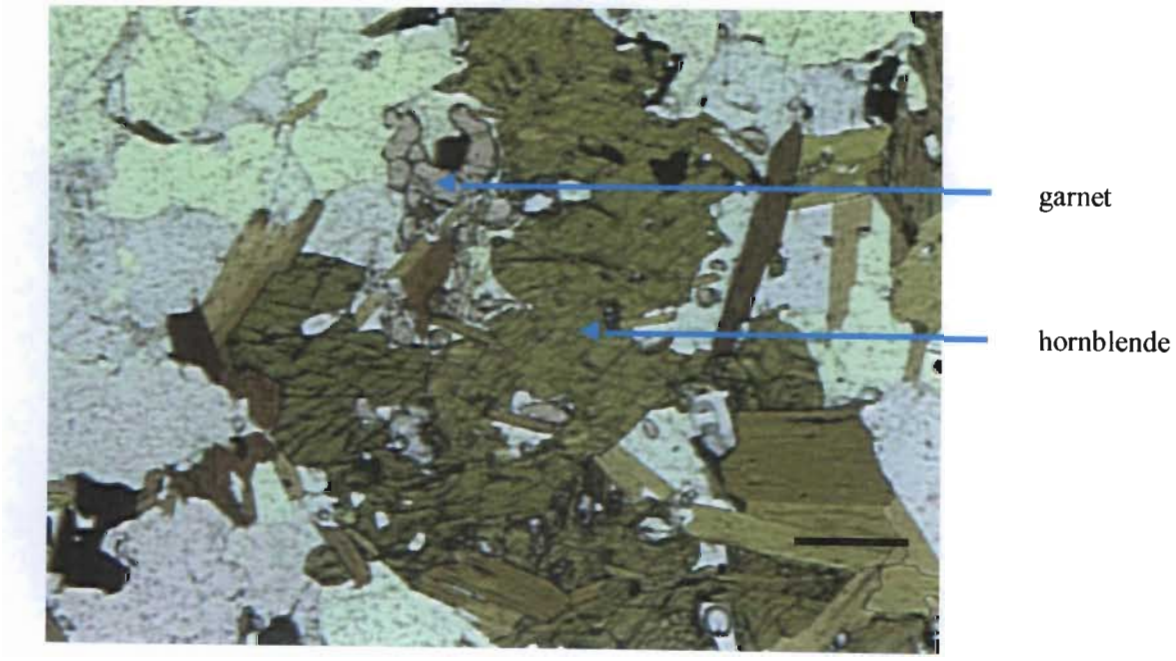

Figure 5.4 Hornblende gneiss of Nhansipfe megacrystic gneiss showing the petrographical and textural equilibria between garnet and amphibole. Scale Bar = 250 μm (See Figure 5.1 for locality).

$Gr_{Fe} + St_{Mg} = St_{Fe} + Gr_{Mg}$ (1)

and

$St + Qz + Mu = Bi + Gr + Al_2SiO_5 + H_2O$ (2)

The first of these equilibria depends only on temperature and mineral composition, the second on temperature, pressure and chemical potential of H_2O. The relationship of $\ln K_{D(Mg)}$ for equation (1) to inverse temperature was obtained for the parageneses in biotite + garnet + staurolite with the known mineral compositions.

From the compositions of the associations of equation (2) coexisting with staurolite, Perchuk (1991) established the relationship of $\ln K_{D(Mg)} = \ln(X_{Mg(St)}/X_{Mg(Gr)})$ for both pressure and temperature.

Applying the staurolite-garnet (Perchuk, 1991) geobarometer calibration to the staurolite-garnet-mica schist (SIT 02) values varying from 3.1 kbar to 5.5 kbar around the Sitatonga area (Table 5.25) have been obtained. These pressures are well constrained by a metamorphic mineral assemblage of amphibolite facies (quartz + biotite + muscovite + garnet + staurolite + plagioclase) for the metapelites. Furthermore, these values are well constrained by similar pelitic metamorphic mineral assemblages in the Chimanimani mountain in Zimbabwe, indicating amphibolite metamorphic conditions of ~570°C and 5.7 kbar (Munyanyiwa, 1997).

5.4.2 Garnet-hornblende-plagioclase-quartz

The geobarometer garnet-hornblende-plagioclase-quartz has been empirically calibrated by Kohn & Spear (1990), which is based on the equilibrium:

6 anorthite + 3 tremolite = 2 grossular + 1 pyrope + 3 tschermarkite + 6 quartz

and its Fe end-member equivalent.

The geobarometer was applied to the VAN 07 and VAN 10 samples of the Nhansipfe megacrystic gneiss of Báruè Complex, which contain appropriate assemblages (Figure 5.5).

For the Mg end-member, the geobarometer calibration gives higher estimated pressure values of around 9.8 kbar for both the mafic enclave (VAN 07) and the hornblende gneiss (VAN 10), while the Fe end-member calibration gives lower pressure values of around 7.5 kbar (Table 5.26).

5.5 DISCUSSION

The calculated temperatures values (619-664°C) within the granite-greenstone Archaean terrains suggest an increase from low amphibolite facies for the Vumba granite gneiss to medium amphibolite facies for the Messica granite gneiss (Figure 5.6).

Temperatures of 530°C and 570°C at < 4kbar were obtained by Manhiça (1998) for the Vumba granite gneiss using garnet-hornblende by Perchuck *et al.* (1985) and Graham & Powell (1984) respectively. This suggests that there was an increase in the prevailing P-T conditions from greenschist facies to amphibolite facies near the Zimbabwe-Moçambique border.

Taking into account the similar ages of the Vumba granite gneiss (biotite $^{40}Ar/^{39}Ar$ age of 1084 ± 4-1064 ± 4 Ma), the Chimoio gneiss ($^{207}Pb/^{206}Pb$ age of 1108 ± 12 Ma), and the Nhansipfe megacrystic gneiss ($^{207}Pb/^{206}Pb$ age of 1112 ± 12 Ma) obtained by Manhiça (1998) it is proposed that the emplacement of the Báruè Complex was related to a continental collision environment during the Kibaran orogeny, which is most likely responsible for increasing metamorphism and deformation within the granite-greenstone terrains of Archaean age.

Table 5.25 Calculated metamorphic pressure of metapelites using the staurolite-garnet Perchuck (1991) geobarometer calibration.

Sample	$X_{Mg,St}$		$X_{Mg,Gr}$		$X_{Mg,Bi}$		P Kbar	
	core	rim	core	rim	core	rim	core	rim
SIT 02	0.175	0.174	0.094	0.59	0.530	0.528	**3.1**	**5.5**

Table 5.26 Calculated metamorphic pressure of mafic enclave and hornblende gneiss using the Kohn & Spear (1990) geobarometer calibration for the assemblage garnet + hornblende + plagioclase + quartz.

Sample	K_{eq1}		X_{Prp}		X_{Alm}		X_{Sps}		X_{Grs}		P_{Mg}		P_{Fe}	
	core	rim	core	rim	core	rim	core	rim	core	rim	core	rim	core	rim
VAN 07	8.84E-06	2.96E-06	0.14	0.14	0.66	0.66	0.05	0.06	0.15	0.14	**9.8**	**9.8**	**7.5**	**7.5**
VAN 10	1.02E-08	6.14E-09	0.05	0.04	0.64	0.62	0.14	0.14	0.18	0.20	**9.8**	**9.8**	**7.5**	**7.5**

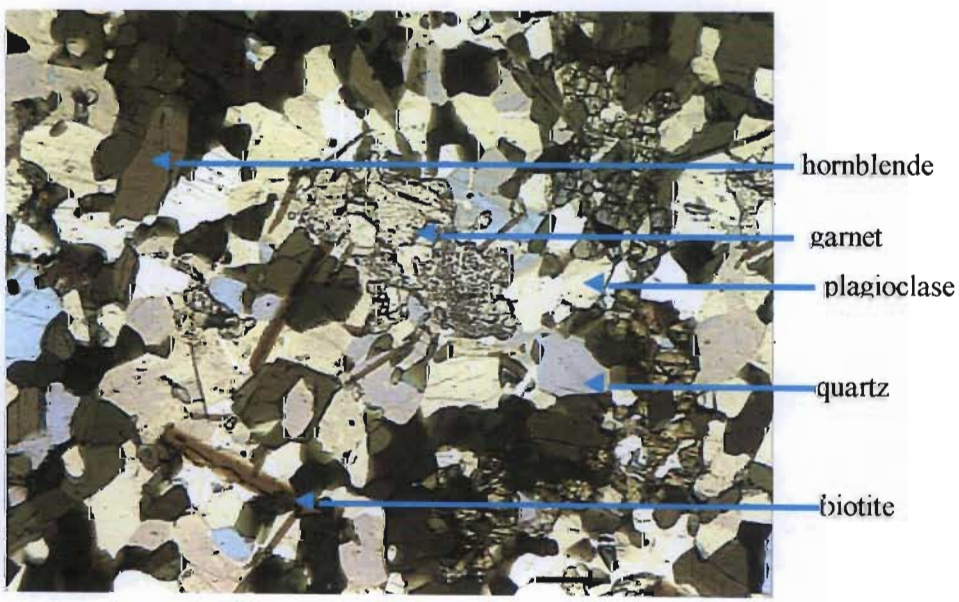

Figure 5.5 Mafic enclave of Nhansipfe megacrystic gneiss of Báruè Complex showing metamorphic mineral assemblages. Scale bar = 250 μm (See Figure 5.1 for locality).

Within the Báruè Complex the temperatures increase eastwards, as around the Bandula region the calculated temperatures are 670±35 - 680±35°C and in the Nhansipfe region the temperatures are 680±35 - 740±35, whereas around Chimoio region the temperatures are 900±35 - 905±35°C suggesting amphibolte/granulites facies metamorphism (Figure 5.6).

The calculated pressure of between 7.5-9.8 kbar (Figure 5.6) indicates that the amphibolite and granulite facies terrains were formed under medium to high pressure, suggesting an origin from deeper crustal levels (~30 Km). This observation is well constrained by geochemical studies, which suggest a mixed (crustal and mantle) origin of the magma.

The relatively similar biotite $^{40}Ar/^{39}Ar$ ages of 535-460 Ma (Manhiça 1998) for the Messica granite gneiss, Chimoio and Nhansipfe gneisses as well as the Chicamba quartzites (Vail, 1965), suggest that these formations were affected by the Pan-African event (~500 Ma), where the P-T conditions increased to granulite facies in the easternmost part of the study area.

It is significant to note that these younger Pan-African ages coincide with areas with a strong planar N-S fabric, which reflects a Pan-African reactivation along specific zones.

In the south of the study area where the terrain is dominated by metasedimentary rocks, the metamorphic mineral assemblages indicated by petrographic studies, combined with the geothermometer and geobarometer results, suggest an increase of P-T conditions from greenchist facies in the west (around the Espungabera region) to amphibolite facies in the east (Sitatonga region).

Nevertheless this preliminary study shows that it is difficult to place quantitative limits on P-T paths from east to west within the study area due to a lack of suitable geothermometer and geobarometer metamorphic mineral assemblages.

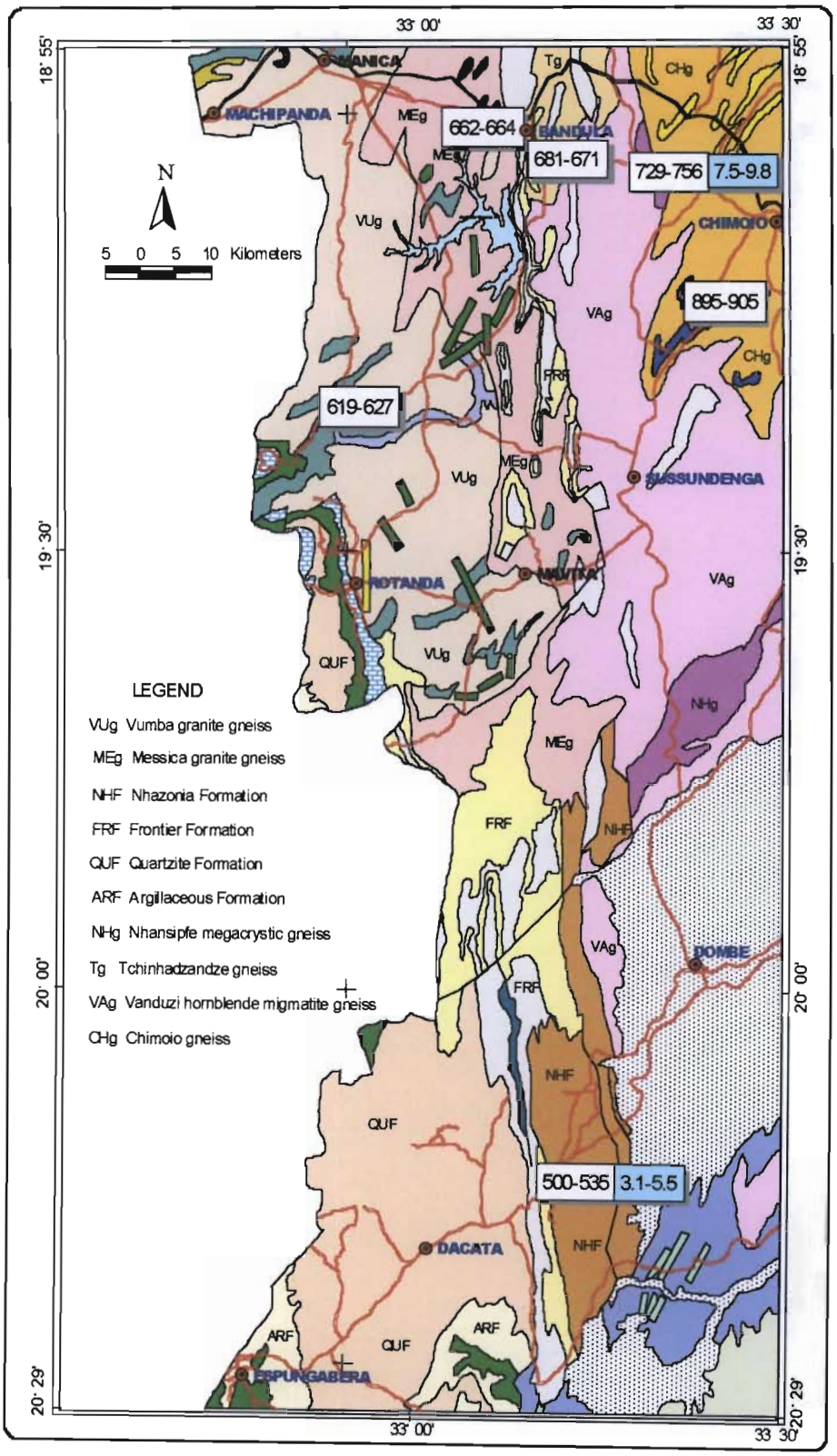

Figure 5.6 Geological map of western central Moçambique showing the calculated temperatures and pressures.

CHAPTER 6

GEOCHRONOLOGY

6.1 INTRODUCTION

There has been great controversy about the relationship between the Gairezi and Umkondo Groups. Tyndale-Biscoe (1957), Vail (1962), Johnson (1963) suggested that Gairezi and Umkondo Groups were deposited contemporaneously in the same sedimentary basin. Due to a combination of sedimentary facies changes and subsequent tectonic and metamorphic modification they differ in appearance. In contrast, Watson (1969) suggested that the Gairezi and Umkondo Groups are separate basins, with the latter being young. The Nhazónia Formation of the Gairezi Group has been interpreted as being older than the Frontier Formation (Afonso, 1978).

The age of the Umkondo Group has been a subject of several publications. The best estimated age of crystallisation of the sill based on data for baddeleyite and the four most concordant zircons (1099 ± 9 Ma) yields a weighted mean of 1105 ± 5 Ma (Wingate, 2001). As the uppermost Umkondo contains volcanic rocks, which are considered contemporaneous with the sills this age suggests that the Umkondo sediments were been deposited at the same time as the Kibaran orogeny. However there are no precise age determinations of Gairezi group metasediments, which is the challenge of this chapter. Previous geochronology studies done by Vail (1965) on muscovite of Chicamba Real Dam quartzites, where he obtained the K-Ar age of 465 ± 20 Ma. This dates metamorphism, representing the final stage of Pan-African event.

The advantage of SHRIMP over conventional (ID-TIMS, multi-grain or even single grains analysis) means of zircon analysis is the ability to target zones within crystals at the 20-30 μm scale, and so address histories of inheritance, magmatism, metamorphism, and alteration at a scale approaching that at which crystals grow (Claoué-Long *et al.*, 1995).

This chapter attempts to discuss the depositional age and provenance of the Proterozoic sediments as well as different tectonometamorphic events and hence assists in the interpretation of the tectonic evolution of the region. As Nelson (2001) observed it might be based on analyses obtained from a few grains, a single grain, or even a single analysis. The new precise, SHRIMP U-Th-Pb ages of zircon from the Nhazónia Formation gneisses and Frontier Formation metapelites clarify the correlation between two controversial units: *viz.* the Gairezi Group and Umkondo Group. This has profound implications for understanding the crustal evolution between early Archaean and early Palaeozoic times of western central Moçambique and consequently the evolution of Rodinia and Gondwana.

For this purpose five rock samples were selected for U/Pb Sensitive High Resolution Ion Microprobe (SHRIMP) analyses of detrital zircons. A mica-schist (BB16), and a quartzite (BB18) of the Frontier Formation were collected from Chicamba Real Dam area. From the Sitatonga Range region a mica-schist (BB39) and a red quartzite (BB40) of the Frontier Formation, and quartzofeldspathic gneiss (BB38) of the Nhazónia Formation (Figure 6.1) were collected.

For the provenance study spot analyses were conducted on the detrital zircon grains, whereas the metamorphic overgrowths were used to determine the ages of metamorphism and deformation events of metasediments.

To understand the age and nature of the possible sources, the SHRIMP analyses are plotted on Wetherill U-Pb concordia diagrams. In order to estimate the most likely ages, proportions and number of distinct groups the data are also plotted as combined histogram and cumulative probability curve diagrams. Unfortunately many of the zircons analysed from these samples were altered and/or metamict, resulting in high common Pb and/or severe discordance in some analyses. These factors introduce some uncertainty into the calculated ages of the individual U-Pb and Pb/Pb analyses, and a decision has to be made on which analyses should be included in the final assessment of populations. Although interpretation is assisted by the fact that most discordant analyses plot on apparently coherent discordia trends (albeit with some scatter) with geologically reasonable lower intercepts (e.g. relating to Kibaran or Pan-African tectono-metamorphism) it is possible that they have suffered repeated Pb-loss at different times, and so only those analyses which are most concordant are used to define sub-populations in the combined histogram/cumulative probability plots. Zircons with very high common Pb contents (or the order of 5% or more) were excluded from the final data assessment, and usually an arbitrary cut-off of 10-15% discordance is applied (depending on the total number of analyses available). The ages quoted are $^{207}Pb/^{206}Pb$ ages unless stated otherwise. $^{206}Pb/^{238}U$ ages are considered more reliable for younger (<800 Ma) zircons as the measurement of ^{207}Pb is very imprecise in this younger age range.

All analyses were aimed to be random in order to eliminate the possibility of pre-selection of a particular sub-population. As a result many discordant grains were analysed.

6.2 SHRIMP RESULTS

6.2.1 MICA-SCHIST (BB16)

Zircons from a mica-schist of the Frontier Formation of the Gairezi Group are subhedral to anhedral in form, a few are rounded and many fragmented. This is clearly an heterogeneous population. Most of them are pitted and exhibit different sizes, showing high percentage of dark inclusions. Some of zircon grains show damaged and broken edges, which are most likely related to the sample preparation process.

Forty-four grains of sample BB16 were analysed and the SHRIMP U-Th-Pb isotopic data are presented in Table 6.1 (Appendix 6) and plotted on a conventional Wetherill U-Pb concordia diagram (Figure 6.2b), and as a combined cumulative probability curve and histogram diagram (Figure 6.2c). Although many analyses show significant and probably episodic radiogenic Pb-loss, there are a number of concordant or near-concordant analyses, which appear to be representative of the general population.

Only data, which are less than 15% discordance, are plotted on a histogram/cumulative probability diagram, minimising the uncertainty in the $^{207}Pb/^{206}Pb$ ages (Figure 6.2c). Thirteen (13) spot analyses plotted on the histogram diagram show three distinct groups. Examples of single spot analysis are shown on cathodoluminescence images (Figure 6.2a).

Zircons of the predominant group are rounded, showing the effects of extensive mechanical abrasion during the erosion/transportation/depositional process. They have moderate to low U concentrations (<476 ppm) and Th (<429 ppm), and high Th/U ratios (up to 1.69), suggesting detrital igneous zircons. These grains are less than 200 μm in size, and are generally structured, being characterized by rounded cores and irregular overgrowths Which appear to have formed in situ, in all probability during post-depositional tectonometamorphic processes irregular overgrowths, suggesting that they might

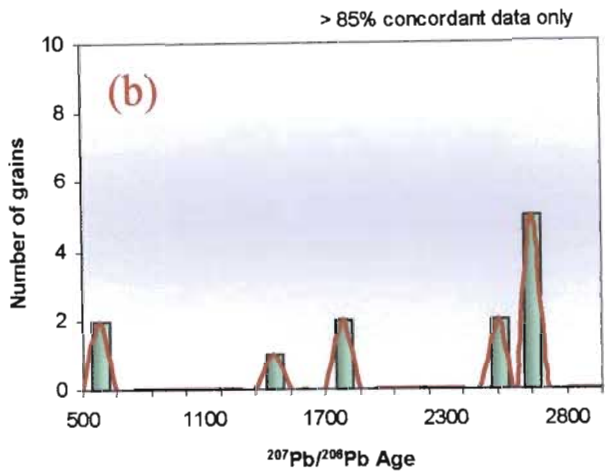

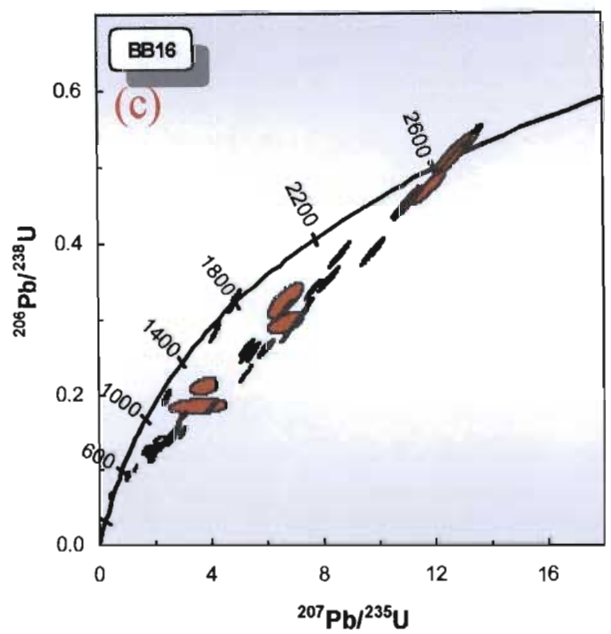

Figure 6.2 (a) Cathodoluminescence images of selected zircons from mica-schist (BB16). (b) Histogram diagram and cumulative probability curve plot of SHRIMP analyses for the sample BB16 (>85% concordant). (c) The U-Pb concordia plot of zircon analyses.

have formed *in situ* in all probability during metamorphic and deformation process. The cores give late Archaean ages (2658 ± 12-2475 ± 9.4 Ma), representing most likely the crystallization of source rocks. The overgrowths, where they appear, are too small and altered to analyse.

Zircons of the second group are also characterized by rounded habit. The U and Th contents as well as Th/U ratio are higher than the predominant group. Zircon cores from this group yielded Palaeoproterozoic $^{207}Pb/^{206}Pb$ ages ranging between 1805 ± 18 Ma and 1763 ± 11 Ma. One of zircons gives a $^{207}Pb/^{206}Pb$ age of 1430 ± 33 Ma, but this grain is highly altered and the analysis is 14% discordant and must be considered a minimum age. No other grains of this apparent age were found and this single "age" must be treated with caution.

Zircons of the third group are elongated, subhedral and anhedral with slight zoning and structureless domains. Some of the grains show overgrowths with extremely high U contents (up to 4377 ppm) and low Th contents (83-84 ppm) and relatively low Th/U ratios (0.03-0.02) suggesting either a metamorphic origin or extreme radiogenic Pb-loss. They provide following $^{206}Pb/^{238}U$ ages: 523 ± 14 Ma (grain 30) and 531 ± 14 Ma (grain 43.1). These ages are interpreted as being related to the final Pan-African event.

6.2.2 QUARTZITE (BB18)

Zircons from quartzite rocks of the Frontier Formation of the Gairezi Group are subhedral, anhedral, fragmented, and rounded, showing a heterogeneous population. Most of zircons are pitted from the transportation and sedimentation cycle with others showing damaged and broken edges, which are most likely related to the sample preparation process.

Fifty-three grains of quartzite were analysed and the SHRIMP results are provided in Table 6.2 (Appendix 6) and plotted on a conventional Wetherill U-Pb concordia diagram (Figure 6.3b), and as a combined cumulative probability curve and histogram diagram (Figure 6.3c). Three of them were rejected because they have very high common Pb contents (with $^{206}Pb_C$ percentage between 5.12 and 8.02). The overall trend of the data follows a discordia plot (with scatter) between an upper age defined by concordant data at about 2633 ± 9.7 Ma (analysis 24.1) and a lower age of 498 ± 14 Ma (the $^{206}Pb/^{238}U$ age for analysis 48.1).

Thirteen (13) spot analyses with <15% discordance were plotted on a combined histogram/cumulative probability plot (Figure 6.3b), resulting in three individual age subpopulations. Examples of single spot results are shown on cathodoluminescence images on the Figure 6.3a.

Zircons of the predominant age population are characterized by rounded habit with round terminations, and are small in size (<200 μm). They do not generally show strongly developed zoning and overgrowths. They exhibit relatively low U contents (<252 ppm), high Th content (up to 296 ppm) and high Th/U ratio (up to 1.79), probably representing original igneous zircons from rocks of a more basic composition? Cores of these zircons give late Archaean ages (2653 ± 14 to 2470 ± 42 Ma), which are interpreted to be related to the crystallization ages of possible source rocks.

The second group consists of only a single near concordant analysis (spot 18.1 which is 4% reverse discordant) and gives a $^{207}Pb/^{206}Pb$ apparent age of 1073 ± 25Ma. There are several more discordant analyses, which also appear to have $^{207}Pb/^{206}Pb$ ages in this vicinity. These zircons are variable in shape, size and state of preservation and appear to be overgrown by dark, metamict metamorphic zircon. The spot analysed in grain #18 appears to be within a relatively

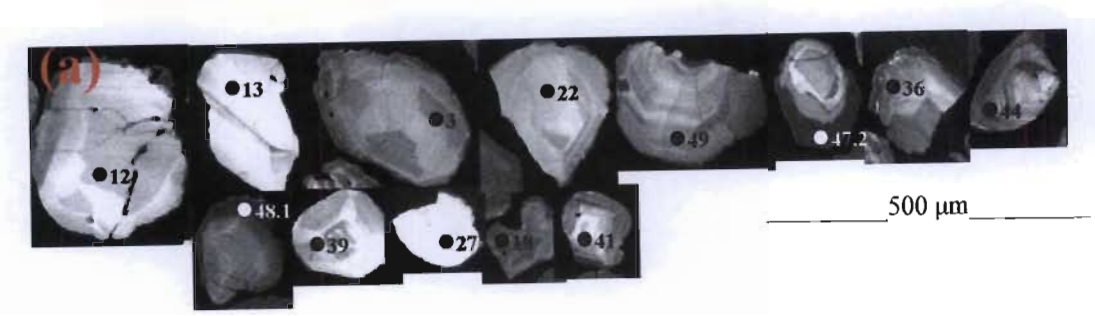

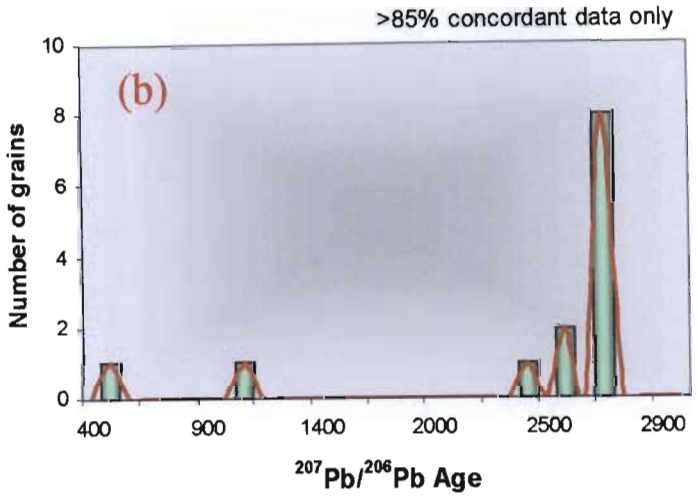

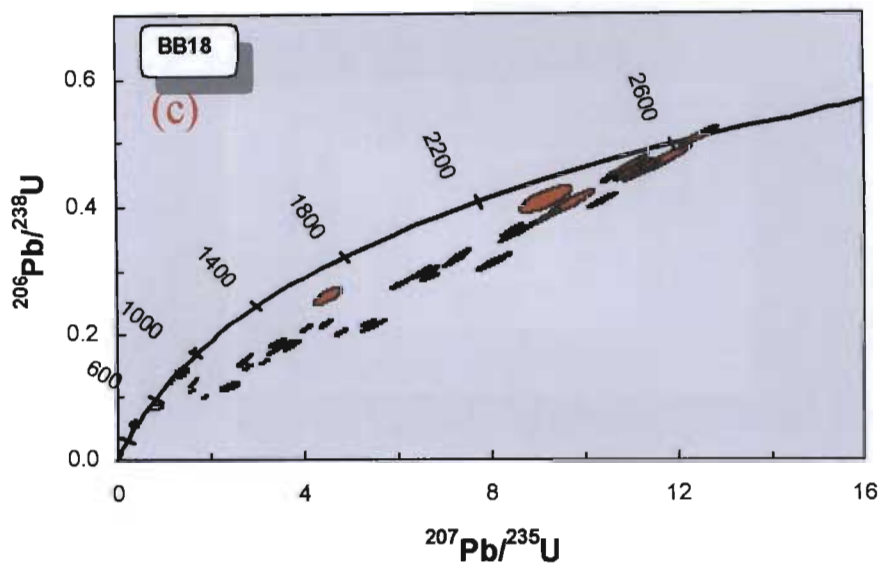

Figure 6.3 (a) Cathodoluminescence images of selected zircons from sample BB18. (b) Histogram diagram and cumulative probability plot of SHRIMP analyses for quartzite (>85% concordant). (c) The U-Pb concordia plot of zircon analyses.

bright (in Cl) zone of very patchy zircon that appears to be altered or recrystallised (and then overgrown by the darker metamorphic zircon). The zone analysed is interpreted to be a highly altered original metamorphic growth zone probably associated with the Moçambique belt orogeny around Chicamba Real Dam region. It is not considered to be from the detrital population.

The third age of significance to come out of this data set comes from small rims of metamorphic growth on rounded detrital grains. The rim on grain 48.1 is a classic example and gives an extremely high U content (1264 ppm), low Th concentration (34 ppm) and extremely low Th/U ratio (0.03) typical of metamorphic zircon. This rim gives a $^{206}Pb/^{238}U$ age of 498 ± 14 Ma and relates to the Pan-African orogeny.

6.2.3 MICA-SCHIST (BB39)

Zircons from the mica-schist of the Frontier Formation around the Sitatonga Range region are all rounded with some elongated forms, and sizes ranging between 60 μm and 250 μm. The overall impression is of a homogenous population of zircon grains. These zircons show extensive mechanical abrasion related to the depositional process.

The SHRIMP U-Th-Pb isotopic data are presented in Table 6-3 (Appendix 6) and are plotted on a Wetherill U-Pb concordia diagram (Figure 6.4b), and a cumulative probability curve and histogram diagram (Figure 6.4c). The U-Pb concordia plot of SHRIMP analyses for BB39 reveals radiogenic Pb-loss, however concordant or near- concordant data yield $^{207}Pb/^{206}Pb$ ages from3283 ± 6.4 Ma to 2015 ± 15 Ma.

Twenty-five (25) spot analyses (<10% of discordant) are plotted on histogram diagram and they reveal two distinct groups. Examples of single spot results are shown on cathodoluminescence images (Figure 6.4a).

All zircons are characterized by rounded and elongated habit, some of them pitted. The surfaces are abraded, suggesting that they suffered a prolonged transport process before deposition. Zircon grains have low U contents (73-425 ppm), low to moderate Th concentrations (42-349 ppm), and moderate to high Th/U ratios (0.19-1.85). They show weak or no zoning and overgrowths. These zircons are interpreted to be detrital magmatic zircons from a heterogenous source.

The predominant group yields late Archaean ages (2727 ± 6.1-2453 ± 9.1 Ma), and followed by early Archaean ages (3283 ± 6.4-2858 ± 7.4 Ma), representing the crystallization ages of the zircon grains in the possible source rocks.

A single zircon grain with low U (115 ppm) and Th contents (42 ppm) yields a $^{207}Pb/^{206}Pb$ concordant age of 2015 ± 15 Ma.

6.2.4 QUARTZITE (BB40)

All zircons from quartzite rocks of the Frontier Formation of the Gairezi Group around the Sitatonga Range are generally rounded with abraded terminations, although some are fragmented. They exhibit different sizes varying between 60 μm and 500 μm with abraded surfaces suggesting prolonged transport before deposition.

In all, fifty-six grains were analysed and the SHRIMP results are presented in Table 6-4 (Appendix 6) and plotted on a Wetherill U-Pb concordia diagram (Figure 6.5b), and a cumulative probability curve and histogram (Figure 6.5c).

Grains with high U content and high Th content are highly discordant. The U-Pb concordia diagram recorded concordant or near-concordant ages between 3276 ± 7.1 Ma and 2057 ± 11 Ma.

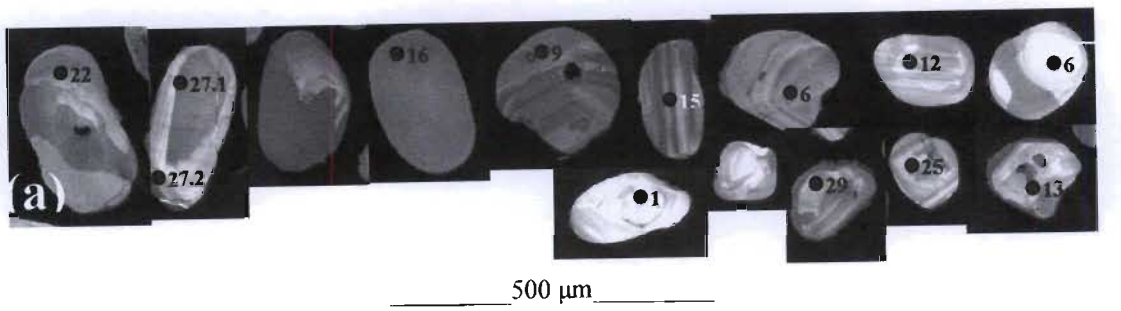

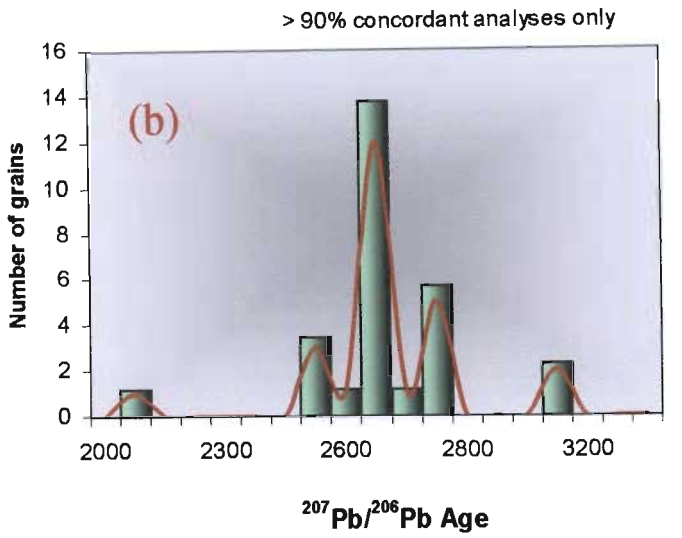

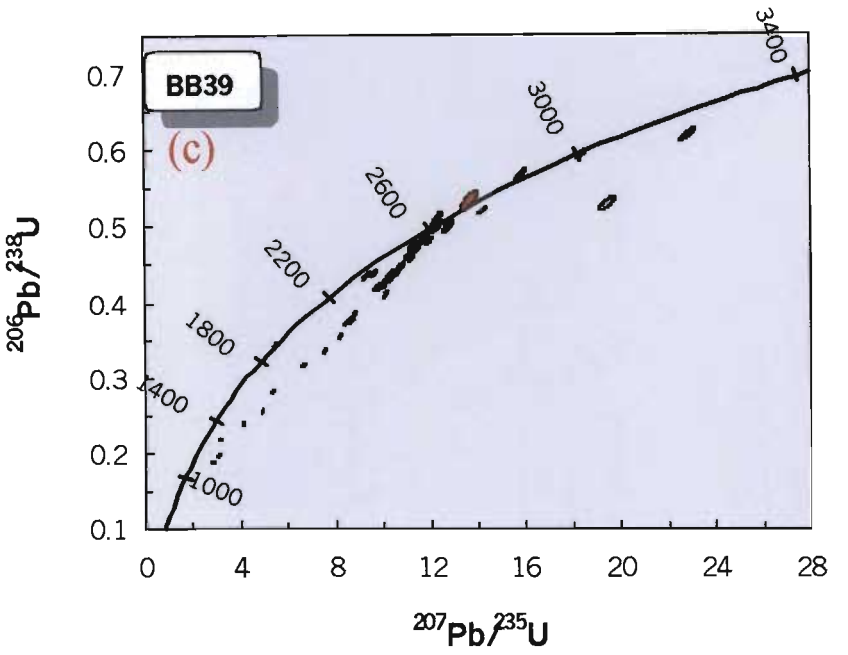

Figure 6.4 (a) Cathodoluminescence images of selected zircons from mica-schist (BB39). (b) Histogram diagram and cumulative probability plot of SHRIMP analyses for the sample BB39 (> 90% concordant). (c) The U-Pb concordia plot of zircon analyses.

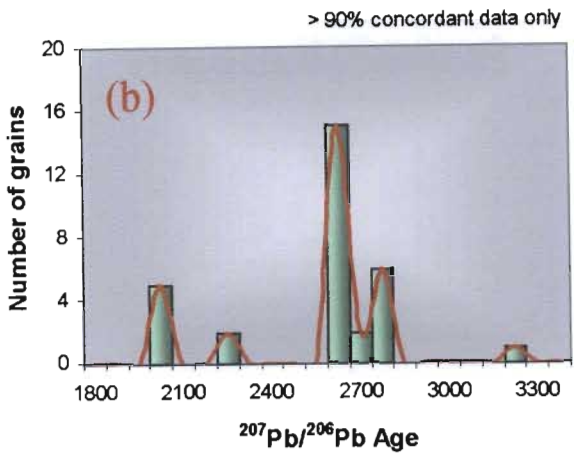

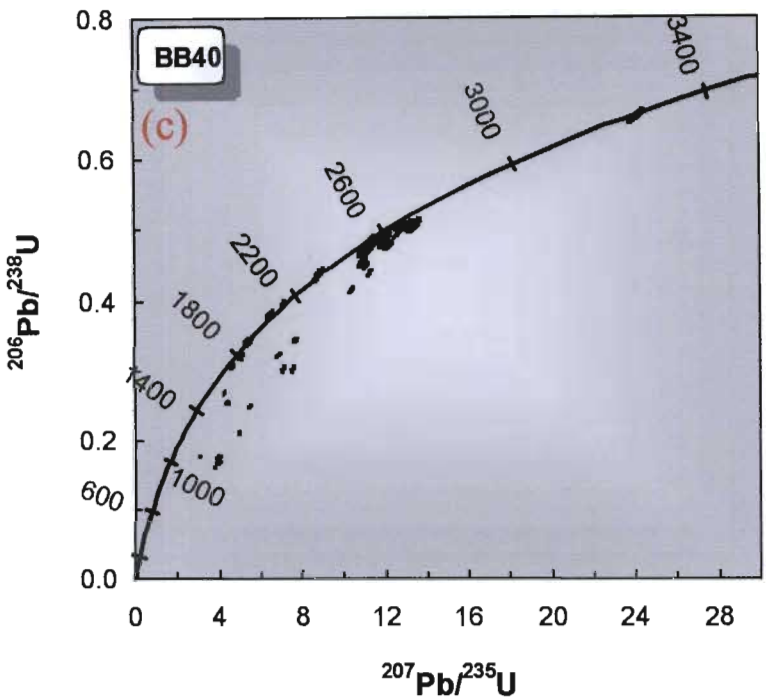

Figure 6.5 (a) Cathodoluminescence images of selected zircons from quartzite (BB40). (b) Histogram diagram and cumulative probability plot of SHRIMP analyses for quartzite (> 90% concordant). (c) The U-Pb concordia plot of zircon analyses.

Thirty-one (31) spot analyses with uncertainties 90% confidence limits are plotted on a combined histogram and cumulative probability diagram (Figure 6.5b), showing three distinct age populations. Examples of single spot results are shown on cathodoluminescence images on the Figure 6.5a.

All zircons are characterized by rounded and elongated habit, some of them pitted. The surfaces are abraded, suggesting a prolonged transport process before deposition. Zircons have variable U contents (49-558 ppm), low-to-moderate Th concentrations (25-250 ppm), and record high Th/U ratios (0.30-1.53). These zircons are interpreted as detrital igneous zircons from variable sources.

The predominant ages vary between 2791 ± 14 Ma and 2690 ± 13 Ma, following by second group provides ages from 2384 ± 15 Ma to 2043 ± 25 Ma. The oldest zircon yields age of 3275± 7.1 Ma with 99% concordance making the result reliable.

6.2.5 PARAGNEISS (BB38)

Most zircons from gneisses of the Nhazónia Formation around the Sitatonga Range are rounded and somewhat elongated with sizes (longest dimension) ranging between 60 μm and 200 μm. They are variably zoned to structureless and occasionally have overgrowths. A few have broken anhedral habit, are semi-opaque to opaque and are pitted. Generally they show extensive mechanical abrasion suggesting a prolonged transport effect before depositional process.

The SHRIMP U-Th-Pb results of forty grains are presented in Table 6-5 (Appendix 6) and plotted on a conventional Wetherill U-Pb concordia diagram (Figure 6.6b), and a cumulative probability curve and histogram diagram (Figure 6.6c). The concordant or near-concordant data record $^{207}Pb/^{206}Pb$ ages between 2718 ± 5.9 Ma and 1182 ± 33 Ma.

Forty spot analyses of thirty-nine grains were analysed but only 24 (<10% of discordant) were plotted on histogram diagram and they reveal four distinct groups. Examples of single spot results are shown on cathodoluminescence images (Figure 6.6a). The zircon grains with moderate U contents (155-464 ppm), moderate Th concentrations (101-382 ppm) and moderate Th/U ratios (0.47-0.94) are considered detrital zircons. All zircon grains of the predominant group are characterized by well-rounded habit with dark overgrowth and spherical core. Cores yield late Archaean ages ranging between 2718 ± 5.9 Ma and 2632 ± 8.4 Ma.

Subhedral and rounded zircons with relatively low-Th contents (95-156 ppm) and moderate Th/U ratios (0.41-0.47) give a $^{207}Pb/^{206}Pb$ age between 2133 ± 7.5 Ma and 2035 ± 11 Ma. The concordant ages of different populations from 2718 ± 5.9 Ma to 2035 ± 11 Ma are interpreted as ages of source rocks.

The following group are characterized by rounded habit, zoning and structureless domains. The zircons of this group are characterized by low to moderate U contents (96-447 ppm) and low to moderate Th concentrations (62-473). Few of them are spherical with no clear structure. They provide core and rim $^{207}Pb/^{206}Pb$ ages between 1884 ± 13 Ma and 1703± 12 Ma.

The zircon grains of third group are rounded and zoned with spherical core, suggesting metamorphic core. These grains zircons analysed yielded minimum $^{207}Pb/^{206}Pb$ ages (1307 ± 30 Ma–1182 ± 33 Ma), which are understood as the record of Moçambique Belt orogeny event around this area.

The Pb-loss is most likely related to The Kibaran orogeny and is more accentuated in the zircon grains with subhedral to anhedral

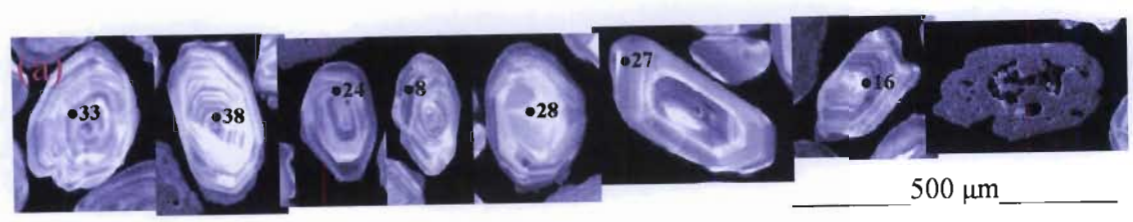

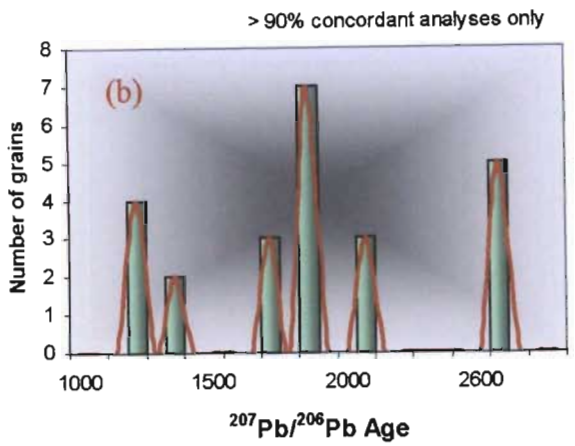

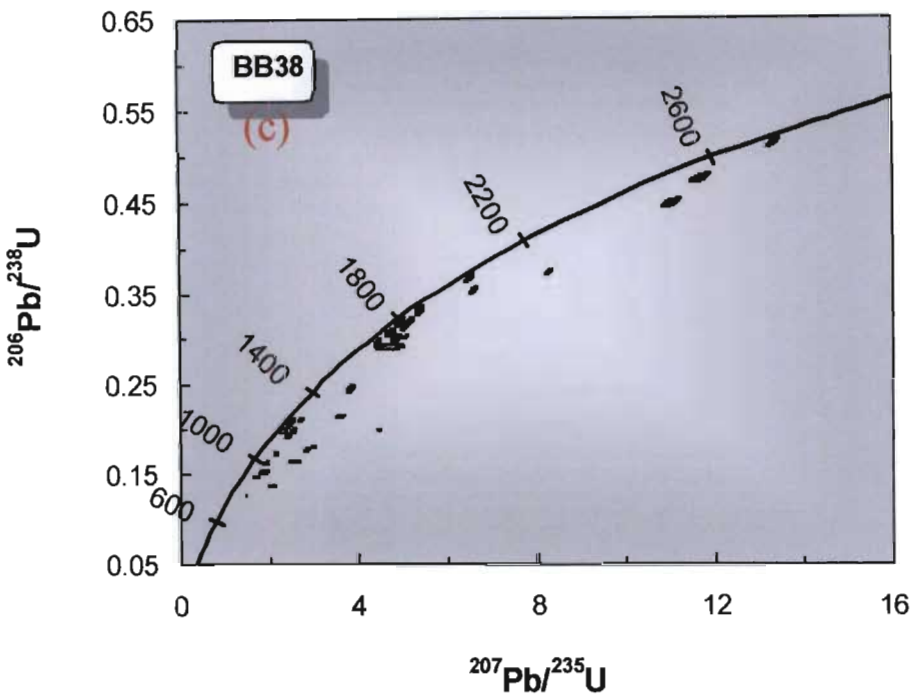

Figure 6.6 (a) Cathodoluminescence images of selected zircons from sample BB38. (b) Histogram diagram and cumulative probability plot of SHRIMP analyses for paragneiss of Nhazónia Formation. (> 90% concordant). (c) The U-Pb concordia plot of zircon analyses.

6.2.6 DISCUSSION

The Mesoproterozoic metasediments of the Frontier Formation of the Gairezi Group in the Chicamba Real Dam area were sourced from late Archaean terrain. The age well matches possible source rocks of Vumba granite gneiss correlated to the Sesombi granite dated at 2700-2600 Ma (Hawkesworth *et al.*, 1975; Blenkinsop *et al.*, 1997) and Messica granite gneiss correlated to the Chilimanzi suite granites dated at 2600-2500Ma (Hickman, 1975; Goodwin, 1981; Jelsma *et al.*, 1996). Furthermore the zircon cores show moderate to high Th/U ratios in the range 0.09-1.79 and by absence of abrasion effect suggesting that they predominantly come from an igneous and proximal source area.

The Mesoproterozoic metasediments of the Nhazónia and Frontier Formations of the Gairezi Group in the Sitatonga Range region, sourced from terrane of Archaean to Palaeoproterozoic age. These ages are well correlated to the possible source rocks of high-grade events of the Limpopo Belt dated at 3200-3000 Ma, 2650-2520 Ma and 2000 Ma (Hölzer *et al.*, 1998). Furthermore most of zircons have low U and Th contents and high Th/U ratios suggesting detrital igneous zircons.

The $^{207}Pb/^{206}Pb$ ages of 1800-1700 Ma and 1430 Ma are unknown among rocks exposed in the study area. The $^{207}Pb/^{206}Pb$ age of 1430 Ma as highly altered igneous zircon is considered a minimum age of deposition, whilst the $^{207}Pb/^{206}Pb$ ages of 1800-1700 Ma indicated by analyses as detrital origin provides a maximum depositional age Gairezi Group metasediments. This depositional age is consistent with maximum possible age for the Itremo Group (Madagascar) of about 1850 Ma (Cox *et al.*, 1998) and 1800 Ma for metasedimentary rocks of the Highland Complex (Hölzer *et al.*, 1994). The 1800 Ma age in southern Africa is that of the emplacement of Mashonaland dolerites (Compston & McElhinny 1975) and of reactivation of wrench fault to normal fault along Palala Shear zone, which controlled deposition of the rocks of the Soutpansberg associated with continental rifting (Barton *et al.*, 1994).

Alternatively if the 1430 Ma is considered a *minimum* age of a discordant detrital zircon, the Gairezi Group can be constrained as deposited between 1430 Ma and 1300 Ma. The lower boundary is fixed by the 1100-1300 Ma ages which are interpreted as metamorphic ages (due to the Kibaran event).

Future researches are required to determine the approximate age of Gairezi Group sediments depositions.

Similar ages have been recently recognised by Perritt (2001) within Ahlmannryggen Group (Antarctic), in which the detrital zircons of sedimentary rocks give Archaean ages (3300 to 2400 Ma) and Proterozoic ages (2100 to 200 and 1700 to 1600 Ma).

The metamorphic zircon grains giving the $^{207}Pb/^{206}Pb$ ages of 1300-1100 Ma are interpreted as the record of Moçambique belt orogeny. The youngest $^{206}Pb/^{238}U$ ages of 530-498 Ma provided by metamorphic zircon grain are interpreted as being related to the final Pan-African event within the study. De Wit *et al.* (2001) observed similar ages (520-490 Ma) in southwestern Madagascar which were interpreted as being related to accelerated exhumation accompanied by extensional tectonics.

In summary, the new SHRIMP U-Th-Pb ages suggest that the Mesoproterozoic metasediments of Gairezi Group are older than the Umkondo Group, confirming Watson's (1969) observations and interpretations. They represent the western passive margin of the pre-Moçambique belt ocean, deposited between 1800 Ma and 1430 Ma or alternatively between 1430 Ma and 1300 Ma. Then they were deformed at least twice, during the assembly of Rodinia followed by Gondwana amalgamation.

CHAPTER 7

CRUSTAL EVOLUTION AND CONCLUSIONS

7.1 INTRODUCTION

This chapter describes the crustal evolution of western central Moçambique, about which very little was known before the present study. This synthesis involves integrating the sparse previous geological work with data obtained during this study, which includes lithological aspects, geochemical data, metamorphic petrology, structural geology, AMS data and new SHRIMP ages. These are combined into a model of crustal evolution.

7.2 REGIONAL CORRELATION

It has been proposed that, prior to the break-up of Gondwana during the Mesozoic, the Moçambique Belt and the Maudheim Province of Western Dronning Maud Land (WDML) formed a continuous Kibaran orogenic belt, which linked up with the Namaqua-Natal Belt of South Africa (see Groenewald et al., 1991and references therein).

The Moçambique Belt and the Maudheim Province lie to the east of the Archaean Zimbabwe craton and the Grunehogna Province (Barton et al., 1987) respectively. Tectonic setting and metamorphic descriptions of the Báruè Complex (Moçambique Belt) propose a correlation with the Sverdrupfjella Group (Groenewald et al., 1991; Groenewald & Hunter, 1991) and Sör Rondane (Jacobs et al., 1993) in central WDML, Natal Belt (Thomas & Eglington, 1990; Groenewald et al., 1991; Jacobs et al., 1993; Thomas et al., 1993; Eglington et al., 1989) as well as with the Uluguru, Pare and Usambara Mountains in Tanzania (Appel et al., 1993).

Previously the contact between the Zimbabwe craton and Moçambique Belt has been interpreted as being a sinistral strike-slip zone (Manhiça et al., 2001). The same interpretation has been placed on the contact between the Grunehogna Province and the Maudheim Province (Perritt and Watkeys, 2003). This would seem to add support to the direct connection between western central Moçambique and WDML. However, in this thesis, it has been demonstrated that the contact between the Zimbabwe craton and the Moçambique Belt is a duplex zone formed by the westward thrusting of the Kibaran rocks over the Archaean craton during Pan-African times. Consequently a direct connection between the study area and WDML seems unlikely as in the latter area, the Kibaran rocks were thrust over the Archaean and then affected by sinistral strike-slip shear. Perritt and Watkeys (2003) propose that this strike-slip zone now underlies the southern end of the East Africa Rift, about 300 km east of the eastern side of the study area.

Another line of evidence the proposed connection between the two regions are the Proterozoic supracrustal sequences: the Umkondo Group on the Zimbabwe craton and the Ritchersflya Supergroup on the Grunehogna Province. The similarity in stratigraphy and probable identical age suggest that these sequences may have been part of the same sedimentary basin (see Groenewald et al., 1991 and reference therein). The palaeomagnetic data support the suggestion that these sequences were originally close, at least as regards palaeolatitute (Powell et al., 1993, Powell et al., 2001).

However, when investigated in detail, these correlations are not equivocal. The Umkondo Group was derived from a

cratonic or a recycled orogen provenance, whereas the Ritschersflya Supergroup show the signatures of input from an active island arc or active continental margin. Although these data could be interpreted as being different source regions around the same basin, this is considered unlikely. In such a refit, on the basis of the palaeocurrent data, the mature part of the basin would have to be the proximal area while the immature sediments would have to lie in the distal regions. Consequently, although the two sequences are of the same age, it seems that they were deposited in separate basins. The palaeomagnetic data show that they must have been at similar latitudes, but their positions with regard to longitude is completely unconstrained.

From the discussion above, it is apparent that the Moçambique Belt and the Maudheim Province do not appear to have been directly connected, nor were the Umkondo Group and Ritscherflya Supegroup part of the same sedimentary basin, despite the similarities in age and successions. Consequently, in a refit of Gondwana, WDML cannot be positioned tightly against the eastern edge of the Zimbabwe and Kaapvaal cratons, as proposed by Groenewald et al. (1991). Instead the looser fit of Perritt and Watkeys (2003) is more likely. This has to be taken into account when considering the tectonic evolution of the study area.

7.3 TECTONIC EVOLUTION

The Proterozoic crustal evolution in western central Moçambique corresponds to a complete Wilson Cycle, from early extension and continental rifting to continental fragmentation and ocean basin development, followed by plate convergence, subduction, and continent-continent collision.

The Archaean granite-greenstones of the eastern edge of the Zimbabwe craton were generated in an extensional environment in a continental setting (Hunter, 1997) during the late Archaean (Hawkesworth et al., 1975). They were subsequently metamorphosed and deformed during the late Archaean, resulting in east-west fold axes and synformal greenstone belts (Figure 7.1A). This was followed by uplift and erosion during the early Proterozoic.

The Gairezi Group sediments were deposited in a passive continental margin most likely between 1800 Ma and 1430 Ma or between 1430 Ma and 1300 Ma (Figure 7.1B). This event might be related to extension and rifting across the Limpopo Belt and Kaapvaal craton, which formed the Soutpansberg Group, Waterberg Group, Palapye Group and Volop Group (Olifantshoek Supergroup) (SACS, 1980; Tankard et al., 1982).

The Gairezi sediments were derived predominantly from the Zimbabwe craton in the northern part of the study area and from the Limpopo Belt in the southern part. The new SHRIMP ages clearly demonstrate that the Frontier Formation is older than the Umkondo Group. This confirms Watson's (1969) observations and interpretations. The time gap between the Gairezi Group and Umkondo Group represents a period of crustal extension, accretion, metamorphism, deformation, uplift and erosion.

The following stage of crustal evolution is controlled by events that occurred off-craton in the Moçambique Belt. It was characterized by subduction and subsequent continental collision resulting in the assembly of the Rodinia supercontinent during the Kibaran event (1300-1100 Ma). The emplacement of the granitic rocks of the Báruè Complex took place during the subduction period.

The thrusting of the Moçambique Belt onto the eastern edge of the Zimbabwe craton during the Kibaran events resulted in the formation of the Umkondo peripheral foreland basin (Figure 7.1C). This basin was filled by sediments derived from the Limpopo Belt and Zimbabwe craton. The

basin deepened towards the east (Stocklmayer, 1978) as shown in Figure 7.1C.

The Umkondo dolerite sills show evidence of intrusion before lithification of the host sedimentary rocks (Munyanyiwa, 1997), demonstrating that that the interval between deposition of Umkondo sediments and intrusion of the Umkondo dolerites is minimal. Consequently the SHRIMP date of 1105 Ma (Wingate, 2001) for the sills also gives the age of deposition of the Umkondo Group and contemporaneous uppermost volcanic rocks.

This igneous event is also recorded across in WDML, where sills also intruded wet sediments (Krynauw et al., 1988). Due to other intrusions of similar ages across southern Africa, it has been proposed that the igneous activity is part of the Umkondo Large Igneous Province that was induced by a plume (Hanson et al., 1998). Such a scenario would explain the widespread distribution of synchronous igneous activity across a number of tectonic environments.

The two convergent tectonic settings, related to the Kibaran and Pan-African events, were possibly separated by an extensional phase. It heralded the break up of Rodinia to form the Moçambique Ocean (Stern, 1994). However, there is no evidence of such extension affecting the study area, beyond the preservation of the Umkondo igneous activity. The Zimbabwe craton and Moçambique Belt in this region seem to have remained as a single unit during this time. However, the contact between these two crustal provinces became reactivated during Pan-African amalgamation of Gondwana.

During the Pan-African collisions, the Báruè Complex of the Moçambique Belt was involved in thick-skinned tectonics as it was thrust westwards over the Gairezi Group that, together with the eastern Messica granite gneiss, formed a duplex zone that now marks the eastern limit of exposure of the Zimbabwe craton. The craton may continue further east underneath the western part of the Mocambique Belt.

This reworking of the eastern edge of the Zimbabwe craton resulted in the development of a new north-south, steeply dipping planar fabric in the eastern Messica granite gneiss. Further west, where the orogenic wedge was thinner, the Frontier Formation was thrust over the younger Umkondo Group in a thin-skinned event (Figure 7.2). During this approximately east-west compression, the Umkondo Group was slightly deformed into with sub-horizontal to gently plunging very open folds (Figure 7.1D).

Perritt and Watkeys (2003) proposed two events in the Pan-African of Moçambique and WDML. The first involved approximately east-west compression, while the second was sinistral strike-slip faulting. The small-scale ductile shears observed affecting the north-south fabric in the reworked portion of the Zimbabwe craton might be related to these two events. The first event, which would have had an element of transpression in the study area, would have been responsible for the dextral shears, while the second event would have caused the minor sinistral shears.

The final geological stage in the crustal evolution of western central Moçambique relates to the formation of the Karoo Supergroup and the break-up of Gondwana during the Jurassic and Cretaceous. In these events, pre-existing fracture trends and contacts between crustal provinces were reactivated as faults.

7.4 CONCLUSIONS

The main conclusions from this thesis are as follows.

On the basis of geological patterns and ages, the Archaean Vumba and Messica granite gneisses along the eastern edge of the Zimbabwe craton correlate respectively

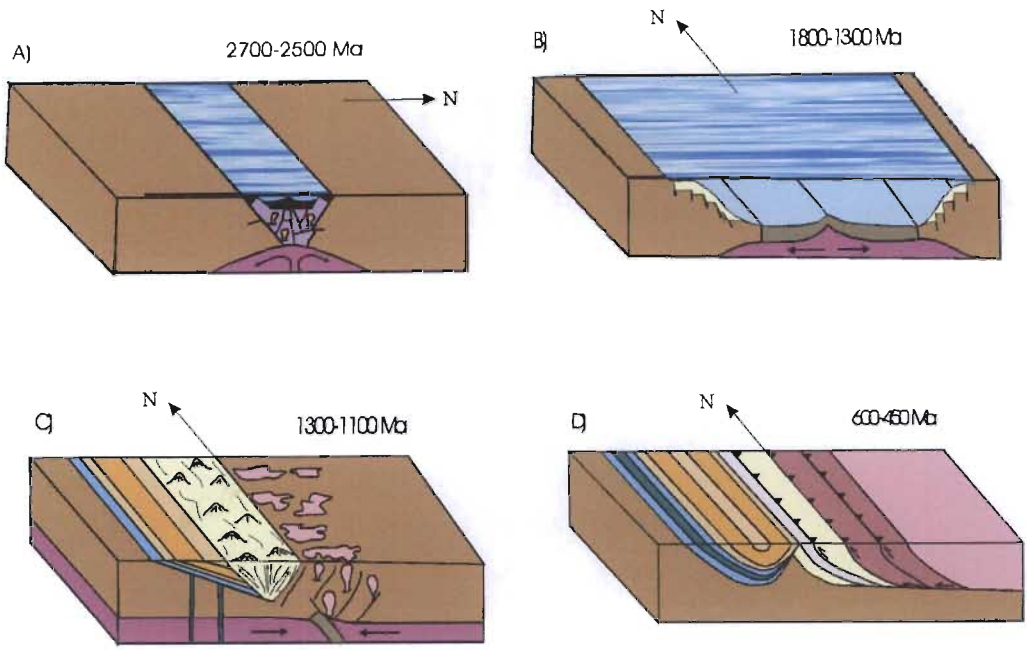

Figure 7.1 Crustal tectonic evolution model of central Moçambique: A) Granite-greenstone formation. B) Deposition of Gairezi Group sediments on the passive continental margin. C) Deformation of Gairezi Group (yellow) metasediments and Umkondo sediments (orange & blue) deposition in peripheral foreland basin, simultaneously with Báruè Complex granitic (pink) emplacement followed by Umkondo dolerite (green) intrusion at Moçambique belt orogeny. D) High grade metamorphism and strong deformation in the east produced thrusting of the Gairezi Group metapelites over Umkondo Group sediments during Pan-African orogeny.

with Sesombi granite suite, that is found as plutons elsewhere on craton, and Chilimanzi granite suite that occurs as sills.

They represent the last Archaean granitic magmatic activity in western central Moçambique.

The Mesoproterozoic Gairezi Group, consisting of the Nhazónia and Frontier Formations, are older than the Umkondo Group. They were deposited between 1800 Ma and 140 Ma or between 1430 Ma and 1300 Ma, probably along a passive continental margin, and their source areas were the Zimbabwe craton and Limpopo Belt. They were deformed and metamorphosed, and underwent uplift and erosion before deposition of the Umkondo Group. These events are poorly understood and require further investigation.

Future researches are required to determine the approximate age of Gairezi Group sediments depositions.

The Umkondo Group formed in a peripheral foreland basin at about 1105 Ma. The sediments were derived from the Zimbabwe craton and Limpopo Belt and were deposited in braided stream and shallow marine environments. They were intruded by dolerites dykes and sills prior to lithification. This event was part of the Umkondo Large Igneous Province that is recorded by widespread igneous activity in southern Africa as well as in WDML, Antarctica. Despite the similarity in lithostratigraphy, deposition age and tectonic setting, the Umkondo Group and the Ritchersflya Supergroup of WDML were deposited in different basins.

Development of the Umkondo foreland basin was due the Moçambique Belt being accreted to and thrust onto the eastern edge of the Zimbabwe craton during Kibaran collisional events. The granitic intrusions related to this event include the Nhansipfe megacrystic gneiss which is an A-type granite, and the Tchinhadzandze gneiss and Chimoio gneiss which are I-type granites.

This contact zone was reactivated during Pan-African events. Consequently the present position of the boundary between the craton and the Moçambique Belt is not the site of the original Kibaran collisional zone. Consequently, the Zimbabwe craton may continue further east underneath the Moçambique Belt. This suggestion can only be tested through geophysics.

The east-west to east-northeast compression resulted in thick-skinned thrusting of the high grade Moçambique Belt over the Gairezi Group and Messica granite gneiss which formed a duplex zone (Figure 7.2 - southern portion). In the same event, thin-skinned tectonics occurred as the Gairezi Group was thrust westwards over the younger Umkondo Group (Figure 7.2 – southern portion). No evidence could be found for a proposed sinistral strike-slip zone between the Zimbabwe craton and the Moçambique Belt.

In the west of the study area, the Vumba and western Messica granite gneisses have a distinctive paramagnetic characteristic with a well developed magnetic lineation but a weak magnetic foliation. In contrast, the eastern Messica granite gneiss exhibits a ferromagnetic nature with a well defined north-northwest planar fabric but a weak magnetic lineation plunging to north. This change in magnetic characteristic is considered to mark the boundary east of which the craton was reworked during Pan-African events.

As regards the metamorphic characteristics of the study area, the petrographic investigations and the geothermobarometry show a west to east increase in PT conditions up to granulite facies. An accompanying increase in deformation also occurs. SHRIMP dating demonstrates that, in the zone of Pan-African reworking, the Proterozoic rocks preserve evidence of a previously unsuspected pre-Kibaran event as well as Kibaran and Pan-African events.

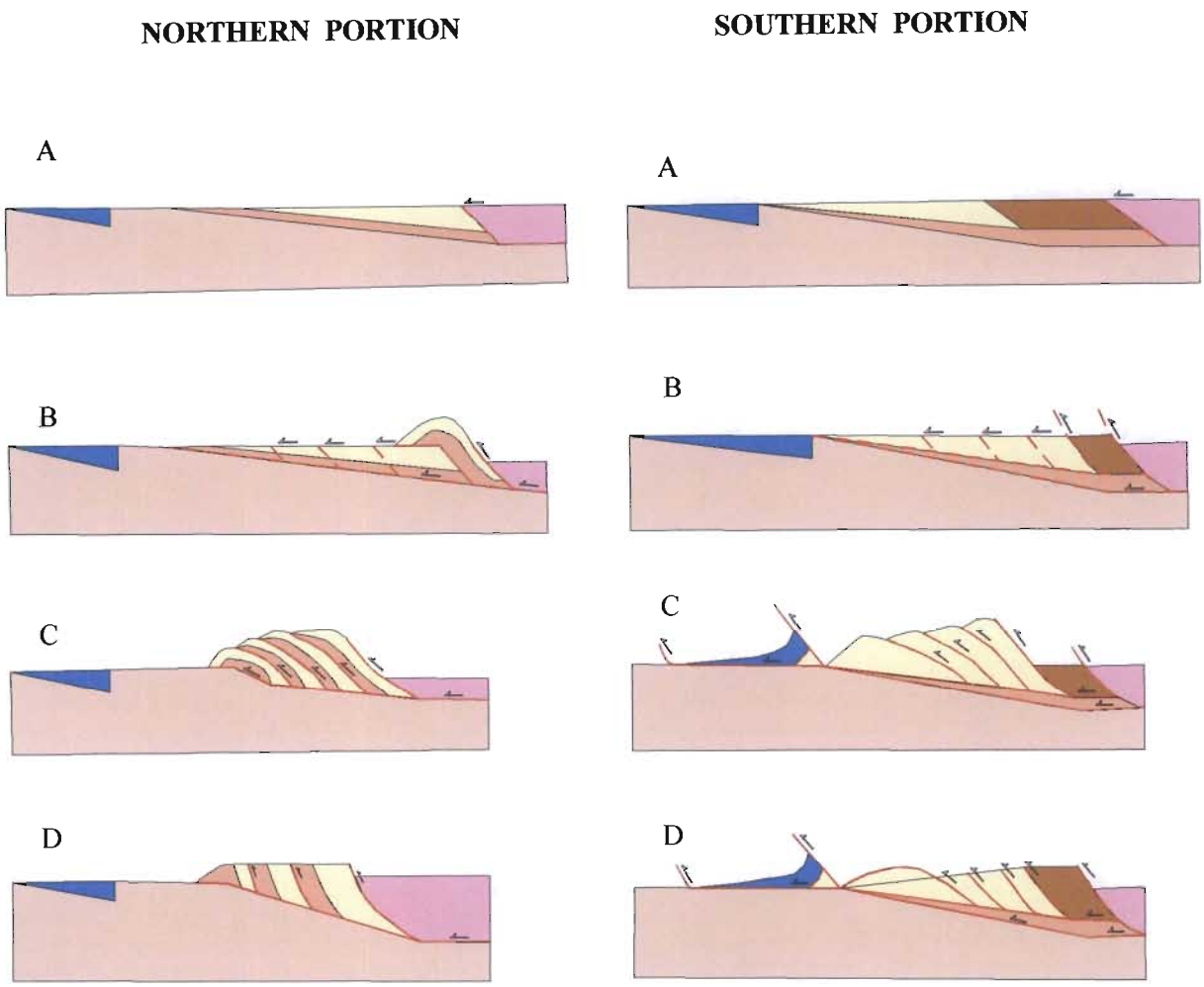

Figure 7.2 Progressive collapse of a footwall ramp during duplex formation in western central Moçambique during the Pan-African event. The blue colour in the both portions represents Umkondo Group sediments.
Northern portion: A) Thick-skinned thrusting of the Báruè Complex (pink) over Frontier Formation (yellow). B and C) Formation of the Frontier duplex structures involving Messica granite gneiss (peach). D) Erosion to present level.
Southern portion: A) Thick-skinned thrusting of the Báruè Complex (pink) over Gairezi Group. B and C) Formation of the Frontier duplex structures and thin-skinned

These require further detailed investigations involving structural, metamorphic and geochronological studies in order to establish precisely the conditions that prevailed during each event.

REFERENCES

Abbey, S. (1989). The evolution of reference material for rock analysis. In: Ahmedali, S. T. (Ed), X-ray fluorescence analysis in the geological sciences: Advances in methodology. *Geol. Assoc. Canada*: Short Curse 7, 38pp.

Afonso, R. S. (1978). Noticia explicative da Carta Geológica de Moçambique 1:2000000. *Direcção dos Serviços de Geologia e Minas,* 191pp.

Allsop, H. L.,Kramers, J. D., Jones, D. L. & Erlank, A. J. (1989). The age of the Umkondo Group, eastern Zimbabwe and implications for palaeomagnetic correlations. *South African Journal of Geology*, **92**, 11-19.

Andrade, C. F. (1894). Reconhecimento geólogico dos Territórios Portugueses compreendidos entre Lourenço Marques e o Rio Zambeze. *Imprensa Nacional*, Lisboa.

Andrade, C. F. (1929). Esboço Geológico da Província de Moçambique. *Imprensa Nacional,* Lisboa.

Appel, P., Möller, A., Schenk, V. & Muhongo, S. (1993). Granulite facies metamorphism and P-T evolution in the Moçambique Belt of Tanzania. In: *Geoscientific Reasearch in NE Africa* (Edited by Thorweihe, U. & Schandelmeier, H.), 171-175. A.A. Balkema, Rotterdarm.

Araújo, J. R. & Gouveia, J. C., (1965). Contribuição para o Estudo da Geologia do Distrito de Manica e Sofala. Formações Precambricas. *Boletim dos Serviços Geológicos e Mineiros de Moçambique,* **53**, 45-60.

Araújo, J. R., Afonso, R. S., Pinto, M. S., Pinto, A. F., Barradas, J. M. & Leal, V. P. (1973). Geologia das regiões de Espungabera, Dombe e Rotanda. *Serviços de Geologia e Minas de Moçambique,* 66pp.

Barker, F. (1979). *Trondhjemite: definition, environment and hypothesis of origin, 1-13. In: F. Barker (Ed.), Trondhjemites, Dacites and Related Rocks*. Elsevier, Armsterdam, 659 pp.

Barton, J. M., Young, S. W., Suttner, L. J., James, W. C. and Mack, G. H. (1987). The geology and geochronology of the Annandagstoppane granite, western Dronning Maud Land, Antarctica. *Contib. Mineral. Petrol.*, **97**, 488-496.

Barton, J. M., Hölzer, L., Kamber, B.S., Doig,R., Kramers, J. D. & Nyfeler, D. (1994). Discrete metamorphic events in the Limpopo Belt, southern Africa: Implications for the application of P-T paths in complex metamorphic terrains. *Contrib. Mineral. Petrol.*, **22**, 1035-1038.

Bhatia, M. R. (1983). Plate tectonics and geochemical composition of sandstones. *Journ. Geol.*, **91**, 611-627.

Blatt, H., Middleton, G. & Murray, R. (1980). *Origin of Sedimentary Rocks*. 2nd ed., Prentice-Hall, New Jersey.

Blenkinsop, T., Martin, A., Jelsma, H. A. & Vinyu, M. L. (1997). The Zimbabwe Craton. In De Wit, M. J. & Ashwall L. D.: *Greenstone Belts.* 807pp.

Blundy, J. D. & Holland T. J.B (1990). Calcic amphibole equilibria and new amphibole-plagioclase geothermometer. *Contrib. Mineral Petrol.*, **104**, 208-224.

Boothroyd, J. C. & Ashley, G. M., (1975). Processes, bar morphology, and sedimentary structures on braide outwash fans, northeastern Gulf of Alaska, 193-222.

In: Jopling A. V. & MacDonald 9Eds.), Glaciofluvial and Glaciolacustrine Sedimentation. *Spec. Publ. 23, Soc. Econ. Pal. Min.*, 320 pp.

Borradaile, G. J. (1988). Magnetic susceptibility, petrofabrics and strain. *Tectonophysices*, **156**, 1-20.

Bouchez, J. L., Gleizes G., Djouadi, T. & Rochette, P. (1990). Microstructures and magnetic susceptibility applied to emplacement kinematics of granites: the example of the Foix pluton (French Pyrenees). *Tectonophysices*, **184,** 157-171.

Bouchez, J. L. & Gleizes, G. (1995).Two-stage deformation of the Mont-Louis-Andorra granite pluton (Variscan Pyrenees) inferred from magnetic susceptibility anisotropy. *Journal of the Geological Society (London)*, **152**, 667-679.

Brackenbury, C. (1906). Some copper deposits in Rhodesia. *Trans. Geol. Soc. S. Afr.*, **LIV**, 69-84.

Button, A. (1977). Stratigraphic history of the middle Proterozoic Umkondo basin in the Chipinga area, southeastern Rhodesia. *Economic Geology Research Unit,* Information Circular 108.

Chappell, B. W. & White, A. J. R. (1974). Two contrasting granite types. *Pac. Geol.*, **8**: 173-174.

Chipera, S. J. & Perkins, D. (1988). Evaluation of biotite-garnet geothermometers: application to the English River subprovince, Ontario. *Contrib. Mineral. Petrol.*, 98, 40-48.

Claoué-Long J.C., Compston, W., Roberts, J. & Fanning, C. M. (1995). Two carboniferous ages: A comparison of SHRIMP zircon dating with conventional zircon ages and $^{40}Ar/^{39}Ar$ analysis. *Geochronology Times Scales and Global Stratigraphic Correlation, SEPM Special Publication*, **54**, 3-21.

Clarke, D. B. (1992). *Granitoid Rocks. Chapman* & Hall, London. 283pp.

Compston, W. & McElhinny, M. W. (1975). The Rb-Sr age of the Mashonaland dolerites of Rhodesia and its significance for Palaeomagnetic correlation in Southern Africa. *Precambrian Research*, **2**, 305-315.

Cox, R., Armstrong, R. A. & Ashwal, L.D. (1998). Sedimentology, geochronology and provenance of the Proterozoic Itremo Group central Madagascar, and implications from pre-Gondwana palaeogeography. *Journal of the Geological Society, London,* **155**, 1009-1024.

Cullers, R. L., Barrett, T., Carlson, R. & Robinson, B. (1987). REE and mineralogic changes in Holocene soil and stream sediment: a case study in the Wet Mountains, Colorado, U.S.A. *Chem.Geol.* **63**, 275-297.

Dasgupta, S., Sengupta, P., Guha, D. & Fukuoka, M. (1991). A refined garnet-biotite Fe-Mg exchange geothermometer and its application in amphibolites and granulites. *Contrib. Mineral. Petrol.*, **109**, 130-137.

Deer, W. A., Howie, R. A., & Zussman, J. (1992). An introduction to the Rock-Forming Minerals, 2nd Edition. *Longman Scientific and Technical, Harlow, England,* 696p.

de Wit, M. J., Bowtinr, S. A., Ashwal, L. A., Randrinanasolo, L. G., Morel, V. P. I. & Rambeloson, A. (2001). Age and tectonic evolution of Neoproterozoic ductile shear zones in southwestern Madagascar, with implications fro Gondwana studies. *Tectonics,* **20**, 1-45.

Dias, M. B. (1956). Structural map of Moçambique (1:3 000 000). *Serviços de Industria e Geologia, Bulletin* **18**.

Dickinson, W. R & Suczek, C. A. (1979). Plate Tectonics and Sandstone Compositions. *The American Association of*

Petroleum Geologists Bulletin, **63(12),** 2164-2182.

Dieterich, J. H. (1969). Origin of cleavage in folded rocks: *American Journal of Science,* **267**, 155-165.

Dupuy, C., Dostal, J. & Frata, M. (1982). Geochemistry of the Adamello Massif (Northern Italy). *Contrib. Mineral. Petrol.,* **80**, 41-48.

Eby, G. N. (1990). The A-type granitoids: A review of their occurrence and chemical characteristics and speculations on their petrogenesis. *Lithos,* **26**, 115-134.

Eglington, B. M., Harmer, R. E. & Kerr, A. (1989). Isotope and Geochemical Constraints on Proterozoic Crustal Evolution in southeastern Africa. *Precambrian Research,* **45**, 159-174.

Ferry, J. M. & Spear, F. S. (1978). Experimental calibration of the partitioning of Fe and Mg between biotite and garnet. *Contrib. Mineral. Petrol.,* **66**, 113-117.

Floyd, P. A. & Winchester, J. A., (1975). Magma type and tectonic setting discrimination using immobile elememts. *Earth Planet. Sci. Lett.,* **27**, 211-218.

Folk, R. L., Andrew, P. B. & Lewis, D. W. (1970). Detrital sedimentary rock classification and nomenclature for use in New Zealand. *New Zealand Journal of Geology and Geophysics*, **13**, 947-968.

Freitas, A. J. (1949). Explanatory notes of the geological map of Moçambique (1:2 000 000). *Serv. Geologia e Minas.* Lourenço Marques.

Freitas, A. J. (1957). Notícia explicative do esboço geológico de Moçambique (1:2 000 000). *Boletim dos Serviços de Geologia e Minas de Moçambique*, **23.**

Gleizes, G., Leblanc, D., Olivier, P. & Bouchez, J. L. (2001). Strain partitioning in a pluton during emplacement in transpressional regime: the example of the Néouvielle granite (Pyrenees). *Int. J. Earth Sciences (Geol. Rundsch)*, **90** 325-340.

Goodwin, A. M. (1981). Archaean plates and greenstone belts. In A. Kröner (ed), *Precambrian Plate Tectonics.* Elsevier, Amsterdam, 105-135.

Gouveia, J. C. (1965). Contribuição par o estudo de geologia do distrito de Manica e Sofala – Formações Precâmbricas. *Serv. Geologia e Minas. Boletim* **33** – Lourenço Marques.

Graham, C. M. & Powell, R. (1984). A garnet-hornblende geothermometer: calibration, testing, and application to the Pelona Schist, Southern California. *J. Metamorphic Geol.,* **2**, 13-31.

Groenewald, P. B. & Hunter, D. R. (1991). Granulites of northern H.U. Sverdrupfjella, western Dronning Maud Land: metamorphic history from garnet-pyroxene assemblages, coronas and hydration reactions. In: Thompson, M. R. A., Crame, J. A. and Thompson, J. W. (Eds), *Geological Evolution of Antarctica, Cambridge* University Press, Cambridge, 61-66.

Groenewald, P. B., Grantham, G. H. & Watkeys, M. K. (1991). Geological evidence for a Proterozoic to Mesozoic link between southeastern Africa and Dronning Maud Land, Antarctica. *Journal of the Geological Society, London,* **148**, 1115-1123.

Hanson, R. E., Martin, M. W., Bowring, S. A. & Munyanyiwa H. (1998). U-Pb zircon age for the Umkondo dolerites, eastern Zimbabwe: 1 Ga large igneous province in southern Africa-East Antarctica and possible Rodinia correlations. *Geology,* **26**, 1143-1146.

Hargraves, R. B., Hattingh, P. J. & Onstott, T, C. (1994). Paleomagnetic results from the Timbavati Gabbros in the Kruger

National Park, South Africa: *South African Journal of Geology,* **97**, 114-118.

Hawkesworth, C. J., Moorbath, S., O'Nions, R. K. & Wilson, J. F. (1975). Age relationships between greenstone belts and granites in the Rhodesian Archaean craton. *Earth Planet. Sci. Lett.,* **25**, 251-262.

Herron, M. M. (1988). Geochemical classification of terrigenous sands and shales from core or log data. *Journal of Sedimentar Petrology,* **58(5),** 820-829.

Hickman, A. H. (1975). Precambrian structural geology of part of the Pilbara region. Geol. Surv. W. *Aust. Annu. Rep.,* 1974, 68-73.

Hoinkes, G. (1986). Effect of grossular-content in garnet on the partitioning of Fe and Mg between garnet and biotite. *Contrib. Mineral. Petrol.,* **92**, 393-399.

Hölzer, L.,Frei, R., Barton, J. M. & Kramers, J.D. (1998). Unraveling the record of successive high grade events in the Central Zone of the Limpop Belt using Pb single phase dating of metamorphic minerals. *Precambrian Research,* **87**, 87-115.

Hölzer L., Hofmann, A. W., Todt, W. & Köhler, H. (1994). U-Pb geochronology of the Sri Lankan basement. In: Raith, M. & Hoernes S. (Editors), Tectonic, Metamorphic and Isotopic Evolution of Deep-Crustal Rocks, With Special Emphasis on Sri Lanka. *Precambrian Research,* **66** 123-149.

Holland, T. & Blundy, J. (1994). Non-ideal interactions in calcic amphiboles and their bearing on amphibole-plagioclase thermometry. *Contrib. Mineral. Petrol.,* **116**, 433-447.

Hunter, M. A. (1997). Archaean Volcanism Extensional or Compressional? A new look at an old issue. *Journal of Conference Abstracts.* **2**, 1.

Hunting Geology and Geophysics Limited (1984). *Final Report, Mineral Inventary Project.* Direcção Nacional de Geologia, Maputo, Moçambique.

Indares, A. & Martignole, J. (1985). Biotite-garnet geothermometry in the granulite facies: the influence of Ti and Al in biotite. *Merican Mineralogist,* **70**, 272-278.

Irvine, T. N and Baragar, W. R. A. (1971). A guide to the chemical classification of the common volcanic rocks. *Can. J. Earth Sci.,* **8**, 523-548.

Jacobs, J., Thomas, R. J & Weber, K. (1993). Accretion and indentation tectonics at the southern edge of the Kaapval craton during the Kibaran (Grenville) orogeny. *Geology,* **21**, 203-206

Jahn B. M., Glickson, A. Y., Foster, R. W., Zbinden, E. & Kimberly, M. M. (1981). REE geochemistry and isotopic data of Archaean silicic volcanics and granitoids from the Pilbara Block. Estern Australia; implications for the early crustal evolution. *Geochim. Cosmochim. Acta* **45**, 1633-1652.

Jelinek, V. (1981). Characterization of the magnetic fabrics of rocks. Tectonophysics **79**, 63-67.

Jelsma, A. H., Vinyu, M. L., Valbracht, P. J., Davies, G. R., Wijbrans, J. R. & Verdurmen, Ed. A. T. (1996). Constraints on Archaean crustal evolution of the Zimbabwe craton: a U-Pb zircon, Sm-Nd and Pb-Pb whole-rock isotope study. *Contrib. Mineral Petrol.,* **124**, 55-70.

Jensen, L. S. (1976). A new cation plot for classifying subalkalic volcanic rocks. *Ontario Division of Mines Miscellaneous* Paper **66**.

Johnson, R. L. (1963). Progress report on work in the Manica Belt and adjacent areas of Central Africa. *Leeds Univ. Res. Inst. Afr. Geol. VII Ann. Rept.,* 1961-62.

Jones, D. L. & McElhinny, M. W. (1966). Palaeomagnetic correlation of the basic intrusions in the Precambrian of Southern *Africa. J. Geophys. Res.*, **71**, 543-552.

Jover, O., Rochette, P., Lorand, J. P., Maeder, M. & Bouchez, J. L. (1989). Magnetic mineralogy of some granites from the French Massif Central: Origin of their low field susceptibility. *Phys. Earth Planet. Inter.*, **55**, 79-92.

Kennedy, W. Q. (1964). The structural differentiation of Africa in the Pan-African (±500 Ma) tectonic episode. *Annual Report.* **8**, 48-49. Research Institue of African Geology, University of Leeds, England.

Kohn, M. J. & Spear, F. S. (1990). Two new geobarometers for garnet amphibolites, with applications to southeastern Vermont. *American Mineralogist.* **75**, 89-96.

Kröner, A., Sacchi, R., Jaeckel & Costa, M. (1997). Kibaran magmatism and Pan-African granulite metamorphism in northern Moçambique: single zircon ages and regional implications. *Journal of African Earth Sciences,* **25 (3),** 467-484.

Krynauw, J. R., Waters, B.R., Hunter, D. R. & Wilson, A. H. (1988). Emplacement of sills into wet sediments at Grunehonga, western Dronning Maud Land, Antarctica. *Journ. Geol. Soc. Lond.*, **145**, 1019-1032.

Leake, E. B. (1978). Nomenclature of Amphiboles. *Mineralogical Magazine*, **42**, 533-563.

Ludwig, K. R.(1999). Isoplot/Exversion 2.00: A geochronology Toolkit for Microsoft Excel. Berkley geochronological Center, *Special Publication,* 1a, 46pp.

MacDonald, G. A. & Katsura, T. (1964). Chemical composition of Hawaiian lavas. *J. Petrol.*, **5**, 83-133.

Manhiça, A. D. S. T. (1998). *The geology of the Moçambique belt and the Zimbabwe Craton around Manica, western Moçambique.* Unpublished MSc Thesis, University of Pretoria.

Manhiça, A. D. S. T., Grantham, G. H., Armstrong, P. G., Guise, P. G. & Gruger, F. J. (2001). Polyphase deformation and metamorphism at the Kalahari Craton-Moçambique Belt boundary. *Geological Society, London, Special Publications.* **184**, 303-322.

Manuel, I. R. V. (1992). *Geologie, Petrographie, Geochemie und Lagerstatten der Manica – Greenstone Belt (Moçambique).* PhD Thesis, Rheinisch – Westfalishen Technishen Hochschule Aachen.

Martins, J. R. (1957). A geologia da região de Mavita. *Serviços de Industria e Geologia, Bulletin* **15**.

Martin, H., Chauvel, C., Jahn, B. M. & Vidal, Ph. (1983). *Major and trace element geochemistry and crustal evolution of Archaean granodioritic rocks from eastern Finaland,* Ibid., **21**, 159-80.

Martin, H. (1987). Petrogenesis of Archaean Trondhjemites, Tonalites and Granidiorites from Eastern Finland: Major and Trace Element Geochemistry. *Journal of Petrology,* **28(5),** 921-953.

Mennell, F. P. (1920). Geology of the Sabi Valley, Mashonaland. Transactions of the *Geological Society of South Africa,* XXII. Johannesburg.

McElhinny, M. W. & Opdyke, N. D.(1964). The palaeomagnetism of the Precambrian dolerites of eastern Southern Rhodesia, and example of geologic rock correlation by rock magnetism. *J. Geophys. Res.*, **69**, 2465-75.

McLennan, S. M., Hemming, S., McDaniel, D. K. & Hanson, G. N. (1993). Geochemical approaches to sedimentation, provenance, and tectonics. In Johnson, M. J. & Basu, A. (Eds.). Processes controlling the composition of clastic sediments:

Boulder, Colorado. *Geological Society of America Special Paper*, **284**, 21-40.

Mukwakwami, J., Blenkinsop, T. G., Hanson R. & Munyanyiwa, H. (2001). Umkondo igneous province and Mesoproterozoic Umkondo basin in eastern Zimbabwe: possible relevance to Rodinia. *GSA Annual Meeting.* Session **63**.

Munyanyiwa, H. (1997). The Moçambique Belt of Zimbabwe: Fieldtrip Guide for Conference on Intraplate Magmatism and Tectonics of Southern Africa (Harare, Zimbabwe, 13-17 September), 32pp.

Munyanyiwa, H. (1999). Geochemical study of the Umkondo dolerites and lavas in the Chimanimani and Chipinge Districts (eastern Zimbabwe) and their regional implications. *Journal of African Earth Sciences,* **28(2),** 349-365.

Nelson, D.R. (2001). An assessment of the determination of deposition ages for Precambrian clastic sedimentary rocks by U-Pb dating of detrital zircons. *Sedimentary Geology,* **141-142**, 37-60.

Nesbitt, H. W. & Young, G. M. (1982). Early Proterozoic climates and plate motions inferred from major element chemistry of lutittes. *Nature,* **299**, 715-717.

Nesbitt, H. W. M. & Young, G. M. (1984). Prediction of some weathering trends of plutonic and volcanic rocks based on thermodynamic and kinetic considerations. *Geochimica et Cosmochimica Acta,* **48**, 1523-1534.

Nesbitt, H. W. M & Young, G. M. (1989). Formation and diagenesis of weathering profiles. *J. Geol.* **97**, 129-147.

Norrish, K. & Hutton, J. T. (1969). An accurate X-ray spectrographic method for the analysis of a wide range of geological samples.*Geochim. Cosmochim. Acta,* **33**, 431-435.

Oberholzer, W. F. (1964). A geologia da Mancha de Manica. Unpubl, *Direcção dos Serviços da Geologia e Minas,* 14 pp.

Oberholzer, W. F. & Afonso, R. S. (1977). Carta Geológica da Provincia de Moçambique. Escala 1:2000000. *Instituto Nacional de Geologia.* Maputo – Moçambique.

Olivier, Ph. & Archanjo, C. J. (1994). Magnetic and magmatic structures of the Emas granodioritic pluton (Cachoeirinha belt, NE Brazil). Relationships with Pan-African stike-slip fault systems. *Tectonophysics,* **229**, 239-250.

Paces, J. B. & Miller, J. D. (1993). Precise U-Pb ages of Duluth Complex and related mafic intrusions, Northeastern Minnesota: Geochronological insights to physical, petrogenic, paleomagnetic and tectonomagmatic processes associated with the 1.1 Ga midcontinent rift system. *Journ. Geophys. Res.*, 98B, 13997-14016.

Passchier C. W & Trouw R. A. J. (1996). *Microtectonics.* Springer Verlag Berlin Heidelberg New York. 289pp.

Pearce, J. A. & Norry, M. J. (1979). Petrogenic implications of Ti, Zr, Y and Nb variations in volcanic rocks. *Contrib. Mineral. Petrol.*, **69**, 33-47.

Pearce, J. A., Harris, N. B. W. & Tindle, A. G. (1984). Trace element discrimination diagram for the tectonic interpretation of granitic rocks. *J. Petrol.*, **25**, 956-983.

Pearce, T. H., Gorman, B. E. & Birkett, T. C. (1975). The TiO_2-K_2O-P_2O_5 diagram: a method of discriminating between oceanic and non-oceanic basalts. *Earth and Planetary Science Letters,* 24, 419-426.

Pearce, T.H. (1977). The relationship between major element chemistry and tectonic environment of basic and intermediate volcanic rocks. *Earth and Planetary Science Letters,* 36, 121-132.

Peccerillo, A. & Taylor, S. R. (1976). Geochemistry of Eocene calc-alkaline volcanic rocks from the Kastamotu area. Northern Turkey. *Contrib. Mineral. Petrol.*, **58**, 63-81.

Perchuck, L. L., Aranovish, L.Ya., Podlesskii, K. K., Lanrant'eva, I. V., Gerasimov, V. Yu., Fed'kin, V. V., Kitsul, V. I., Karsakov, L. P. and Berdnikov, N. V. (1985). Precambrian granulites of Aldan shield, eastern Siberia, USSR. *Journal of Metamorphic Geology.* **3**, 285-310.

Perchuk, L.L. (1991). Thermodynamic control of metamorphic processes. In Saxena, S. K. (Ed.). *Kinetics and equilibrium in mineral systems*. Spring Verlag, New York, 285-352.

Perritt, S.H. (2001). *The Ahlmannryggen Group, western Dronning Maud Land, Antarctica.* Unpublished Ph.D thesis, University of Natal, South Africa, 153pp.

Perritt, S.H. & Watkeys, M.K.(2003). Implications of late Pan-African shearing in western Dronning Maud Land, Antarctica. *Geological Society, London, Special Publications,* **201**, 135-143.

Petro, W. L., Vogel, T. A. and Wilband, J. T. (1979). Major-element chemistry of plutonic rock suites from compressional and extensional plate boundaries. *Chem. Geol.* **26**, 217-235.

Phaup, A. E. (1964). The revised stratigraphical nomenclature for the Umkondo System. Unpublished. *Rhod. Geol. Surv.* Technical Files.

Pinna, P., Marteau, P., Becq-Giraudon, J.-F. & Manigault, B. (1987). Noticia explicative da carta geologica de Moçambique na escala 1:1000 000. *Instituto Nacional de Geologia.* Maputo- Moçambique.

Pinna, P., Jourde, G., Caluez, J. Y., Mroz, J. P. & Marques, J. M. (1993). The Moçambique Belt in northern Moçambique: Neoproterozoic (1100-850 Ma) crustal growth and tectogenesis, and superimposed Pan-African (800-550 Ma) tectonism. *Precambrian Research,* **62**, 1-59.

Pinto, M. S. (1969). Geochemistry of some granites of the Manica and Sofala district of Moçambique. *Instituto Nacional de Geologia.* Maputo- Moçambique.

Plyusnina, L. P. (1982). Geothermometry and geobarometry of Plagioclase-Hornblende Bearing Assemblages. *Contrib. Mineral Petrol.* 80: 140-146.

Potts, P. J. (1987). Inductively coupled plasma-mass spectrometry. In: *A handbook of silicate rock analysis.* Black, Glasgow, 575-586.

Powell, C. McA., McElhinny, M. W., Li, Z. X., Meert, J. G. and Park, J.K., (1993). Palaeomagnetic constraints on timing of the Neoproterozoic break-up of Rodinia and Cambrian formation of Gondwana. *Geologia,* **21**, 889-892.

Powell, C. McA., Jones, D. L., Pisaresvsky, S. & Wingate, M. T. D. (2001). Palaeomagnetic constrains on the position of the Kalahari craton in Rodinia. *Precamb. Res.*, **110**, 33-46.

Ramsay, J. G. (1962). The geometry and mechanics of formation of "similar" type folds. *J. Geol* **70**: 309-327.

Ramsay,, J. G. & Huber, M. I. (1987). *The Techniques of Modern Structural Geology. Volume 2: Folds and Fractures.* Academic Press, London.

Rebolo, J. R. F. (1972). Prospecção geoquímica sistemática na região de Mavita. *Serviços Geológia e Minas, Lourenço Marques, Moçambique.*

Reid, D. L. & Barton, E. S. (1983). Geochemical characterization of granitoids in the Namaqualand geotraverse, 67-82. In: Botha, B. J. V. (Ed.), Namaqualand Metamorphic Complex,. *Spec. Publ. Geol. Soc. S. Afr.*, **10**, 198 pp.

Robb, L. J., Armstrong, R. A. & Waters, D. J. (1999). The History of Granulite-Facies Metamorphism and Crustal Growth from Single Zircon U-Pb Geochronololy: Namaqualand, South Africa. *Journal of Petrology* (?), 1747-1770.

Rochette, P. (1987). Magnetic susceptibility of the rock matrix related to a magnetic fabric studies. *J. Struct. Geol.*, **3**, 349-363.

Rochette, P., Jackson, M. & Aubourg, C. (1992). Rock magnetism and the interpretation of anisotropy of magnetic susceptibility. *Rev. Geophys.*, **30(3)**, 209-226.

Rollinson, H. R. (1983). The geochemistry of mafic and ultramafic rocks from the Archaean greenstone belts of Sierra Leone. *Mineralogical Magazine*, **47**, 344.

Rollinson, H. R. (1993). *Using Geochemical Data*: Longman Scientific & Technical, England, 352pp.

Roser, B. P. & Korsch, R. J. (1986). Determination of tectonic setting of sandstone-mudstone suites using SiO_2 content and K_2O/Na_2O ratio. *The Journal of Geology*, **94**, 635-650.

Roser, B. P., Cooper, R. A., Nathan, S. & Tulloch, A. J. (1996). Reconnaissance sandstone geochemistry, provenance, and tectonic setting of the lower Palaeozoic terranes of the West Coast and Nelson, New Zealand. *New Zealand Journal of Geology and Geophysics*, **39**, 1-16.

SACS, South African Commission for Stratigraphy, (1980). Stratigraphy of South Africa, Part 1: (Comp. Kent, L. E.), Lithostratigraphy of the Republic of South Africa, South West Africa/Namibia, and the Republics of Bophuthatswana, Transkei and Venda. *Geological Survey of South Africa Handbook*, 8, 690pp.

Schwab, F. L. (1986). Sedimentary "signatures" of foreland basin assemblages: real or counterfeit. *Special Publication International Association of Sedimentologists.* **8**, 395-410.

Shackleton, R. M. (1986). Precambrian collision tectonic in Africa. From Coward, M. P. & Ries, A. C. (eds), *Collision Tectonics, Geological Society Special Publication*, **19**, 329-349.

Sousa, A. F. G. (1951). Dendrologia de Moçambique Vol. I e Vol. II. *Imprensa Nacional de Moçambique.* Lourenço Marques.

Spear, F. S. (1980). NaSi=CaAl Exchange Equilibrium between plagioclase and amphibole. *Contrib. Mineral. Petrol.*, **72**, 33-41.

Spear, F. S. (1981). Amphibole-Plagioclase Equilibria: An Emperical Model for the Relation Albite + Tremolite = Edenite + 4 Quartz. *Contrib. Mineral Petrol.*, **44**, 355-364.

Stacey, J. S. & Kramers, J. D. (1975). Approximation of terrestrial lead isotope evolution by a two-stage model. *Earth Planet. Sci. Lett.*, **26**, 207-221.

Stern, R. J. (1994). Arc Assembly and continental collision in the Neoproterozoic East African orogen: Implications for the consolidation of Gondwanaland. *Annual Review Earth Planetary Sciences*, **22**, 319-351.

Stildolph, P. A. & Stocklmayer, R. C. (1976). Proposed classification of granitic rocks in Rhodesia. In: Harrison, N. M. *Annals of the Rhodesia Geological Survey* Salisbury, 1977.

Stocklmayer, V. R. (1975). Revised stratigraphical nomenclature for the Umkondo rocks. *Rhod. Geol. Surv.Annals.* **1**, 23-34.

Stocklmayer, V. R. (1978). The geology of the country around Inyanga. *Rhod. Geol. Surv. Bull.*, **79**.

Stocklmayer, V. R. (1980). The geology of the Inyanga-North-Malaka area. *Zim. Geol. Surv. Bull.*, **89**.

Stocklmayer, V. R. (1981). *The Umkondo Group.* In: Hunter, D. R., (Ed.), Precambrian of the Southern Hemisphere: Amsterdam, Elsevier, 556-562.

Streckeisen, A. L. (1976). To each plutonic rock its proper name. *Earth Sci. Rev.*, 12: 1-33.

Swift, W. H., White, W. C., Wiles, J.W. & Worst, B.G. (1953). The geology of the Lower Sabi Coalfield. *S. Rhod. geol. Surv. Bull.*, 40

Swift, W. H. (1962). The geology of the Middle Sabi Valley. *S. Rhod. geol. Surv. Bull.*, 52.

Tankard, A. J., Jackson, M. P. A., Eriksson, K. A., Hobday, D. K., Hunter, D. R. & Minter, W. E. L. (1982). *Crustal Evolution of Southern Africa. 3.8 Billion Years of Earth History.* Springer-Verlag, 523pp.

Taylor, S. R. & McLennan, S.M. (1985). *The continental Crust:* Its Composition and Evolution. Blackwell, London, 312pp.

Teale, E. O. & Wilson (1915). Portuguese East Africa between the Zambeze river and the Sabi river; a consideration of the relation of its tectonic and fisiographique feature. *Geol. Jour.* **LXVL**.

Teale, E. O. (1923). The geology of Portuguese East Africa between the Zambezi and Sabi Rivers. *Trans. Geol. Soc. S. Afr.* **XXVI**, 103-159.

Teale, E. O. (1924). The Geology of Portuguese East Africa between the Zambezi and Sabi Rivers. *Transactions of the Geological Society of South Africa*, **XXVI**. Johannesburg.

Tennant, R. (1995). A structural re-appraisal of the Chimanimani Mountains, Zimbabwe. *B. Sc. (Hon) dissertation (unpubl.),* University of Zimbabwe, Harare, 61pp.

Thomas, R. J. & Eglington, B. .M. (1990). A Rb-Sr, Sm-Nd and U-Pb zircon isotopic study of the Mzumbe Suite, the oldest intusive granitoid in southern Natal. South Africa. *South African Journal of Geology* **93**, 761-765.

Thomas, R. J., Von Veh, M. & McCourt, S. (1993). The tectonic evolution of southern Africa: an overview. *J. African Earth Sci.*, **16**, 5-24.

Tyndale-Biscoe, R. (1957). The geology of a portion of the Inyanga District. *S. Rhod. Geol. Surv. Short Report*, **37**.

Vail, J. R. (1962). The Manica Orogenic Belt. Leeds Univ. Res. Inst. *Afr. Geol. VI Ann. Rept.*, 1960-1, 37-9.

Vail, J. R. (1964). Esboço geral da geologia da região entre os rios Lucite e Révuè, distrito de Manica e Sofala, Moçambique. *Boletim dos Serviços de Geologia e Minas de Moçambique*, **32**, 1-70.

Vail, J. R. (1965). Estrutura e geocronologia da parte oriental da Africa central com referência a Moçambique. *Boletim dos Serviços de Geologia e Minas de Moçambique*, **33**, 1-60.

Vail, J. R. (1966). Aspects of the stratigraphy and the structure of the Umkondo System in the Manica Belt of southern Rhodesia and Moçambique, and an outline of the regional geology. *Transactions of the Geological Society of South Africa*, **13**, 13-29.

Watkeys, M. K. (2002). Development of the Lebombo rifted volcanic margin of southeast Africa. *Geological Society of America. Special Paper*, **362**, 27-46.

Watson, R. L. A. (1969). The geology of the Cashel, Melsetter and Chipinga areas. *Geol. Surv. S. Rhodesia Bull.*, **60**, 85pp.

Whalen, J. B., Currie, K. L. & Chappell, B. W. (1987). A-type granites: geochemical characteristics, discrimination and petrogenesis. *Contrib. Mineral Petrol.*, **95**, 407- 419.

Wingate, M. T. D. (2001). SHRIMP baddeleyite and zircon ages for an Umkondo dolerite sill, Nyanga Mountains, Eastern Zimbabwe. *S. Afr. J. Geol.*, **140**, 13-22.

Winkler, H. G. F. (1979). *Petrogenesis of Metamorphic Rocks*, 5th Edition Springer-Verlag, Berlin: 348pp.

Wronkiewicz, D. J. & Condie, K. C. (1987). Geochemical of Archaean shales from the Witwatersrand Supergroup, South Africa: Source are weathering and provenance. *Geochimica et Cosmochimica Acta*, **51**, 2401-2416.

APPENDIX 1

METHODS OF INVESTIGATION

METHODS OF INVESTIGATION

FIELD MAPPING

Before any fieldwork was undertaken a 1:250 000 geological map of eastern Zimbabwe and western Moçambique was generated from existing maps. This gave a better understanding of the nature of the geology and possible correlations between the different stratigraphy units along the international border.

Field mapping for the present thesis was conducted over 6 months. For this purpose 1:50 000 topographic base maps were used combined with 1:50 000 aerial photographs. The map of this thesis is result of combination of field mapping and laboratory results.

Because of the poor exposures and difficulties in access due not only to the terrain but also the landmines, most of the outcrops studied are restricted to river and to road-cuts, where good exposures occur. The best exposures formed the focus of detailed studies.

PETROGRAPHY

Thin sections were prepared by Mukesh Seyambu of the School of Geological and Computer Sciences of the University of Natal. Gazzi-Dickinson point counting method was used for selected thin sections of the Umkondo Group, to determine the modal composition of the sandstones. All thin sections were chemically stained to avoid errors in identifying the mineralogy of the rocks. The samples were counted to 400-500 points.

XRF WHOLE-ROCK CHEMISTRY

Whole-rock analysis for major and trace elements using X-ray fluorescence spectrometry were determined at the School of Geological and Computer Sciences of the University of Natal. XRF whole-rock analyses were carried out using a Philips PW 1404 Spectrometer and major and trace elements were obtained using fused glass discs and pressed powder pellets. Instrument calibration was controlled with international standards and internal synthetic standards and blanks. International standards used were DTS-1, PCC-1, GSP-1, W-1, BCR-1, G-2, AGV, NIM-G, NIM-P, NIM-D, NIM-S, NIM-L, BHVO, and DRN. International accepted standards are from Abbey (1989). Prof. A. H. Wilson of the School of geological and Computer Sciences, University of Natal, Durban compiled the computer programs for reduction of count data and calculation of mass absorption coefficients.

One or two kg of sample was cleaned and fine crushed in a jaw crusher. The crusher was statistically split to 100g and milled. Part of the milled sample was used for preparation of fusion discs and pressed powder pellets, part was used for ICP-MS analysis and the remainder has been stored for possible future use. Major and minor elements were analysed using the lithium tetraborate fusion method of Norrish & Hutton (1969).

Preparation of Norrish Fusion Discs

Silica crucibles were cleaned in a diluted solution of HCL. Approximately 0.5g of sample was weighted into the silica crucibles and dried at 100° C. These crucibles were placed in a furnace at 1000°C for 4 hours, then removed and allowed to cool in the desiccator. The spectroflux used for the fusion discs was preheated in Pt crucibles at 1000°C, and approximately 0.4g of the ashed sample was added as close to the ratio

weight sample/weight flux = 2.2 as possible. The samples were fused at 1000°C and the product cast in a brass die maintained at 250°C. Discs were annealed approximately 3 hours on a heated asbestos plate and then allowed to cool gradually. The flux was Johnson Mattey Spectroflux 105. Each new batch of flux was homogenized and a new set of standards made up. Fusion discs were stored separately in sealed plastic bags.

Pressed Powder Pellets

Approximately 8g of finely milled sample was mixed with 0.6 Mowiol and homogenized using an agate mortar and pestle. The sample was place in a metal die (position cylinder), and compressed to a pellet *ca.* 5mm thick under a pressure of 8 tonnes for *ca.* 10 seconds. The pellets were hardened in an oven at 110°C for 3-4 hours. Ragged edges on the pellets were trimmed. Contact with the surface to be radiated was avoided. Pellets separated by cardboard discs, were stored in airtight containers.

Precision of XRF Analyses

Precision of major and trace element analyses by XRF ia as follows:

	Detection Limits	Analytical Accuracy(%)	Tube Anode
SiO2	0.004%	0.2	Sc/Mo
Al2O3	0.005%	0.5	Sc/Mo
Fe2O3	0.001%	0.5	Sc/Mo
MnO	0.001%	0.5	Sc/Mo
MgO	0.011%	0.3	Sc/Mo
CaO	0.0003%	0.2	Sc/Mo
K2O	0.0003%	0.2	Sc/Mo
TiO2	0.0004%	0.2	Sc/Mo
P2O5	0.001%	0.2	Sc/Mo
Na2O	0.018%	2	Cr
Sc	0.3ppm	10	Cr
Ba	1ppm	20	Au
Zn	0.3ppm	5	Au
Cu	0.2ppm	5	Au
Ni	0.1ppm	5	Au
Cr	0.6ppm	5	Au
V	0.5ppm	10	Au
La	1.5ppm	15	Au
Zr	0.3ppm	3	Rh
Sr	0.3ppm	3	Rh
Nb	0.1ppm	3	Rh
Y	0.3ppm	3	Rh
Rb	0.4ppm	2	Rh
U	0.1ppm	20	Rh
Th	0.5ppm	20	Rh
Pb	1ppm	10	Au
Ga	0.2ppm	10	Au
Co	1ppm	10	Au
Ce	0.13ppm	5	Au
Nd	0.3ppm	5	Au
As	0.001ppm	10	Au
S	0.001ppm	10	Cr
F	2ppm	10	Cr
Cl	1ppm	10	Cr
Sn	2ppm	10	Au
W	0.5ppm	10	Au
Mo	1ppm	10	Au
Cd	0.6ppm	10	Au
Ta	3ppm	10	Rh

ICP-MS TRACE ELEMENT CHEMISTRY

The Rare Earth Elements (REE) and some trace elements were analysed using inductively coupled plasma-mass spectrometry (ICP-MS) in order to determine the provenance of the sediments. Approximately 100mg of powder from selected samples was determined at the School of Geological and Computer Sciences of the University of Natal. The analyses were carried out through an ELAN 6100 Spectrometer using techniques described in Potts (1987).

Laboratory Procedures

Sample preparation involved digesting 50mg of sample powder in closed, heated Teflon beakers using HF and HNO_3. The digested samples were analysed in 5% HNO_3 using a Perkin Elmer/Sciex ELAN 6100 ICP-MS. 103Rh, 115In, 187Re and 209Bi were used as internal standards, whereas calibration was achieced using synthetic multi-element standard solutions. Only high purity bottle-distilled acids and water were used. The instrument was optimised to minimise the formation of doubly-charged ions (++Ba/Ba = 0.019) and oxides (CeO/Ce = 0.025). Instrument sensitivity: 34903 cps/ppb 103 Rh.

Instrument operating conditions:

Nebuliser gas flow: 0.85 L/min
Main gas flow: ~15L/min
Auxiliary gas flow: `0.75L/min
ICP RF power: 1100W
Autolens voltages: 9Be = 6.8V; 59Co = 7.4V; 115In = 8.6V

Vacuum: 2.77e-5 Torr.

ELECTRON MICROPROBE MINERAL ANALYSES

Critical mineral assemblages were selected for metamorphism studies. For this purpose Carbon coated polished thin sections were analysed for the mineral chemistry of garnet, staurolite, biotite, amphibolite and plagioclase. Mineral analyses were obtained at the Department of Geology of the University of Durban-Westville. Analyses were performed at operating conditions: acceleration voltage of 15 Kv; a probe current of 30 nA; specimen current varied between 0.5 and 0.10 microamps; integrating time of 60 seconds and an electron beam diameter of 1 to 10 microns. Prior to analyse, all thin sections were washed with soap water, distilled water and ethanol to ensure removal of dirt and grease.

U/PB DETRITAL ZIRCON SHRIMP ANALYSES

Five rock samples were selected for U/Pb Sensitive High Resolution Ion Microprobe (SHRIMP) analyses of detrital zircons. The mica-schist (BB16) and quartzite (BB18) of the Frontier Formation were collected from the Chicamba Dam area, whereas mica-schist (BB39) and red quartzite (BB40) of the Frontier Formation and quartzofeldspathic gneiss (BB38) of the Nhazónia Formation were collected from the Sitatonga Range region.

The zircon separation was carried out at the University of the Witwatersrand using conventional methods of crushing, heavy liquid separation and magnetic separation techniques.

All U-Pb analyses were done on the SHRIMP-RG at the Research School of Earth Sciences at the Australian National University. Zicons were mounted in epoxy, together with the RSES zircon standards FC1 and SL13. All grains were then polished to half their thicknesses to expose internal structures. As preparation for the SHRIMP analyses, extensive use was made of transmitted and reflected light microphotography, together with SEM cathodoluminescence imaging to decipher the growth complexities in the zircons and to target the best areas for *in situ* analysis. For the zircon calibration the Pb/U ratios have been normalised relative to a value of 0.1859 for the $^{206*}Pb/^{238}U$ ratio of the FC1 reference zircons, equivalent to an age of 1099 Ma (Paces & Miller, 1993). U and Th concentrations were determined relative to the SL13 standard. For detrital studies such as this (where the aim is to analyse large numbers of zircons to characterise the sample populations, rather than to achieve high precision on individual spots) data are collected in 4 or 5 scans through the mass species $^{204}Zr_2O$, ^{204}Pb (common Pb), background, ^{206}Pb, ^{207}Pb, ^{208}Pb, ^{238}U, ^{248}ThO and ^{254}UO. The data were reduced in a manner similar to that described by Williams (1998, and references therein), using the SQUID Excel Macro of Ludwig (1999). Corrections for common Pb were made using the measured ^{204}Pb and the appropriate model values of Stacey & Kramers (1975). Uncertainties given for individual analyses (ratios and ages) are at the 1 σ level, however uncertainties in the any calculated weighted mean ages are reported at 95% confidence limits. Concordia plots and age calculations were carried out using Isoplot/Ex (Ludwig, 1999) or SQUID.

ANISOTROPY OF MAGNETIC SUSCEPTIBILITY

Oriented cores from 30 stations of the Vumba and Messica granite gneisses, located along east-west profile were drilled for Anisotropy of Magnetic Susceptibility (AMS). At each station, three cores of 25 mm diameter were collected. One of the cores was used for thin sections and two 22

mm long specimens were cut from each core, providing four specimens per station. The measurements were performed using the Kappabridge device, KLY-3S susceptometer (AGICO, Brno, Czech Republic) at *Laboratoire des Mécanismes de Transfert en Géologie at Université Paul-Sabatier.*

Magnetic susceptibility (K) reflects the magnetization (M) acquired when a rock is subjected to an inducing magnetic field (H) where K=M/H. (Borradaile 1988). This is carried by magnetic minerals, which include Fe-oxides, such as magnetite, Fe-sulphides and Fe-bearing silicates such as biotite, hornblende and chlorite.

There are two main types of magnetic susceptibility in rocks: paramagnetic and ferromagnetic. In a paramagnetic rock, the magnetic susceptibility is weak and reflects the petrographic fabrics of the Fe-bearing silicate minerals (Gleizes *et al.*, 2001). In a ferromagnetic rock, the magnetic susceptibility is high due to the susceptibility of magnetite being two orders of magnitude higher for the same amount of Fe in paramagnetic minerals

According to Rochette *et al.* (1992), the output of AMS measurements is an ellipsoid of magnetic susceptibility defined by the length and orientations of its three principal axes, $K_1 \geq K_2 \geq K_3$, i.e., the three eigen-vectors of the susceptibility tensor. The parameters usually presented are the mean susceptibility $Km = (K_1 + K_2 + K_3)/3$ and the anisotropy ratios $L = K_1/K_2$, $F = K_2/K_3$ and $P = K_1/K_3$. The orientation of the ellipsoid can be represented on a stereographic projection. The K_1 axis represents the susceptibility lineation while the susceptibility foliation is the plane containing K_1 and K_2. The anisotropy percentage (Pp%) is calculated from K_1 and K_3 from which is subtracted the diamagnetic contribution (D) of quartz and feldspar, a contribution assumed to be constant isotropic and equal to $D = -1.4 \times 10^{-5}$ SI (Rochette *et al.* 1992), thus giving $(Pp\%) = 100\ [((K_1 + D)/(K_3 + D)) - 1]$ (Bouchez & Gleizes 1995).

APPENDIX 2

MODAL ANALYSES

Table 2.2 Modal analyses of Vumba granite gneiss

	VUM 01	VUM 02	VUM 03	VUM 04	TSE 01	TSE 05	TSE 07	TSE 08	TSE 09	ROT 17	ROT 26
Quartz	33	26	32	28	27	30	27	44	26	28	58
Plagioclase	56	68	52	59	41	22	66	44	64	50	31
K-feldspar	5	1	12	9	23	45	-	2	-	11	6
Hornblende	+	+	+	-	3	+	-	-	-	1	-
Mica	4	3	2	2	4	-	-	-	4	7	5
Sphene	-	+	+	-	-	+	-	-	-	-	-
Epidote	1	1	2	-	2	3	7	10	6	3	-
Chlorite	-	-	-	+	-	+	+	+	-	-	-
Total	99	99	100	98	100	100	100	100	100	100	100

Table 2.3 Modal analyses of Messica granite gneiss

	CHI 01	CHI 04	CHI 06	BAN 02	SUS 10	SUS 11	SUS 14
Quartz	26	28	21	27	24	11	43
Plagioclase	32	44	27	31	62	57	46
K-feldspar	29	19	46	31	1	-	+
Apatite	-	-	-	-	-	-	-
Mica	14	8	6	10	13	32	10
Sphene	-	-	-	-	-	-	-
Epidote	-	+	-	+	+	+	+
Chlorite	-	-	-	-	-	-	-
Total	101	99	100	99	100	100	99

Table 2.4 Modal analyses of the Umkondo Group sandstone (Gazzi-Dickinson point-counting method)

Sample	Formation	Quartz %	Feldspar %	Lithic Fragment %	QFL
ESP 01	Upper Argillaceous	85	10	5	Subarkose
ESP02	Upper Argillaceous	78	16	6	Subarkose
ESP 03	Upper Argillaceous	87	7	6	Subarkose
ESP 04	Upper Argillaceous	62	28	10	Arkose/Litharkose
ESP 05	Upper Argillaceous	69	25	6	Arkose/Litharkose
ESP 06	Upper Argillaceous	80	11	9	Subarkose
ESP 07	Upper Argillaceous	88	8	4	Subarkose
ESP 12	Upper Argillaceous	83	12	5	Subarkose
ESP 13	Upper Argillaceous	71	20	9	Arkose/Litharkose
ESP 21	Quartzite	62	2	36	Litharenite
ESP 28	Quartzite	45	1	54	Litharenite
DAC 01	Quartzite	41	0	59	Litharenite
ROT 01	Quartzite	55	1	44	Litharenite
ROT 06	Quartzite	97	1	2	Quartzarenite

Table 2.5 Modal analyses of Báruè Complex gneiss

	BAN 04	BAN 08	VAN 02	VAN 03	VAN 04	VAN 08	VAN 09	VAN 10	CHM 02
Quartz	27	30	14	5	-	21	19	25	13
Plagioclase	61	38	39	38	42	40	32	41	45
K-feldspar	2	15	27	28	-	11	44	22	33
Hornblende	+	10	13	12	40	19	-	7	1
Biotite	10	7	8	15	10	8	1	4	5
Pyroxene	+	-	+	-	+	+	+	-	-
Epidote	-	+	-	-	-	+	-	+	1
Garnet	-	-	-	-	4	-	-	-	-
Magnetite					4	1	4	-	+
Sphene	-	-	-	-	-	-	+	-	2
Total	100	100	101	98	100	100	100	99	100

APPENDIX 3

GEOCHEMICAL ANALYSES

Table 3.1 Major (wt%) and trace elements (ppm) geochemistry for the greenstone samples

Formation	Maceq.	Maceq.	Maceq.	Maceq.	Maceq.	Maceq.	Maceq.	Maceq.
Sample	TSE 02	TSE 12	TSE 13	TSE 14	TSE 15	ROT 25	SUS 08	SUS 02
SIO2	47.31	49.73	45.81	53.22	52.03	49.72	46.35	46.28
Al2O3	4.74	14.35	15.17	15.44	16.43	16.22	9.40	2.74
Fe2O3	10.91	14.24	14.56	9.45	8.49	24.01	8.99	5.81
MnO	0.16	0.21	0.23	0.14	0.13	0.10	0.12	0.09
MgO	31.33	6.22	6.75	7.38	7.98	8.71	28.09	44.39
CaO	4.62	10.78	14.61	12.63	12.88	0.09	5.43	0.00
Na2O	0.14	2.48	1.23	1.06	1.54	0.00	0.23	0.07
K2O	0.07	0.16	0.27	0.15	0.18	0.00	0.07	0.01
TiO2	0.23	1.56	1.26	0.56	0.45	0.78	0.44	0.10
P2O5	0.02	0.15	0.10	0.05	0.04	0.07	0.02	0.01
TOTAL	99.52	99.89	99.99	100.08	100.19	99.74	99.14	99.51
L.O.I.	7.62	0.22	1.93	1.54	0.91	3.15	6.48	11.65
Nb	1.3	5.5	2.7	1.5	1.8	0.8	0.4	0.9
Y	7.7	35.4	31.4	13.8	11.5	3.2	13.9	1.2
Rb	9.4	3.3	8.4	5.9	3.8	1.1	7.3	0.0
Zr	11.7	96.5	63.8	28.0	21.2	40.0	20.2	5.4
Sr	3.9	111.5	271.5	73.3	98.1	0.0	6.9	0.3
U	0.0	2.2	1.2	0.0	1.8	0.4	0.0	1.5
Th	1.5	2.9	1.3	0.3	3.1	3.1	6.0	0.8
Cr	3120.7	230.2	328.7	387.2	564.3	1240.5	3474.5	2287.6
V	104.9	357.1	414.1	226.7	183.8	462.1	150.8	66.0
La	0.0	0.6	0.5	0.2	0.2	0.0	0.0	0.0
Zn	65.6	106.4	142.7	56.0	48.6	101.7	65.9	30.0
Cu	4.8	65.7	118.2	61.5	63.5	22.2	8.0	7.3
Ni	1797.6	77.1	128.9	135.6	110.3	1229.0	795.7	2544.4
Pb	11.6	7.9	0.0	15.8	4.4	9.1	5.0	7.0
Ga	4.5	21.0	24.7	15.9	11.0	20.1	6.0	0.3
Co	117.8	39.6	40.1	36.1	34.6	42.3	56.2	137.3
Ce	0.0	0.0	0.0	0.0	0.0	0.0	0.0	0.0
Nd	0.0	0.0	0.0	0.0	0.0	0.0	0.0	0.0
As	0.0	0.0	0.0	0.0	0.0	0.3	0.0	4.8
Ba	121.6	107.5	136.3	84.5	95.9	89.9	23.2	17.3
Sc	32.2	59.7	62.0	57.2	59.5	69.2	42.8	8.2
S	70.0	2055.0	548.0	801.0	31.0	29.0	30.0	1659.0

Table 3.2 Correlation matrix of chemical elements for the greenstone samples.

	SiO2	Al2O3	Fe2O3	MnO	MgO	CaO	Na2O	K2O	TiO2	P2O5	Nb	Y	Rb	Zr	Sr	U	Th	Cr	V	La	Zn	Cu	Ni	Pb	Ga	Co	Ce	Nd	As	Ba	Sc	S
SiO2	1.000																															
Al2O3	0.619	1.000																														
Fe2O3	0.067	0.522	1.000																													
MnO	-0.158	0.287	0.112	1.000																												
MgO	-0.605	-0.970	-0.533	-0.465	1.000																											
CaO	0.376	0.608	-0.171	0.708	-0.682	1.000																										
Na2O	0.417	0.563	-0.030	0.672	-0.661	0.776	1.000																									
K2O	0.154	0.546	-0.100	0.817	-0.631	0.961	0.736	1.000																								
TiO2	0.065	0.629	0.530	0.748	-0.726	0.512	0.735	0.585	1.000																							
P2O5	0.158	0.607	0.527	0.710	-0.719	0.471	0.772	0.527	0.982	1.000																						
Nb	0.154	0.352	0.150	0.758	-0.506	0.530	0.896	0.561	0.834	0.890	1.000																					
Y	-0.038	0.449	0.118	0.901	-0.574	0.732	0.819	0.792	0.882	0.837	0.847	1.000																				
Rb	-0.221	-0.028	-0.154	0.554	-0.085	0.471	0.026	0.487	0.052	-0.054	-0.012	0.351	1.000																			
Zr	0.076	0.560	0.490	0.729	-0.670	0.462	0.763	0.524	0.989	0.992	0.889	0.874	-0.005	1.000																		
Sr	-0.051	0.521	0.096	0.824	-0.595	0.808	0.625	0.929	0.680	0.613	0.551	0.785	0.345	0.607	1.000																	
U	0.046	0.177	-0.090	0.335	-0.014	0.280	0.684	0.357	0.455	0.523	0.687	0.442	-0.475	0.505	0.419	1.000																
Th	-0.170	0.121	0.134	-0.178	-0.014	-0.150	-0.044	-0.179	0.068	-0.022	-0.113	0.054	0.052	0.059	-0.246	-0.079	1.000															
Cr	-0.579	-0.788	-0.294	-0.449	0.828	-0.661	-0.747	-0.646	-0.671	-0.718	-0.823	-0.541	0.221	-0.645	-0.676	-0.539	0.387	1.000														
V	0.141	0.760	0.872	0.408	-0.780	0.244	0.341	0.324	0.812	0.785	0.426	0.492	-0.097	0.754	0.511	0.165	0.048	-0.637	1.000													
La	0.123	0.524	0.139	0.859	-0.647	0.750	0.902	0.808	0.889	0.889	0.913	0.944	0.133	0.889	0.827	0.625	-0.160	-0.753	0.540	1.000												
Zn	-0.232	0.517	0.701	0.724	-0.604	0.350	0.347	0.505	0.849	0.776	0.507	0.703	0.286	0.786	0.688	0.134	0.083	-0.433	0.864	0.649	1.000											
Cu	0.200	0.687	0.152	0.748	-0.748	0.860	0.711	0.927	0.710	0.868	0.582	0.760	0.230	0.641	0.965	0.431	-0.283	-0.831	0.581	0.848	0.639	1.000										
Ni	-0.508	-0.658	-0.162	-0.559	0.883	-0.874	-0.771	-0.798	-0.669	-0.819	-0.526	-0.725	-0.305	-0.616	-0.662	-0.208	-0.177	0.691	-0.517	-0.709	-0.476	-0.773	1.000									
Pb	0.554	-0.108	-0.017	-0.342	0.049	-0.208	-0.165	-0.406	-0.299	-0.191	-0.137	-0.367	-0.056	-0.238	-0.556	-0.483	-0.359	0.065	-0.220	-0.323	-0.424	-0.408	0.168	1.000								
Ga	0.272	0.640	0.692	0.597	-0.896	0.539	0.563	0.588	0.882	0.855	0.572	0.676	0.064	0.822	0.698	0.221	-0.077	-0.789	0.942	0.731	0.855	0.784	-0.723	-0.182	1.000							
Co	-0.544	-0.963	-0.429	-0.317	0.927	-0.646	-0.580	-0.568	-0.643	-0.590	-0.351	-0.535	-0.096	-0.575	-0.503	-0.105	-0.303	0.668	-0.691	-0.531	-0.512	-0.647	0.922	0.145	-0.789	1.000						
Ce	#DIV/0!	#DIV/0!	#DIV/0!	#DIV/0!	#DIV/0!	#DIV/0!	#DIV/0!	#DIV/0!	#DIV/0!	#DIV/0!	#DIV/0!	#DIV/0!	#DIV/0!	#DIV/0!	#DIV/0!	#DIV/0!	#DIV/0!	#DIV/0!	#DIV/0!	#DIV/0!	#DIV/0!	#DIV/0!	#DIV/0!	#DIV/0!	#DIV/0!	#DIV/0!	#DIV/0!	#DIV/0!					
Nd	#DIV/0!	#DIV/0!	#DIV/0!	#DIV/0!	#DIV/0!	#DIV/0!	#DIV/0!	#DIV/0!	#DIV/0!	#DIV/0!	#DIV/0!	#DIV/0!	#DIV/0!	#DIV/0!	#DIV/0!	#DIV/0!	#DIV/0!	#DIV/0!	#DIV/0!	#DIV/0!	#DIV/0!	#DIV/0!	#DIV/0!	#DIV/0!	#DIV/0!	#DIV/0!	#DIV/0!	#DIV/0!	#DIV/0!				
As	-0.358	-0.654	-0.396	-0.466	0.720	-0.563	-0.378	-0.488	-0.458	-0.398	-0.257	-0.467	-0.613	-0.403	-0.325	0.264	-0.342	0.252	-0.457	-0.335	-0.503	-0.384	0.748	-0.043	-0.562	0.730	#DIV/0!	#DIV/0!	1.000			
Ba	0.204	0.486	0.451	0.744	-0.651	0.559	0.464	0.621	0.560	0.576	0.517	0.518	0.447	0.522	0.617	0.127	-0.328	-0.539	0.547	0.575	0.657	0.631	-0.486	-0.046	0.665	-0.383	#DIV/0!	#DIV/0!	-0.631	1.000		
Sc	0.511	0.486	0.666	0.365	-0.962	0.536	0.491	0.495	0.678	0.645	0.358	0.477	0.120	0.609	0.478	0.047	0.208	-0.666	0.825	0.494	0.648	0.613	-0.822	-0.086	0.872	-0.938	#DIV/0!	#DIV/0!	-0.794	0.598	1.000	
S	-0.029	-0.175	-0.206	0.244	0.091	0.040	0.478	0.062	0.374	0.464	0.648	0.390	-0.441	0.471	0.136	0.815	-0.361	-0.330	0.000	0.511	-0.001	0.155	0.056	0.081	0.076	0.189	#DIV/0!	#DIV/0!	0.490	-0.143	-0.279	1.000

Table 3.3 Major (wt%) and trace (ppm) elements geochemistry for the Vumba granite gneiss

Formation	Vumba	Vumba	Vumba	Vumba	Vumba	Vumba	Vumba	Vumba
Sample	ROT 17	VUM 01	VUM 04	TSE 01	TSE 05	TSE 07	TSE 08	TSE 09
SIO2	70.76	70.49	74	72.99	72.73	71	74.61	71.99
Al2O3	14.93	15.44	14.39	14.4	14.25	16.52	13.56	15.57
Fe2O3	2.43	2.62	1.66	1.73	1.88	2.31	1.62	2.1
MnO	0.03	0.03	0.04	0.03	0.03	0.07	0.03	0.03
MgO	0.86	0.87	0.42	0.26	0.31	0.62	0.07	0.72
CaO	2.59	2.8	2.03	1.17	1.25	2.91	2.78	2.58
Na2O	4.32	4.52	3.99	3.75	3.37	4.11	4.65	4.9
K2O	3.15	2.54	3.44	5.55	5.3	2.38	2.44	1.9
TiO2	0.32	0.29	0.16	0.19	0.22	0.22	0.17	0.26
P2O5	0.15	0.09	0.05	0.06	0.06	0.03	0.12	0.09
TOTAL	99.54	99.7	100.16	100.13	99.4	100.16	100.05	100.13
L.O.I.	1	0.97	0.94	0.89	0.8	1.61	0.64	1.22
Nb	3.8	4.2	4.5	11.1	13.7	2.7	3.1	3.1
Y	7.1	7.3	2.8	16.1	17.8	7.8	5.6	5.4
Rb	111.2	87.7	123.7	265.3	285.1	194.2	48.1	55.4
Zr	91.2	103.7	69.0	150.9	168.4	81.7	80.1	110.2
Sr	425.3	418.3	263.5	120.3	109.8	278.8	354.3	394.1
U	4.0	3.8	7.4	4.7	5.1	4.5	3.4	2.2
Th	14.4	19.7	16.4	31.5	39.2	3.5	7.6	4.6
Cr	106.4	139.3	117.7	111.3	96.1	79.5	148.2	89.8
V	32.4	36.2	20.7	20.4	21.3	29.2	21.9	31.4
La	45.4	42.4	5.1	45.9	36.7	1.4	0.8	39.5
Zn	42.7	32.7	23.7	27.8	33.9	29.8	12.6	45.7
Cu	0.9	1.6	0.0	0.4	0.3	1.9	0.4	1.8
Ni	8.0	9.6	5.2	2.4	1.4	5.1	1.6	3.6
Pb	41.2	22.8	37.0	55.2	40.1	14.1	40.1	14.9
Ga	15.9	16.4	15.7	16.5	18.3	16.9	15.0	17.7
Co	0.9	3.8	1.2	2.2	1.9	6.2	2.8	2.3
Ce	45.1	59.8	16.2	105.7	140.3	16.7	23.2	24.4
Nd	14.0	17.4	3.0	38.5	32.2	3.4	3.1	4.8
As	11.4	3.5	9.5	19.6	14.1	1.4	8.6	2.6
Ba	35.7	16.7	838.8	897.4	846.9	538.8	395.3	702.3
Sc	3.5	5.2	5.2	5.8	6.0	4.8	6.9	5.3
S	0.0	0.0	0.0	0.0	0.0	0.0	0.0	1.0

Table 3.4 C.I.P.W norm calculation (anhydrous; in wt%) for the Vumba granite gneiss.

Formation	Vumba	Vumba	Vumba	Vumba	Vumba	Vumba	Vumba	Vumba
Sample	ROT 17	VUM 01	VUM 04	TSE 01	TSE 05	TSE 07	TSE 08	TSE 09
Quartz	27.17	27.44	32.79	27.21	29.87	30.91	33.38	29.87
Anorthite	11.87	13.30	9.74	5.41	5.81	14.24	8.92	12.21
Hypersthene	2.14	2.17	1.05	0.65	0.77	1.54	0.38	1.79
Albite	36.55	38.25	33.76	31.73	28.52	34.78	0.33	41.46
Orthoclase	18.62	15.01	20.33	32.80	31.32	14.06	39.35	11.23
Apatite	0.35	0.21	0.12	0.14	0.14	0.07	14.42	0.21
Ilmenite	0.06	0.06	0.09	0.06	0.06	0.15	1.31	0.06
Corundum	0.06	0.38	0.53	0.24	0.84	1.96	0.28	0.98
Rutile	0.29	0.26	0.11	0.15	0.18	0.14	0.06	0.23
Hematite	2.43	2.62	1.66	1.73	1.88	2.31	1.62	2.10
Total	99.54	99.69	100.18	100.12	99.39	100.17	100.05	100.14
	67.04	66.56	63.84	69.94	65.65	63.08	48.60	64.90
An	17.70	19.99	15.26	7.74	8.85	22.57	18.35	18.82
Ab	54.53	57.46	52.89	45.37	43.44	55.13	0.69	63.88
Or	27.77	22.55	31.85	46.89	47.71	22.30	80.96	17.30
Total	100.00	100.00	100.00	100.00	100.00	100.00	100.00	100.00
	82.34	80.69	86.88	91.74	89.71	79.75	73.07	82.56
Q	33.00	34.00	37.74	29.66	33.30	38.76	45.69	36.18
Ab	44.40	47.40	38.86	34.59	31.79	43.61	0.46	50.22
Or	22.61	18.60	23.40	35.75	34.91	17.64	53.85	13.60
Total	100	100	100	100	100	100	100	100

Table 3.5 Correlation matrix of chemical elelments for the Vumba Granite Gneiss.

	SiO2	Al2O3	Fe2O3	MnO	MgO	CaO	Na2O	K2O	TiO2	P2O5	Nb	Y	Rb	Zr	Sr	U	Th	Cr	V	La	Zn	Cu	Ni	Pb	Ga	Co	Ce	Nd	As	Ba	Sc	S
SiO2	1.000																															
Al2O3	-0.792	1.000																														
Fe2O3	-0.884	0.698	1.000																													
MnO	-0.171	0.529	0.353	1.000																												
MgO	-0.835	0.707	0.922	0.233	1.000																											
Na2O	-0.097	0.204	0.475	0.304	0.491	0.886	1.000																									
K2O	0.166	-0.358	-0.547	-0.545	-0.544	-0.964	-0.943	1.000																								
TiO2	-0.851	0.460	0.840	-0.141	0.831	0.348	0.304	-0.263	1.000																							
P2O5	-0.105	-0.311	0.251	-0.440	0.249	0.340	0.442	-0.271	0.569	1.000																						
Nb	0.212	-0.400	-0.277	-0.136	-0.362	-0.647	-0.489	0.542	-0.213	-0.294	1.000																					
Y	-0.019	-0.203	-0.175	-0.148	-0.344	-0.678	-0.597	0.653	-0.066	-0.274	0.897	1.000																				
Rb	-0.005	-0.054	-0.311	-0.017	-0.394	-0.800	-0.864	0.807	-0.270	-0.579	0.741	0.849	1.000																			
Zr	-0.028	-0.206	-0.294	-0.525	-0.353	-0.843	-0.709	0.817	-0.005	-0.217	0.724	0.863	0.765	1.000																		
Sr	-0.356	0.301	0.651	0.160	0.887	0.894	0.874	-0.856	0.578	0.625	-0.705	-0.742	-0.914	-0.746	1.000																	
U	0.344	-0.238	-0.297	0.273	-0.208	-0.266	-0.378	0.220	-0.513	-0.485	0.313	0.032	0.351	-0.141	-0.393	1.000																
Th	0.067	-0.337	-0.428	-0.631	-0.438	-0.919	-0.907	0.964	-0.128	-0.206	0.518	0.623	0.727	0.841	-0.762	0.152	1.000															
Cr	0.372	-0.809	-0.184	-0.416	-0.277	0.094	0.164	-0.026	-0.134	0.436	-0.159	-0.245	-0.406	-0.188	0.232	-0.004	0.073	1.000														
V	-0.818	0.876	0.947	0.206	0.926	0.708	0.623	-0.643	0.853	0.378	-0.478	-0.377	-0.540	-0.376	0.802	-0.477	-0.507	-0.087	1.000													
La	-0.485	0.045	0.355	-0.528	0.399	-0.306	-0.075	0.272	0.655	0.324	0.420	0.479	0.204	0.577	-0.014	-0.337	0.354	-0.105	0.334	1.000												
Zn	-0.701	0.546	0.624	-0.053	0.768	0.122	0.205	-0.182	0.774	0.197	0.032	0.069	-0.046	0.151	0.300	-0.336	-0.122	-0.610	0.630	0.687	1.000											
Cu	-0.260	0.227	-0.143	-0.450	-0.111	-0.424	-0.551	0.553	0.107	-0.104	-0.288	0.019	0.243	0.410	-0.270	-0.329	0.598	-0.064	-0.052	0.069	0.005	1.000										
Ni	-0.670	0.486	0.850	0.261	0.874	0.623	0.488	-0.547	0.665	0.287	-0.401	-0.447	-0.462	-0.538	0.715	0.047	-0.439	0.110	0.822	0.217	0.403	-0.237	1.000									
Pb	0.411	-0.700	-0.641	-0.635	-0.635	-0.793	-0.696	0.839	-0.306	0.116	0.434	0.462	0.519	0.548	-0.627	0.239	0.766	0.327	-0.694	0.203	-0.383	0.286	-0.478	1.000								
Ga	-0.289	0.280	-0.074	-0.279	-0.042	-0.596	-0.800	0.568	0.127	-0.399	0.347	0.521	0.593	0.775	-0.542	-0.217	0.624	-0.554	-0.102	0.369	0.410	0.618	-0.397	0.083	1.000							
Co	-0.356	0.615	0.208	0.439	0.010	0.181	-0.129	-0.024	-0.058	-0.475	-0.330	-0.012	0.154	-0.012	-0.083	-0.255	-0.015	-0.176	0.181	-0.370	-0.209	0.492	-0.020	-0.335	0.267	1.000						
Ce	-0.008	-0.331	-0.196	-0.398	-0.314	-0.786	-0.664	0.744	0.009	-0.164	0.890	0.939	0.786	0.917	-0.712	0.076	0.779	-0.071	-0.366	0.583	0.087	0.111	-0.380	0.564	0.563	-0.161	1.000					
Nd	-0.062	-0.273	-0.235	-0.504	-0.315	-0.843	-0.731	0.857	0.011	-0.158	0.750	0.872	0.798	0.919	-0.730	0.034	0.859	-0.022	-0.372	0.624	0.050	0.309	-0.350	0.703	0.537	-0.081	0.931	1.000				
As	0.347	-0.617	-0.617	-0.600	-0.600	-0.890	-0.761	0.900	-0.284	-0.008	0.596	0.625	0.672	0.694	-0.743	0.246	0.817	0.132	-0.702	0.324	-0.235	0.263	-0.530	0.968	0.249	-0.342	0.702	0.817	1.000			
Ba	0.525	-0.229	-0.784	-0.180	-0.656	-0.763	-0.631	0.634	-0.698	-0.658	0.441	0.394	0.816	0.537	-0.835	0.309	0.519	-0.343	-0.795	-0.134	-0.212	0.272	-0.798	0.405	0.536	-0.002	0.365	0.397	0.520	1.000		
Sc	0.735	-0.565	-0.583	-0.067	-0.730	-0.146	0.031	0.050	-0.667	-0.203	0.333	0.234	0.026	0.179	-0.312	-0.033	0.049	0.417	-0.534	-0.319	-0.843	-0.232	-0.624	0.125	-0.089	0.035	0.199	0.073	0.104	0.353	1.000	
S	-0.084	0.302	0.103	-0.143	0.302	0.219	0.483	-0.378	0.227	0.101	-0.237	-0.263	-0.416	-0.028	0.336	-0.558	-0.353	-0.367	0.323	0.235	0.571	0.030	-0.077	-0.494	0.285	-0.120	-0.279	-0.305	-0.409	0.121	0.000	1.000

Table 3.6 Major (wt%) and trace (ppm) elements geochemistry for the Messica granite gneiss

Formation	Messica	Messica	Messica	Messica
Sample	SUS 10	BAN 02	BAN 04	CHI 06
SIO2	77.76	74.05	74.91	72.23
Al2O3	11.91	13.72	14.49	14.74
Fe2O3	2.22	1.72	1.17	1.6
MnO	0.02	0.01	0.01	0.01
MgO	0.65	0.36	0.22	0.22
CaO	1.87	1.52	2.28	0.72
Na2O	4.02	3.6	5.66	2.79
K2O	1.44	4.73	1.01	7.46
TiO2	0.24	0.26	0.17	0.22
P2O5	0.03	0.08	0.08	0.07
TOTAL	100.18	100.04	99.99	100.06
L.O.I.	0.39	0.57	0.51	0.53
Nb	4.5	3.2	4.3	4.2
Y	4.3	6.6	12.7	10.3
Rb	60.1	122.7	37.4	242.7
Zr	116.5	162.2	217.3	162.3
Sr	202.8	182.8	104.2	120.4
U	1.1	3.0	2.6	3.8
Th	22.6	68.3	145.7	58.1
Cr	158.9	126.1	140.3	114.8
V	31.1	23.8	20.5	20.8
La	3.5	53.2	147.4	28.9
Zn	42.4	29.7	16.6	26.2
Cu	0.2	0.8	0.4	7.3
Ni	4.7	1.8	0.0	1.1
Pb	22.0	52.4	25.1	59.1
Ga	15.7	14.7	18.3	18.6
Co	5.8	4.4	0.0	4.2
Ce	34.1	156.2	270.9	85.0
Nd	11.0	42.3	98.0	33.0
As	4.4	16.2	6.3	19.0
Ba	376.7	890.0	183.9	985.0
Sc	8.8	5.3	6.5	5.0
S	40.0	0.0	22.0	0.0

Table 3.7 C.I.P.W norm calculation (anhydrous; in wt%) for the Messica granite gneiss

Formation	Messica	Messica	Messica	Messica
Sample	SUS 10	BAN 02	BAN 04	CHI 06
Quartz	43.97	31.44	33.13	25.78
Anorthite	9.08	7.02	10.79	3.11
Hypersthene	1.62	0.90	0.55	0.55
Albite	34.02	30.46	47.89	23.61
Orthoclase	8.51	27.95	5.97	44.09
Apatite	0.07	0.19	0.19	0.16
Ilmenite	0.04	0.02	0.02	0.02
Corundum	0.41	0.11	0.13	0.93
Rutile	0.22	0.25	0.16	0.21
Hematite	2.22	1.72	1.17	1.60
Total	100.16	100.05	100.00	100.06
	51.61	65.43	64.65	70.81
An	17.60	10.73	16.69	4.40
Ab	65.91	46.55	74.08	33.34
Or	16.49	42.72	9.23	62.26
Total	100.00	100.00	100.00	100.00
	86.50	89.85	87.00	93.47
Q	50.84	34.99	38.09	27.58
Ab	39.32	33.90	55.05	25.26
Or	9.84	31.11	6.86	47.16
Total	100	100	100	100

Table 3.8 Correlation matrix of chemical elements for the Messica Granite Gneiss

	SiO2	Al2O3	Fe2O3	MnO	MgO	CaO	Na2O	K2O	TiO2	P2O5	Nb	Y	Rb	Zr	Sr	U	Th	Cr	V	La	Zn	Cu	Ni	Pb	Ga	Co	Ce	Nd	As	Ba	Sc	S
SiO2	1.000																															
Al2O3	-0.892	1.000																														
Fe2O3	-0.052	-0.183	1.000																													
MnO	-0.012	-0.011	0.885	1.000																												
MgO	0.164	-0.357	0.976	0.889	1.000																											
CaO	-0.297	0.516	0.403	0.753	0.369	1.000																										
Na2O	-0.022	0.471	-0.559	-0.112	-0.524	0.511	1.000																									
K2O	-0.303	-0.040	-0.204	-0.622	-0.304	-0.804	-0.637	1.000																								
TiO2	-0.203	-0.201	0.865	0.539	0.792	-0.023	-0.869	0.314	1.000																							
P2O5	-0.981	0.962	-0.043	0.008	-0.246	0.403	0.214	0.161	0.038	1.000																						
Nb	0.713	-0.507	-0.732	-0.662	-0.573	-0.550	0.310	0.009	-0.703	-0.648	1.000																					
Y	-0.076	0.411	-0.938	-0.684	-0.929	-0.061	0.799	-0.069	-0.946	0.218	0.577	1.000																				
Rb	-0.175	-0.185	-0.152	-0.592	-0.226	-0.858	-0.710	0.989	0.360	0.022	0.063	-0.149	1.000																			
Zr	-0.506	0.794	-0.714	-0.445	-0.796	0.247	0.792	-0.092	-0.741	0.641	0.120	0.880	-0.220	1.000																		
Sr	-0.238	-0.028	0.981	0.840	0.915	0.406	-0.578	-0.097	0.901	0.135	-0.842	-0.912	-0.068	-0.619	1.000																	
U	-0.489	0.486	-0.775	-0.863	-0.884	-0.466	0.176	0.644	-0.423	0.497	0.236	0.682	0.549	0.690	-0.644	1.000																
Th	-0.137	0.443	-0.947	-0.723	-0.954	-0.103	0.755	0.010	-0.914	0.267	0.547	0.996	-0.076	0.893	-0.907	0.743	1.000															
Cr	0.661	-0.536	-0.732	-0.753	-0.591	-0.706	0.151	0.206	-0.602	-0.630	0.980	0.520	0.262	0.062	-0.822	0.330	0.506	1.000														
V	0.257	-0.449	0.952	0.855	0.995	0.303	-0.544	-0.295	0.773	-0.341	-0.490	-0.930	-0.205	-0.844	0.876	-0.902	-0.957	-0.507	1.000													
La	-0.194	0.518	-0.908	-0.652	-0.924	0.000	0.804	-0.056	-0.910	0.334	0.475	0.993	-0.151	0.931	-0.861	0.714	0.994	0.420	-0.937	1.000												
Zn	0.519	-0.791	0.730	0.481	0.616	-0.205	-0.764	0.042	0.732	-0.647	-0.127	-0.882	0.172	-0.999	0.630	-0.725	-0.898	-0.078	0.864	-0.933	1.000											
Cu	-0.554	0.444	0.795	0.836	0.679	0.744	-0.152	-0.300	0.616	0.527	-0.955	-0.577	-0.339	-0.146	0.861	-0.454	-0.573	-0.991	0.601	-0.487	0.167	1.000										
Ni	0.609	-0.825	0.707	0.514	0.817	-0.144	-0.665	-0.082	0.646	-0.715	-0.058	-0.837	0.053	-0.963	0.585	-0.792	-0.865	-0.035	0.870	-0.896	0.990	0.137	1.000									
Pb	-0.319	0.055	-0.415	-0.771	-0.512	-0.809	-0.449	0.974	0.096	0.210	0.139	0.159	0.945	0.110	-0.303	0.793	0.236	0.321	-0.503	0.170	-0.159	-0.427	-0.272	1.000								
Ga	0.256	0.173	-0.792	-0.428	-0.704	0.119	0.904	-0.435	-0.991	-0.082	0.681	0.901	-0.474	0.700	-0.845	0.303	0.859	0.556	-0.685	0.863	-0.684	-0.557	-0.584	-0.226	1.000							
Co	0.168	-0.527	0.866	0.564	0.873	-0.103	-0.869	0.175	0.931	-0.323	-0.455	-0.985	0.269	-0.933	0.831	-0.629	-0.978	-0.378	0.888	-0.993	0.930	0.434	0.879	-0.051	-0.898	1.000						
Ce	-0.248	0.509	-0.939	-0.759	-0.973	-0.143	0.685	0.122	-0.849	0.362	0.472	0.974	0.026	0.909	-0.873	0.824	0.990	0.453	-0.984	0.984	-0.920	-0.537	-0.906	0.343	0.780	-0.956	1.000					
Nd	-0.153	0.466	-0.936	-0.701	-0.945	-0.070	0.773	-0.013	-0.915	0.287	0.527	0.996	-0.102	0.905	-0.894	0.733	0.999	0.480	-0.951	0.997	-0.910	-0.548	-0.875	0.213	0.863	-0.984	0.989	1.000				
As	-0.169	-0.020	-0.583	-0.888	-0.643	-0.867	-0.316	0.912	-0.097	0.088	0.353	0.316	0.890	0.177	-0.496	0.828	0.383	0.517	-0.619	0.307	-0.225	-0.614	-0.315	0.974	-0.032	-0.191	0.468	0.358	1.000			
Ba	-0.363	-0.061	0.122	-0.334	0.006	-0.660	-0.818	0.946	0.603	0.190	-0.259	-0.369	0.946	-0.301	0.231	0.413	-0.291	-0.059	0.003	-0.342	0.256	-0.018	0.121	0.852	-0.702	0.448	-0.171	-0.310	0.730	1.000		
Sc	0.900	-0.752	-0.466	-0.438	-0.271	-0.533	0.118	-0.071	-0.486	-0.864	0.944	0.289	0.024	-0.197	-0.616	-0.063	0.247	0.921	-0.175	0.171	0.195	-0.859	0.272	-0.006	0.491	-0.184	0.156	0.225	0.189	-0.261	1.000	
S	-0.304	0.264	0.843	0.956	0.785	0.823	-0.068	-0.527	0.546	0.300	-0.830	-0.605	-0.538	-0.252	0.853	-0.677	-0.627	-0.908	0.725	-0.541	0.284	0.956	0.292	-0.659	-0.455	0.462	-0.631	-0.600	-0.810	-0.241	-0.677	1.000

Table 3.9 Major (wt%) and trace (ppm) elements geochemistry for the Umkondo Group sandstone samples

Formation	Argillaceous	Argillaceous	Argillaceous	Argillaceous	Argillaceous	Argillaceous	Argillaceous	Argillaceous	Argillaceous	Quartzite	Quartzite	Quartzite	Quartzite	Quartzite
Sample	ESP 01	ESP 02	ESP 03	ESP 04	ESP 05	ESP 06	ESP 07	ESP 12	ESP 13	ESP 28	DAC 01	ESP 21	ROT 01	ROT 06
SIO2	93.50	93.47	96.00	94.90	91.04	86.38	94.08	93.16	89.65	77.14	77.59	84.17	82.7	98.29
Al2O3	4.07	4.35	2.80	3.33	6.80	10.44	4.21	3.92	6.71	9.11	9.16	6.75	8.53	0.58
Fe2O3	0.62	0.77	0.33	0.57	0.84	0.59	0.66	1.42	0.94	4.18	4.32	1.35	3.41	0.63
MnO	0.00	0.00	0.00	0.00	0.00	0.00	0.00	0.01	0.01	0.05	0.05	0.0988	0.005	0.0032
MgO	0.08	0.07	0.01	0.09	0.07	0.11	0.08	0.29	0.27	2.66	2.44	0.71	0.85	0.02
CaO	0.00	0.01	0.00	0.00	0.00	0.00	0.00	0.02	0.01	3.11	2.97	3.61	0.5	0
Na2O	0.15	0.06	0.00	0.00	0.04	0.07	0.01	0.51	0.03	1.16	0.97	1.45	1.31	0
K2O	1.50	1.22	0.93	0.98	0.74	1.74	0.91	0.42	2.22	1.95	2.11	1.05	2.23	0.23
TiO2	0.09	0.07	0.04	0.05	0.34	0.45	0.08	0.26	0.27	0.49	0.48	0.2982	0.5418	0.0277
P2O5	0.03	0.03	0.02	0.04	0.05	0.03	0.03	0.02	0.02	0.09	0.08	0.06	0.09	0.02
TOTAL	100.05	100.05	100.12	99.95	99.91	99.82	100.05	100.02	100.12	99.94	100.16	99.54	100.15	99.79
L.O.I.	1.60	1.86	1.21	1.31	3.20	4.70	1.80	1.71	2.00	1.12	1.10	3.99	1.31	0.32
V	21.50	24.40	20.60	20.40	42.70	47.00	26.40	125.30	43.60	71.30	69.10			
Nb	2.5	1.9	0.4	2.1	6.0	7.8	1.7	16.6	5.3	7.2	7.2	4.7	10.8	0.3
Y	10.1	4.8	21.8	5.6	8.4	18.3	5.2	98.4	5.9	25.1	24.7	9.3	28.6	2.3
Rb	47.0	33.6	27.9	47.0	30.2	58.4	33.8	182.2	78.3	72.8	71.4	41.8	92.9	7
Zr	57.9	46.8	28.0	35.3	189.4	327.5	48.4	201.1	181.6	177.8	164.2	153.8	213.2	37.7
Sr	18.6	15.8	15.9	16.7	15.2	14.9	10.9	37.2	12.2	160.1	171.5	55.7	24.6	2.6
U	1.1	1.0	0.0	1.0	1.6	0.2	0.0	2.5	0.7	1.7	0.8	0.2	2.9	0
Th	4.1	2.4	0.8	2.4	6.0	9.2	3.0	16.8	7.9	10.5	8.3	5.9	14.2	2
Cr	145.7	155.9	184.2	161.3	210.8	205.7	179.7	133.0	221.5	199.3	206.4	232.2	492.2	7.1
V	21.5	24.4	20.6	20.4	42.7	47.0	26.4	125.3	43.6	71.3	69.1	8.2	3.5	1.1
La	7.6	0.0	0.0	0.0	25.0	0.0	0.0	120.0	0.0	1.2	2.1	6	57	24
Zn	10.6	7.3	0.5	9.3	4.0	4.3	4.1	50.1	11.8	40.2	42.3	115.6	34.3	22.4
Cu	7.2	5.6	4.0	3.1	20.0	8.8	5.5	0.0	2.8	10.6	14.9	35.7	61.7	6.7
Ni	3.8	3.7	3.4	4.2	9.0	3.6	3.1	23.7	8.7	16.5	16.8	0	3.3	3.6
Pb	13.8	13.2	9.5	12.5	17.6	7.7	7.0	27.3	6.3	10.0	19.7	12.5	2.7	9
Ga	2.3	4.8	2.2	4.0	7.2	6.3	4.7	21.3	6.7	11.6	11.5	13.1	2.6	7
Co	6.1	7.8	3.3	2.9	3.2	4.5	9.7	8.8	6.3	13.7	6.3	12.3	16	3.8
Ce	14.5	1.0	21.2	28.2	55.1	45.1	9.2	204.6	11.2	41.4	31.9	9.7	10	0.5
Nd	11.5	0.0	9.4	14.9	32.1	25.0	0.0	134.2	0.4	11.8	10.9	5.6	8	0
As	0.0	0.0	0.0	0.0	4.1	2.5	0.0	9.5	0.0	0.0	0.0	2	4.4	3.3
Ba	634.2	628.5	344.3	522.5	355.5	471.6	345.9	884.0	562.2	517.3	605.5	12.8	64.7	1.9
Sc	4.5	4.4	2.0	2.4	9.9	14.0	3.7	28.3	7.1	13.2	11.3	2.7	33.6	1.1
S	7.0	20.0	0.0	0.0	28.0	56.0	0.0	0.0	0.0	505.0	588.0	0	0	0

Table 3.10 Major (wt%) and trace (ppm) elements geochemistry for the Umkondo mudstone samples

Formation	Argillaceous	Argillaceous	Argillaceous	Argillaceous	Argillaceous	Quartzite	Quartzite	Quartzite
Sample	ESP 10	ESP 11	ESP 16	ESP 17	ESP 19	DAC 02	DAC 03	DAC 04
SIO2	64.65	65.30	73.45	59.60	71.73	56.96	56.33	58.33
Al2O3	19.25	18.12	14.77	22.22	17.09	22.56	22.43	21.78
Fe2O3	6.72	7.34	4.38	10.01	4.68	8.52	9.50	8.28
MnO	0.01	0.03	0.02	0.02	0.03	0.05	0.05	0.03
MgO	1.80	2.62	1.33	0.85	0.91	2.51	2.75	2.47
CaO	0.06	0.04	0.09	0.09	0.14	0.05	0.06	0.05
Na2O	0.24	0.29	0.87	2.01	1.32	0.13	0.20	0.20
K2O	5.89	5.45	3.90	3.43	2.93	7.75	7.60	7.63
TiO2	0.84	0.72	0.87	0.96	0.91	0.81	0.80	0.93
P2O5	0.09	0.12	0.08	0.07	0.10	0.04	0.05	0.04
TOTAL	99.55	100.05	99.77	99.27	99.82	99.37	99.76	99.75
L.O.I.	6.79	6.50	4.23	4.21	3.26	4.73	5.10	4.70
Nb	4.4	13.4	15.0	18.4	17.6	12.9	12.5	12.1
Y	16.4	35.5	28.0	57.2	34.1	34.0	40.1	80.7
Rb	16.8	188.9	159.3	174.7	148.8	288.0	281.8	277.8
Zr	181.1	158.3	320.5	208.5	314.4	142.9	140.0	147.5
Sr	8.3	32.1	28.3	204.4	140.3	34.8	32.9	27.2
U	1.7	3.2	1.7	4.8	5.4	2.8	3.7	2.3
Th	7.2	15.0	16.3	18.2	19.5	19.0	19.1	17.6
Cr	218.1	211.1	319.1	185.1	237.4	148.0	154.1	156.3
V	27.6	142.1	110.5	135.2	122.1	163.3	163.9	197.5
La	15.9	37.4	52.3	27.6	16.9	18.8	53.8	121.1
Zn	18.6	119.5	33.3	38.3	43.7	106.3	87.2	56.1
Cu	8.7	0.0	1.3	0.0	0.0	14.8	8.9	11.9
Ni	13.8	92.4	32.4	73.3	49.8	50.5	57.4	59.4
Pb	0.0	6.9	3.4	14.5	16.0	3.9	8.5	0.0
Ga	5.9	19.8	17.4	29.5	18.6	27.9	30.1	26.1
Co	8.0	22.6	11.0	21.4	22.5	13.4	12.4	21.5
Ce	41.4	79.5	44.9	21.4	22.2	9.2	19.4	69.3
Nd	32.5	59.5	34.0	34.7	27.0	28.3	63.8	150.6
As	0.0	0.8	0.0	4.6	1.5	2.1	5.0	0.7
Ba	244.3	155.4	933.4	976.7	787.2	965.6	961.0	131.1
Sc	5.3	28.4	28.4	39.0	29.9	38.9	40.3	38.4
S	86.0	5.0	1.0	0.0	0.0	0.0	0.0	0.0

Table 3.11 Correlation matrix of chemical elements for the Umkondo Group sandstone samples

	SiO2	Al2O3	Fe2O3	MnO	MgO	CaO	Na2O	K2O	TiO2	P2O5	Nb	Y	Rb	Zr	Sr	U	Th	Cr	V	La	Zn	Cu	Ni	Pb	Ga	Co	Ce	Nd	As	Ba	Sc	S
SiO2	1.000																															
Al2O3	-0.861	1.000																														
Fe2O3	-0.914	0.583	1.000																													
MnO	-0.912	0.583	0.995	1.000																												
MgO	-0.925	0.606	0.990	0.994	1.000																											
CaO	-0.917	0.596	0.982	0.985	0.996	1.000																										
Na2O	-0.856	0.522	0.967	0.966	0.953	0.937	1.000																									
K2O	-0.711	0.688	0.522	0.550	0.574	0.566	0.409	1.000																								
TiO2	-0.882	0.933	0.708	0.696	0.691	0.666	0.683	0.536	1.000																							
P2O5	-0.860	0.605	0.892	0.876	0.910	0.925	0.826	0.443	0.654	1.000																						
Nb	-0.335	0.342	0.357	0.338	0.266	0.206	0.483	-0.092	0.598	0.112	1.000																					
Y	-0.046	-0.076	0.211	0.209	0.127	0.080	0.394	-0.372	0.222	-0.089	0.862	1.000																				
Rb	-0.153	0.050	0.273	0.274	0.187	0.118	0.422	-0.122	0.320	-0.066	0.911	0.916	1.000																			
Zr	-0.537	0.808	0.271	0.259	0.240	0.200	0.294	0.326	0.852	0.188	0.703	0.332	0.436	1.000																		
Sr	-0.902	0.569	0.991	0.990	0.991	0.992	0.960	0.516	0.670	0.901	0.292	0.184	0.212	0.218	1.000																	
U	-0.157	-0.005	0.323	0.291	0.241	0.195	0.453	-0.259	0.283	0.249	0.703	0.635	0.673	0.236	0.259	1.000																
Th	-0.460	0.448	0.453	0.443	0.379	0.314	0.572	0.085	0.680	0.195	0.975	0.796	0.896	0.743	0.382	0.669	1.000															
Cr	-0.542	0.703	0.297	0.315	0.340	0.344	0.124	0.599	0.597	0.378	-0.105	-0.437	-0.329	0.472	0.276	-0.369	-0.009	1.000														
V	-0.415	0.298	0.514	0.501	0.426	0.369	0.635	-0.066	0.581	0.230	0.964	0.893	0.919	0.577	0.454	0.705	0.953	-0.115	1.000													
La	0.182	-0.227	-0.012	-0.034	-0.119	-0.169	0.160	-0.563	0.079	-0.240	0.826	0.922	0.861	0.268	-0.065	0.735	0.723	-0.508	0.804	1.000												
Zn	-0.599	0.285	0.782	0.774	0.715	0.672	0.868	0.150	0.545	0.515	0.784	0.731	0.791	0.321	0.746	0.679	0.794	-0.156	0.880	0.574	1.000											
Cu	-0.509	0.574	0.395	0.347	0.385	0.422	0.281	0.195	0.558	0.643	-0.024	-0.315	-0.382	0.311	0.396	0.070	-0.027	0.553	-0.046	-0.259	-0.008	1.000										
Ni	-0.518	0.278	0.683	0.672	0.600	0.551	0.767	0.023	0.584	0.425	0.857	0.792	0.833	0.428	0.627	0.753	0.862	-0.053	0.947	0.699	0.949	0.069	1.000									
Pb	-0.040	-0.123	0.264	0.216	0.145	0.127	0.359	-0.427	0.165	0.121	0.678	0.740	0.646	0.132	0.242	0.755	0.545	-0.463	0.692	0.803	0.657	0.116	0.717	1.000								
Ga	-0.385	0.245	0.515	0.496	0.420	0.364	0.625	-0.119	0.533	0.245	0.944	0.877	0.909	0.511	0.449	0.738	0.922	-0.153	0.990	0.813	0.886	-0.050	0.952	0.724	1.000							
Co	-0.455	0.207	0.563	0.562	0.561	0.528	0.640	0.210	0.282	0.406	0.297	0.275	0.351	0.071	0.510	0.327	0.428	-0.107	0.440	0.154	0.568	-0.119	0.467	0.001	0.458	1.000						
Ce	0.025	-0.057	0.100	0.085	0.007	-0.043	0.274	-0.481	0.246	-0.113	0.899	0.954	0.888	0.416	0.057	0.720	0.810	-0.398	0.874	0.968	0.641	-0.204	0.757	0.771	0.870	0.161	1.000					
Nd	0.125	-0.135	0.002	-0.017	-0.095	-0.143	0.182	-0.536	0.158	-0.206	0.864	0.939	0.866	0.368	-0.039	0.707	0.759	-0.471	0.822	0.981	0.575	-0.241	0.691	0.783	0.819	0.097	0.992	1.000				
As	0.149	-0.047	-0.090	-0.121	-0.193	-0.238	0.063	-0.564	0.217	-0.241	0.848	0.842	0.764	0.478	-0.145	0.667	0.733	-0.329	0.765	0.944	0.434	-0.083	0.609	0.733	0.762	0.017	0.949	0.961	1.000			
Ba	-0.077	-0.077	0.226	0.209	0.138	0.087	0.354	-0.003	0.105	-0.077	0.662	0.686	0.811	0.168	0.182	0.672	0.641	-0.575	0.661	0.669	0.694	-0.402	0.626	0.667	0.672	0.288	0.627	0.646	0.510	1.000		
Sc	-0.324	0.330	0.348	0.328	0.260	0.204	0.491	-0.136	0.581	0.107	0.991	0.884	0.893	0.691	0.288	0.690	0.964	-0.147	0.962	0.832	0.752	-0.029	0.839	0.668	0.938	0.344	0.908	0.873	0.858	0.641	1.000	
S	-0.934	0.648	0.974	0.971	0.983	0.991	0.914	0.586	0.701	0.920	0.212	0.062	0.096	0.248	0.988	0.151	0.307	0.379	0.360	-0.188	0.650	0.480	0.530	0.152	0.352	0.451	-0.056	-0.152	-0.231	0.081	0.208	1.000

Table 3.12 Correlation matrix of chemical elelments for the Umkondo Group mudstone samples.

	SiO2	Al2O3	Fe2O3	MnO	MgO	CaO	Na2O	K2O	TiO2	P2O5	Nb	Y	Rb	Zr	Sr	U	Th	Cr	V	La	Zn	Cu	Ni	Pb	Ga	Co	Ce	Nd	As	Ba	Sc	S
SiO2	1.000																															
Al2O3	-0.976	1.000																														
Fe2O3	-0.938	0.932	1.000																													
MnO	-0.612	0.566	0.480	1.000																												
MgO	-0.590	0.427	0.407	0.640	1.000																											
CaO	0.618	-0.455	-0.527	-0.278	-0.852	1.000																										
Na2O	0.321	-0.164	-0.056	-0.408	-0.892	0.740	1.000																									
K2O	-0.753	0.635	0.518	0.623	0.906	-0.802	-0.848	1.000																								
TiO2	0.048	0.104	0.016	-0.384	-0.683	0.555	0.684	-0.394	1.000																							
P2O5	0.708	-0.701	-0.544	-0.514	-0.334	0.288	0.241	-0.648	-0.315	1.000																						
Nb	0.185	-0.099	-0.010	0.143	-0.474	0.571	0.721	-0.553	0.377	0.043	1.000																					
Y	-0.481	0.500	0.496	0.175	0.122	-0.142	0.134	0.228	0.530	-0.508	0.345	1.000																				
Rb	-0.598	0.540	0.497	0.826	0.552	-0.319	-0.282	0.565	-0.082	-0.669	0.370	0.586	1.000																			
Zr	0.888	-0.802	-0.801	-0.511	-0.809	0.858	0.602	-0.842	0.388	0.431	0.461	-0.303	-0.437	1.000																		
Sr	0.064	0.113	0.174	-0.161	-0.740	0.660	0.934	-0.679	0.622	0.129	0.743	0.262	-0.077	0.368	1.000																	
U	-0.017	0.168	0.178	0.256	-0.421	0.810	0.655	-0.469	0.277	0.178	0.712	0.178	0.135	0.213	0.835	1.000																
Th	-0.202	0.247	0.213	0.632	-0.019	0.301	0.290	-0.018	0.226	-0.401	0.817	0.482	0.790	0.101	0.428	0.589	1.000															
Cr	0.941	-0.951	-0.851	-0.659	-0.567	0.494	0.315	-0.703	0.052	0.590	0.138	-0.490	-0.583	0.855	-0.010	-0.201	-0.258	1.000														
V	-0.504	0.467	0.449	0.683	0.430	-0.223	-0.115	0.411	0.062	-0.547	0.495	0.753	0.953	-0.351	0.066	0.241	0.816	-0.531	1.000													
La	-0.263	0.177	0.169	0.116	0.385	-0.335	-0.300	0.429	0.247	-0.467	-0.026	0.777	0.500	-0.251	-0.310	-0.330	0.209	-0.203	0.605	1.000												
Zn	-0.426	0.318	0.368	0.743	0.737	-0.549	-0.480	0.510	-0.719	-0.068	0.102	0.059	0.659	-0.572	-0.276	0.085	0.380	-0.482	0.585	0.019	1.000											
Cu	-0.675	0.623	0.392	0.480	0.643	-0.573	-0.708	0.894	-0.109	-0.776	-0.560	0.168	0.431	-0.656	-0.559	-0.468	-0.043	-0.640	0.259	0.299	0.227	1.000										
Ni	-0.299	0.274	0.461	0.362	0.240	-0.210	0.187	-0.004	-0.187	0.135	0.554	0.494	0.517	-0.322	0.340	0.491	0.512	-0.368	0.652	0.176	0.863	-0.313	1.000									
Pb	0.163	-0.021	0.049	0.128	-0.557	0.697	0.766	-0.641	0.256	0.299	0.775	0.025	0.018	0.393	0.862	0.960	0.546	0.032	0.110	-0.436	0.002	-0.641	0.432	1.000								
Ga	-0.641	0.647	0.680	0.705	0.242	-0.123	0.146	0.294	0.157	-0.619	0.590	0.640	0.884	-0.353	0.337	0.427	0.847	-0.597	0.872	0.321	0.487	0.190	0.620	0.344	1.000							
Co	0.003	0.067	0.124	0.047	-0.158	0.226	0.414	-0.305	0.261	0.230	0.646	0.614	0.279	0.042	0.566	0.840	0.497	-0.193	0.530	0.228	0.246	-0.427	0.787	0.542	0.390	1.000						
Ce	0.207	-0.328	-0.190	-0.355	0.309	-0.422	-0.318	0.073	-0.235	0.391	-0.235	0.258	-0.107	-0.136	-0.408	-0.425	-0.359	0.195	0.064	0.541	0.121	-0.186	0.299	-0.443	-0.304	0.314	1.000					
Nd	-0.396	0.324	0.289	0.165	0.489	-0.433	-0.382	0.522	0.172	-0.409	-0.136	0.806	0.474	-0.444	-0.303	-0.251	0.127	-0.407	0.597	0.947	0.122	0.370	0.272	-0.423	0.292	0.340	0.592	1.000				
As	-0.597	0.656	0.733	0.568	0.011	0.067	0.339	0.082	0.129	-0.384	0.416	0.265	0.449	-0.295	0.521	0.622	0.545	-0.543	0.386	-0.117	0.220	0.001	0.403	0.588	0.752	0.139	-0.590	-0.104	1.000			
Ba	-0.017	0.088	0.084	0.330	-0.366	0.462	0.461	-0.248	0.209	-0.321	0.555	-0.179	0.260	0.347	0.442	0.400	0.579	0.085	0.121	-0.385	-0.042	-0.098	-0.090	0.518	0.468	-0.215	-0.845	-0.568	0.603	1.000		
Sc	-0.477	0.483	0.499	0.673	0.184	-0.013	0.168	0.208	0.189	-0.568	0.690	0.652	0.906	-0.193	0.327	0.429	0.929	-0.458	0.921	0.380	0.471	0.116	0.614	0.359	0.973	0.460	-0.243	0.317	0.629	0.470	1.000	
S	0.098	-0.095	-0.147	-0.518	-0.036	-0.176	-0.258	0.060	-0.120	0.265	-0.842	-0.511	-0.783	-0.118	-0.336	-0.452	-0.943	0.116	-0.846	-0.318	-0.456	0.176	-0.645	-0.447	-0.805	-0.566	0.088	-0.208	-0.399	-0.441	-0.911	1.000

Table 3.13 Average chemical composition and useful element ratios for different tectonic settings (From Bathia 1983) and average values for Umkondo Group

		Oceanic	Continental	Andean	Passive	Umkondo
		Island Arc	Island Arc	Type	Margin	Group
SiO2	wt%	58.83	70.69	73.86	81.95	89.43
Al2O3	wt%	17.11	14.04	12.89	8.41	5.77
Fe2O3	wt%	1.95	1.43	1.3	1.32	1.47
MnO	wt%	0.15	0.1	0.1	0.05	0.02
MgO	wt%	3.65	1.97	1.23	1.39	0.55
CaO	wt%	5.83	2.68	2.48	1.89	0.73
Na2O	wt%	4.1	3.12	2.77	1.07	0.41
K2O	wt%	1.6	1.89	2.9	1.71	1.3
TiO2	wt%	1.06	0.64	0.46	0.49	0.25
P2O5	wt%	0.26	0.16	0.09	0.12	0.06
Fe2O3+MgO	wt%	11.73	6.79	4.63	2.89	2.02
Al2O3/SiO2	wt%	0.29	0.2	0.18	0.1	0.06
K2O/Na2O	wt%	0.39	0.61	0.99	1.6	3.17
Al2O3/(Ca+Na)	wt%	1.72	2.42	2.56	4.15	5.06
Nb	ppm	2	8.5	10.7	7.9	5.15
Y	ppm	19.5	24.2	24.9	27.3	15.32
Rb	ppm	18	67	115	61	48.52
Zr	ppm	96	229	179	298	124.75
Sr	ppm	637	250	141	66	72.52
U	ppm	10.9	2.53	3.9	3.2	1.33
Th	ppm	2.27	11.1	18.8	16.7	5.37
Cr	ppm	37	51	26	39	199.03
V	ppm	131	89	48	31	38.72
La	ppm	8.72	24.4	33	33.5	20.33
Zn	ppm	89	74	52	26	35.4
Cu	ppm	23	11	8	6	14.83
Ni	ppm	11	13	10	8	8.32
Pb	ppm	6.9	15.1	24	16	10.63
Ga	ppm	17	13	14	8	8.27
Co	ppm	18	12	10	5	6.95
Ce	ppm	22.53	50.5	72.7	71.9	35.81
Nd	ppm	11.36	20.8	25.4	29	18.08
Ba	ppm	370	444	522	253	312.77
Sc	ppm	19.5	14.8	8	6	6.92
Rb/Sr		0.05	0.65	0.89	1.19	0.67
Ba/Rb		21.3	7.5	4.5	4.7	6.45
Ba/Sr		0.95	3.55	3.8	4.7	4.31
Th/U		2.1	4.6	4.8	5.6	4.04
Zr/Th		48	21.5	9.5	19.1	23.23
Zr/Nb		49.3	31.5	16.7	37.2	24.22
Zr/Y		5.67	9.6	7.2	12.4	8.14
Nb/Y		0.11	0.36	0.43	0.3	0.34
La/Y		0.48	1.02	1.33	1.31	1.32
La/Th		4.26	2.36	1.77	2.2	3.79
La/Sc		0.55	1.82	4.55	6.25	2.94
Th/Sc		0.15	0.85	2.59	3.06	0.78
Ni/Co		0.62	1.22	1.04	1.42	1.2
Sc/Ni		2.3	1.44	0.77	1.9	0.83
Sc/Cr		0.57	0.32	0.3	0.16	0.03
V/Ni		0.57	8.1	5	7.55	4.65
V/La		15.02	3.65	1.45	0.93	1.09
Ce/Sc		1.56	3.41	9.08	11.98	5.17
Th/Co		0.13	0.93	1.88	3.34	0.77

Table 3.14 Average trace (ppm) and rare earth element and useful element ratio of and Umkondo Group shales.

element	ppm	
Zr	194.32	
Th	14.78	
Sc	34.92	
V	152.04	
Cr	187.58	
Co	20.28	
Ni	65.08	
Cr/Th	12.69	
Co/Th	1.37	
Th/Sc	0.42	
Cr/Zr	0.97	
Cr/V	1.23	
Cr/Ni	2.88	
Ni/Co	3.21	
V/Ni	2.34	
REE (average)		
	ppm	N*
La	52.19	142.22
Ce	42.42	44.32
Pr	14.42	105.24
Nd	53.67	75.49
Sm	10.43	45.13
Eu	2.02	23.22
Gd	8.68	28.36
Tb	1.33	22.86
Dy	7.42	19.48
Ho	1.48	17.34
Er	4.19	16.82
Tm	0.66	18.56
Yb	4.23	17.06
Lu	0.65	17.01
(La/Yb)n		8.58
Eu/Eu*		0.65
(Gd/Yb)n		1.65
(Ce/Yb)		2.60
CIA		73

N* represents condrite normalized value
Eu/Eu* = Eu/(Sm x Gd) n05

Table 3.16 Major (wt%) and trace (ppm) elements geochemistry for the Báruè Complex gneiss

Complex	Barue	Barue	Barue	Barue	Barue	Barue
Sample	VAN 02	VAN 03	BAN 08	VAN 08	VAN 10	CHM 02
SIO2	70.65	57.99	70.64	62.50	69.18	69.05
Al2O3	14.21	14.44	14.16	14.81	13.56	14.60
Fe2O3	3.00	10.09	3.24	7.73	5.07	3.74
MnO	0.05	0.19	0.07	0.14	0.08	0.06
MgO	1.37	2.07	1.61	1.58	0.79	0.83
CaO	2.73	5.51	2.55	3.85	2.30	2.02
Na2O	3.60	3.50	3.76	3.36	2.97	3.34
K2O	3.99	2.80	3.33	3.64	4.65	5.26
TiO2	0.32	1.80	0.34	1.29	0.72	0.67
P2O5	0.12	0.70	0.12	0.45	0.20	0.22
TOTAL	100.04	99.08	99.82	99.35	99.52	99.80
L.O.I.	0.68	0.47	0.52	0.15	0.22	0.57
Nb	3.7	37.6	3.5	28.5	26.7	18.4
Y	16.0	73.7	19.2	60.6	64.3	35.3
Rb	97.7	68.1	93.4	94.5	102.2	122.7
Zr	87.8	540.0	122.0	409.3	390.0	269.2
Sr	247.8	475.2	249.8	406.9	261.4	389.8
U	0.0	3.8	0.7	1.5	3.5	0.5
Th	11.3	9.6	21.4	12.5	9.8	18.5
Cr	150.4	115.1	81.0	11.5	2.0	5.3
V	41.3	106.1	33.0	70.6	34.7	35.8
La	17.0	57.3	39.4	43.6	71.4	92.1
Zn	44.9	157.8	47.4	114.9	81.1	54.5
Cu	0.9	7.8	0.9	7.4	6.1	7.0
Ni	16.6	2.6	20.5	1.1	1.7	1.1
Pb	39.9	31.6	27.3	18.8	24.3	27.8
Ga	16.7	21.5	16.4	19.5	15.7	19.2
Co	5.2	9.0	6.6	9.0	19.1	5.6
Ce	56.6	171.4	79.0	153.4	158.4	159.4
Nd	18.9	81.7	27.7	71.4	88.4	55.9
As	9.3	4.2	0.0	0.0	0.0	0.0
Ba	838.0	829.9	733.4	2165.3	1901.0	2139.9
Sc	22.9	33.2	15.3	18.2	6.8	0.0
S	9.0	1401.0	66.0	476.0	343.0	53.0

Table 3.17 C.I.P.W norm calculation (anhydrous; in wt%) for the Báruè Complex gneiss

Complex	Barue	Barue	Barue	Barue	Barue	Barue
Sample	VAN 02	VAN 03	BAN 08	VAN 08	VAN 10	CHM 02
Quartz	27.30	15.58	28.50	20.03	28.60	24.55
Anorthite	10.83	15.42	11.87	14.58	9.93	8.58
Hypersth.	3.05	4.50	4.01	3.94	1.97	2.07
Albite	30.46	29.62	31.82	28.43	25.13	28.26
Orthoclase	23.58	16.65	19.68	21.51	27.48	31.08
Apatite	0.28	1.62	0.28	1.04	0.46	0.51
Ilmenite	0.11	0.41	0.15	0.30	0.17	0.13
Diopside	0.79	1.42				
Corundum			0.02			0.27
Hematite	3.00	10.09	3.24	7.73	5.07	3.74
Rutile			0.26	0.68	0.58	0.60
Sphene	0.65	3.89				
Total	100.05	99.10	99.82	99.36	99.52	99.80
An+Ab+Or	64.87	61.59	63.07	64.52	62.54	67.62
An	16.69	25.04	18.82	22.60	15.88	12.69
Ab	46.96	48.09	50.45	44.06	40.18	41.79
Or	36.35	26.87	31.20	33.34	43.94	45.96
Total	100.00	100.00	100.47	100.00	100.00	100.44
Q+Ab+Or	81.34	61.85	80.00	69.97	81.21	83.89
Q	33.56	25.19	35.63	28.63	35.22	29.26
Ab	37.45	47.89	39.78	40.63	30.94	33.69
Or	28.99	26.92	24.60	30.74	33.84	37.05
Total	100	100	100	100	100	100

Table 3.18 Correlation matrix of chemical elelments for the Barue Complex gneiss samples.

	SiO2	Al2O3	Fe2O3	MnO	MgO	CaO	Na2O	K2O	TiO2	P2O5	Nb	Y	Rb	Zr	Sr	U	Th	Cr	V	La	Zn	Cu	Ni	Pb	Ga	Co	Ce	Nd	As	Ba	Sc	S
SiO2	1.000																															
Al2O3	-0.476	1.000																														
Fe2O3	-0.985	0.341	1.000																													
MnO	-0.982	0.359	0.992	1.000																												
MgO	-0.678	0.409	0.616	0.702	1.000																											
CaO	-0.943	0.386	0.917	0.944	0.852	1.000																										
Na2O	0.043	0.384	-0.168	-0.088	0.642	0.191	1.000																									
K2O	0.592	-0.185	-0.570	-0.663	-0.964	-0.792	-0.574	1.000																								
TiO2	-0.987	0.409	0.989	0.988	0.559	0.889	-0.190	-0.481	1.000																							
P2O5	-0.996	0.449	0.981	0.971	0.652	0.935	-0.062	-0.561	0.990	1.000																						
Nb	-0.809	0.095	0.872	0.809	0.186	0.632	-0.596	-0.143	0.892	0.829	1.000																					
Y	-0.825	0.105	0.898	0.852	0.232	0.660	-0.572	-0.235	0.895	0.828	0.980	1.000																				
Rb	0.595	0.225	-0.635	-0.680	-0.748	-0.779	-0.195	0.837	-0.547	-0.598	-0.401	-0.437	1.000																			
Zr	-0.828	0.087	0.892	0.838	0.224	0.664	-0.552	-0.210	0.905	0.846	0.996	0.984	-0.455	1.000																		
Sr	-0.502	-0.163	0.546	0.461	-0.038	0.380	-0.496	0.076	0.606	0.573	0.782	0.856	-0.343	0.774	1.000																	
U	-0.946	0.369	0.972	0.975	0.598	0.858	-0.183	-0.572	0.947	0.924	0.833	0.898	-0.561	0.859	0.400	1.000																
Th	0.632	-0.102	-0.666	-0.642	-0.307	-0.832	0.337	0.295	-0.627	-0.609	-0.595	-0.637	0.452	-0.571	-0.232	-0.622	1.000															
Cr	-0.027	-0.097	-0.036	0.025	0.565	0.339	0.665	-0.561	-0.087	0.034	-0.352	-0.372	-0.569	-0.330	-0.134	-0.171	-0.185	1.000														
V	-0.663	-0.255	0.718	0.685	0.381	0.697	-0.255	-0.409	0.702	0.708	0.741	0.683	-0.797	0.758	0.823	0.574	-0.521	0.277	1.000													
La	-0.353	0.592	0.312	0.250	-0.186	0.059	-0.302	0.346	0.426	0.372	0.475	0.416	0.444	0.454	0.388	0.340	0.140	-0.722	-0.066	1.000												
Zn	-0.784	-0.145	0.858	0.821	0.362	0.737	-0.409	-0.398	0.839	0.812	0.903	0.884	-0.729	0.921	0.802	0.776	-0.592	0.003	0.941	0.123	1.000											
Cu	-0.600	0.102	0.855	0.581	-0.158	0.342	-0.733	0.215	0.720	0.635	0.925	0.862	-0.063	0.901	0.819	0.615	-0.386	-0.573	0.561	0.684	0.725	1.000										
Ni	0.534	-0.181	-0.583	-0.484	0.259	-0.251	0.785	-0.332	-0.652	-0.557	-0.866	-0.818	-0.101	-0.627	-0.885	-0.565	0.450	0.646	-0.403	-0.707	-0.595	-0.970	1.000									
Pb	0.028	0.284	-0.153	-0.115	0.399	0.201	0.682	-0.276	-0.144	-0.024	-0.447	-0.498	-0.150	-0.459	-0.252	-0.287	-0.140	0.850	-0.025	-0.421	-0.275	-0.542	0.520	1.000								
Ga	-0.437	-0.223	0.470	0.393	0.011	0.374	-0.372	0.025	0.525	0.515	0.670	0.530	-0.408	0.665	0.979	0.293	-0.194	0.050	0.850	0.249	0.761	0.690	-0.538	-0.095	1.000							
Co	-0.554	0.428	0.589	0.604	0.265	0.411	-0.262	-0.270	0.549	0.489	0.486	0.628	-0.063	0.493	-0.156	0.746	-0.511	-0.481	-0.045	0.327	0.264	0.355	-0.446	-0.437	-0.320	1.000						
Ce	-0.662	0.240	0.704	0.626	-0.056	0.393	-0.832	0.124	0.768	0.687	0.915	0.874	-0.051	0.902	0.742	0.695	-0.319	-0.630	0.484	0.774	0.688	0.977	-0.943	-0.584	0.596	0.466	1.000					
Nd	-0.774	0.257	0.833	0.781	0.128	0.547	-0.595	-0.100	0.850	0.770	0.940	0.965	-0.212	0.936	0.565	0.869	-0.539	-0.564	0.485	0.603	0.739	0.888	-0.879	-0.581	0.405	0.722	0.930	1.000				
As	0.006	-0.024	-0.067	-0.048	0.303	0.233	0.382	-0.255	-0.093	-0.004	-0.277	-0.311	-0.318	-0.297	-0.143	-0.211	-0.439	0.865	0.189	-0.840	-0.053	-0.428	0.396	0.893	0.008	-0.367	-0.538	-0.463	1.000			
Ba	0.091	-0.016	-0.021	-0.117	-0.749	-0.402	-0.849	0.763	0.044	-0.084	0.387	0.365	0.822	0.334	0.244	0.052	-0.046	-0.907	-0.184	0.626	0.030	0.843	-0.757	-0.898	0.082	0.345	0.616	0.524	-0.600	1.000		
Sc	-0.388	-0.362	0.416	0.450	0.597	0.622	0.203	-0.678	0.339	0.404	0.226	0.224	-0.926	0.260	0.317	0.288	-0.470	0.763	0.772	-0.636	0.602	-0.074	0.214	0.387	0.436	-0.208	-0.153	-0.034	0.601	-0.879	1.000	
S	-0.868	0.028	0.899	0.864	0.577	0.871	-0.149	-0.568	0.885	0.895	0.825	0.800	-0.807	0.852	0.748	0.797	-0.558	0.187	0.940	0.110	0.959	0.608	-0.460	-0.065	0.738	0.212	0.598	0.848	0.068	-0.191	0.677	1.000

APPENDIX 4

ANISOTROPY OF MAGNETIC SUSCEPTIBILITY DATA

Table 4.1 Field and AMS Data

		Field Data		Anisotropy of Magnetic Susceptibility Data								
		Foliation		Lineation		Foliation						
	Km	Trend	Dip	Trend	Plung	Trend	Dip	Pp%	Lp%	Fp%	T	Pflinn
BM003	47.8			41	59	203	29	1.6	1.0	0.6	-0.22	1.58
BM004	3294.1			327	82	67	1	24.7	17.3	6.3	-0.45	2.74
BM005	2447.5			50	58	294	15	24.5	14.8	8.4	-0.26	1.75
BM006	127.5			47	58	228	32	2.7	2.4	0.2	-0.82	10.53
BM007	122.0			275	30	174	18	0.7	0.4	0.3	-0.17	1.40
BM008	2680.4			326	80	155	10	26.0	21.9	3.4	-0.71	6.48
BM009	3156.1			357	81	105	3	8.7	5.1	3.4	-0.19	1.48
BM010	2065.6	280	23	33	44	288	15	11.3	4.5	6.5	0.17	0.70
BM011	1726.9			191	51	87	10	9.8	3.7	5.9	0.23	0.61
BM012	3052.1			244	32	101	52	12.1	4.3	7.5	0.27	0.57
BM013	11020.0			164	52	64	8	25.2	7.7	16.2	0.34	0.48
BM014	240.9			225	28	356	51	12.5	2.4	9.9	0.60	0.24
BM015	192.8			337	33	75	13	14.2	4.9	8.9	0.29	0.54
BM020	133.4			52	59	245	30	4.7	3.5	1.1	-0.52	3.21
BM021	110.6			117	74	261	13	3.8	1.8	2.0	0.04	0.93
BM022	141.8			19	58	178	30	3.4	2.3	1.0	-0.38	2.26
BM023	91.1			54	53	243	37	3.0	1.6	1.4	-0.07	1.16
BM024	63.2	262	40	54	53	274	30	4.3	3.2	1.0	-0.50	3.08
BM025	2737.5			355	57	254	7	8.5	3.6	4.7	0.12	0.78
BM027	1461.8	50	10	174	56	73	7	7.6	2.1	5.3	0.42	0.41
BM028	80.2			58	72	213	16	2.1	1.6	0.6	-0.47	2.79
BM029	98.1			57	54	243	36	3.2	2.1	1.1	-0.31	1.90
BM030	1175.3	2	20	98	69	4	2	14.2	10.8	3.1	-0.55	3.53
BM031	79.3			115	68	317	21	3.4	1.4	1.9	0.15	0.73
BM032	612.0	240	20	69	66	255	24	14.9	12.3	2.4	-0.66	5.20
BM033	718.2			27	78	239	10	19.4	6.2	12.4	0.32	0.50
BM034	1260.5	252	20	44	69	235	21	47.6	12.4	31.3	0.40	0.39
BM035	6864.3			359	72	252	5	32.8	16.7	13.8	-0.09	1.21
BM036	2766.1			3	54	261	8	16.9	10.2	6.0	-0.25	1.70
BM037	111.5			337	40	76	10	8.7	2.9	5.6	0.31	0.52

Table 4.2 Anisotropy of magnetic susceptibility data for the 30 sampling stations

	Km	K1	K2	K3	L	F	T	K1D	K1I	K2D	K2I	K3D	K3I	Pp%	Lp%	Fp%	X1	Y1	X2	Y2	X3	Y3
BM003A1	40.9	41.5	40.6	40.5	1.0	1.0	-0.8	52	58	227	32	319	2	1.840	0.216	0.122	0.306	0.242	-0.504	-0.466	-0.651	0.736
BM003C1	51.8	52.2	51.8	51.3	1.0	1.0	0.1	24	69	115	1	206	21	1.398	0.740	-0.007	0.103	0.235	0.898	-0.426	-0.347	-0.723
BM003A2	44.4	44.9	44.3	43.9	1.0	1.0	-0.1	52	63	298	12	202	24	1.785	0.815	0.012	0.257	0.204	-0.792	0.414	-0.294	-0.714
BM003C2	54.2	54.8	54.3	53.6	1.0	1.0	0.1	25	48	115	0	205	42	1.742	0.989	-0.020	0.211	0.460	0.903	-0.422	-0.247	-0.520
BM004A1	2590.3	2831.8	2507.7	2431.4	1.1	1.0	-0.6	19	88	197	2	287	0	16.368	3.119	0.626	0.008	0.025	-0.293	-0.936	-0.954	0.299
BM004A2	2973.5	3402.1	2843.3	2675.2	1.2	1.1	-0.5	338	86	161	4	71	0	27.024	6.247	0.854	-0.017	0.043	0.319	-0.913	0.943	0.330
BM004B1	3797.0	4344.7	3649.1	3397.1	1.2	1.1	-0.4	319	81	158	8	68	3	27.774	7.387	0.743	-0.072	0.081	0.347	-0.857	0.901	0.372
BM004B2	3815.5	4341.9	3717.2	3387.3	1.2	1.1	-0.3	326	75	148	15	58	1	28.061	9.700	0.450	-0.102	0.149	0.458	-0.733	0.843	0.529
BM005A1	2844.4	3205.2	2773.5	2554.4	1.2	1.1	-0.3	37	57	182	28	281	16	25.333	8.528	0.446	0.242	0.322	-0.031	-0.725	-0.837	0.166
BM005A2	3249.6	3648.6	3192.2	2907.9	1.1	1.1	-0.2	39	55	216	35	307	2	25.345	9.727	0.288	0.271	0.332	-0.379	-0.529	-0.789	0.590
BM005C1	1503.1	1671.5	1482.4	1355.2	1.1	1.1	-0.1	78	63	194	13	290	24	23.092	9.290	0.214	0.329	0.068	-0.220	-0.854	-0.724	0.267
BM005C2	2192.9	2508.8	2132.2	1937.8	1.2	1.1	-0.3	70	59	200	21	298	22	29.244	9.958	0.486	0.352	0.127	-0.269	-0.758	-0.701	0.374
BM006A1	130.7	133.6	130.3	128.3	1.0	1.0	-0.2	43	58	159	15	257	27	3.722	1.382	0.066	0.266	0.282	0.314	-0.803	-0.714	-0.170
BM006A2	115.4	117.6	114.6	114.0	1.0	1.0	-0.6	42	48	159	22	265	34	2.825	0.494	0.132	0.342	0.380	0.287	-0.734	-0.662	-0.063
BM006B1	150.7	153.4	149.8	148.9	1.0	1.0	-0.6	54	70	281	14	188	14	2.760	0.586	0.111	0.195	0.140	-0.857	0.165	-0.114	-0.867
BM006B2	113.2	115.4	112.7	111.4	1.0	1.0	-0.3	48	54	275	26	173	23	3.131	1.039	0.074	0.326	0.292	-0.742	0.066	0.094	-0.778
BM007A1	107.4	108.3	107.2	106.6	1.0	1.0	-0.3	111	16	219	47	7	39	1.441	0.530	0.027	0.793	-0.301	-0.327	-0.408	0.076	0.605
BM007A2	102.6	103.3	102.9	101.6	1.0	1.0	0.5	96	17	289	73	188	4	1.461	1.128	-0.059	0.837	-0.095	-0.200	0.070	-0.127	-0.960
BM007C1	137.5	138.2	137.7	136.6	1.0	1.0	0.4	261	53	47	32	147	17	1.086	0.768	-0.032	-0.440	-0.074	0.499	0.473	0.459	-0.710
BM007C2	140.6	141.7	140.8	139.2	1.0	1.0	0.3	307	41	215	2	123	49	1.603	1.030	-0.033	-0.467	0.349	-0.565	-0.805	0.420	-0.272
BM008B1	4513.4	5152.4	4248.2	4139.5	1.2	1.0	-0.8	339	77	228	5	137	12	24.384	2.617	1.194	-0.060	0.154	-0.707	-0.644	0.609	-0.643
BM008B2	2422.0	2769.9	2277.3	2218.8	1.2	1.0	-0.8	355	79	231	6	140	9	24.673	2.619	1.215	-0.012	0.131	-0.738	-0.593	0.588	-0.708
BM008C1	1863.6	2198.7	1736.4	1655.7	1.3	1.0	-0.7	303	77	89	11	181	7	32.506	4.829	1.390	-0.132	0.085	0.902	0.009	-0.012	-0.939
BM008C2	1922.8	2216.1	1848.6	1703.7	1.2	1.1	-0.4	276	81	73	8	164	3	29.824	8.437	0.725	-0.106	0.011	0.889	0.265	0.270	-0.933
BM009B1	3409.4	3536.0	3403.7	3288.6	1.0	1.0	-0.1	307	76	210	2	119	14	7.488	3.485	0.025	-0.135	0.103	-0.488	-0.854	0.762	-0.428
BM009B2	2927.6	3105.4	2885.6	2791.8	1.1	1.0	-0.4	356	80	192	9	102	3	11.175	3.342	0.272	-0.008	0.121	-0.193	-0.894	0.956	-0.199
BM009C1	3059.5	3167.9	3066.3	2944.5	1.0	1.0	0.1	167	82	4	7	273	2	7.550	4.117	-0.053	0.022	-0.093	0.060	0.931	-0.979	0.058
BM009C2	3227.9	3403.6	3197.0	3083.3	1.1	1.0	-0.3	19	74	195	16	285	1	10.339	3.671	0.177	0.066	0.188	-0.222	-0.820	-0.954	0.264
BM010A1	106.0	112.1	106.5	99.5	1.1	1.1	0.1	220	75	357	11	89	10	11.111	6.168	-0.113	-0.118	-0.139	-0.044	0.899	0.910	0.014
BM010A2	107.5	113.5	107.7	101.4	1.1	1.1	0.1	219	78	5	10	96	6	10.451	5.453	-0.055	-0.089	-0.111	0.076	0.910	0.939	-0.096
BM010B1	3272.6	3386.2	3321.1	3110.6	1.0	1.1	0.5	23	43	175	44	279	14	8.818	6.737	-0.307	0.219	0.525	0.048	-0.551	-0.857	0.139
BM010B2	4776.3	5089.4	4765.9	4473.6	1.1	1.1	0.0	37	42	188	44	293	15	13.721	6.513	0.016	0.342	0.456	-0.082	-0.548	-0.796	0.338
BM011B1	2348.6	2446.3	2336.1	2263.5	1.0	1.0	-0.2	204	36	326	37	86	33	8.024	3.190	0.096	-0.260	-0.592	-0.352	0.525	0.670	0.051
BM011B2	1534.1	1599.3	1535.5	1467.7	1.0	1.0	0.1	192	62	19	28	288	3	8.879	4.575	-0.030	-0.074	-0.339	0.240	0.685	-0.928	0.297
BM011C1	1680.2	1789.7	1714.0	1536.9	1.0	1.1	0.4	171	37	343	53	78	4	16.294	11.416	-0.452	0.101	-0.628	-0.127	0.427	0.948	0.198
BM011C2	1344.7	1426.8	1354.5	1252.8	1.1	1.1	0.2	232	77	356	8	88	11	13.725	8.018	-0.177	-0.129	-0.102	-0.058	0.928	0.901	0.033
BM012D1	3398.0	3607.0	3341.4	3245.5	1.1	1.0	-0.4	251	15	341	1	76	75	11.089	2.941	0.320	-0.815	-0.280	-0.316	0.938	0.179	0.046
BM012D2	3337.4	3491.0	3379.1	3142.2	1.0	1.1	0.4	254	26	357	25	125	52	11.048	7.505	-0.270	-0.718	-0.209	-0.037	0.756	0.378	-0.260
BM012E1	3150.5	3377.9	3252.9	2820.6	1.0	1.2	0.6	224	32	333	27	94	46	19.660	15.251	-0.729	-0.476	-0.493	-0.341	0.656	0.531	-0.037
BM012E2	2322.7	2463.9	2350.8	2153.2	1.0	1.1	0.3	250	50	350	9	88	39	14.332	9.113	-0.278	-0.455	-0.168	-0.152	0.906	0.611	0.024
BM013A1	8810.8	10211.6	9237.3	6983.5	1.1	1.3	0.5	141	30	257	38	25	38	46.128	32.206	-1.364	0.446	-0.554	-0.609	-0.138	0.256	0.562
BM013A2	6836.6	7921.3	7183.4	5405.2	1.1	1.3	0.5	138	25	250	39	24	41	46.424	32.811	-1.421	0.508	-0.568	-0.574	-0.209	0.243	0.533
BM013C1	15834.7	18278.3	16286.8	12939.0	1.1	1.3	0.3	357	82	171	8	261	1	41.219	25.845	-0.861	-0.005	0.103	0.148	-0.913	-0.980	-0.157
BM013C2	12597.8	13738.2	13644.2	10411.1	1.0	1.3	1.0	347	15	164	75	257	1	31.913	31.011	-1.908	-0.187	0.837	0.052	-0.182	-0.968	-0.220
BM014A1	794.9	856.5	780.7	747.5	1.1	1.0	-0.4	253	6	153	61	346	28	14.301	4.349	0.338	-0.910	-0.275	0.159	-0.314	-0.174	0.705

	Km	K1	K2	K3	L	F	T	K1D	K1I	K2D	K2I	K3D	K3I	Pp%	Lp%	Fp%	X1	Y1	X2	Y2	X3	Y3
BM014A2	271.9	323.5	266.5	225.8	1.2	1.2	-0.1	176	30	270	7	12	59	40.607	16.939	0.210	0.047	-0.703	-0.936	0.005	0.080	0.373
BM014C1	62.0	66.3	61.1	58.7	1.1	1.0	-0.4	165	44	302	37	51	23	10.348	3.173	0.298	0.139	-0.534	-0.535	0.336	0.604	0.491
BM014C2	103.7	113.2	107.5	90.3	1.1	1.2	0.5	114	17	221	44	8	41	21.800	16.368	-0.868	0.767	-0.338	-0.364	-0.413	0.084	0.583
BM014D1	141.8	152.4	137.5	135.4	1.1	1.0	-0.7	194	41	86	20	336	43	11.311	1.377	0.596	-0.137	-0.571	0.812	0.064	-0.228	0.521
BM014D2	71.3	73.6	70.6	69.8	1.0	1.0	-0.6	154	42	288	37	39	25	4.510	0.965	0.197	0.251	-0.514	-0.596	0.194	0.477	0.591
BM015C1	246.2	260.2	248.4	230.2	1.0	1.1	0.2	356	34	192	55	91	8	12.252	7.448	-0.203	-0.048	0.662	-0.087	-0.417	0.932	-0.016
BM015C2	87.2	92.5	86.7	82.4	1.1	1.1	-0.1	155	14	32	66	250	19	10.359	4.429	0.091	0.367	-0.792	0.157	0.251	-0.768	-0.278
BM015D1	116.1	119.9	118.5	110.0	1.0	1.1	0.7	359	2	225	87	89	2	7.954	6.853	-0.421	-0.011	0.984	-0.022	-0.022	0.984	0.010
BM015D2	321.7	357.6	324.4	283.2	1.1	1.1	0.2	324	36	179	48	68	18	24.979	13.836	-0.274	-0.372	0.520	0.008	-0.503	0.773	0.312
BM020A1	124.7	128.9	123.2	121.8	1.0	1.0	-0.6	51	59	149	5	242	31	5.182	0.990	0.226	0.293	0.240	0.489	-0.820	-0.620	-0.327
BM020A2	133.1	137.0	132.0	130.4	1.0	1.0	-0.5	46	62	148	6	241	28	4.564	1.128	0.161	0.251	0.239	0.507	-0.799	-0.639	-0.358
BM020B1	128.6	132.3	127.5	126.0	1.0	1.0	-0.5	45	56	159	15	257	29	4.459	1.034	0.168	0.291	0.288	0.313	-0.803	-0.696	-0.157
BM020B2	120.5	124.1	119.3	118.2	1.0	1.0	-0.6	42	57	141	5	234	32	4.388	0.780	0.201	0.271	0.296	0.606	-0.736	-0.550	-0.402
BM020C1	151.3	156.1	150.1	147.8	1.0	1.0	-0.4	62	58	156	2	248	32	5.085	1.405	0.156	0.347	0.180	0.397	-0.896	-0.634	-0.262
BM020C2	142.5	146.6	141.4	139.5	1.0	1.0	-0.5	62	60	155	2	247	30	4.602	1.231	0.148	0.321	0.174	0.407	-0.892	-0.652	-0.280
BM021A1	101.4	104.3	100.5	99.4	1.0	1.0	-0.6	357	39	261	8	162	50	4.301	0.932	0.176	-0.026	0.603	-0.921	-0.142	0.149	-0.466
BM021A2	102.7	105.8	101.6	100.7	1.0	1.0	-0.6	354	41	260	4	165	49	4.439	0.774	0.210	-0.065	0.585	-0.950	-0.165	0.124	-0.480
BM021B1	114.2	120.1	112.2	110.4	1.1	1.0	-0.6	139	64	355	22	260	14	7.823	1.484	0.344	0.208	-0.242	-0.065	0.792	-0.858	-0.156
BM021B2	124.0	130.1	121.9	120.0	1.1	1.0	-0.6	152	59	24	20	285	22	7.509	1.391	0.333	0.178	-0.328	0.328	0.743	-0.760	0.209
BM022A1	120.0	123.8	119.2	117.1	1.0	1.0	-0.4	54	49	324	0	234	41	5.118	1.607	0.133	0.400	0.289	-0.588	0.806	-0.474	-0.348
BM022A2	148.3	152.8	147.4	144.6	1.0	1.0	-0.3	71	50	337	4	244	40	5.124	1.769	0.107	0.457	0.153	-0.377	0.891	-0.541	-0.264
BM022C1	166.1	171.0	165.8	161.5	1.0	1.0	-0.1	324	58	55	1	145	32	5.387	2.410	0.034	-0.232	0.315	0.812	0.574	0.391	-0.562
BM022C2	132.9	136.4	132.3	130.0	1.0	1.0	-0.3	315	60	225	0	134	30	4.454	1.554	0.092	-0.260	0.263	-0.701	-0.708	0.502	-0.493
BM023A1	106.3	108.3	106.1	104.4	1.0	1.0	-0.1	46	55	144	6	238	34	3.262	1.401	0.031	0.302	0.296	0.553	-0.768	-0.564	-0.348
BM023A2	103.3	105.2	103.1	101.5	1.0	1.0	-0.1	51	56	149	5	243	33	3.167	1.366	0.030	0.321	0.255	0.488	-0.820	-0.597	-0.309
BM023C1	75.7	77.0	75.5	74.5	1.0	1.0	-0.2	60	46	153	2	245	44	2.800	1.160	0.035	0.462	0.262	0.446	-0.871	-0.501	-0.231
BM023C2	79.0	80.2	79.2	77.7	1.0	1.0	0.2	62	51	155	3	248	39	2.763	1.606	-0.036	0.415	0.220	0.406	-0.888	-0.566	-0.234
BM024A1	61.4	63.2	60.7	60.2	1.0	1.0	-0.7	41	48	154	19	258	36	4.124	0.705	0.214	0.333	0.384	0.362	-0.734	-0.632	-0.130
BM024A2	61.2	63.3	60.7	59.6	1.0	1.0	-0.4	42	54	157	17	258	30	5.026	1.436	0.167	0.291	0.319	0.325	-0.778	-0.688	-0.152
BM024C1	59.3	60.4	58.8	58.5	1.0	1.0	-0.7	46	60	179	22	278	20	2.644	0.431	0.142	0.265	0.256	0.010	-0.793	-0.805	0.107
BM024C2	70.8	73.6	70.3	68.6	1.0	1.0	-0.3	74	52	192	20	294	30	5.992	1.944	0.156	0.439	0.129	-0.166	-0.793	-0.640	0.288
BM025A1	1392.2	1458.2	1397.6	1320.7	1.0	1.1	0.1	194	58	349	30	86	11	10.294	5.757	-0.095	-0.098	-0.383	-0.135	0.696	0.892	0.067
BM025A2	1351.6	1420.2	1344.1	1290.6	1.1	1.0	-0.2	192	62	349	26	84	9	9.928	4.098	0.097	-0.069	-0.331	-0.138	0.738	0.912	0.097
BM025B1	3798.6	3986.2	3786.1	3623.4	1.1	1.0	-0.1	358	50	148	35	249	15	9.972	4.471	0.051	-0.015	0.478	0.345	-0.548	-0.802	-0.308
BM025B2	4407.4	4632.7	4391.4	4198.2	1.1	1.0	-0.1	355	52	138	33	241	18	10.315	4.587	0.057	-0.040	0.464	0.451	-0.509	-0.722	-0.407
BM027A1	103.8	108.2	104.0	99.1	1.0	1.0	0.1	68	79	337	0	247	11	7.927	4.263	-0.056	0.121	0.050	-0.390	0.920	-0.831	-0.353
BM027A2	112.6	118.4	112.8	106.7	1.0	1.1	0.1	47	75	163	7	255	13	9.617	5.042	-0.052	0.135	0.125	0.273	-0.900	-0.846	-0.231
BM027B1	2667.6	2768.6	2692.9	2541.3	1.0	1.1	0.4	168	52	330	36	66	9	8.893	5.932	-0.202	0.094	-0.450	-0.323	0.550	0.841	0.368
BM027B2	2963.3	3044.8	2994.8	2850.3	1.0	1.1	0.5	182	56	346	33	81	8	6.788	5.044	-0.217	-0.016	-0.409	-0.169	0.659	0.918	0.153
BM028B1	82.5	83.6	82.1	81.8	1.0	1.0	-0.6	50	74	296	6	205	14	1.892	0.357	0.089	0.147	0.122	-0.843	0.420	-0.366	-0.789
BM028B2	74.8	75.8	74.5	74.2	1.0	1.0	-0.7	47	68	299	7	206	20	1.775	0.285	0.092	0.194	0.181	-0.822	0.448	-0.353	-0.727
BM028C1	82.3	83.5	82.1	81.4	1.0	1.0	-0.4	56	73	310	5	219	16	2.118	0.674	0.057	0.175	0.118	-0.729	0.621	-0.532	-0.658
BM028C2	81.1	82.5	80.8	79.9	1.0	1.0	-0.3	75	72	306	12	213	14	2.853	0.954	0.070	0.217	0.057	-0.723	0.522	-0.474	-0.733
BM029A1	95.0	96.8	94.5	93.8	1.0	1.0	-0.5	51	57	317	2	226	33	2.762	0.719	0.097	0.308	0.254	-0.667	0.719	-0.485	-0.473
BM029A2	95.9	97.7	95.4	94.5	1.0	1.0	-0.4	58	56	327	1	237	34	2.950	0.830	0.094	0.354	0.223	-0.541	0.835	-0.551	-0.362
BM029B1	100.8	103.2	100.5	98.9	1.0	1.0	-0.3	55	51	153	7	249	38	3.780	1.394	0.070	0.384	0.269	0.421	-0.841	-0.578	-0.227
BM029B2	100.8	102.8	100.6	98.8	1.0	1.0	-0.1	64	52	157	3	249	38	3.495	1.578	0.022	0.415	0.205	0.382	-0.900	-0.578	-0.222

	Km	K1	K2	K3	L	F	T	K1D	K1I	K2D	K2I	K3D	K3I	Pp%	Lp%	Fp%	X1	Y1	X2	Y2	X3	Y3
BM030B1	696.2	735.5	687.9	665.2	1.1	1.0	-0.3	98	64	260	25	353	7	10.338	3.336	0.225	0.318	-0.043	-0.747	-0.129	-0.107	0.932
BM030B2	764.8	821.4	739.6	733.4	1.1	1.0	-0.9	76	62	251	28	342	2	11.760	0.824	0.655	0.330	0.084	-0.692	-0.235	-0.300	0.937
BM030C1	1343.8	1457.5	1294.0	1279.9	1.1	1.0	-0.8	91	69	261	21	353	3	13.720	1.090	0.739	0.257	-0.004	-0.795	-0.121	-0.125	0.964
BM030C2	1896.6	2073.2	1860.3	1756.3	1.1	1.1	-0.3	111	72	280	18	11	3	17.896	5.874	0.353	0.211	-0.081	-0.817	0.146	0.189	0.953
BM031A1	81.4	82.9	81.4	79.8	1.0	1.0	0.0	120	64	228	8	322	24	3.200	1.627	-0.006	0.273	-0.161	-0.685	-0.622	-0.477	0.600
BM031A2	77.7	79.0	77.9	76.3	1.0	1.0	0.2	133	66	228	2	319	24	3.065	1.758	-0.036	0.211	-0.199	-0.730	-0.656	-0.508	0.584
BM031C1	85.3	87.2	85.5	83.0	1.0	1.0	0.2	119	66	225	7	318	23	4.306	2.521	-0.059	0.261	-0.147	-0.664	-0.660	-0.518	0.580
BM031C2	73.0	74.4	73.2	71.5	1.0	1.0	0.2	68	69	219	18	312	9	3.286	1.913	-0.044	0.238	0.096	-0.519	-0.644	-0.679	0.612
BM032A1	594.1	647.6	573.2	561.6	1.1	1.0	-0.7	62	81	175	4	266	8	14.922	2.017	0.698	0.100	0.053	0.078	-0.965	-0.922	-0.066
BM032A2	776.8	857.8	755.4	717.2	1.1	1.1	-0.4	64	58	168	9	263	30	19.203	5.209	0.527	0.346	0.169	0.189	-0.903	-0.701	-0.083
BM032C1	530.4	563.5	526.4	501.2	1.1	1.1	-0.2	50	65	175	14	270	19	12.082	4.890	0.129	0.230	0.192	0.082	-0.862	-0.818	-0.003
BM032C2	546.8	607.1	530.1	503.3	1.1	1.1	-0.4	85	61	296	26	199	13	20.045	5.167	0.589	0.358	0.031	-0.676	0.325	-0.289	-0.831
BM033A1	963.1	1080.1	945.7	863.3	1.1	1.1	-0.2	20	79	136	5	227	10	24.698	9.387	0.297	0.048	0.131	0.663	-0.688	-0.663	-0.620
BM033A2	495.5	542.2	495.1	449.1	1.1	1.1	0.0	335	78	145	12	235	2	20.082	9.926	-0.047	-0.064	0.138	0.513	-0.725	-0.805	-0.560
BM033B1	423.2	445.9	433.7	389.8	1.0	1.1	0.6	135	46	351	38	246	19	13.867	10.839	-0.536	0.371	-0.376	-0.096	0.612	-0.753	-0.338
BM033B2	991.2	1049.0	1043.8	880.8	1.0	1.2	0.9	3	65	150	22	245	12	18.785	18.207	-1.141	0.014	0.309	0.399	-0.687	-0.802	-0.377
BM034A1	726.7	942.6	654.0	583.5	1.4	1.1	-0.5	62	52	153	1	244	38	60.054	11.800	2.037	0.405	0.213	0.450	-0.887	-0.558	-0.278
BM034A2	446.5	527.1	447.3	365.2	1.2	1.2	0.1	354	50	151	38	250	11	42.608	21.598	-0.292	-0.050	0.479	0.301	-0.548	-0.843	-0.306
BM034C1	2381.4	2754.5	2594.4	1795.3	1.1	1.4	0.7	77	79	319	5	228	9	53.001	44.154	-2.390	0.127	0.029	-0.624	0.723	-0.685	-0.608
BM034C2	1487.6	1803.7	1529.7	1129.3	1.2	1.4	0.3	28	56	143	16	243	29	58.963	35.004	-1.099	0.194	0.364	0.507	-0.683	-0.637	-0.331
BM035A1	5058.8	6043.5	4847.5	4285.4	1.2	1.1	-0.3	326	86	159	4	69	1	40.886	13.074	0.734	-0.028	0.041	0.342	-0.902	0.927	0.353
BM035A2	8637.9	9840.0	8584.3	7489.5	1.1	1.1	0.0	4	73	166	16	257	5	31.322	14.589	0.001	0.014	0.206	0.205	-0.826	-0.934	-0.208
BM035C1	7775.8	9000.5	7532.4	6794.5	1.2	1.1	-0.3	1	67	160	21	253	7	32.397	10.837	0.549	0.006	0.280	0.268	-0.750	-0.894	-0.269
BM035C2	5984.6	6840.7	5993.2	5119.9	1.1	1.2	0.1	353	58	148	29	244	12	33.513	17.009	-0.185	-0.044	0.385	0.382	-0.605	-0.806	-0.388
BM036B1	544.1	725.6	493.6	413.1	1.5	1.2	-0.4	28	67	186	22	279	8	73.050	18.824	1.741	0.132	0.252	-0.076	-0.791	-0.917	0.140
BM036B2	75.9	80.2	79.9	67.4	1.0	1.2	1.0	134	15	316	75	224	0	15.577	15.231	-1.151	0.618	-0.602	-0.128	0.131	-0.697	-0.713
BM036C1	5490.7	5945.1	5407.6	5119.5	1.1	1.1	-0.3	3	52	167	37	263	8	16.082	5.612	0.275	0.022	0.466	0.137	-0.610	-0.925	-0.111
BM036C2	4953.6	5303.3	4898.9	4658.6	1.1	1.1	-0.2	355	48	160	41	257	7	13.797	5.142	0.198	-0.046	0.506	0.197	-0.550	-0.909	-0.215
BM037B1	37.9	39.4	38.6	35.8	1.0	1.1	0.6	324	51	187	30	84	22	7.093	5.588	-0.376	-0.275	0.377	-0.085	-0.700	0.791	0.088
BM037B2	59.6	62.2	60.9	55.8	1.0	1.1	0.6	347	32	196	54	86	14	9.124	7.197	-0.437	-0.159	0.662	-0.120	-0.422	0.867	0.065
BM037C1	34.9	36.2	35.2	33.2	1.0	1.1	0.4	342	52	167	38	75	2	6.338	4.276	-0.215	-0.140	0.444	0.143	-0.599	0.949	0.254
BM037C2	313.6	327.4	315.8	297.7	1.0	1.1	0.2	336	39	171	50	72	7	9.506	5.767	-0.150	-0.249	0.558	0.078	-0.474	0.888	0.291

APPENDIX 5

MICROPROBE ANALYSES

Table 5.1 Microprobe analyses of amphibole for the Vumba granite gneiss (TSE 12)

	core	rim	core	rim	core	rim	core	rim	core	rim	average core	average rim	average
SiO_2	44.899	45.874	44.952	45.888	45.314	45.394	45.353	44.576	45.670	45.480	45.238	45.442	45.340
TiO_2	0.010	0.041	0.000	0.041	0.071	0.051	0.102	0.020	0.081	0.030	0.053	0.037	0.045
Al_2O_3	12.645	11.408	12.031	11.537	12.210	11.826	11.205	12.067	11.602	11.896	11.939	11.747	11.843
FeO	16.430	15.633	16.344	16.236	16.199	15.854	15.770	16.439	15.731	16.266	16.095	16.086	16.090
MnO	0.268	0.329	0.220	0.265	0.266	0.284	0.269	0.246	0.242	0.289	0.253	0.283	0.268
MgO	10.742	11.171	10.801	11.085	10.748	10.642	10.718	10.503	10.844	10.754	10.771	10.831	10.801
CaO	11.178	11.301	11.152	11.237	11.483	11.548	11.391	11.350	11.585	11.401	11.358	11.367	11.363
Na_2O	1.181	1.063	1.058	1.022	1.221	1.178	1.296	1.084	1.082	1.258	1.168	1.121	1.144
K_2O	0.511	0.451	0.468	0.446	0.481	0.458	0.452	0.476	0.454	0.442	0.473	0.455	0.464
Cr_2O3	0.000	0.000	0.000	0.000	0.000	0.000	0.018	0.014	0.000	0.037	0.004	0.010	0.007
NiO	0.003	0.034	0.000	0.101	0.083	0.000	0.018	0.000	0.043	0.000	0.029	0.027	0.028
Total	97.867	97.305	97.026	97.858	98.076	97.235	96.592	96.775	97.334	97.853	97.379	97.405	97.392
Ox	*24*	*24*	*24*	*24*	*24*	*24*	*24*	*24*	*24*	*24*	24	24	24
Si	6.925	7.083	6.987	7.062	6.972	7.031	7.075	6.962	7.059	7.011	7.004	7.030	7.017
Ti	0.001	0.005	0.000	0.005	0.008	0.006	0.012	0.002	0.009	0.003	0.006	0.004	0.005
Al	2.299	2.076	2.204	2.093	2.214	2.159	2.060	2.221	2.114	2.162	2.178	2.142	2.160
Fe	2.119	2.019	2.125	2.090	2.085	2.054	2.057	2.147	2.033	2.097	2.084	2.081	2.083
Mn	0.035	0.043	0.029	0.035	0.035	0.037	0.036	0.033	0.032	0.038	0.033	0.037	0.035
Mg	2.470	2.571	2.503	2.543	2.465	2.457	2.492	2.445	2.498	2.471	2.486	2.498	2.492
Ca	1.847	1.870	1.857	1.853	1.893	1.917	1.904	1.899	1.919	1.883	1.884	1.884	1.884
Na	0.353	0.318	0.319	0.305	0.364	0.354	0.392	0.328	0.324	0.376	0.351	0.336	0.343
K	0.101	0.089	0.093	0.088	0.094	0.091	0.090	0.095	0.090	0.087	0.093	0.090	0.092
Cr	0.000	0.000	0.000	0.000	0.000	0.000	0.002	0.002	0.000	0.005	0.000	0.001	0.001
Ni	0.000	0.004	0.000	0.013	0.010	0.000	0.002	0.000	0.005	0.000	0.004	0.003	0.003
Sum	16.151	16.078	16.117	16.084	16.142	16.105	16.123	16.136	16.082	16.134	16.123	16.107	16.115

Table 5.2 Microprobe analyses of amphibole for the Messica granite gneiss (BAN 03)

	core	rim	core	rim	core	rim	core	rim	core	rim	average core	average rim	average
SiO_2	46.707	46.100	46.140	46.305	46.811	46.712	46.580	46.363	46.264	45.888	46.500	46.274	46.387
TiO_2	0.061	0.000	0.081	0.091	0.000	0.000	0.061	0.010	0.000	0.071	0.041	0.034	0.038
Al_2O_3	8.642	8.738	8.524	8.368	9.350	8.445	8.322	9.020	8.828	10.942	8.733	9.103	8.918
FeO	17.605	18.172	18.219	18.090	18.355	18.355	18.271	17.493	17.920	18.909	18.074	18.204	18.139
MnO	0.240	0.229	0.278	0.277	0.276	0.280	0.231	0.274	0.338	0.271	0.273	0.266	0.269
MgO	10.725	10.063	10.150	10.364	9.941	9.969	10.343	10.051	10.270	9.309	10.286	9.951	10.119
CaO	11.651	11.574	11.543	11.608	11.799	11.684	11.705	11.797	11.735	11.583	11.687	11.649	11.668
Na_2O	0.832	0.941	0.737	0.960	0.776	0.913	0.739	0.935	0.834	0.885	0.784	0.927	0.855
K_2O	0.241	0.242	0.254	0.205	0.272	0.236	0.230	0.226	0.257	0.346	0.251	0.251	0.251
Cr_2O3	0.060	0.000	0.000	0.041	0.000	0.000	0.000	0.005	0.000	0.041	0.012	0.017	0.015
NiO	0.000	0.064	0.000	0.015	0.061	0.034	0.034	0.034	0.000	0.034	0.019	0.036	0.028
Total	96.764	96.123	95.926	96.324	97.641	96.628	96.516	96.208	96.446	98.279	96.659	96.712	96.686
Ox	*24*	*24*	*24*	*24*	*24*	*24*	*24*	*24*	*24*	*24*	24	24	24
Si	7.316	7.300	7.318	7.316	7.287	7.357	7.341	7.308	7.292	7.118	7.311	7.280	7.295
Ti	0.007	0.000	0.009	0.011	0.000	0.000	0.007	0.001	0.000	0.008	0.005	0.004	0.004
Al	1.596	1.631	1.594	1.558	1.716	1.568	1.546	1.676	1.640	2.001	1.618	1.687	1.652
Fe	2.306	2.407	2.417	2.390	2.390	2.418	2.408	2.306	2.362	2.453	2.377	2.395	2.386
Mn	0.032	0.031	0.037	0.037	0.036	0.037	0.031	0.037	0.045	0.036	0.036	0.035	0.036
Mg	2.504	2.375	2.400	2.441	2.307	2.340	2.430	2.362	2.413	2.153	2.411	2.334	2.373
Ca	1.956	1.964	1.962	1.965	1.968	1.972	1.977	1.992	1.982	1.925	1.969	1.964	1.966
Na	0.253	0.289	0.227	0.294	0.234	0.279	0.226	0.286	0.255	0.266	0.239	0.283	0.261
K	0.048	0.049	0.051	0.041	0.054	0.047	0.046	0.045	0.052	0.068	0.050	0.050	0.050
Cr	0.007	0.000	0.000	0.005	0.000	0.000	0.000	0.001	0.000	0.005	0.001	0.002	0.002
Ni	0.000	0.008	0.000	0.002	0.008	0.004	0.004	0.004	0.000	0.004	0.002	0.005	0.003
Sum	16.025	16.053	16.015	16.060	15.999	16.022	16.015	16.018	16.041	16.038	16.019	16.038	16.029

Table 5.3 Microprobe analyses of amphibole for the Nhansipfe megacrystic gneiss (BAN 07)

	core	rim	core	rim	core	rrm	core	rim	core	rim	average core	average rim	average
SiO_2	40.531	40.944	41.362	41.584	41.549	42.285	42.451	41.935	42.004	41.653	41.579	41.680	41.630
TiO_2	0.293	0.192	0.232	0.293	0.121	0.111	0.182	0.171	0.172	0.04	0.200	0.161	0.181
Al_2O_3	11.524	10.986	11.062	11.277	11.034	11.236	10.966	11.229	11.258	11.327	11.169	11.211	11.190
FeO	21.356	20.793	21.28	21.202	21.13	21.073	21.726	20.662	21.51	20.969	21.400	20.940	21.170
MnO	0.253	0.191	0.265	0.176	0.243	0.233	0.183	0.229	0.257	0.222	0.240	0.210	0.225
MgO	7.698	7.921	7.868	7.751	7.935	7.943	7.868	7.912	8.262	7.723	7.926	7.850	7.888
CaO	11.018	11.139	10.782	11.028	10.813	10.974	10.906	11.234	10.828	10.965	10.869	11.068	10.969
Na_2O	1.614	1.525	1.604	1.613	1.674	1.625	1.538	1.456	1.565	1.744	1.599	1.593	1.596
K_2O	1.647	1.609	1.534	1.575	1.551	1.547	1.527	1.622	1.523	1.542	1.556	1.579	1.568
Cr_2O3	0.1	0	0	0.009	0.023	0	0	0.027	0	0	0.025	0.007	0.016
NiO	0.061	0	0	0	0.031	0.107	0.04	0.006	0	0.04	0.026	0.031	0.029
Total	96.095	95.3	95.989	96.508	96.104	97.134	97.387	96.483	97.379	96.225	96.591	96.330	96.460
Ox	*24*	*24*	*24*	*24*	*24*	*24*	*24*	*24*	*24*	*24*	24	24	24
Si	6.662	6.759	6.778	6.772	6.795	6.826	6.847	6.811	6.776	6.797	6.772	6.793	6.782
Ti	0.035	0.023	0.028	0.035	0.015	0.013	0.022	0.020	0.020	0.005	0.024	0.019	0.022
Al	2.233	2.137	2.137	2.165	2.127	2.138	2.085	2.150	2.141	2.178	2.144	2.154	2.149
Fe	2.936	2.871	2.916	2.888	2.890	2.845	2.931	2.807	2.902	2.862	2.915	2.854	2.885
Mn	0.035	0.027	0.037	0.024	0.034	0.032	0.025	0.032	0.035	0.031	0.033	0.029	0.031
Mg	1.886	1.949	1.922	1.882	1.935	1.911	1.892	1.916	1.987	1.879	1.924	1.907	1.916
Ca	1.941	1.970	1.893	1.924	1.895	1.898	1.885	1.955	1.872	1.917	1.897	1.933	1.915
Na	0.514	0.488	0.510	0.509	0.531	0.509	0.481	0.459	0.490	0.552	0.505	0.503	0.504
K	0.345	0.339	0.321	0.327	0.324	0.319	0.314	0.336	0.313	0.321	0.323	0.328	0.326
Cr	0.013	0.000	0.000	0.001	0.003	0.000	0.000	0.003	0.000	0.000	0.003	0.001	0.002
Ni	0.008	0.000	0.000	0.000	0.004	0.014	0.005	0.001	0.000	0.005	0.003	0.004	0.004
Sum	16.609	16.563	16.541	16.528	16.552	16.505	16.486	16.489	16.535	16.546	16.545	16.526	16.536

Table 5.4 Microprobe ananlyses of amphibole for the Tchinhadzandze gneiss (BAN 08)

	core	rim	core	rim	core	rim	core	rim	core	rim	average core	average rim	average
SiO_2	43.807	44.187	43.067	43.079	43.006	43.609	43.551	44.199	43.703	43.164	43.427	43.648	43.537
TiO_2	0.000	0.030	0.122	0.081	0.091	0.101	0.020	0.081	0.030	0.071	0.053	0.073	0.063
Al_2O_3	10.342	10.173	10.503	10.282	10.500	10.637	10.252	9.721	10.196	10.006	10.359	10.164	10.261
FeO	18.291	18.674	18.038	18.082	17.827	17.712	18.627	17.881	18.305	18.147	18.218	18.099	18.158
MnO	0.590	0.545	0.610	0.559	0.511	0.578	0.523	0.538	0.500	0.571	0.547	0.558	0.553
MgO	10.260	10.495	10.378	10.078	10.318	10.425	10.532	10.926	10.355	10.510	10.369	10.487	10.428
CaO	11.547	11.456	11.438	11.394	11.405	11.483	11.555	11.583	11.505	11.535	11.490	11.490	11.490
Na_2O	1.459	1.474	1.555	1.489	1.486	1.607	1.416	1.125	1.431	1.373	1.469	1.414	1.442
K_2O	1.396	1.344	1.474	1.445	1.457	1.509	1.357	1.166	1.343	1.336	1.405	1.360	1.383
Cr_2O3	0.018	0.000	0.000	0.032	0.037	0.037	0.064	0.028	0.014	0.046	0.027	0.029	0.028
NiO	0.052	0.000	0.018	0.000	0.046	0.046	0.049	0.000	0.034	0.003	0.040	0.010	0.025
Total	97.762	98.378	97.203	96.521	96.684	97.744	97.946	97.248	97.416	96.762	97.402	97.331	97.366
Ox	*24*	*24*	*24*	*24*	*24*	*24*	*24*	*24*	*24*	*24*	24	24	24
Si	6.929	6.945	6.860	6.907	6.876	6.889	6.889	6.994	6.934	6.904	6.898	6.928	6.913
Ti	0.000	0.003	0.014	0.010	0.011	0.012	0.002	0.009	0.003	0.008	0.006	0.008	0.007
Al	1.928	1.885	1.972	1.943	1.979	1.981	1.912	1.813	1.907	1.886	1.939	1.902	1.921
Fe	2.420	2.455	2.403	2.425	2.384	2.340	2.464	2.366	2.429	2.427	2.420	2.403	2.411
Mn	0.079	0.073	0.082	0.076	0.069	0.077	0.070	0.072	0.067	0.077	0.074	0.075	0.074
Mg	2.419	2.459	2.464	2.409	2.459	2.455	2.484	2.577	2.449	2.506	2.455	2.481	2.468
Ca	1.957	1.929	1.952	1.957	1.954	1.944	1.959	1.964	1.956	1.977	1.956	1.954	1.955
Na	0.447	0.449	0.480	0.463	0.461	0.492	0.434	0.345	0.440	0.426	0.453	0.435	0.444
K	0.282	0.270	0.300	0.296	0.297	0.304	0.274	0.235	0.272	0.273	0.285	0.275	0.280
Cr	0.002	0.000	0.000	0.004	0.005	0.005	0.008	0.004	0.002	0.006	0.003	0.004	0.003
Ni	0.007	0.000	0.002	0.000	0.006	0.006	0.006	0.000	0.004	0.000	0.005	0.001	0.003
Sum	16.470	16.468	16.530	16.489	16.500	16.505	16.503	16.379	16.464	16.491	16.493	16.466	16.480

Table 5.5 Microprobe analyses of amphibole for the Nhansipfe megacrystic gneiss (VAN 08)

	core	rim	core	rim	core	rim	average core	average rim	average
SiO_2	41.517	41.402	40.985	41.310	41.163	41.051	41.222	41.254	41.238
TiO_2	0.071	0.171	0.252	0.020	0.171	0.050	0.165	0.080	0.123
Al_2O_3	11.435	11.580	11.429	11.372	11.325	11.432	11.396	11.461	11.429
FeO	22.671	22.344	22.427	22.285	22.441	22.688	22.513	22.439	22.476
MnO	0.548	0.489	0.509	0.500	0.515	0.473	0.524	0.487	0.506
MgO	6.816	7.216	7.015	7.405	6.928	6.833	6.920	7.151	7.036
CaO	11.109	11.038	11.038	10.996	10.964	11.110	11.037	11.048	11.043
Na_2O	1.351	1.442	1.530	1.618	1.609	1.280	1.497	1.447	1.472
K_2O	1.590	1.632	1.678	1.596	1.578	1.647	1.615	1.625	1.620
Cr_2O3	0.059	0.041	0.000	0.000	0.000	0.059	0.020	0.033	0.027
NiO	0.058	0.000	0.046	0.012	0.031	0.000	0.045	0.004	0.025
Total	97.225	97.355	96.909	97.114	96.725	96.623	96.953	97.031	96.992
Ox	*24*	*24*	*24*	*24*	*24*	*24*	24	24	24
Si	6.765	6.727	6.709	6.734	6.745	6.738	6.740	6.733	6.736
Ti	0.008	0.020	0.030	0.002	0.021	0.006	0.020	0.010	0.015
Al	2.196	2.218	2.205	2.185	2.187	2.212	2.196	2.205	2.201
Fe	3.090	3.036	3.070	3.038	3.075	3.115	3.078	3.063	3.071
Mn	0.076	0.067	0.071	0.069	0.071	0.066	0.073	0.067	0.070
Mg	1.656	1.748	1.712	1.799	1.692	1.672	1.687	1.740	1.713
Ca	1.940	1.922	1.936	1.921	1.925	1.954	1.934	1.932	1.933
Na	0.427	0.454	0.486	0.511	0.511	0.407	0.475	0.458	0.466
K	0.331	0.338	0.350	0.332	0.330	0.345	0.337	0.338	0.338
Cr	0.008	0.005	0.000	0.000	0.000	0.008	0.003	0.004	0.003
Ni	0.008	0.000	0.006	0.002	0.004	0.000	0.006	0.001	0.003
Sum	16.503	16.537	16.576	16.593	16.562	16.522	16.547	16.551	16.549

Table 5.6 Microprobe analyses of amphibole for the Nhansipfe megacrystic gneiss (VAN 10)

	core	rim	core	rim	core	rim	average core	average rim	average
SiO_2	40.725	40.880	40.491	40.413	41.555	41.621	40.924	40.971	40.948
TiO_2	0.150	0.181	0.080	0.170	0.080	0.090	0.103	0.147	0.125
Al_2O_3	10.844	11.044	11.020	10.757	11.118	11.486	10.994	11.096	11.045
FeO	24.589	24.836	24.856	24.682	25.379	25.165	24.941	24.894	24.918
MnO	0.501	0.511	0.465	0.485	0.436	0.477	0.467	0.491	0.479
MgO	4.884	4.952	5.065	5.211	4.999	5.144	4.983	5.102	5.043
CaO	10.818	10.800	10.753	10.724	10.810	10.848	10.794	10.791	10.792
Na_2O	1.538	1.840	1.507	1.539	1.385	1.321	1.477	1.567	1.522
K_2O	1.567	1.612	1.651	1.665	1.679	1.628	1.632	1.635	1.634
Cr_2O3	0.000	0.018	0.000	0.067	0.090	0.000	0.030	0.028	0.029
NiO	0.000	0.000	0.000	0.034	0.058	0.015	0.019	0.016	0.018
Total	95.616	96.674	95.888	95.747	97.589	97.795	96.364	96.739	96.552
Ox	*24*	*24*	*24*	*24*	*24*	*24*	24	24	24
Si	6.826	6.788	6.779	6.779	6.827	6.807	6.811	6.791	6.801
Ti	0.018	0.022	0.010	0.021	0.010	0.011	0.013	0.018	0.015
Al	2.142	2.161	2.175	2.127	2.153	2.214	2.157	2.167	2.162
Fe	3.447	3.449	3.480	3.463	3.487	3.442	3.471	3.451	3.461
Mn	0.071	0.072	0.066	0.069	0.061	0.066	0.066	0.069	0.067
Mg	1.220	1.226	1.264	1.303	1.224	1.254	1.236	1.261	1.249
Ca	1.943	1.921	1.929	1.928	1.903	1.901	1.925	1.917	1.921
Na	0.500	0.592	0.489	0.501	0.441	0.419	0.477	0.504	0.490
K	0.335	0.341	0.353	0.356	0.352	0.340	0.347	0.346	0.346
Cr	0.000	0.002	0.000	0.009	0.012	0.000	0.004	0.004	0.004
Ni	0.000	0.000	0.000	0.005	0.008	0.002	0.003	0.002	0.002
Sum	16.502	16.575	16.545	16.560	16.477	16.455	16.508	16.530	16.519

Table 5.7 Microprobe analyses of amphibole for the Chimoio gneiss (CHM 02)

	core	rim	core	rim	core	rim	average core	average rim	average
SiO_2	40.670	41.721	41.517	41.700	41.241	40.840	41.143	41.420	41.282
TiO_2	0.091	0.020	0.040	0.050	0.060	0.000	0.064	0.023	0.044
Al_2O_3	11.200	11.456	11.233	11.224	11.155	11.209	11.196	11.296	11.246
FeO	21.429	21.610	21.395	21.561	21.184	21.471	21.336	21.547	21.442
MnO	0.733	0.733	0.770	0.739	0.759	0.795	0.754	0.756	0.755
MgO	7.973	8.048	8.206	8.424	8.095	8.004	8.091	8.159	8.125
CaO	10.958	11.195	11.154	11.164	11.110	11.216	11.074	11.192	11.133
Na_2O	1.456	1.494	1.511	1.350	1.388	1.552	1.452	1.465	1.459
K_2O	1.858	1.720	1.752	1.737	1.811	1.832	1.807	1.763	1.785
Cr_2O3	0.000	0.000	0.018	0.059	0.014	0.000	0.011	0.020	0.015
NiO	0.006	0.006	0.104	0.000	0.000	0.000	0.037	0.002	0.019
Total	96.374	98.003	97.700	98.008	96.817	96.919	96.964	97.643	97.304
Ox	*24*	*24*	*24*	*24*	*24*	*24*	24	24	24
Si	6.683	6.722	6.716	6.718	6.727	6.679	6.709	6.706	6.707
Ti	0.011	0.002	0.005	0.006	0.007	0.000	0.008	0.003	0.005
Al	2.169	2.176	2.142	2.131	2.145	2.161	2.152	2.156	2.154
Fe	2.945	2.912	2.894	2.905	2.890	2.937	2.910	2.918	2.914
Mn	0.102	0.100	0.106	0.101	0.105	0.110	0.104	0.104	0.104
Mg	1.953	1.933	1.979	2.023	1.968	1.951	1.967	1.969	1.968
Ca	1.930	1.933	1.933	1.927	1.942	1.965	1.935	1.942	1.938
Na	0.464	0.467	0.474	0.422	0.439	0.492	0.459	0.460	0.460
K	0.390	0.354	0.362	0.357	0.377	0.382	0.376	0.364	0.370
Cr	0.000	0.000	0.002	0.008	0.002	0.000	0.001	0.003	0.002
Ni	0.001	0.001	0.014	0.000	0.000	0.000	0.005	0.000	0.003
Sum	16.648	16.598	16.625	16.597	16.601	16.678	16.625	16.624	16.624

Table 5.8 Microprobe analyses of plagioclase for the Vumba granite gneiss (TSE 12)

	core	rim	core	rim	core	rim	core	rim	core	rim	average core	average rim	average
SiO_2	56.651	55.320	55.612	56.884	56.772	56.810	55.663	55.741	57.377	56.681	56.415	56.287	56.351
TiO_2	0.000	0.000	0.000	0.000	0.000	0.052	0.010	0.062	0.000	0.000	0.002	0.023	0.012
Al_2O_3	26.843	27.655	28.113	27.215	27.231	26.777	27.812	27.584	26.582	27.313	27.316	27.309	27.313
FeO	0.003	0.084	0.005	0.000	0.045	0.021	0.004	0.081	0.104	0.030	0.032	0.043	0.038
MnO	0.000	0.000	0.000	0.000	0.000	0.000	0.000	0.000	0.000	0.000	0.000	0.000	0.000
MgO	0.000	0.000	0.000	0.000	0.000	0.000	0.000	0.000	0.000	0.000	0.000	0.000	0.000
CaO	9.315	10.390	10.441	9.455	9.334	9.048	10.172	9.974	8.808	9.332	9.614	9.640	9.627
Na_2O	6.235	5.603	5.333	6.145	5.985	6.213	5.506	5.818	6.432	6.016	5.898	5.959	5.929
K_2O	0.112	0.073	0.096	0.085	0.072	0.078	0.074	0.048	0.085	0.081	0.088	0.073	0.080
Cr_2O3	0.000	0.000	0.000	0.000	0.000	0.000	0.000	0.000	0.000	0.000	0.000	0.000	0.000
NiO	0.000	0.000	0.000	0.000	0.000	0.000	0.000	0.000	0.000	0.000	0.000	0.000	0.000
Total	99.159	99.125	99.600	99.784	99.439	98.999	99.241	99.308	99.388	99.453	99.365	99.334	99.350
Ox	*32*	*32*	*32*	*32*	*32*	*32*	*32*	*32*	*32*	*32*	32	32	32
Si	10.250	10.046	10.034	10.225	10.231	10.281	10.075	10.091	10.340	10.215	10.186	10.171	10.179
Ti	0.000	0.000	0.000	0.000	0.000	0.007	0.001	0.008	0.000	0.000	0.000	0.003	0.002
Al	5.725	5.919	5.979	5.766	5.784	5.712	5.933	5.886	5.646	5.802	5.813	5.817	5.815
Fe	0.000	0.013	0.001	0.000	0.007	0.003	0.001	0.012	0.016	0.005	0.005	0.007	0.006
Mn	0.000	0.000	0.000	0.000	0.000	0.000	0.000	0.000	0.000	0.000	0.000	0.000	0.000
Mg	0.000	0.000	0.000	0.000	0.000	0.000	0.000	0.000	0.000	0.000	0.000	0.000	0.000
Ca	1.806	2.022	2.019	1.821	1.802	1.755	1.973	1.935	1.701	1.802	1.860	1.867	1.863
Na	2.187	1.973	1.866	2.142	2.091	2.180	1.932	2.042	2.248	2.102	2.065	2.088	2.076
K	0.026	0.017	0.022	0.019	0.017	0.018	0.017	0.011	0.020	0.019	0.020	0.017	0.019
Cr	0.000	0.000	0.000	0.000	0.000	0.000	0.000	0.000	0.000	0.000	0.000	0.000	0.000
Ni	0.000	0.000	0.000	0.000	0.000	0.000	0.000	0.000	0.000	0.000	0.000	0.000	0.000
Sum	19.994	19.989	19.920	19.973	19.931	19.955	19.932	19.985	19.970	19.944	19.950	19.969	19.960

Table 5.9 Microprobe analyses of plagioclase for the Messica granite gneiss (BAN 03)

	core	rim	core	rim	core	rim	core	rim	core	rim	average rim	average rim	average
SiO_2	56.456	51.445	55.329	55.481	58.324	55.654	53.488	53.670	55.209	53.832	55.761	54.016	54.889
TiO_2	0.052	0.000	0.000	0.000	0.000	0.021	0.083	0.000	0.000	0.063	0.027	0.017	0.022
Al_2O_3	28.191	30.916	28.587	28.675	26.214	27.767	29.634	29.666	29.140	29.623	28.353	29.329	28.841
FeO	0.124	0.152	0.059	0.109	0.122	0.108	0.224	0.259	0.165	0.129	0.139	0.151	0.145
MnO	0.000	0.000	0.000	0.000	0.000	0.000	0.000	0.000	0.000	0.000	0.000	0.000	0.000
MgO	0.000	0.000	0.000	0.000	0.000	0.000	0.000	0.000	0.000	0.000	0.000	0.000	0.000
CaO	10.319	13.703	10.977	10.681	8.156	10.224	12.119	12.069	11.319	11.965	10.578	11.728	11.153
Na_2O	5.586	3.637	5.120	5.455	6.762	5.557	4.400	4.498	4.978	4.448	5.369	4.719	5.044
K_2O	0.021	0.018	0.023	0.031	0.045	0.032	0.025	0.030	0.030	0.057	0.029	0.034	0.031
Cr_2O3	0.000	0.000	0.000	0.000	0.000	0.000	0.000	0.000	0.000	0.000	0.000	0.000	0.000
NiO	0.000	0.000	0.000	0.000	0.000	0.000	0.000	0.000	0.000	0.000	0.000	0.000	0.000
Total	100.749	99.871	100.095	100.432	99.623	99.363	99.973	100.192	100.841	100.117	100.256	99.995	100.126
Ox	*32*	*32*	*32*	*32*	*32*	*32*	*32*	*32*	*32*	*32*	32	32	32
Si	10.069	9.359	9.947	9.946	10.460	10.068	9.673	9.686	9.867	9.710	10.003	9.754	9.879
Ti	0.007	0.000	0.000	0.000	0.000	0.003	0.011	0.000	0.000	0.008	0.004	0.002	0.003
Al	5.926	6.629	6.058	6.059	5.542	5.921	6.317	6.310	6.139	6.298	5.996	6.244	6.120
Fe	0.018	0.023	0.009	0.016	0.018	0.016	0.034	0.039	0.025	0.019	0.021	0.023	0.022
Mn	0.000	0.000	0.000	0.000	0.000	0.000	0.000	0.000	0.000	0.000	0.000	0.000	0.000
Mg	0.000	0.000	0.000	0.000	0.000	0.000	0.000	0.000	0.000	0.000	0.000	0.000	0.000
Ca	1.972	2.671	2.115	2.052	1.567	1.982	2.348	2.334	2.168	2.313	2.034	2.270	2.152
Na	1.932	1.283	1.785	1.896	2.352	1.949	1.543	1.574	1.725	1.556	1.867	1.652	1.759
K	0.005	0.004	0.005	0.007	0.010	0.007	0.006	0.007	0.007	0.013	0.007	0.008	0.007
Cr	0.000	0.000	0.000	0.000	0.000	0.000	0.000	0.000	0.000	0.000	0.000	0.000	0.000
Ni	0.000	0.000	0.000	0.000	0.000	0.000	0.000	0.000	0.000	0.000	0.000	0.000	0.000
Sum	19.929	19.970	19.919	19.976	19.950	19.947	19.932	19.950	19.930	19.917	19.932	19.952	19.942

Table 5.10 Microprobe analyses of plagioclase for the Nhansipfe megacrystic gneiss (BAN 07)

	core	rim	core	rim	core	rim	core	rim	core	rim	core	rim	core	rim	core	rim	core	rim	core	rim	core	rim	core	rim	av. core	av. rim	average
SiO_2	62.601	62.521	63.424	63.142	63.194	62.239	62.570	62.488	63.351	62.402	63.096	61.688	62.153	61.236	62.101	62.398	63.146	62.605	63.365	62.750	62.629	61.924	62.471	62.202	62.842	62.300	62.571
TiO_2	0.083	0.000	0.000	0.000	0.052	0.114	0.104	0.000	0.062	0.000	0.031	0.062	0.000	0.021	0.052	0.000	0.000	0.000	0.073	0.000	0.000	0.000	0.000	0.000	0.038	0.016	0.027
Al_2O_3	22.715	23.527	23.012	23.716	23.603	23.948	24.133	24.101	23.501	24.033	23.314	24.297	23.398	23.832	23.992	23.403	23.391	24.112	23.462	23.441	23.969	24.247	23.119	23.377	23.467	23.836	23.652
FeO	0.056	0.193	0.173	0.186	0.207	0.239	0.026	0.070	0.077	0.084	0.086	0.483	0.057	0.079	0.000	0.114	0.057	0.184	0.091	0.107	0.103	0.086	0.037	0.093	0.081	0.160	0.120
MnO	0.000	0.000	0.000	0.000	0.000	0.000	0.000	0.000	0.000	0.000	0.000	0.000	0.000	0.000	0.000	0.000	0.000	0.000	0.000	0.000	0.000	0.000	0.000	0.000	0.000	0.000	0.000
MgO	0.000	0.000	0.000	0.000	0.000	0.000	0.000	0.000	0.000	0.000	0.000	0.000	0.000	0.000	0.000	0.000	0.000	0.000	0.000	0.000	0.000	0.000	0.000	0.000	0.000	0.000	0.000
CaO	4.514	5.145	4.868	5.397	5.051	5.400	5.528	5.547	4.949	5.525	4.769	5.809	5.200	5.801	5.721	5.181	5.003	5.550	4.990	5.057	5.414	5.785	4.765	5.135	5.064	5.444	5.254
Na_2O	8.880	8.617	8.600	8.383	8.567	8.637	8.411	8.270	8.486	8.237	8.807	8.239	8.238	8.081	8.129	8.537	8.359	8.210	8.527	8.529	8.273	8.150	8.912	8.664	8.516	8.380	8.448
K_2O	0.410	0.397	0.301	0.268	0.383	0.252	0.263	0.298	0.433	0.370	0.409	0.234	0.418	0.253	0.365	0.395	0.344	0.285	0.410	0.446	0.371	0.231	0.381	0.403	0.374	0.319	0.347
Cr_2O3	0.000	0.000	0.000	0.000	0.000	0.000	0.000	0.000	0.000	0.000	0.000	0.000	0.000	0.000	0.000	0.000	0.000	0.000	0.000	0.000	0.000	0.000	0.000	0.000	0.000	0.000	0.000
NiO	0.000	0.000	0.000	0.000	0.000	0.000	0.000	0.000	0.000	0.000	0.000	0.000	0.000	0.000	0.000	0.000	0.000	0.000	0.000	0.000	0.000	0.000	0.000	0.000	0.000	0.000	0.000
Total	99.26	100.40	100.38	101.09	101.06	100.83	101.04	100.77	100.86	100.65	100.51	100.81	99.46	99.30	100.36	100.03	100.30	100.95	100.92	100.33	100.76	100.42	99.69	99.87	100.38	100.46	100.42
Ox	32	32	32	32	32	32	32	32	32	32	32	32	32	32	32	32	32	32	32	32	32	32	32	32	32	32	32
Si	11.176	11.058	11.187	11.074	11.091	10.973	10.988	10.999	11.126	11.002	11.128	10.895	11.077	10.952	10.983	11.072	11.141	11.002	11.125	11.094	11.025	10.946	11.116	11.060	11.097	11.011	11.054
Ti	0.011	0.000	0.000	0.000	0.007	0.015	0.013	0.000	0.008	0.000	0.004	0.008	0.000	0.003	0.007	0.000	0.000	0.000	0.009	0.000	0.000	0.000	0.000	0.000	0.005	0.002	0.004
Al	4.780	4.905	4.784	4.903	4.883	4.977	4.995	5.000	4.865	4.994	4.847	5.058	4.915	5.024	5.001	4.894	4.864	4.995	4.855	4.885	4.973	5.052	4.849	4.899	4.884	4.965	4.925
Fe	0.008	0.029	0.026	0.027	0.030	0.035	0.004	0.010	0.011	0.012	0.013	0.071	0.008	0.012	0.000	0.017	0.008	0.027	0.013	0.016	0.015	0.013	0.006	0.014	0.012	0.024	0.018
Mn	0.000	0.000	0.000	0.000	0.000	0.000	0.000	0.000	0.000	0.000	0.000	0.000	0.000	0.000	0.000	0.000	0.000	0.000	0.000	0.000	0.000	0.000	0.000	0.000	0.000	0.000	0.000
Mg	0.000	0.000	0.000	0.000	0.000	0.000	0.000	0.000	0.000	0.000	0.000	0.000	0.000	0.000	0.000	0.000	0.000	0.000	0.000	0.000	0.000	0.000	0.000	0.000	0.000	0.000	0.000
Ca	0.864	0.975	0.920	1.014	0.950	1.020	1.040	1.046	0.931	1.044	0.901	1.099	0.993	1.112	1.084	0.985	0.946	1.045	0.939	0.958	1.021	1.096	0.909	0.978	0.958	1.031	0.995
Na	3.074	2.955	2.941	2.851	2.915	2.953	2.864	2.823	2.890	2.816	3.012	2.821	2.847	2.803	2.788	2.937	2.860	2.798	2.903	2.924	2.824	2.793	3.075	2.987	2.916	2.872	2.894
K	0.093	0.090	0.068	0.060	0.086	0.057	0.059	0.067	0.097	0.083	0.092	0.053	0.095	0.058	0.082	0.089	0.077	0.064	0.092	0.101	0.083	0.052	0.086	0.091	0.084	0.072	0.078
Cr	0.000	0.000	0.000	0.000	0.000	0.000	0.000	0.000	0.000	0.000	0.000	0.000	0.000	0.000	0.000	0.000	0.000	0.000	0.000	0.000	0.000	0.000	0.000	0.000	0.000	0.000	0.000
Ni	0.000	0.000	0.000	0.000	0.000	0.000	0.000	0.000	0.000	0.000	0.000	0.000	0.000	0.000	0.000	0.000	0.000	0.000	0.000	0.000	0.000	0.000	0.000	0.000	0.000	0.000	0.000
Sum	20.007	20.012	19.926	19.930	19.962	20.029	19.963	19.945	19.928	19.951	19.997	20.005	19.936	19.963	19.945	19.995	19.896	19.931	19.936	19.976	19.942	19.951	20.040	20.030	19.956	19.976	19.966

Table 5.11 Microprobe analyses of plagioclase for the Tchinhadzandze gneiss (BAN 08)

	core	rim	core	rim	core	rim	core	rim	core	rim	core	rim	average core	average rim	average
SiO_2	63.880	63.788	64.494	64.373	64.160	63.749	63.952	64.079	65.355	64.092	63.711	62.737	64.259	63.803	64.031
TiO_2	0.083	0.135	0.000	0.000	0.000	0.000	0.000	0.010	0.062	0.000	0.000	0.010	0.024	0.026	0.025
Al_2O_3	22.792	23.129	23.288	23.501	23.547	23.216	23.064	22.878	22.309	23.639	23.146	22.943	23.024	23.218	23.121
FeO	0.098	0.071	0.020	0.014	0.098	0.000	0.063	0.024	0.012	0.088	0.000	0.000	0.049	0.033	0.041
MnO	0.000	0.000	0.000	0.000	0.000	0.000	0.000	0.000	0.000	0.000	0.000	0.000	0.000	0.000	0.000
MgO	0.000	0.000	0.000	0.000	0.000	0.000	0.000	0.000	0.000	0.000	0.000	0.000	0.000	0.000	0.000
CaO	4.515	4.448	4.470	4.480	4.739	4.676	4.430	4.429	3.375	4.590	4.409	4.434	4.323	4.510	4.416
Na_2O	9.168	8.853	8.873	9.370	9.228	9.284	9.106	9.294	9.755	8.982	9.287	8.943	9.236	9.121	9.179
K_2O	0.284	0.187	0.276	0.192	0.193	0.094	0.193	0.123	0.136	0.133	0.118	0.178	0.200	0.151	0.176
Cr_2O3	0.000	0.000	0.000	0.000	0.000	0.000	0.000	0.000	0.000	0.000	0.000	0.000	0.000	0.000	0.000
NiO	0.000	0.000	0.000	0.000	0.000	0.000	0.000	0.000	0.000	0.000	0.000	0.000	0.000	0.000	0.000
Total	100.820	100.611	101.421	101.930	101.965	101.019	100.808	100.837	101.004	101.524	100.671	99.245	101.115	100.861	100.988
Ox	*32*	*32*	*32*	*32*	*32*	*32*	*32*	*32*	*32*	*32*	*32*	*32*	32	32	32.000
Si	11.221	11.203	11.232	11.176	11.147	11.171	11.218	11.237	11.402	11.161	11.193	11.179	11.236	11.188	11.212
Ti	0.011	0.017	0.000	0.000	0.000	0.000	0.000	0.001	0.008	0.000	0.000	0.001	0.003	0.003	0.003
Al	4.719	4.788	4.780	4.809	4.822	4.795	4.768	4.729	4.588	4.852	4.793	4.819	4.745	4.799	4.772
Fe	0.014	0.010	0.003	0.002	0.014	0.000	0.009	0.004	0.002	0.013	0.000	0.000	0.007	0.005	0.006
Mn	0.000	0.000	0.000	0.000	0.000	0.000	0.000	0.000	0.000	0.000	0.000	0.000	0.000	0.000	0.000
Mg	0.000	0.000	0.000	0.000	0.000	0.000	0.000	0.000	0.000	0.000	0.000	0.000	0.000	0.000	0.000
Ca	0.850	0.837	0.834	0.833	0.882	0.878	0.833	0.832	0.631	0.856	0.830	0.847	0.810	0.847	0.829
Na	3.123	3.015	2.996	3.154	3.109	3.155	3.097	3.160	3.300	3.033	3.164	3.090	3.131	3.101	3.116
K	0.064	0.042	0.061	0.043	0.043	0.021	0.043	0.028	0.030	0.030	0.026	0.040	0.045	0.034	0.039
Cr	0.000	0.000	0.000	0.000	0.000	0.000	0.000	0.000	0.000	0.000	0.000	0.000	0.000	0.000	0.000
Ni	0.000	0.000	0.000	0.000	0.000	0.000	0.000	0.000	0.000	0.000	0.000	0.000	0.000	0.000	0.000
Sum	20.002	19.914	19.907	20.018	20.017	20.019	19.968	19.991	19.961	19.944	20.006	19.976	19.977	19.977	19.977

Table 5.12 Microprobe analyses of plagioclase for the Nhansipfe megacrystic gneiss (VAN 08)

	core	rim	core	rim	core	rim	core	rim	core	rim	average core	average rim	average
SiO_2	62.296	62.589	61.948	62.276	62.029	63.203	62.677	62.048	62.206	61.983	62.2312	62.4198	62.326
TiO_2	0.021	0.000	0.073	0.000	0.000	0.000	0.000	0.000	0.031	0.000	0.025	0.000	0.013
Al_2O_3	23.314	23.551	23.109	23.509	23.519	23.512	23.352	23.517	23.221	23.277	23.303	23.473	23.388
FeO	0.053	0.062	0.081	0.137	0.043	0.091	0.133	0.090	0.076	0.076	0.077	0.091	0.084
MnO	0.000	0.000	0.000	0.000	0.000	0.000	0.000	0.000	0.000	0.000	0.000	0.000	0.000
MgO	0.000	0.000	0.000	0.000	0.000	0.000	0.000	0.000	0.000	0.000	0.000	0.000	0.000
CaO	4.968	5.123	4.950	5.002	4.976	4.978	4.986	5.086	4.935	4.969	4.963	5.032	4.997
Na_2O	8.339	8.500	8.187	8.739	8.388	8.242	8.137	8.470	8.336	8.459	8.277	8.482	8.380
K_2O	0.235	0.217	0.242	0.241	0.272	0.256	0.321	0.252	0.261	0.327	0.266	0.259	0.262
Cr_2O3	0.000	0.000	0.000	0.000	0.000	0.000	0.000	0.000	0.000	0.000	0.000	0.000	0.000
NiO	0.000	0.000	0.000	0.000	0.000	0.000	0.000	0.000	0.000	0.000	0.000	0.000	0.000
Total	99.226	100.042	98.590	99.904	99.227	100.282	99.606	99.463	99.066	99.091	99.143	99.756	99.450
Ox	*32*	*32*	*32*	*32*	*32*	*32*	*32*	*32*	*32*	*32*	32	32	32
Si	11.109	11.082	11.116	11.058	11.070	11.141	11.131	11.057	11.114	11.086	11.108	11.085	11.096
Ti	0.003	0.000	0.010	0.000	0.000	0.000	0.000	0.000	0.004	0.000	0.003	0.000	0.002
Al	4.900	4.915	4.888	4.920	4.947	4.885	4.888	4.940	4.890	4.907	4.903	4.913	4.908
Fe	0.008	0.009	0.012	0.020	0.006	0.013	0.020	0.013	0.011	0.011	0.012	0.014	0.013
Mn	0.000	0.000	0.000	0.000	0.000	0.000	0.000	0.000	0.000	0.000	0.000	0.000	0.000
Mg	0.000	0.000	0.000	0.000	0.000	0.000	0.000	0.000	0.000	0.000	0.000	0.000	0.000
Ca	0.949	0.972	0.952	0.952	0.952	0.940	0.949	0.971	0.945	0.952	0.949	0.957	0.953
Na	2.884	2.918	2.849	3.009	2.903	2.817	2.802	2.927	2.888	2.934	2.865	2.921	2.893
K	0.053	0.049	0.055	0.055	0.062	0.058	0.073	0.057	0.059	0.075	0.061	0.059	0.060
Cr	0.000	0.000	0.000	0.000	0.000	0.000	0.000	0.000	0.000	0.000	0.000	0.000	0.000
Ni	0.000	0.000	0.000	0.000	0.000	0.000	0.000	0.000	0.000	0.000	0.000	0.000	0.000
Sum	19.906	19.945	19.882	20.014	19.939	19.854	19.862	19.965	19.911	19.965	19.900	19.948	19.924

Table 5.13 Microprobe of plagioclase for the Nhansipfe megacrystic gneiss (VAN 10)

	core	rim	core	rim	core	rim	average core	average rim	average
SiO_2	35.737	35.676	35.939	35.621	35.627	35.823	35.768	35.707	35.737
TiO_2	0.317	0.267	0.436	0.327	0.297	0.347	0.350	0.314	0.332
Al_2O_3	15.024	14.964	14.564	14.787	14.725	14.904	14.771	14.885	14.828
FeO	27.360	26.850	26.968	27.469	27.294	26.790	27.207	27.036	27.122
MnO	0.232	0.219	0.290	0.291	0.277	0.270	0.266	0.260	0.263
MgO	5.655	5.782	5.610	5.908	5.889	5.619	5.718	5.770	5.744
CaO	0.011	0.036	0.009	0.000	0.016	0.001	0.012	0.012	0.012
Na_2O	0.056	0.060	0.000	0.039	0.082	0.062	0.046	0.054	0.050
K_2O	9.294	9.198	9.313	9.395	9.310	9.308	9.306	9.300	9.303
Cr_2O3	0.009	0.000	0.066	0.000	0.000	0.004	0.025	0.001	0.013
NiO	0.000	0.000	0.061	0.000	0.000	0.000	0.020	0.000	0.010
Total	93.695	93.052	93.256	93.837	93.517	93.128	93.489	93.339	93.414
Ox	*24*	*24*	*24*	*24*	*24*	*24*	24	24	24
Si	6.306	6.323	6.365	6.290	6.306	6.344	6.326	6.319	6.322
Ti	0.041	0.035	0.057	0.042	0.039	0.045	0.045	0.041	0.043
Al	3.125	3.126	3.040	3.077	3.072	3.111	3.079	3.105	3.092
Fe	4.038	3.980	3.995	4.056	4.040	3.968	4.024	4.001	4.013
Mn	0.035	0.033	0.044	0.044	0.042	0.041	0.040	0.039	0.039
Mg	1.487	1.528	1.481	1.555	1.554	1.483	1.507	1.522	1.515
Ca	0.002	0.007	0.002	0.000	0.003	0.000	0.002	0.002	0.002
Na	0.019	0.021	0.000	0.013	0.028	0.021	0.016	0.018	0.017
K	2.092	2.080	2.104	2.116	2.102	2.103	2.100	2.100	2.100
Cr	0.001	0.000	0.009	0.000	0.000	0.001	0.003	0.000	0.002
Ni	0.000	0.000	0.009	0.000	0.000	0.000	0.003	0.000	0.001
Sum	17.146	17.130	17.105	17.194	17.185	17.117	17.145	17.147	17.146

Table 5.14 Microprobe analyses of plagioclase for the Chimoio gneiss (CHM 02)

	core	rim	core	rim	core	rim	core	rim	core	rim	average core	average rim	average
SiO_2	62.664	62.103	62.833	62.622	62.915	62.652	62.103	62.747	62.638	62.702	62.631	62.565	62.598
TiO_2	0.000	0.000	0.083	0.052	0.062	0.052	0.000	0.000	0.000	0.093	0.029	0.039	0.034
Al_2O_3	23.518	23.249	23.116	23.383	23.081	23.438	22.943	23.169	23.259	23.550	23.183	23.358	23.271
FeO	0.108	0.041	0.085	0.031	0.012	0.022	0.094	0.072	0.091	0.062	0.078	0.046	0.062
MnO	0.000	0.000	0.000	0.000	0.000	0.000	0.000	0.000	0.000	0.000	0.000	0.000	0.000
MgO	0.000	0.000	0.000	0.000	0.000	0.000	0.000	0.000	0.000	0.000	0.000	0.000	0.000
CaO	4.873	4.954	4.818	5.051	4.879	4.934	4.800	4.700	4.811	4.976	4.836	4.923	4.880
Na_2O	8.571	8.618	8.681	8.624	8.916	8.719	8.589	8.759	8.590	8.672	8.669	8.678	8.674
K_2O	0.142	0.147	0.251	0.164	0.205	0.203	0.266	0.278	0.157	0.174	0.204	0.193	0.199
Cr_2O3	0.000	0.000	0.000	0.000	0.000	0.000	0.000	0.000	0.000	0.000	0.000	0.000	0.000
NiO	0.000	0.000	0.000	0.000	0.000	0.000	0.000	0.000	0.000	0.000	0.000	0.000	0.000
Total	99.876	99.112	99.867	99.927	100.070	100.020	98.795	99.725	99.546	100.229	99.631	99.803	99.717
Ox	*32*	*32*	*32*	*32*	*32*	*32*	*32*	*32*	*32*	*32*	32	32	32
Si	11.102	11.096	11.141	11.098	11.139	11.095	11.134	11.141	11.132	11.081	11.130	11.102	11.116
Ti	0.000	0.000	0.011	0.007	0.008	0.007	0.000	0.000	0.000	0.012	0.004	0.005	0.004
Al	4.911	4.896	4.831	4.884	4.817	4.892	4.848	4.849	4.872	4.905	4.856	4.885	4.871
Fe	0.016	0.006	0.013	0.005	0.002	0.003	0.014	0.011	0.014	0.009	0.012	0.007	0.009
Mn	0.000	0.000	0.000	0.000	0.000	0.000	0.000	0.000	0.000	0.000	0.000	0.000	0.000
Mg	0.000	0.000	0.000	0.000	0.000	0.000	0.000	0.000	0.000	0.000	0.000	0.000	0.000
Ca	0.925	0.948	0.915	0.959	0.926	0.936	0.922	0.894	0.916	0.942	0.921	0.936	0.928
Na	2.944	2.986	2.985	2.964	3.061	2.994	2.986	3.016	2.960	2.972	2.987	2.986	2.987
K	0.032	0.034	0.057	0.037	0.046	0.046	0.061	0.063	0.036	0.039	0.046	0.044	0.045
Cr	0.000	0.000	0.000	0.000	0.000	0.000	0.000	0.000	0.000	0.000	0.000	0.000	0.000
Ni	0.000	0.000	0.000	0.000	0.000	0.000	0.000	0.000	0.000	0.000	0.000	0.000	0.000
Sum	19.931	19.966	19.953	19.953	19.998	19.973	19.965	19.974	19.930	19.960	19.955	19.965	19.960

Table 5.16 Microprobe analyses of garnet for the staurolite-garnet-mica schist (SIT 02)

	core	rim	middle	middle	rim	rim	rim	rim	rim	middle	average ore	average middle	average rim	average
SiO_2	38.380	37.778	38.392	38.167	38.645	38.302	39.042	39.531	38.037	38.066	38.380	38.208	38.556	38.381
TiO_2	0.077	0.022	0.041	0.063	0.002	0.009	0.077	0.012	0.038	0.103	0.077	0.069	0.027	0.058
Al_2O_3	21.567	21.594	21.700	21.563	21.902	21.615	22.201	22.567	21.204	21.647	21.567	21.637	21.847	21.684
FeO	29.293	33.608	29.608	30.580	31.136	32.533	31.114	33.056	32.040	30.088	29.293	30.092	32.248	30.544
MnO	4.721	0.717	3.939	3.842	0.356	1.600	1.701	0.622	1.064	3.468	4.721	3.750	1.010	3.160
MgO	1.974	4.255	2.561	1.959	3.329	3.426	2.347	4.122	3.657	2.147	1.974	2.222	3.523	2.573
CaO	4.138	1.673	3.760	4.401	4.013	2.612	4.057	2.390	2.187	4.678	4.138	4.280	2.822	3.747
Na_2O	0.000	0.000	0.000	0.000	0.000	0.000	0.000	0.000	0.000	0.000	0.000	0.000	0.000	0.000
K_2O	0.000	0.000	0.000	0.000	0.000	0.000	0.000	0.000	0.000	0.000	0.000	0.000	0.000	0.000
Cr_2O3	0.000	0.030	0.000	0.043	0.000	0.017	0.052	0.047	0.060	0.000	0.000	0.014	0.034	0.016
NiO	0.000	0.000	0.000	0.000	0.000	0.000	0.000	0.000	0.000	0.000	0.000	0.000	0.000	0.000
Total	100.150	99.677	100.001	100.618	99.383	100.114	100.591	102.347	98.287	100.197	100.150	100.272	100.067	100.163
Ox	*24*	*24*	*24*	*24*	*24*	*24*	*24*	*24*	*24*	*24*	*24*	24	24	24
Si	6.105	6.018	6.096	6.064	6.117	6.075	6.132	6.085	6.119	6.055	6.105	6.072	6.091	6.089
Ti	0.009	0.003	0.005	0.007	0.000	0.001	0.009	0.001	0.004	0.012	0.009	0.008	0.003	0.007
Al	4.044	4.055	4.061	4.038	4.086	4.041	4.110	4.095	4.021	4.059	4.044	4.053	4.068	4.055
Fe	3.897	4.478	3.932	4.063	4.122	4.315	4.087	4.256	4.311	4.003	3.897	3.999	4.261	4.052
Mn	0.636	0.097	0.530	0.517	0.048	0.215	0.226	0.081	0.145	0.467	0.636	0.505	0.135	0.425
Mg	0.468	1.010	0.606	0.464	0.786	0.810	0.549	0.946	0.877	0.509	0.468	0.526	0.830	0.608
Ca	0.705	0.286	0.640	0.749	0.681	0.444	0.683	0.394	0.377	0.797	0.705	0.729	0.477	0.637
Na	0.000	0.000	0.000	0.000	0.000	0.000	0.000	0.000	0.000	0.000	0.000	0.000	0.000	0.000
K	0.000	0.000	0.000	0.000	0.000	0.000	0.000	0.000	0.000	0.000	0.000	0.000	0.000	0.000
Cr	0.000	0.004	0.000	0.005	0.000	0.002	0.006	0.006	0.008	0.000	0.000	0.002	0.004	0.002
Ni	0.000	0.000	0.000	0.000	0.000	0.000	0.000	0.000	0.000	0.000	0.000	0.000	0.000	0.000
Sum	15.864	15.950	15.869	15.907	15.839	15.903	15.802	15.863	15.862	15.903	15.864	15.893	15.870	15.876

Table 5.17 Microprobe of garnet for the Nhansipfe megacrystic gneiss (VAN 07)

	core	rim	rim	middle	middle	rim	rim	average core	average middle	average rim	average
SiO_2	37.656	38.848	38.961	38.595	38.352	38.408	38.663	37.656	38.474	38.677	38.269
TiO_2	0.021	0.011	0.000	0.024	0.014	0.028	0.027	0.021	0.019	0.018	0.019
Al_2O_3	21.201	21.812	21.853	21.793	21.562	21.396	21.559	21.201	21.678	21.603	21.494
FeO	28.705	29.206	29.390	28.759	29.594	28.772	29.136	28.705	29.177	29.099	28.994
MnO	2.286	2.729	2.345	2.253	2.395	2.655	2.579	2.286	2.324	2.526	2.379
MgO	3.496	3.077	3.422	3.718	3.450	3.067	3.518	3.496	3.584	3.336	3.472
CaO	5.013	4.853	4.823	5.075	4.996	4.931	4.914	5.013	5.036	4.889	4.979
Na_2O	0.000	0.000	0.000	0.000	0.000	0.000	0.000	0.000	0.000	0.000	0.000
K_2O	0.000	0.000	0.000	0.000	0.000	0.000	0.000	0.000	0.000	0.000	0.000
Cr_2O3	0.004	0.035	0.000	0.000	0.022	0.004	0.000	0.004	0.011	0.001	0.005
NiO	0.000	0.000	0.000	0.000	0.000	0.000	0.000	0.000	0.000	0.000	0.000
Total	98.382	100.571	100.794	100.217	100.385	99.261	100.396	98.382	100.301	100.150	99.611
Ox	*24*	*24*	*24*	*24*	*24*	*24*	*24*	*24*	24	24	24
Si	6.051	6.100	6.096	6.066	6.050	6.110	6.083	6.051	6.058	6.096	6.068
Ti	0.002	0.001	0.000	0.003	0.002	0.003	0.003	0.002	0.002	0.002	0.002
Al	4.015	4.037	4.030	4.037	4.009	4.012	3.998	4.015	4.023	4.013	4.017
Fe	3.858	3.835	3.846	3.780	3.904	3.828	3.834	3.858	3.842	3.836	3.845
Mn	0.311	0.363	0.311	0.300	0.320	0.358	0.344	0.311	0.310	0.337	0.320
Mg	0.837	0.720	0.798	0.871	0.811	0.727	0.825	0.837	0.841	0.784	0.821
Ca	0.863	0.817	0.809	0.855	0.844	0.841	0.828	0.863	0.850	0.826	0.846
Na	0.000	0.000	0.000	0.000	0.000	0.000	0.000	0.000	0.000	0.000	0.000
K	0.000	0.000	0.000	0.000	0.000	0.000	0.000	0.000	0.000	0.000	0.000
Cr	0.001	0.004	0.000	0.000	0.003	0.001	0.000	0.001	0.001	0.000	0.001
Ni	0.000	0.000	0.000	0.000	0.000	0.000	0.000	0.000	0.000	0.000	0.000
Sum	15.939	15.878	15.889	15.912	15.943	15.880	15.915	15.939	15.928	15.895	15.920

Table 5.18 Microprobe analyses of garnet for the Nhansipfe megacrystic gneiss (VAN 10)

	core	rim	rim	rim	core	rim	core	average core	average rim	average
SiO_2	37.588	37.592	37.561	37.554	37.408	38.236	37.412	37.469	37.736	37.603
TiO_2	0.039	0.023	0.027	0.020	0.010	0.029	0.029	0.026	0.025	0.025
Al_2O_3	20.832	20.892	20.701	20.303	20.300	21.077	20.308	20.480	20.743	20.612
FeO	27.535	26.872	26.272	26.970	26.848	24.888	27.908	27.430	26.251	26.840
MnO	5.705	5.854	6.355	5.651	5.641	5.488	5.850	5.732	5.837	5.785
MgO	1.172	1.022	0.854	1.107	1.075	0.897	1.129	1.125	0.970	1.048
CaO	5.754	6.485	6.732	6.370	6.275	6.963	5.911	5.980	6.638	6.309
Na_2O	0.000	0.000	0.000	0.000	0.000	0.000	0.000	0.000	0.000	0.000
K_2O	0.000	0.000	0.000	0.000	0.000	0.000	0.000	0.000	0.000	0.000
Cr_2O3	0.039	0.145	0.022	0.018	0.035	0.173	0.194	0.089	0.090	0.089
NiO	0.000	0.000	0.000	0.000	0.000	0.000	0.000	0.000	0.000	0.000
Total	98.664	98.885	98.524	97.993	97.592	97.751	98.741	98.332	98.288	98.310
Ox	*24*	*24*	*24*	*24*	*24*	*24*	*24*	24	24	24
Si	6.100	6.086	6.106	6.137	6.136	6.190	6.095	6.110	6.130	6.120
Ti	0.005	0.003	0.003	0.002	0.001	0.003	0.003	0.003	0.003	0.003
Al	3.985	3.987	3.967	3.910	3.925	4.022	3.900	3.936	3.972	3.954
Fe	3.737	3.639	3.572	3.686	3.683	3.370	3.803	3.741	3.567	3.654
Mn	0.784	0.803	0.875	0.782	0.784	0.753	0.807	0.792	0.803	0.797
Mg	0.284	0.247	0.207	0.270	0.263	0.216	0.274	0.274	0.235	0.254
Ca	1.001	1.125	1.173	1.115	1.103	1.208	1.032	1.045	1.155	1.100
Na	0.000	0.000	0.000	0.000	0.000	0.000	0.000	0.000	0.000	0.000
K	0.000	0.000	0.000	0.000	0.000	0.000	0.000	0.000	0.000	0.000
Cr	0.005	0.019	0.003	0.002	0.005	0.022	0.025	0.012	0.011	0.011
Ni	0.000	0.000	0.000	0.000	0.000	0.000	0.000	0.000	0.000	0.000
Sum	15.900	15.908	15.906	15.905	15.898	15.784	15.939	15.913	15.876	15.894

Table 5.19 Microrpobe analyses of biotite for the staurolite-garnet-mica schist (SIT 02)

	core	rim	core	rim	core	rim	core	rim	average core	average rim	average
SiO_2	37.222	36.794	36.582	35.280	37.312	37.135	37.061	36.904	37.044	36.528	36.786
TiO_2	0.151	0.040	0.201	0.111	0.091	0.050	0.151	0.060	0.149	0.065	0.107
Al_2O_3	19.329	19.146	19.217	19.026	19.244	19.229	19.974	18.701	19.441	19.026	19.233
FeO	18.347	17.799	17.570	18.156	17.246	17.453	16.678	17.924	17.460	17.833	17.647
MnO	0.028	0.054	0.046	0.002	0.033	0.047	0.000	0.026	0.027	0.032	0.030
MgO	10.975	10.618	11.052	11.295	11.541	11.494	10.663	11.373	11.058	11.195	11.126
CaO	0.000	0.038	0.000	0.016	0.000	0.002	0.005	0.024	0.001	0.020	0.011
Na_2O	0.272	0.254	0.198	0.141	0.304	0.200	0.188	0.031	0.241	0.157	0.199
K_2O	8.892	8.742	9.171	7.954	9.141	9.203	8.838	8.823	9.011	8.681	8.846
Cr_2O3	0.000	0.005	0.059	0.018	0.000	0.009	0.000	0.009	0.015	0.010	0.013
NiO	0.000	0.000	0.015	0.000	0.000	0.125	0.000	0.000	0.004	0.031	0.018
Total	95.216	93.490	94.111	91.999	94.912	94.947	93.558	93.875	94.449	93.578	94.014
Ox	*22*	*22*	*22*	*22*	*22*	*22*	*22*	*22*	22	22	22
Si	5.590	5.616	5.559	5.480	5.601	5.585	5.610	5.614	5.590	5.574	5.582
Ti	0.017	0.004	0.022	0.013	0.010	0.006	0.017	0.007	0.016	0.007	0.012
Al	3.421	3.445	3.442	3.483	3.405	3.409	3.564	3.353	3.458	3.422	3.440
Fe	2.304	2.272	2.233	2.359	2.165	2.195	2.112	2.280	2.203	2.277	2.240
Mn	0.004	0.007	0.006	0.000	0.004	0.006	0.000	0.003	0.003	0.004	0.004
Mg	2.457	2.416	2.504	2.615	2.582	2.577	2.406	2.579	2.487	2.547	2.517
Ca	0.000	0.006	0.000	0.003	0.000	0.000	0.001	0.004	0.000	0.003	0.002
Na	0.079	0.075	0.058	0.042	0.088	0.058	0.055	0.009	0.070	0.046	0.058
K	1.703	1.702	1.778	1.576	1.750	1.766	1.707	1.712	1.735	1.689	1.712
Cr	0.000	0.001	0.007	0.002	0.000	0.001	0.000	0.001	0.002	0.001	0.002
Ni	0.000	0.000	0.002	0.000	0.000	0.015	0.000	0.000	0.000	0.004	0.002
Sum	15.575	15.545	15.612	15.574	15.606	15.617	15.472	15.563	15.566	15.575	15.570

Table 5.20 Microprobe analyses of biotite for the Nhansipfe gneiss (VAN 07)

	core	rim	core	rim	core	rim	average core	average rim	average
SiO_2	36.114	36.222	36.225	36.414	35.827	36.116	36.055	36.251	36.153
TiO_2	0.410	0.330	0.230	0.339	0.230	0.301	0.290	0.323	0.307
Al_2O_3	14.333	14.481	14.578	14.684	14.313	14.665	14.408	14.610	14.509
FeO	22.626	22.843	22.876	22.590	22.559	23.017	22.687	22.817	22.752
MnO	0.112	0.090	0.099	0.104	0.107	0.099	0.106	0.098	0.102
MgO	8.991	9.144	9.038	8.985	8.656	8.766	8.895	8.965	8.930
CaO	0.000	0.020	0.050	0.064	0.046	0.036	0.032	0.040	0.036
Na_2O	0.076	0.047	0.115	0.072	0.037	0.041	0.076	0.053	0.065
K_2O	9.389	9.395	9.271	9.175	9.371	9.371	9.344	9.314	9.329
Cr_2O3	0.009	0.000	0.022	0.000	0.000	0.000	0.010	0.000	0.005
NiO	0.024	0.085	0.015	0.064	0.070	0.000	0.036	0.050	0.043
Total	92.084	92.657	92.519	92.491	91.216	92.412	91.940	92.520	92.230
Ox	*24*	*24*	*24*	*24*	*24*	*24*	24	24	24
Si	6.341	6.324	6.329	6.346	6.356	6.324	6.342	6.331	6.337
Ti	0.053	0.042	0.029	0.043	0.030	0.039	0.037	0.041	0.039
Al	2.966	2.980	3.002	3.017	2.993	3.027	2.987	3.008	2.997
Fe	3.323	3.335	3.343	3.293	3.347	3.371	3.337	3.333	3.335
Mn	0.017	0.013	0.015	0.015	0.016	0.015	0.016	0.014	0.015
Mg	2.353	2.380	2.354	2.334	2.289	2.288	2.332	2.334	2.333
Ca	0.000	0.004	0.009	0.012	0.009	0.007	0.006	0.007	0.007
Na	0.026	0.016	0.039	0.024	0.013	0.014	0.026	0.018	0.022
K	2.103	2.092	2.066	2.040	2.121	2.093	2.097	2.075	2.086
Cr	0.001	0.000	0.003	0.000	0.000	0.000	0.001	0.000	0.001
Ni	0.003	0.012	0.002	0.009	0.010	0.000	0.005	0.007	0.006
Sum	17.187	17.198	17.192	17.134	17.184	17.177	17.188	17.170	17.179

Table 5.21 Microprobe analyses of biotite for the Nhansipfe megacrystic gneiss (VAN 10)

	core	rim	core	rim	core	rim	average core	average rim	average
SiO_2	35.737	35.676	35.939	35.621	35.627	35.823	35.768	35.707	35.737
TiO_2	0.317	0.267	0.436	0.327	0.297	0.347	0.350	0.314	0.332
Al_2O_3	15.024	14.964	14.564	14.787	14.725	14.904	14.771	14.885	14.828
FeO	27.360	26.850	26.968	27.469	27.294	26.790	27.207	27.036	27.122
MnO	0.232	0.219	0.290	0.291	0.277	0.270	0.266	0.260	0.263
MgO	5.655	5.782	5.610	5.908	5.889	5.619	5.718	5.770	5.744
CaO	0.011	0.036	0.009	0.000	0.016	0.001	0.012	0.012	0.012
Na_2O	0.056	0.060	0.000	0.039	0.082	0.062	0.046	0.054	0.050
K_2O	9.294	9.198	9.313	9.395	9.310	9.308	9.306	9.300	9.303
Cr_2O3	0.009	0.000	0.066	0.000	0.000	0.004	0.025	0.001	0.013
NiO	0.000	0.000	0.061	0.000	0.000	0.000	0.020	0.000	0.010
Total	93.695	93.052	93.256	93.837	93.517	93.128	93.489	93.339	93.414
Ox	*24*	*24*	*24*	*24*	*24*	*24*	24	24	24
Si	6.306	6.323	6.365	6.290	6.306	6.344	6.326	6.319	6.322
Ti	0.041	0.035	0.057	0.042	0.039	0.045	0.045	0.041	0.043
Al	3.125	3.126	3.040	3.077	3.072	3.111	3.079	3.105	3.092
Fe	4.038	3.980	3.995	4.056	4.040	3.968	4.024	4.001	4.013
Mn	0.035	0.033	0.044	0.044	0.042	0.041	0.040	0.039	0.039
Mg	1.487	1.528	1.481	1.555	1.554	1.483	1.507	1.522	1.515
Ca	0.002	0.007	0.002	0.000	0.003	0.000	0.002	0.002	0.002
Na	0.019	0.021	0.000	0.013	0.028	0.021	0.016	0.018	0.017
K	2.092	2.080	2.104	2.116	2.102	2.103	2.100	2.100	2.100
Cr	0.001	0.000	0.009	0.000	0.000	0.001	0.003	0.000	0.002
Ni	0.000	0.000	0.009	0.000	0.000	0.000	0.003	0.000	0.001
Sum	17.146	17.130	17.105	17.194	17.185	17.117	17.145	17.147	17.146

Table 5.24 Microprobe analyses of staurolite for the staurolite-garnet-mica schist (SIT 02)

	core	rim	core	rim	core	rim	core	rim	core	rim	average core	average rim	average
SiO_2	28.196	28.163	28.886	28.321	28.303	28.971	28.266	28.102	28.565	28.468	28.443	28.405	28.424
TiO_2	0.030	0.050	0.120	0.040	0.060	0.111	0.000	0.010	0.000	0.110	0.042	0.064	0.053
Al_2O_3	55.808	56.217	56.348	55.911	56.561	56.720	56.276	56.065	55.895	55.788	56.178	56.140	56.159
FeO	12.639	13.095	12.761	12.800	12.428	11.769	12.738	12.094	12.444	12.815	12.602	12.515	12.558
MnO	0.112	0.111	0.106	0.152	0.168	0.125	0.150	0.098	0.097	0.134	0.127	0.124	0.125
MgO	1.638	1.658	1.649	1.559	1.304	1.264	1.408	1.417	1.583	1.554	1.516	1.490	1.503
CaO	0.000	0.000	0.000	0.000	0.000	0.000	0.000	0.000	0.000	0.000	0.000	0.000	0.000
Na_2O	0.000	0.000	0.000	0.000	0.000	0.000	0.000	0.000	0.000	0.000	0.000	0.000	0.000
K_2O	0.000	0.000	0.000	0.000	0.000	0.000	0.000	0.000	0.000	0.000	0.000	0.000	0.000
Cr_2O3	0.000	0.000	0.000	0.000	0.000	0.000	0.000	0.000	0.000	0.000	0.000	0.000	0.000
NiO	1.371	1.316	1.170	1.384	1.650	1.618	1.487	1.511	1.403	1.446	1.416	1.455	1.436
Total	99.794	100.610	101.040	100.167	100.474	100.578	100.325	99.297	99.987	100.315	100.324	100.193	100.259
Ox	48	48	48	48	48	48	48	48	48	48	48	48	48
Si	7.993	7.935	8.074	8.005	7.968	8.107	7.976	7.988	8.069	8.036	8.016	8.014	8.015
Ti	0.006	0.010	0.025	0.008	0.012	0.023	0.000	0.002	0.000	0.023	0.009	0.013	0.011
Al	18.648	18.669	18.564	18.627	18.768	18.709	18.717	18.784	18.610	18.562	18.661	18.670	18.666
Fe	2.997	3.086	2.983	3.026	2.926	2.754	3.006	2.875	2.940	3.025	2.970	2.953	2.962
Mn	0.027	0.026	0.025	0.036	0.040	0.030	0.036	0.024	0.023	0.032	0.030	0.030	0.030
Mg	0.692	0.696	0.687	0.657	0.547	0.527	0.592	0.600	0.667	0.654	0.637	0.627	0.632
Ca	0.000	0.000	0.000	0.000	0.000	0.000	0.000	0.000	0.000	0.000	0.000	0.000	0.000
Na	0.000	0.000	0.000	0.000	0.000	0.000	0.000	0.000	0.000	0.000	0.000	0.000	0.000
K	0.000	0.000	0.000	0.000	0.000	0.000	0.000	0.000	0.000	0.000	0.000	0.000	0.000
Cr	0.000	0.000	0.000	0.000	0.000	0.000	0.000	0.000	0.000	0.000	0.000	0.000	0.000
Ni	0.313	0.298	0.263	0.315	0.374	0.364	0.337	0.345	0.319	0.328	0.321	0.330	0.326
Sum	30.676	30.721	30.620	30.673	30.636	30.515	30.665	30.618	30.627	30.660	30.645	30.638	30.641

APPENDIX 6

SHRIMP U-Pb ZIRCON ANALYSES

Table 6.1 Summary of SHRIMP U-Pb zircon data for the sample BB16

Grain.Spot	% $^{206}Pb_c$	ppm U	ppm Th	$^{232}Th/^{238}U$	ppm $^{206}Pb^*$	(1) $^{206}Pb/^{238}U$ Age		(1) $^{207}Pb/^{206}Pb$ Age		% Discordant	(1) $^{207}Pb^*/^{206}Pb^*$	±%	(1) $^{207}Pb^*/^{235}U$	±%	(1) $^{206}Pb^*/^{238}U$	±%	err corr
1.1	0.41	808	197	0.25	118	1,004	±27	2,073	± 15	52	0.1281	0.85	2.978	3.0	0.1685	2.9	.959
2.1	1.07	930	371	0.41	113	847	±23	1,810	± 38	53	0.1106	2.1	2.141	3.5	0.1403	2.9	.809
3.1	1.90	903	328	0.38	105	804	±22	1,874	± 54	57	0.1146	3.0	2.099	4.1	0.1328	2.9	.693
4.1	0.27	234	211	0.93	67.3	1,857	±48	1,805	± 18	-3	0.1103	0.99	5.08	3.1	0.3338	3.0	.948
5.1	0.15	67	92	1.41	30.0	2,700	±70	2,620	± 15	-3	0.1764	0.93	12.65	3.3	0.520	3.2	.959
6.1	0.30	644	287	0.46	152	1,562	±40	2,277	± 11	31	0.14411	0.61	5.45	2.9	0.2742	2.9	.978
7.1	0.86	1072	334	0.32	132	858	±23	1,568	± 54	45	0.0970	2.9	1.904	4.1	0.1424	2.9	.709
8.1	0.94	762	249	0.34	122	1,090	±29	2,014	± 24	46	0.1239	1.4	3.147	3.2	0.1842	2.9	.904
9.1	0.19	492	356	0.75	147	1,919	±48	2,477	± 11	23	0.1620	0.64	7.74	2.9	0.3467	2.9	.976
10.1	0.00	115	137	1.23	50.1	2,655	±66	2,648	± 12	0	0.1794	0.70	12.61	3.1	0.510	3.0	.974
11.1	0.23	432	238	0.57	146	2,132	±52	2,475.0	± 9.4	14	0.16185	0.56	8.75	2.9	0.392	2.9	.982
12.1	13.76	603	245	0.42	119	1,166	±33	2,167	±320	46	0.135	18	3.70	18	0.1983	3.1	.170
13.1	0.10	223	129	0.60	87.9	2,436	±59	2,599.1	± 9.1	6	0.17427	0.55	11.03	3.0	0.459	2.9	.983
14.1	0.10	228	172	0.78	77.6	2,153	±54	2,658	± 12	19	0.1805	0.71	9.87	3.0	0.397	2.9	.972
15.1	0.82	1311	377	0.30	125	671	±18	1,254	± 50	46	0.0824	2.5	1.247	3.8	0.1098	2.9	.746
16.1	0.09	239	267	1.15	93.6	2,422	±59	2,618.0	± 8.8	7	0.17626	0.53	11.08	3.0	0.456	2.9	.984
17.1	0.73	838	275	0.34	116	955	±26	2,020	± 28	53	0.1244	1.6	2.738	3.3	0.1596	2.9	.877
17.2	0.25	345	204	0.61	95.6	1,799	±46	2,532	± 12	29	0.1674	0.70	7.43	3.0	0.3220	2.9	.972
18.1	0.21	442	350	0.82	104	1,559	±40	2,477	± 20	37	0.1620	1.2	6.11	3.1	0.2735	2.9	.928
22.1	0.92	851	281	0.34	103	841	±23	1,730	± 25	51	0.1059	1.4	2.035	3.2	0.1394	2.9	.901
23.1	0.52	1042	344	0.34	190	1,233	±32	1,430	± 33	14	0.0902	1.7	2.622	3.3	0.2108	2.9	.857
24.1	0.40	644	191	0.31	110	1,166	±30	2,354	± 11	50	0.15074	0.66	4.12	2.9	0.1982	2.9	.974
25.1	1.50	574	376	0.68	82.5	984	±26	2,215	± 28	56	0.1390	1.6	3.16	3.3	0.1649	2.9	.873
26.1	0.45	1284	440	0.35	133	730	±20	1,470	± 17	50	0.09214	0.90	1.524	3.0	0.1200	2.8	.953
27.1	0.04	276	106	0.40	113	2,506	±60	2,653	± 21	6	0.1800	1.3	11.79	3.2	0.475	2.9	.914
28.1	0.63	763	417	0.56	97.3	887	±24	1,976	± 17	55	0.1214	0.93	2.469	3.0	0.1475	2.8	.950
28.2	--	70	114	1.69	31.9	2,744	±69	2,645	± 12	-4	0.1792	0.73	13.11	3.2	0.531	3.1	.974
29.1	0.78	1187	563	0.49	111	661	±18	1,293	± 30	49	0.0840	1.5	1.251	3.2	0.1080	2.8	.879
29.2	0.50	816	334	0.42	109	929	±25	2,082	± 16	55	0.1288	0.92	2.754	3.0	0.1551	2.9	.952
30.1	0.07	3067	83	0.03	223	523	±14	532	± 13	2	0.05805	0.61	0.677	2.9	0.0846	2.8	.978
31.1	0.27	364	277	0.79	83.4	1,520	±39	2,335	± 10	35	0.14901	0.61	5.46	2.9	0.2659	2.9	.978
32.1	5.11	250	173	0.71	69.2	1,717	±45	2,463	± 81	30	0.1607	4.8	6.76	5.6	0.3052	3.0	.525
33.1	--	9	14	1.55	2.66	1,855	±72	2,309	± 62	20	0.1468	3.6	6.75	5.7	0.333	4.4	.777
34.1	0.64	840	260	0.32	106	876	±23	1,912	± 17	54	0.1171	0.96	2.348	3.0	0.1455	2.9	.948
35.1	3.97	830	400	0.50	114	923	±25	1,851	± 87	50	0.1131	4.8	2.40	5.6	0.1539	2.9	.515
36.1	0.11	437	209	0.49	118	1,756	±44	2,441.0	± 7.5	28	0.15862	0.45	6.85	2.9	0.3130	2.9	.988
37.1	0.03	487	178	0.38	123	1,663	±42	2,541.4	± 6.8	35	0.16836	0.41	6.83	2.9	0.2942	2.9	.990
38.1	0.82	1018	407	0.41	125	856	±23	1,708	± 22	50	0.1046	1.2	2.048	3.1	0.1420	2.8	.919
39.1	4.04	810	406	0.52	162	1,298	±34	2,066	±140	37	0.1276	7.8	3.93	8.3	0.2231	2.9	.352
40.1	0.51	731	544	0.77	109	1,028	±27	2,020	± 15	49	0.1244	0.86	2.965	3.0	0.1729	2.8	.958
41.1	0.07	667	183	0.28	138	1,393	±36	2,488.1	± 6.8	44	0.16310	0.40	5.43	2.9	0.2413	2.8	.990
42.1	0.30	204	207	1.05	63.7	1,993	±50	2,521	± 11	21	0.1664	0.65	8.31	3.0	0.362	2.9	.976
43.1	0.10	4377	84	0.02	323	531	±14	480	± 11	-11	0.05671	0.50	0.671	2.9	0.0858	2.8	.985
43.2	0.26	416	355	0.88	96.2	1,532	±39	2,387.8	± 9.6	36	0.15373	0.57	5.69	2.9	0.2683	2.9	.981
44.1	0.25	476	429	0.93	120	1,652	±42	1,763	± 11	6	0.10782	0.62	4.34	2.9	0.2921	2.9	.978

Errors are 1-sigma; Pb_c and Pb^* indicate the common and radiogenic portions, respectively.

(1) Common Pb corrected using measured ^{204}Pb.

Table 6.2 Summary fo SHRIMP U-Pb zircon data for the sample BB18

Grain. Spot	% $^{206}Pb_c$	ppm U	ppm Th	$^{232}Th/^{238}U$	ppm $^{206}Pb^*$	(1) $^{206}Pb/^{238}U$ Age		(1) $^{207}Pb/^{206}Pb$ Age		% Dis-cor-dant	(1) $^{207}Pb^*/^{206}Pb^*$	±%	(1) $^{207}Pb^*/^{235}U$	±%	(1) $^{206}Pb^*/^{238}U$	±%	err corr
1.1	0.32	738	417	0.58	127	1,173	±19	2,123	± 14	45	0.1319	0.77	3.628	1.9	0.1995	1.7	.911
2.1	0.34	1596	593	0.38	197	864	±14	1,111	± 18	22	0.07661	0.88	1.516	1.9	0.1435	1.7	.886
3.1	0.10	157	140	0.92	61.6	2,421	±38	2,605.0	± 9.4	7	0.17490	0.56	10.99	2.0	0.4559	1.9	.958
4.1	0.05	364	275	0.78	116	2,032	±31	2,533.0	± 8.2	20	0.16752	0.49	8.56	1.8	0.3705	1.8	.964
5.1	0.16	699	365	0.54	120	1,173	±22	2,247	± 24	48	0.1416	1.4	3.898	2.5	0.1996	2.1	.832
5.2	0.64	1794	399	0.23	121	484	± 13	1,070	± 26	55	0.07507	1.3	0.807	3.1	0.0779	2.8	.908
6.1	0.35	735	594	0.83	76.1	730	±12	2,119	± 19	66	0.1316	1.1	2.176	2.1	0.1200	1.8	.849
6.2	1.20	2002	368	0.19	145	514.8	± 8.3	794	± 58	35	0.0656	2.8	0.752	3.2	0.0831	1.7	.522
7.1	0.35	304	323	1.10	52.7	1,180	±20	2,157	± 20	45	0.1345	1.1	3.723	2.1	0.2008	1.8	.849
8.1	0.19	383	241	0.65	98.7	1,688	±27	2,515	± 12	33	0.1658	0.71	6.84	1.9	0.2993	1.8	.929
9.1	0.08	335	400	1.23	113	2,125	±32	2,587.5	± 8.7	18	0.17308	0.52	9.32	1.9	0.3905	1.8	.960
10.1	0.08	1903	569	0.31	114	435.4	± 7.5	905	± 38	52	0.0692	1.9	0.667	2.6	0.0699	1.8	.692
11.1	0.16	359	711	2.05	89.0	1,634	±26	2,420	± 11	32	0.1567	0.64	6.23	1.9	0.2885	1.8	.940
12.1	0.25	153	130	0.87	60.4	2,427	±40	2,600	± 11	7	0.1744	0.67	10.99	2.1	0.4571	2.0	.945
13.1	0.16	115	66	0.59	45.8	2,448	±41	2,615	± 13	6	0.1760	0.80	11.21	2.2	0.4620	2.0	.929
14.1	4.41	457	339	0.77	183	2,362	±35	1,848	± 94	-28	0.1132	4.9	6.89	5.5	0.4425	1.8	.324
15.1	0.15	1124	350	0.32	124	778	±12	1,766	± 13	56	0.10803	0.70	1.910	1.8	0.1282	1.7	.925
16.1	0.09	436	357	0.85	121	1,806	±28	2,497	± 10	28	0.16402	0.59	7.31	1.9	0.3234	1.8	.947
17.1	0.18	605	477	0.81	120	1,336	±21	2,609.4	± 9.4	49	0.17538	0.56	5.57	1.8	0.2302	1.7	.951
18.1	0.28	426	249	0.60	69.2	1,112	±18	1,073	± 25	-4	0.07516	1.2	1.952	2.2	0.1883	1.8	.819
20.1	0.33	701	230	0.34	134	1,287	±20	2,234	± 11	42	0.14054	0.64	4.280	1.8	0.2209	1.7	.935
21.1	0.44	442	643	1.50	57.8	909	±16	1,242	± 41	27	0.0819	2.1	1.709	2.8	0.1514	1.8	.659
22.1	0.18	142	71	0.51	58.6	2,523	±41	2,648	± 16	5	0.1795	0.98	11.85	2.2	0.4791	2.0	.894
23.1	0.15	258	141	0.56	68.4	1,729	±28	2,469	± 13	30	0.1613	0.75	6.84	2.0	0.3076	1.9	.926
24.1	0.04	176	69	0.40	76.9	2,648	±41	2,633.1	± 9.7	-1	0.1779	0.58	12.46	2.0	0.5080	1.9	.956
26.1	0.08	301	221	0.76	107	2,231	±34	2,682.2	± 8.4	17	0.18322	0.51	10.44	1.9	0.4134	1.8	.962
27.1	0.10	140	149	1.10	55.8	2,452	±40	2,628	± 12	7	0.1773	0.70	11.31	2.1	0.4629	2.0	.941
28.1	0.16	409	318	0.80	75.4	1,252	±20	2,549	± 13	51	0.1692	0.79	5.001	2.0	0.2144	1.8	.914
29.1	0.40	624	481	0.80	123	1,328	±21	2,335	± 12	43	0.1491	0.68	4.700	1.9	0.2287	1.7	.928
29.2	0.24	262	245	0.97	75.2	1,855	±30	2,481	± 13	25	0.1625	0.74	7.47	2.0	0.3334	1.8	.925
30.1	1.00	695	420	0.62	101	1,002	±16	2,062	± 26	51	0.1274	1.4	2.953	2.3	0.1681	1.7	.767
31.1	2.60	335	331	1.02	46.6	944	±16	1,173	± 98	20	0.0790	4.9	1.717	5.3	0.1576	1.8	.349
32.1	0.30	904	313	0.36	133	1,015	±16	2,291	± 11	56	0.14534	0.64	3.416	1.8	0.1705	1.7	.934
33.1	0.08	493	367	0.77	68.8	969	±16	2,189	± 12	56	0.13696	0.66	3.063	1.9	0.1622	1.8	.937
34.1	1.40	658	2351	3.69	76.7	809	± 25	2,305	± 51	65	0.1465	3.0	2.70	4.5	0.1338	3.3	.743
36.1	0.05	252	198	0.81	100.0	2,453	± 60	2,640.4	± 9.1	7	0.17865	0.55	11.41	3.0	0.463	3.0	.983
37.1	7.60	359	374	1.08	137	2,221	± 65	2,162	±240	-3	0.135	14	7.6	14	0.411	3.5	.239
39.1	0.13	112	109	1.00	45.6	2,494	± 65	2,653	± 14	6	0.1800	0.87	11.73	3.2	0.472	3.1	.964
40.1	0.20	349	300	0.89	67.9	1,316	± 35	2,676	± 12	51	0.1825	0.72	5.70	3.0	0.2264	2.9	.971
40.2	0.25	974	345	0.37	118	851	± 23	1,631	± 13	48	0.10037	0.68	1.954	2.9	0.1412	2.8	.973
41.1	0.05	179	296	1.71	70.7	2,440	± 61	2,576	± 11	5	0.1719	0.67	10.90	3.1	0.460	3.0	.976
42.1	2.48	455	505	1.15	108	1,541	± 40	2,064	± 49	25	0.1275	2.8	4.75	4.0	0.2700	2.9	.723
43.1	0.02	623	743	1.23	105	1,150	± 30	2,325.1	± 9.2	51	0.14819	0.54	3.99	2.9	0.1954	2.9	.983
44.1	1.18	210	364	1.79	76.1	2,247	± 56	2,470	± 42	9	0.1613	2.5	9.28	3.9	0.417	3.0	.763
45.1	0.14	301	138	0.47	95.2	2,019	± 50	2,570.2	± 8.1	21	0.17128	0.49	8.69	2.9	0.368	2.9	.986
46.1	8.02	358	166	0.48	137	2,214	± 59	2,143	±210	-3	0.133	12	7.53	12	0.410	3.1	.255
47.1	0.10	274	214	0.81	76.1	1,804	± 45	2,687	± 14	33	0.1838	0.83	8.18	3.0	0.3229	2.9	.961
47.2	0.39	1996	938	0.49	134	484	± 13	680	± 25	29	0.06216	1.2	0.669	3.1	0.0780	2.8	.923
48.1	0.26	1264	34	0.03	87.5	498	± 14	473	± 32	-5	0.05652	1.5	0.626	3.2	0.0803	2.9	.890
48.2	0.17	364	195	0.55	95.2	1,712	± 43	2,431	± 11	30	0.1577	0.66	6.61	2.9	0.3042	2.9	.974
49.1	0.03	246	182	0.76	87.2	2,226	± 55	2,584	± 19	14	0.1727	1.1	9.82	3.1	0.412	2.9	.930
50.1	5.12	662	646	1.01	62.7	642	± 18	1,204	±160	47	0.0803	8.1	1.158	8.6	0.1046	2.9	.334
51.1	0.24	577	499	0.89	94.9	1,126	± 29	2,207	± 14	49	0.1384	0.81	3.64	3.0	0.1909	2.8	.962
51.2	0.22	683	193	0.29	104	1,050	± 28	2,035	± 11	48	0.12544	0.61	3.059	2.9	0.1769	2.8	.978
53.1	0.35	1360	299	0.23	119	625	± 17	972	± 20	36	0.07151	1.0	1.004	3.0	0.1018	2.8	.943

Errors are 1-sigma; Pb_c and Pb* indicate the common and radiogenic portions, respectively.
(1) Common Pb corrected using measured ^{204}Pb.

Table 6.3 Summary of SHRIMP U-Pb zircon data for the sample BB39

Grain. Spot	% $^{206}Pb_c$	ppm U	ppm Th	$^{232}Th/^{238}U$	ppm $^{206}Pb^*$	(1) $^{206}Pb/^{238}U$ Age		(1) $^{207}Pb/^{206}Pb$ Age		% Dis-cor-dant	(1) $^{207}Pb^*/^{206}Pb^*$	±%	(1) $^{207}Pb^*/^{235}U$	±%	(1) $^{206}Pb^*/^{238}U$	±%	err corr
1.1	0.06	115	42	0.38	36.1	2,009	±16	2,012	±15	0	0.1238	0.82	6.242	1.3	0.3657	0.94	.754
2.1	0.11	664	246	0.38	177	1,741.7	± 8.9	2,273	±11	23	0.14378	0.62	6.150	0.86	0.3102	0.58	.684
3.1	0.04	279	202	0.75	106	2,355	±15	2,610.6	± 6.7	10	0.17548	0.40	10.671	0.86	0.4411	0.76	.885
4.1	0.04	279	129	0.48	122	2,655	±16	2,726.5	± 6.1	3	0.18820	0.37	13.22	0.83	0.5096	0.75	.897
4.2	0.07	711	95	0.14	209	1,899	±10	2,423.5	± 9.4	22	0.15699	0.55	7.413	0.82	0.3425	0.61	.742
5.1	--	287	196	0.71	130	2,737	±16	2,817.2	± 5.8	3	0.19890	0.35	14.50	0.78	0.5289	0.70	.892
6.1	0.04	73	55	0.78	33.8	2,786	±28	2,723	±15	-2	0.1878	0.90	14.00	1.5	0.5405	1.2	.809
7.1	0.15	108	110	1.05	48.1	2,690	±23	2,634	±12	-2	0.1780	0.70	12.71	1.3	0.5178	1.1	.836
8.1	0.04	337	94	0.29	127	2,340	±13	2,573.8	± 6.4	9	0.17165	0.39	10.359	0.77	0.4377	0.66	.865
9.1	0.03	335	169	0.52	142	2,581	±14	2,678.4	± 6.8	4	0.18279	0.41	12.409	0.78	0.4923	0.67	.852
10.1	0.06	239	135	0.58	93.1	2,412	±15	2,596.1	± 7.3	7	0.17396	0.44	10.885	0.85	0.4538	0.73	.858
11.1	0.04	515	116	0.23	190	2,301	±12	2,655.2	± 4.9	13	0.18025	0.29	10.658	0.67	0.4289	0.60	.899
12.1	0.07	167	71	0.44	65.4	2,414	±16	2,476.1	± 9.5	3	0.16194	0.56	10.14	0.99	0.4543	0.81	.822
13.1	0.05	166	177	1.10	70.8	2,596	±17	2,641.5	± 8.1	2	0.17877	0.49	12.22	0.94	0.4958	0.81	.855
14.1	0.57	708	324	0.47	137	1,303.7	± 6.9	1,989	±14	34	0.12220	0.80	3.776	0.99	0.2241	0.59	.594
15.1	0.00	294	159	0.56	119	2,494	±14	2,650.9	± 6.2	6	0.17979	0.38	11.710	0.79	0.4724	0.69	.878
16.1	0.03	425	186	0.45	186	2,654	±14	2,639.2	± 5.1	-1	0.17852	0.30	12.540	0.70	0.5094	0.63	.901
17.1	0.08	128	117	0.95	54.4	2,587	±19	2,633.6	± 9.9	2	0.1779	0.59	12.12	1.1	0.4939	0.89	.831
18.1	0.23	739	406	0.57	148	1,347.2	± 7.0	2,031.9	± 8.9	34	0.12522	0.50	4.013	0.77	0.2324	0.58	.753
19.1	0.04	288	320	1.15	118	2,505	±16	2,628.2	± 6.2	5	0.17734	0.38	11.614	0.84	0.4750	0.75	.895
20.1	0.07	610	270	0.46	198	2,068	±10	2,555.1	± 5.1	19	0.16974	0.31	8.851	0.66	0.3782	0.59	.888
21.1	0.16	161	140	0.90	54.9	2,155	±15	2,557	±10	16	0.1699	0.61	9.300	1.0	0.3969	0.80	.794
22.1	0.01	305	56	0.19	156	3,014	±17	3,019.9	± 5.1	0	0.22543	0.31	18.53	0.75	0.5960	0.69	.909
23.1	0.13	759	217	0.30	178	1,551.1	± 7.9	2,152.0	± 7.3	28	0.13407	0.42	5.028	0.71	0.2720	0.57	.809
24.1	0.04	105	90	0.89	45.8	2,652	±21	2,717	±10	2	0.1871	0.61	13.13	1.2	0.5090	0.98	.848
25.1	0.01	169	105	0.64	65.1	2,391	±17	2,452.8	± 9.1	3	0.15973	0.54	9.891	10	0.4491	0.84	.840
26.1	0.04	282	61	0.22	118	2,552	±15	2,610.6	± 6.6	2	0.17548	0.40	11.754	0.81	0.4858	0.71	.872
27.1	0.06	230	140	0.63	96.2	2,559	±16	2,601.7	± 7.5	2	0.17454	0.45	11.73	0.87	0.4874	0.75	.858
27.2	0.10	142	67	0.49	55.6	2,422	±20	2,617	±10	7	0.1762	0.60	11.08	1.2	0.4561	0.99	.853
28.1	0.03	161	116	0.74	78.9	2,914	±19	2,857.8	± 7.4	-2	0.20391	0.45	16.07	0.94	0.5716	0.83	.877
29.1	0.01	195	349	1.85	77.4	2,446	±16	2,626.2	± 8.1	7	0.17713	0.48	11.27	0.94	0.4615	0.80	.856
30.1	0.04	253	142	0.58	97.7	2,390	±21	2,623.9	± 7.5	9	0.17689	0.45	10.95	1.1	0.4488	1.0	.917
31.1	0.02	135	88	0.67	55.7	2,533	±21	2,633.1	± 9.6	4	0.1779	0.58	11.81	1.1	0.4814	0.99	.864
31.2	0.39	800	75	0.10	174	1,448.7	± 7.4	1,924	±11	25	0.11788	0.62	4.095	0.84	0.2520	0.57	.681
32.1	0.14	433	240	0.57	146	2,137	±13	2,543.4	± 6.7	16	0.16856	0.40	9.137	0.80	0.3931	0.69	.865
33.1	--	151	67	0.46	80.3	3,107	±21	3,283.2	± 6.4	5	0.2661	0.41	22.72	0.94	0.6193	0.84	.900
34.1	0.15	680	151	0.23	168	1,627	±10	2,292.9	± 7.2	29	0.14544	0.42	5.756	0.83	0.2871	0.72	.864
35.1	0.01	210	64	0.32	85.6	2,506	±16	2,627.7	± 7.6	5	0.17730	0.46	11.62	0.90	0.4752	0.77	.859
36.1	0.06	161	93	0.60	70.8	2,663	±18	2,663.8	± 8.9	0	0.18119	0.54	12.78	10	0.5114	0.84	.842
37.1	0.07	580	376	0.67	179	1,979	±10	2,517.6	± 5.6	21	0.16599	0.33	8.224	0.69	0.3593	0.60	.875
38.1	0.04	373	275	0.76	141	2,349	±22	2,595.6	± 6.1	10	0.17391	0.36	10.54	1.2	0.4397	1.1	.952
39.1	0.03	422	266	0.65	146	2,184	±12	2,549.6	± 6.1	14	0.16918	0.36	9.409	0.75	0.4034	0.65	.874
40.1	0.12	134	88	0.67	62.1	2,773	±20	3,267	±11	15	0.2634	0.70	19.52	1.1	0.5376	0.89	.783

Errors are 1-sigma; Pb_c and Pb^* indicate the common and radiogenic portions, respectively.

Error in Standard calibration was 0.14% (not included in above errors but required when comparing data from different mounts).

(1) Common Pb corrected using measured ^{204}Pb.

Table 6.4 Summary of SHRIMP U-Pb zircon data for the sample BB40

Grain.Spot	% $^{206}Pb_c$	ppm U	ppm Th	$^{232}Th/^{238}U$	ppm $^{206}Pb^*$	(1) $^{206}Pb/^{238}U$ Age		(1) $^{207}Pb/^{206}Pb$ Age		% Discordant	(1) $^{207}Pb^*/^{206}Pb^*$	±%	(1) $^{207}Pb^*/^{235}U$	±%	(1) $^{206}Pb^*/^{238}U$	±%	err corr
1.1	0.02	365	233	0.66	135	2,308	±13	2,697.7	± 5.8	14	0.18494	0.35	10.976	0.76	0.4304	0.67	.884
2.1	0.05	244	226	0.96	103	2,576	±16	2,629.2	± 7.0	2	0.17746	0.42	12.02	0.86	0.4912	0.75	.871
3.1	0.04	448	356	0.82	92.3	1,386.1	± 8.2	2,640.8	± 7.6	48	0.17870	0.46	5.911	0.80	0.2399	0.66	.820
4.1	0.02	431	250	0.60	181	2,569	±15	2,620.4	± 5.3	2	0.17652	0.32	11.919	0.77	0.4897	0.70	.909
5.1	0.13	705	305	0.45	117	1,139.2	± 6.7	2,666.0	± 6.5	57	0.18144	0.39	4.835	0.75	0.1933	0.64	.853
6.1	0.07	223	102	0.47	93.7	2,561	±16	2,623.2	± 8.0	2	0.17681	0.48	11.89	0.91	0.4879	0.77	.846
7.1	0.03	255	232	0.94	109	2,609	±17	2,644.8	± 6.8	1	0.17913	0.41	12.32	0.90	0.4990	0.80	.892
8.1	0.04	284	148	0.54	119	2,552	±15	2,637.1	± 6.6	3	0.17830	0.40	11.943	0.82	0.4858	0.72	.874
9.1	0.09	665	290	0.45	207	1,995	±10	2,543	±13	22	0.1685	0.75	8.429	0.96	0.3628	0.60	.624
10.1	0.16	881	529	0.62	157	1,213.6	± 6.4	2,272.3	± 7.8	47	0.14371	0.45	4.104	0.74	0.2071	0.58	.788
11.1	0.02	558	249	0.46	235	2,570	±22	2,619.3	± 4.7	2	0.17640	0.28	11.91	1.1	0.4899	1.0	.963
12.1	0.06	265	89	0.34	109	2,522	±17	2,634.4	± 7.0	4	0.17801	0.42	11.75	0.90	0.4788	0.80	.884
13.1	0.05	391	155	0.41	167	2,600	±14	2,608	±11	0	0.1752	0.69	12.00	0.95	0.4968	0.66	.694
14.1	0.00	279	97	0.36	120	2,622	±17	2,737.6	± 6.3	4	0.18947	0.38	13.11	0.88	0.5019	0.79	.900
15.1	0.05	258	141	0.57	81.1	2,011	±13	2,057	±11	2	0.12699	0.60	6.412	0.96	0.3662	0.75	.784
16.1	0.12	678	255	0.39	163	1,585.5	± 8.4	2,211	±19	28	0.1387	1.1	5.332	1.2	0.2788	0.60	.482
17.1	0.13	66	32	0.50	29.3	2,679	±26	2,791	±14	4	0.1957	0.84	13.91	1.5	0.5153	1.2	.818
18.1	0.03	297	151	0.52	118	2,452	±15	2,684.3	± 6.5	9	0.18345	0.39	11.704	0.81	0.4627	0.71	.876
19.1	0.10	476	690	1.50	112	1,559.5	± 9.8	2,534.5	± 7.5	38	0.16767	0.45	6.327	0.84	0.2737	0.71	.846
20.1	0.09	549	145	0.27	138	1,654.4	±10.0	2,095.9	± 8.1	21	0.12985	0.46	5.238	0.82	0.2926	0.68	.830
21.1	0.10	141	80	0.59	62.2	2,676	±22	2,754	±10	3	0.1914	0.63	13.58	1.2	0.5146	1.0	.849
22.1	--	407	137	0.35	171	2,562	±14	2,723.3	± 5.7	6	0.18783	0.34	12.636	0.75	0.4879	0.67	.888
23.1	0.03	402	167	0.43	171	2,590	±18	2,650.9	± 7.3	2	0.17979	0.44	12.26	0.93	0.4945	0.82	.882
24.1	0.02	425	218	0.53	165	2,407	±14	2,740.6	± 5.6	12	0.18982	0.34	11.848	0.79	0.4527	0.72	.902
25.1	0.05	311	257	0.86	87.4	1,824	±12	2,014	±11	9	0.12398	0.59	5.589	0.95	0.3269	0.74	.778
26.1	0.04	157	117	0.77	68.2	2,644	±21	2,670.2	± 9.1	1	0.1819	0.55	12.72	1.1	0.5071	0.99	.873
27.1	0.04	479	495	1.07	133	1,810	±11	2,712.8	± 6.4	33	0.18664	0.39	8.340	0.80	0.3241	0.70	.876
28.1	0.09	225	208	0.95	70.3	1,995	±14	2,066	±12	3	0.12766	0.65	6.383	1.0	0.3627	0.80	.776
29.1	0.03	189	90	0.49	79.1	2,562	±18	2,738.2	± 8.4	6	0.18954	0.51	12.75	0.98	0.4879	0.84	.855
30.1	0.11	461	136	0.31	136	1,903	±12	2,471.1	± 7.4	23	0.16147	0.44	7.646	0.83	0.3434	0.71	.851
31.1	0.14	88	109	1.27	37.6	2,591	±27	2,690	±13	4	0.1841	0.77	12.56	1.5	0.4946	1.2	.849
32.1	0.21	114	63	0.57	33.4	1,893	±17	2,071	±18	9	0.1281	1.0	6.026	1.5	0.3413	1.0	.714
33.1	0.02	150	78	0.54	60.1	2,468	±19	2,642	±10	7	0.1788	0.60	11.50	1.1	0.4666	0.93	.838
34.1	0.14	163	89	0.56	68.1	2,547	±19	2,621	±11	3	0.1766	0.63	11.80	1.1	0.4846	0.91	.821
35.1	0.09	154	114	0.77	87.2	3,259	±26	3,275.9	± 7.1	1	0.2649	0.45	24.03	1.1	0.6580	1.0	.913
36.1	0.22	505	492	1.01	86.7	1,172.2	± 7.1	2,659.3	± 8.9	56	0.18070	0.53	4.968	0.85	0.1994	0.66	.779
37.1	0.04	218	135	0.64	92.1	2,575	±15	2,633.7	± 6.4	2	0.17793	0.38	12.044	0.81	0.4909	0.71	.879
38.1	0.05	160	73	0.47	54.7	2,162	±19	2,131	±12	-1	0.13250	0.70	7.280	1.2	0.3985	1.0	.821
39.1	0.05	182	101	0.57	78.6	2,630	±18	2,643	±11	0	0.1789	0.66	12.43	1.1	0.5037	0.85	.790
40.1	0.29	94	63	0.69	29.2	1,982	±19	2,043	±25	3	0.1260	1.4	6.25	1.8	0.3601	1.1	.622
41.1	0.04	327	181	0.57	90.9	1,809	±12	2,615.4	± 8.0	31	0.17598	0.48	7.861	0.92	0.3240	0.79	.854
42.1	0.00	119	80	0.69	52.8	2,675	±22	2,714	±11	1	0.1868	0.66	13.25	1.2	0.5144	1.0	.841
43.1	0.04	85	25	0.30	32.9	2,392	±30	2,384	±15	0	0.1534	0.86	9.50	1.7	0.4493	1.5	.865
44.1	0.28	322	401	1.29	57.3	1,210.1	± 9.0	2,599	±12	53	0.1743	0.71	4.962	1.1	0.2065	0.82	.756
45.1	0.03	49	72	1.53	20.2	2,543	±30	2,600	±18	2	0.1744	1.1	11.63	1.8	0.4836	1.4	.804
46.1	0.04	212	111	0.54	75.2	2,224	±17	2,206	±10	-1	0.13828	0.59	7.856	1.1	0.4121	0.90	.839

Errors are 1-sigma; Pb_c and Pb^* indicate the common and radiogenic portions, respectively.

Error in Standard calibration was 0.14% (not included in above errors but required when comparing data from different mounts).

(1) Common Pb corrected using measured ^{204}Pb.

Table 6.5 Summary of SHRIMP U-Pb zircon data for the sample BB38

Grain. Spot	% $^{206}Pb_c$	ppm U	ppm Th	$^{232}Th/^{238}U$	ppm $^{206}Pb^*$	(1) $^{206}Pb/^{238}U$ Age		(1) $^{207}Pb/^{206}Pb$ Age		% Dis-cor-dant	(1) $^{207}Pb^*/^{206}Pb^*$	±%	(1) $^{207}Pb^*/^{235}U$	±%	(1) $^{206}Pb^*/^{238}U$	±%	err corr
1.1	0.33	142	72	0.52	25.8	1,235	±10	1,182	± 33	-4	0.0794	1.7	2.310	1.9	0.2111	0.91	.479
2.1	0.04	286	177	0.64	54.6	1,292.7	± 8.6	1,274	± 15	-1	0.08319	0.75	2.547	1.0	0.2221	0.73	.698
3.1	0.03	447	473	1.09	132	1,900	±11	1,866.8	± 7.7	-2	0.11417	0.43	5.396	0.80	0.3428	0.68	.847
4.1	–	464	209	0.47	206	2,691	±14	2,717.5	± 5.9	1	0.18717	0.36	13.371	0.72	0.5181	0.62	.866
5.1	0.08	210	95	0.47	68.0	2,062	±13	2,035	± 11	-1	0.12547	0.60	6.523	0.97	0.3770	0.76	.786
6.1	0.13	96	62	0.66	27.1	1,826	±16	1,795	± 19	-2	0.1097	1.1	4.953	1.5	0.3274	1.0	.690
7.1	0.21	363	295	0.84	103	1,832	±11	1,866	± 12	2	0.11410	0.64	5.171	0.93	0.3287	0.67	.725
8.1	0.05	397	156	0.41	123	1,988	±11	2,132.6	± 7.5	7	0.13259	0.43	6.603	0.77	0.3612	0.64	.834
9.1	0.10	1296	188	0.15	348	1,751.2	± 8.3	1,927.6	± 5.8	9	0.11809	0.32	5.082	0.63	0.3121	0.54	.858
10.1	0.07	266	163	0.63	70.2	1,724	±11	1,706	± 12	-1	0.10454	0.66	4.420	0.97	0.3066	0.72	.736
11.1	0.09	271	114	0.43	87.2	2,049	±14	2,046	± 10	0	0.12621	0.58	6.512	0.97	0.3742	0.78	.802
12.1	2.38	736	380	0.53	108	994.4	± 6.1	1,225	± 73	19	0.0812	3.7	1.866	3.8	0.1668	0.66	.175
13.1	0.26	1077	375	0.36	130	844.9	± 4.5	1,130	± 17	25	0.07735	0.85	1.494	1.0	0.14004	0.57	.556
14.1	0.10	660	89	0.14	216	2,076	±11	2,438.0	± 8.5	15	0.15834	0.50	8.295	0.80	0.3799	0.62	.776
15.1	0.03	462	382	0.86	180	2,412	±12	2,608.6	± 5.1	8	0.17527	0.30	10.968	0.69	0.4538	0.62	.897
16.1	1.06	313	273	0.90	82.1	1,700	±12	1,846	± 85	8	0.1129	4.7	4.69	4.8	0.3017	0.83	.173
17.1	1.54	2820	381	0.14	371	904.2	± 4.8	1,616	± 50	44	0.0996	2.7	2.068	2.7	0.15058	0.57	.209
18.1	0.14	125	167	1.38	34.1	1,776	±14	1,777	± 22	0	0.1087	1.2	4.752	1.5	0.3172	0.93	.615
20.1	0.23	715	703	1.02	130	1,235.4	± 6.5	2,386.4	± 7.7	48	0.15360	0.45	4.474	0.73	0.2112	0.58	.788
21.1	0.32	802	299	0.39	134	1,139.5	± 6.2	1,829	± 15	38	0.11181	0.85	2.981	1.0	0.1934	0.59	.574
22.1	0.10	112	104	0.96	29.9	1,745	±14	1,851	± 20	6	0.1132	1.1	4.849	1.4	0.3108	0.92	.634
23.1	0.06	119	92	0.80	21.7	1,240	±11	1,381	± 22	10	0.0879	1.2	2.572	1.5	0.2121	0.94	.628
24.1	0.15	267	173	0.67	51.3	1,297.7	± 9.3	1,381	± 17	6	0.08792	0.88	2.703	1.2	0.2230	0.79	.668
25.1	0.78	261	289	1.14	51.3	1,320.3	± 8.8	1,880	± 24	30	0.1150	1.3	3.605	1.5	0.2273	0.74	.483
25.2	0.73	751	347	0.48	123	1,119.3	± 6.2	1,769	± 27	37	0.1082	1.5	2.828	1.6	0.1896	0.61	.376
26.1	0.15	160	102	0.66	35.5	1,475	±11	1,762	± 19	16	0.1078	1.0	3.821	1.3	0.2571	0.82	.617
27.1	0.08	218	817	3.87	60.5	1,802	±12	1,863	± 12	3	0.11394	0.64	5.065	0.99	0.3224	0.75	.760
28.1	0.24	143	161	1.16	25.4	1,206	±11	1,307	± 30	8	0.0846	1.5	2.401	1.8	0.2058	0.99	.541
29.1	0.10	154	64	0.43	28.9	1,268	±10	1,222	± 28	-4	0.0810	1.4	2.429	1.7	0.2174	0.88	.525
30.1	2.42	2127	1265	0.61	332	1,051.6	± 5.7	1,721	± 57	39	0.1054	3.1	2.574	3.1	0.1772	0.59	.187
31.1	0.96	979	423	0.45	136	959.7	± 5.2	1,139	± 35	16	0.0777	1.8	1.719	1.9	0.16053	0.58	.310
32.1	0.10	231	210	0.94	90.1	2,415	±16	2,629.8	± 7.7	8	0.17752	0.47	11.12	0.92	0.4545	0.79	.863
33.1	0.14	258	226	0.90	47.2	1,242.7	± 8.2	1,229	± 20	-1	0.08130	1.0	2.383	1.2	0.2126	0.73	.585
34.1	0.49	341	303	0.92	54.9	1,102.9	± 6.9	1,273	± 26	13	0.0832	1.3	2.140	1.5	0.1866	0.68	.458
35.1	0.38	550	163	0.31	83.2	1,041.7	± 6.0	1,182	± 24	12	0.07940	1.2	1.920	1.4	0.1754	0.63	.458
36.1	0.06	266	126	0.49	110	2,523	±14	2,617.3	± 6.5	4	0.17618	0.39	11.638	0.79	0.4791	0.69	.869
37.1	0.02	155	101	0.67	64.2	2,530	±17	2,631.5	± 8.4	4	0.17770	0.51	11.77	0.96	0.4805	0.82	.851
38.1	0.07	212	197	0.96	61.9	1,882	±14	1,884	± 13	0	0.11528	0.71	5.388	1.1	0.3390	0.84	.762
39.1	0.15	1024	262	0.26	156	1,048.8	± 5.5	1,191	± 12	12	0.07976	0.59	1.943	0.82	0.1767	0.57	.694

Errors are 1-sigma; Pb_c and Pb^* indicate the common and radiogenic portions, respectively.
(1) Common Pb corrected using measured ^{204}Pb.

GEOLOGICAL LEGEND

RECENT

- Q — Alluvium, clay and sand

NEOPROTEROZOIC MESOZOIC

KARO SUPER GROUP
- Kg — Conglomeratic grit
- R — Tholeiitic basalt
- B — Basaltic dyke

MATAMBO GROUP
- NHg — Nhansipfe megacrystic gneiss
- TCg — Tchinhadzandze gneiss
- VAg — Vanduzi hornblende migmatite gneiss

MADZUIRE GROUP
- CHg — Chimoio gneiss
- Du — Umkondo dolerite

MESOPROTEROZOIC

UMKONDO GROUP
- Uua — Shale, phyllite and siltsone with sandstone bands
- Uq — Quartzarenite intercalated with shale bands
- Uls — Shale and siltstone with sandstone bands
- Uc — Siliceous and calc-hornfels

GAIREZI GROUP
- Fq — Micaceous and white quartzite
- Fs — Staurolite-garnet-chlorite schist and garnet-schist
- NH — Quartzofeldspathic gneiss, quartzofeldspathic schist and staurolite-garnet-mica schist

ARCHAEAN

MANICA GROUP
- MEg — Messica granite gneiss
- VUg — Vumba granite gneiss
- Mss — Schist and metagreywacke
- Mbk — Basalt, komatiite, talc-schist and chlorite-schist
- Mps — Serpentinite, peridotite, tremolite- actinolite- and chlorite-schist, BIF and banded magnetite quartzite

SPECIAL SYMBOLS

- M — Marble
- Q — Quartz vein

GEOLOGICAL SYMBOLS

- 30 — Plunge and plunge direction of minor fold axis
- 45 — Plunge and plunge direction of lineation
- 15 — Strike and dip of fracture
- 10 — Plunge and plunge direction of fold axis
- 32 — Strike and dip of bedding/layering
- 15 — Strike and dip of cleavage
- Shear zones with sinistral displacement
- Shear zones with dextral displacement
- Geolological boundary
- Tectonic contact
- Fault
- Normal fault with downthrow
- Thrust
- Unconformity
- TSE 09 — Outcrop with sample location and number

TOPOGRAPHIC SYMBOLS

- Contour at 100 m intervals
- Road and track
- River
- International border
- Railway
- Binga — Mountain name
- Dombe — Town/village
- 1250 — Altitude (m)
- Lake

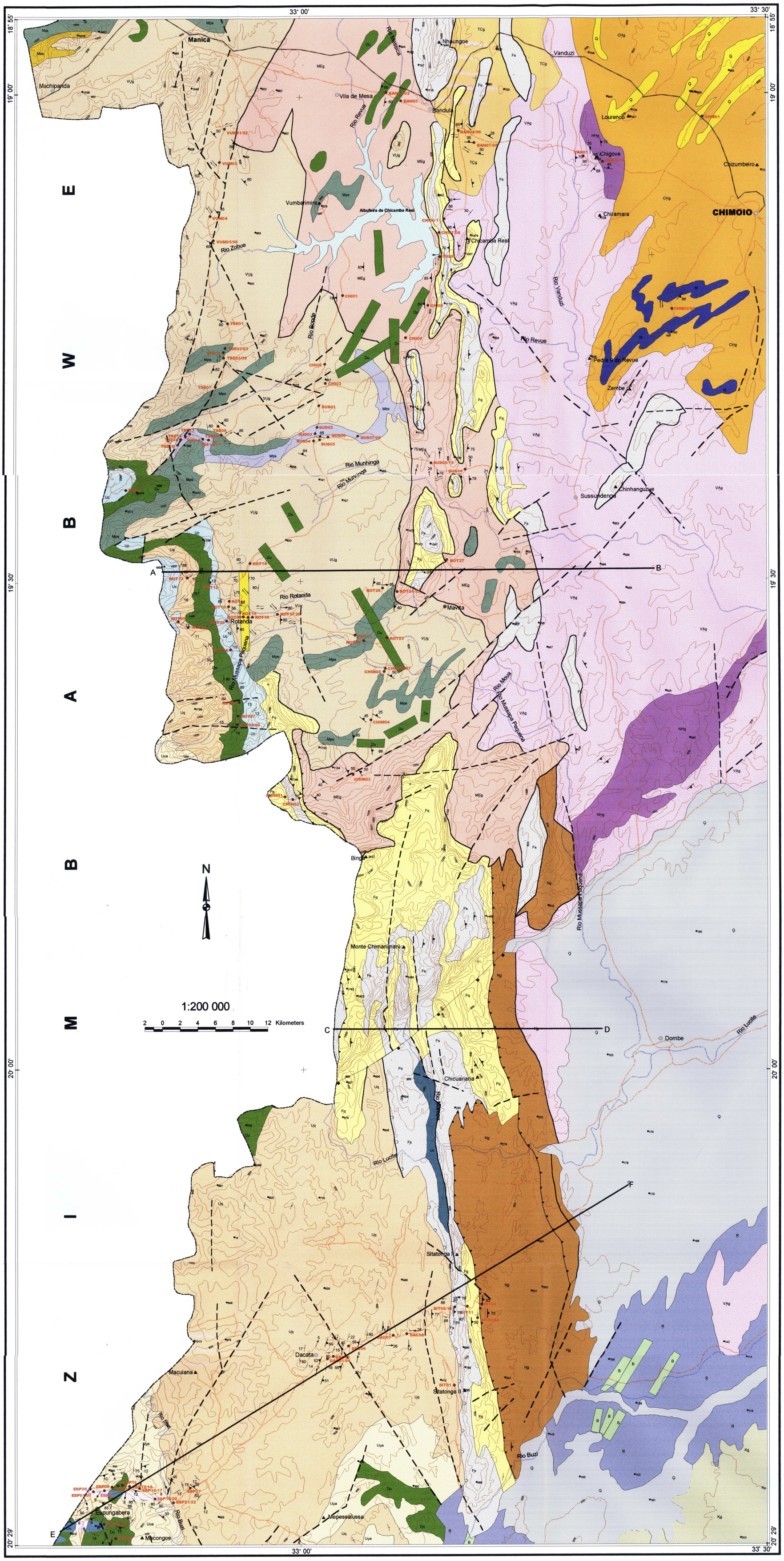

GEOLOGICAL MAP OF WESTERN CENTRAL MOCAMBIQUE (After Hunting G.G. 1984 and Pinna et al., 1987)